Studies of the High Temperature Properties of Graphite and Liquid Carbon Using Pulsed Laser Heating

Vol. 1

by

John W. Steinbeck

S.B., Physics, Massachusetts Institute of Technology
(1983)

S.B., Mathematics, Massachusetts Institute of Technology
(1985)

SUBMITTED TO THE DEPARTMENT OF Physics
IN PARTIAL FULFILLMENT OF THE
REQUIREMENTS FOR THE
DEGREE OF

Doctor of Philosophy

at the

MASSACHUSETTS INSTITUTE OF TECHNOLOGY
11 August 1987

Signature of Author _____
Department of Physics
11 August 1987

Certified by _____
Institute Professor of Electrical Engineering and Physics
Thesis Supervisor

Accepted by _____
George F. Koster
Chairman, Department Committee on Graduate Students

Vol. 1

Studies of the High Temperature Properties of Graphite
and Liquid Carbon Using Pulsed Laser Heating

by

John W. Steinbeck

Submitted to the Department of Physics on 11 August 1987
in partial fulfillment of the requirements for the degree of
Doctor of Philosophy.

Abstract

The properties of high temperature graphite and liquid carbon have been studied through the use of pulsed laser heating. The studies are accomplished through a series of laser heating experiments which directly and indirectly yield information about the thermodynamic properties of liquid carbon. Using pulsed laser heating on the nanosecond time scale, the melting temperature of graphite is shown to be $\sim$ 4500K and the heat of fusion is $\sim$ 125kJ/mole.

Post–heating studies of resolidified carbon indicate that laser–melted carbon exhibits similar crystallization behavior as other laser–melted materials. Transient measurements of the properties of liquid carbon during pulsed laser heating on the nansecond time scale are hindered by rapid vaporization of carbon and the photoconductance of disordered carbons. The results of pulsed laser heating on the picosecond time scale indicate that the melting of graphite at low pressure is a complicated process in which vaporization may play a key role. The results of pulsed current heating studies strongly suggest that liquid carbon is a liquid metal with an electrical resistivity of $\sim 30\mu\Omega$–cm.

Liquid metal theory has been applied to liquid carbon to develop a model for the thermal, electrical and optical properties. Numerical heat flow calculations using the liquid metal model are able to reproduce experimental results obtained from pulsed laser and pulsed current melted graphite. An insulating model for liquid carbon is shown to be unable to reproduce the results of post–heating studies on laser–melted carbon.

From our experimental results and calculations, the low pressure, high temperature portion of the carbon phase diagram is considered to consist of a single solid phase, graphite, a single metallic liquid phase, and a vapor phase.

Thesis Supervisor: Mildred S. Dresselhaus
Title: Institute Professor of Electrical Engineering and Physics

Acknowledgements

There are many individuals whose expertise and support aided the progress of this research. I would like to thank my research supervisor Professor Mildred S. Dresselhaus for her guidance and suggestions throughout the course of this project. A special thanks must also be given to Dr. Gene F. Dresselhaus for many hours of guidance and useful discussions. Their patients and faith in my abilities has greatly enriched my graduate studies.

I would like to thank the members of my thesis committee, Professors H. Haus and T. Greytak, for their continued interest in this project. Their suggestions and comments have been helpful in determining the course this work has taken.

A good portion of this work would not have been possible without support from several industrial sources. The Rutherford backscattering, ion channeling and pulsed laser heating could not have been done without the support of Drs. J.M. Poate, D.C. Jacobson, and W.L. Brown at AT&T Bell Laboratories and Drs. D. Djikkamp, N. Stoffel, C. Palstrom and Mr. B. Wilkens at Bell Communications Research. A special thanks must also be given to Dr. R. Edwards of Bell Communications Research for enabling me to work in the Bell Communications Research laboratories. I would also like to thank Dr. A.W. Moore from Union Carbide for our supply of highly oriented pyrolytic graphite. The pulsed current heating of graphite fibers could not have been done without the kind support of Drs. J. Heremans, and C.H. Olk at General

Motors Research Laboratories. Their interest in this project has been greatly appreciated.

A very special thanks must be given to Dr. T.N. Venkatesan of Bell Communications Research. His expertise in pulsed laser heating and ion spectrometry and his patience with me over the past four years has made my graduate studies particularly enriching. His guidance and support has been much appreciated both in and out of the laboratory.

The pulsed laser heating work on the picosecond time scale could not have been done without colloaborating with C.Y. Huang of Los Alamos National Laboratory and A.M. Malvezzi and N. Bloembergen of Harvard Univeristy. Their interest in this work and their expertise has been greatly appreciated. The laser heating work on the picosecond time scale by Dr. G. Eesley at General Motors Research Laboratories has also been greatly appreciated.

There are many individuals who have contributed to this project at MIT. Thanks must be given to Drs. B.S. Elman and G. Braunstein whose initial interest in the laser heating of graphite has lead to this thesis. There are many other individuals who have been helpful during my graduate studies at MIT. The efforts of A. Chaiken, J. Speck, Dr. K. Sugihara, and Dr. G. Doll at MIT and X. Wu at Rutgers University have been greatly appreciated. I would also like to thank Dr. E. Ippen for useful discussions about laser heating.

This work was supported through the AFOSR and through the National Science Foundation through contract Nos. F-49620-85-C-0147 and DMR 83-10482.

I would especially like to thank my parents for their continued love and support throughout all of my studies.

This section would not be complete without thanking my wife, Karen, for her never ending support over the course of my studies at MIT. Finally, I would

like to thank my daughter, Candice Tiffany, for her smiles which have made all of this worth while.

Contents

List of Figures

List of Tables

Chapter 1

Introduction

The phase diagram of carbon in the low pressure, high temperature regime has been a subject of debate for many years[1]. The subjects for debate in the low pressure, high temperature portion of the carbon phase diagram mainly come from the boundaries denoting the solid–liquid–vapor phase transitions. There are many basic questions which must still be answered such as: what are the properties of high temperature graphite? What are the properties of the liquid phase of carbon at low pressure, if liquid carbon exists at low pressure? Once these questions have been answered, the questions about the phase transitions may be readily answered.

In order to study the high temperature, low pressure portion of the carbon phase diagram, it is necessary to achieve temperatures of $\sim$ 5000K while making measurements with conventional equipment which will melt at temperatures $\sim$ 2000K. A number of techniques have been used to make measurements at such extreme temperatures. Most of these involve the use of rapid electric current heating in a pressure vessel[2,3,4]. A simpler approach was taken by Jones[5] to determine the low pressure properties of liquid carbon using electric welding. More recently, laser heating has been used to create liquid carbon at low pressures[6,7,8,9,10].

A review of the progress in determining the carbon phase diagram has been given by Bundy[1]. A similar review of the progress in the carbon phase diagram, concentrating on the graphite–liquid–vapor transition, is given in the next section. The contributions of several investigators are reviewed in the development of the phase diagram of carbon in the low pressure region. A discussion of the different schools of thought about this portion of the carbon phase diagram is also given. The closing section of this chapter summarizes the contents of this thesis.

1.1 The Phase Diagram of Carbon at Low Pressure

As stated above, the carbon phase diagram has been researched by many investigators. A number of investigators[2,3,4,8,11] have concentrated on the high pressure portion of the phase diagram using pulsed current heating. Bundy[2] and Fateeva and Vereschagin[3] have investigated the graphite melting line in the pressure range from 10 to 200kbar. Bundy *et. al.*[11] have also studied the graphite to diamond phase transition. The graphite to diamond transition has also been studied by Rossini and Jessup[12], Kennedy and Kennedy[13] and Bundy[14].

The carbon phase diagram suggested by Bundy[15] accounting for all of the experimental results is shown in Fig. 1.1. The carbon phase diagram in Fig. 1.1 can be divided into three major regions. The first region is the low pressure and low temperature regime which contains a single stable carbon phase, graphite. As the pressure increases, carbon has several metastable phases and then eventually reaches a stable diamond phase; this defines the second region. At high temperatures carbon has several phases. The high pressure phase is thought to be a metallic solid[16,17]. At intermediate pressures and high

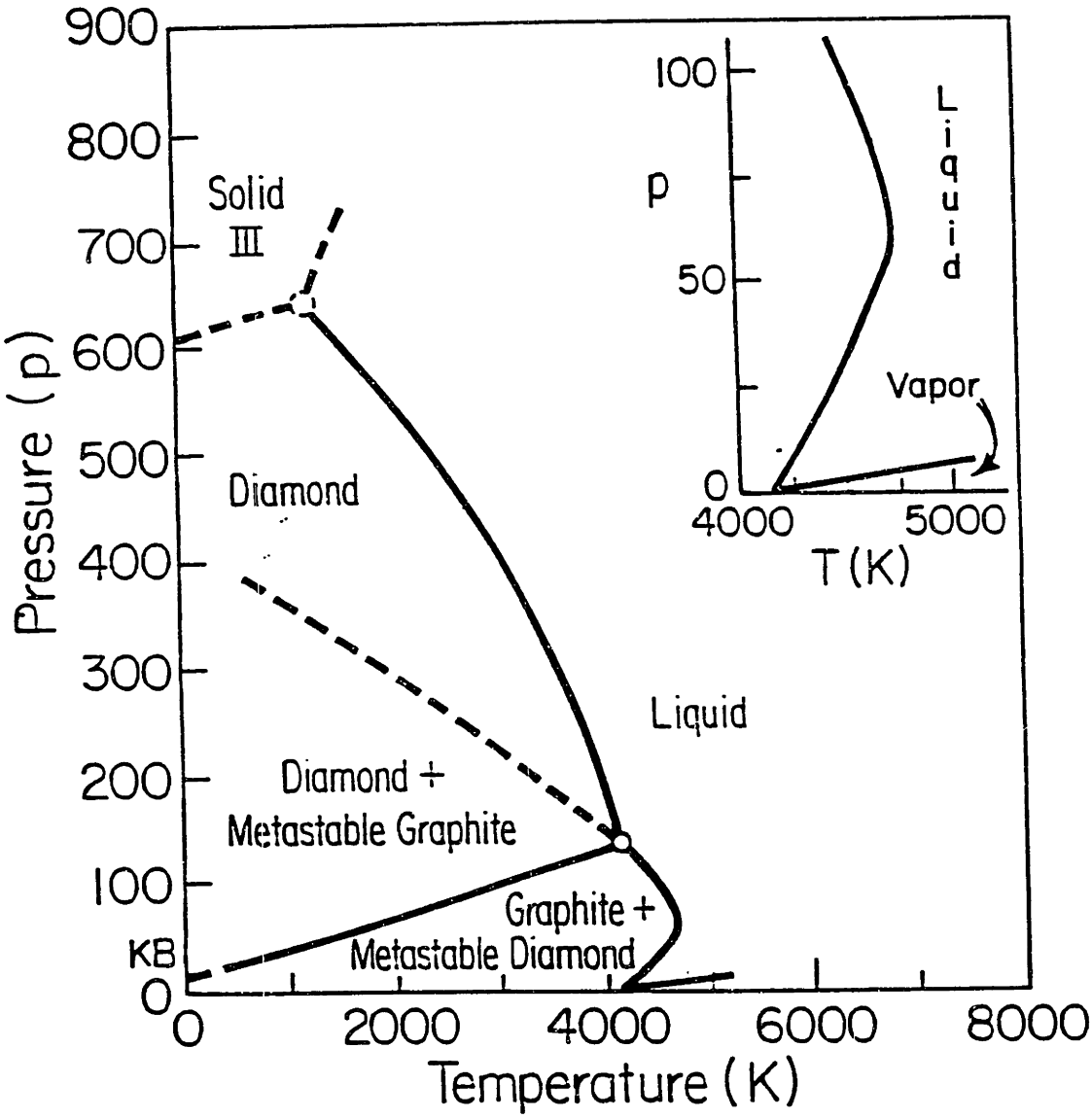

Figure 1.1: The phase diagram suggested by Bundy[15] from the experimental data on the high pressure portion of the phase diagram.

temperatures, carbon enters a liquid state which has been experimentally determined by Bundy[2] to be metallic, similar to theoretical predictions by Van Vechtan[16] and Grover[17].

Although there are many parts of this phase diagram which are debated, there are a few points of agreement. All investigators agree that there are three general regions in the phase diagram, although the details of each region differ from one model to another. Most researchers agree that the triple point for carbon lies at in the pressure range $120 < P < 200$bar and in the temperature range $4100 < T < 4700$K[18,19] although vapor pressure calculations by Leider *et. al.*[20] suggest that the triple point lies at 10bar and 4765K. The transformation of graphite to hexagonal diamond shown in Fig. 1.1 has been reported by both Aust and Drickamer[21] and by Bundy and Kasper[22].

The low pressure portion of the carbon phase diagram has been worked on by many researchers[6,7,9,23,24]. There are a number of different schools of thought on the low pressure portion of the carbon phase diagram. One group of investigators including Gocken *et. al.*[18], Bassett[23], Haaland[25], Baker and Covington[26], and Steinbeck *et. al.*[9] consider graphite to be stable until the lattice melts or until the triple point at $\sim$ 120bar is reached as in Fig. 1.1. Although there is general agreement by these investigators that graphite is the stable form of carbon, the melting temperature and the triple point temperatures vary between research groups in the range $4100 < T < 4500$K.

A second group of investigators including Whittaker[6,27,28,29], and Kasatochikin *et. al.*[30], believes they have found experimental evidence to suggest the existence of stable linearly bonded phases of carbon, carbynes, at temperatures in the range $2700 < T < 4500$K. The phase diagram proposed by Whittaker[28] accounting for the carbyne phases is shown in Fig. 1.2. The evidence for the formation of the carbynes comes from spectroscopic measurements made on

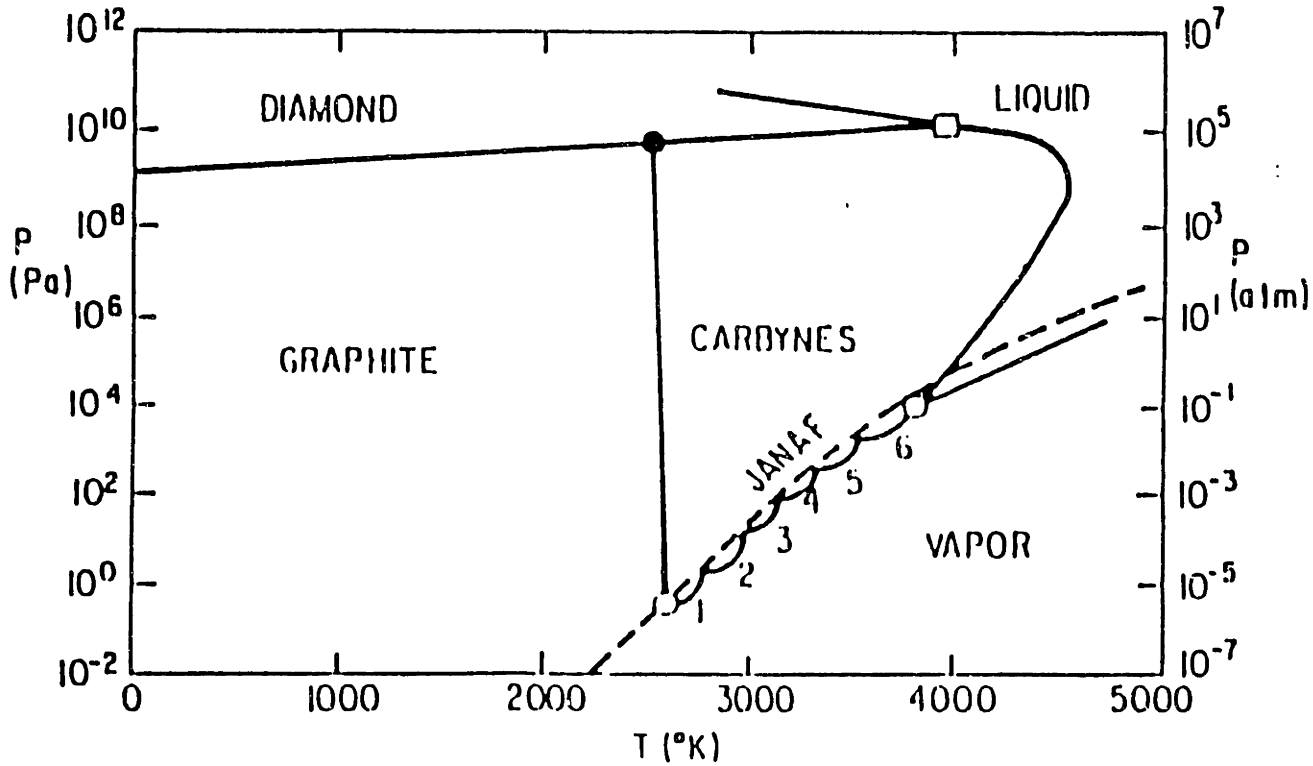

Figure 1.2: The phase diagram of carbon at low pressure according to Whittaker[28]. This phase diagram emphasizes the formation of a solid phase comprised of linear carbon chains (carbynes) at high temperatures.

chaoite, a disordered carbon. The results of the measurements of those who favor this phase diagram are therefore affected by impurities in their starting material. In many cases, the spectroscopic evidence for the carbyne phases cannot be reproduced[31].

Incorporation of liquid carbon in the previous phase diagrams was based solely on the measurements by Bundy[2]. In part, this is due to scarce experimental evidence for the properties of liquid carbon. However, there have been at least several investigations of the properties of the liquid phase of carbon[2,5,9]. The properties of liquid carbon have also been treated theoretically by Leider *et. al.*[20], Gocken *et. al.*[18], and by Kaufman and Nesor[32]. Gocken *et. al.*[18] and Kaufman and Nesor[32] have estimated the entropy of melting of diamond, while Leider *et. al.*[20] have calculated the thermodynamic properties of carbon using the enthalpy of fusion of Bundy[2].

The experiments discussed earlier, that were carried out by Bundy[2] near the graphite–liquid transition, demonstrated that liquid carbon is metallic at pressures greater than 10kbar. The electrical resistivity of the liquid was found by Bundy[2] to be much smaller (by a factor of two) than the electrical resistivity of solid graphite at the melting temperature. Experiments at pressures below 10kbar by Jones[5] indicate that liquid carbon is insulating at low pressure. The experiments by Jones[5] were carried out during graphite welding. When the graphite fused, a large increase in the electrical resistivity was observed. More recent experiments by Shaner *et. al.*[4], indicate that the electrical resistivity of liquid carbon is $\sim$ 1mΩ–cm for temperatures up to 6000K. These observations suggest the existence of at least two liquid phases, one insulating at low pressure, and one metallic at high pressure.

The most extensive study of carbon vaporization has been carried out by Leider *et. al.*[20] where the partial pressures of carbon gas species up to 10000K

Vapor Species	ΔH_f (kJ/mole)	Reference
C_1	710.8	Ref. [33]
C_2	824.2	Ref. [33]
C_3	833.4	Refs. [34,35]
C_4	1010.0	Refs.[34,35]
C_5	1028.9	Refs.[34,35]
C_6	1255.2	Refs.[36]
C_7	1330.5	Refs.[36]

Table 1.1: The heats of formation reported by Drowart *et. al.*[33], Milne *et. al.*[34], Palmer and Shelef[35], and Lee and Sanborn[36] for carbon vapor species C_{1-7}.

were calculated using free energy functions. From their work, Leider *et. al.*[20] concluded that the triple point for carbon was at 4765K and 10bar. The vapor pressure data was confirmed experimentally by Kirillan *et. al.*[37] and by Baker *et. al.*[38], but the triple point in these studies is set at 5000K and $\sim$ 4500K, respectively. The heats of formation for the carbon vapor species have been determined by Drowart *et. al.*[33], Milne *et. al.*[34], Palmer and Shelef[35], and Lee and Sanborn[36]. The values reported for the heats of formation of carbon vapor species are given in Table 1.1. The calculations by Leider *et. al.*[20] also determined that for temperatures near the melting point, the dominant vapor species will be C_3.

The possibility of the existence of two liquid phases was treated theoretically by Ferraz and March[39]. The phase diagram proposed by the Ferraz and March[39] theory is shown in Fig. 1.3. The insulating liquid phase was described as being made up of molecular units of several carbon atoms, possibly carbynes, similar to liquid Se and Te. The metallic liquid phase was described in terms of an atomic liquid metal model analogous to Si and Ge. The theoretical description of the two liquid phases by Ferraz and March[39] was carried out

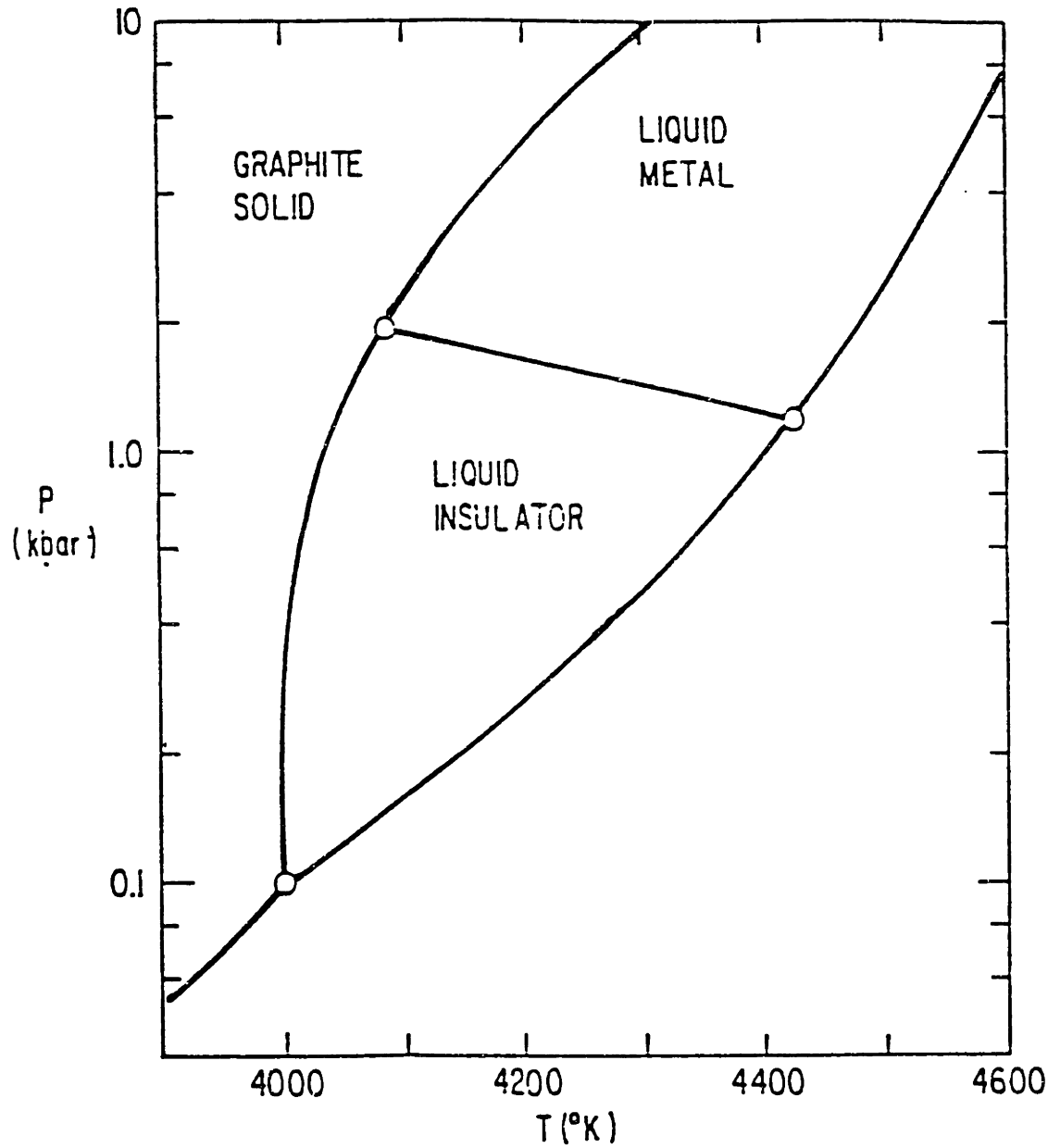

Figure 1.3: The low pressure phase diagram of carbon according to the theory of Ferraz and March[39]. The phase transition between the metallic and insulating liquids is first order.

using Gibbs free energy arguments to demonstrate that the insulating phase of liquid carbon may be a semiconducting liquid with a band gap, Δ, given by

$$\Delta \propto (P_t - P)^{\frac{1}{2}} \tag{1.1}$$

where P is the pressure and P_t is the pressure at which the insulator–metal transition takes place. The phase transition between the two liquid phases is considered to be first order and to occur at a pressure of $\sim$ 1kbar. The dP/dT line of the transition is negative indicating that the metallic liquid phase is more dense than the insulating phase.

The Ferraz–March[39] phase diagram conveniently describes all of the experimental results at low pressure for the liquid phase of carbon. However, the scarcity of experimental measurements on liquid carbon makes any of the proposed carbon phase diagrams questionable at best in the low pressure regime.

A recent calculation by Gustafson[40] gives a simple carbon phase diagram shown in Fig. 1.4. The phase diagram proposed by Gustafson[40] has three carbon phases, a solid graphite phase, a solid diamond phase, and a single liquid phase. Vaporization was not considered in Gustafson's calculations so that the vapor phase is absent from Fig. 1.4.

1.2 The Present Work

This thesis attempts to improve upon the previous work on liquid carbon by providing experimental evidence that liquid carbon is metallic at pressures below 1kbar. The experiments have been carried out using pulsed laser heating with laser pulses on the nanosecond and picosecond time scale. The present study uses high power pulsed laser irradiation as the heating mechanism of graphite samples. The primary advantage of using high power, pulsed, laser radiation as the heating mechanism is that a large amount of energy can be

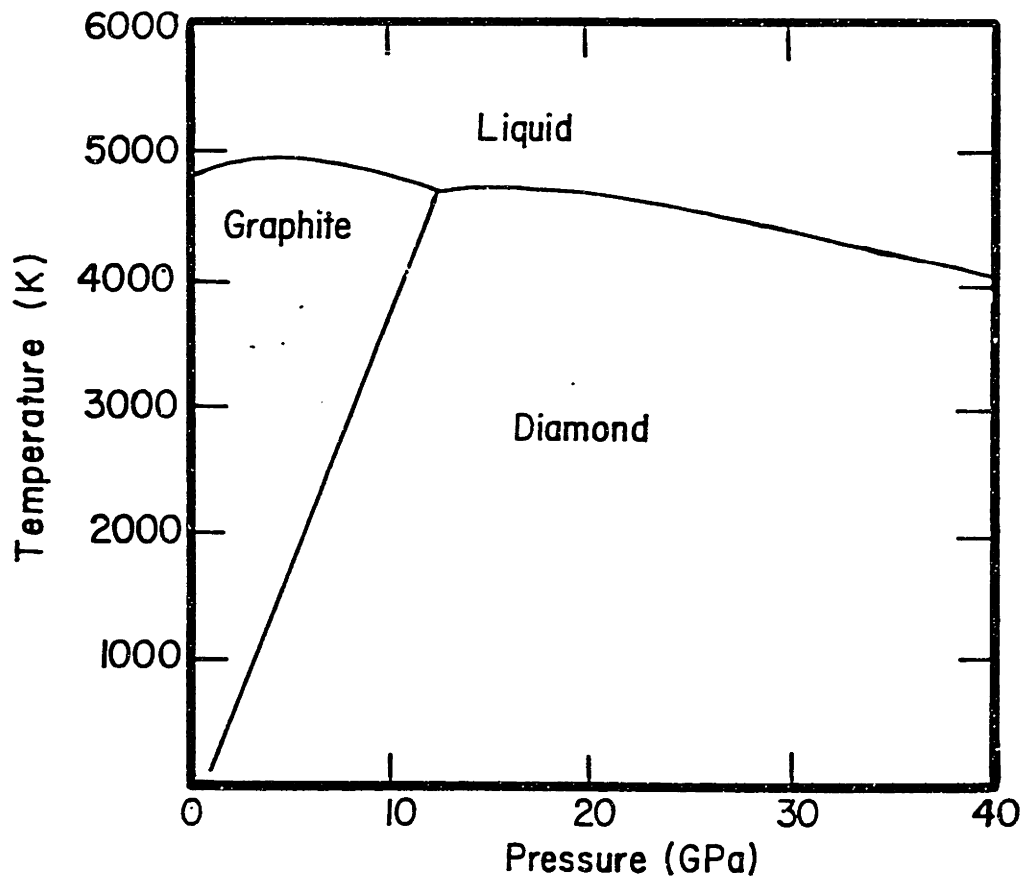

Figure 1.4: The low pressure carbon phase diagram calculated by Gustafson[40].

placed in the graphite lattice in a small time period eliminating the contribution of sublimation processes that have been observed to occur with slower heating techniques such as arc discharge heating. A further advantage is that the graphite substrate will provide its own crucible, eliminating the problems of high temperature confinement and contamination from a noncarbon container.

Pulsed current heating has also been used to create liquid carbon in this study using highly ordered graphite fibers instead of disordered graphites. The advantage of using an ordered graphite is that the differential thermal expansion will not increase the pressure in the fiber which occurs in many of the studies described in the previous section. While studying liquid carbon, the properties of high temperature graphite near the melting temperature will be shown to be a simple extrapolation of the properties of graphite below 3000K.

Chapter 2 will review the properties of graphite at temperatures $T < 3000$K where the properties have been experimentally determined. The chapter will start with a discussion of the structure of the graphite lattice and graphite fibers. The specific heat and thermal conductivity of graphite will then be discussed. The following section will discuss the optical properties of graphite and how the lattice mode spectrum can be used to analyze disordered graphites. The next two sections discuss the electrical properties of graphite and the photoconductance which is present in disordered carbons. The chapter closes with a discussion of carbon vaporization and a model which has been used to describe the high temperature properties of graphite.

Chapter 3 discusses our experimental results from pulsed laser heating of graphite and electric current pulse heating of graphite fibers. The chapter opens with a discussion of laser–materials interactions including phase transitions and the formation of plasmas. We then show that pulsed laser heating can be used to create liquid carbon at low pressure. Graphite is shown to melt using

several complementary post–heating experimental techniques. A discussion of our transient optical and electrical measurements then follows.

The next section in chapter 3 discusses solute segregation in graphite during pulsed laser heating. The solute trapping and segregation phenomena are interesting in that these phenomena depend on the liquid diffusivity of liquid carbon which has never been measured. The segregation coefficient, k, of liquid carbon is also determined from these studies.

The final two sections of chapter 3 are devoted to electric current pulse heating of graphite fibers and pulsed laser heating on the picosecond time scale. These experiments were undertaken to solve the problems encountered in transient measurements during pulsed laser heating on the nanosecond time scale. Post heating studies of the disordered material after picosecond pulse laser heating show that laser heating on the picosecond time scale generates the same liquid as pulsed laser heating on the nanosecond time scale. However, the results of transient optical measurements on the picosecond time scale show that heating on the picosecond time scale is subject to some of the same difficulties as heating on the nanosecond time scale. The results of pulsed current heating measurements on graphite fibers show that liquid carbon is a liquid metal at pressures $<$ 1kbar and that the electrical resistivity of liquid carbon is $\sim 30\mu\Omega$–cm.

The experimental measurements in chapter 3 indicate that liquid carbon is metallic at low pressure. Chapter 4 discusses liquid metal theory and applies liquid metal theory to liquid carbon. The electrical resistivity of liquid carbon is calculated using the model put forth by Ziman[41]. The thermal and optical properties of liquid carbon are calculated using the properties of a Fermi gas, Drude theory, and the Wiedermann–Franz relation which are shown to be applicable to liquid metals.

In chapter 5 the liquid metal model for liquid carbon is tested by using heat flow calculations to reproduce the results obtained from post heating studies on laser heated and electric current heated graphite. The calculations are carried out using the finite difference method of Carslaw and Jaeger[42]. The results of these calculations show that the results from pulsed laser heating and pulsed current heating can be reproduced satisfactorily for all experimental conditions. The calculations also call into question the validity of transient measurements on the picosecond time scale due to a large vaporization of carbon at large pulsed laser energy densities.

In chapter 6 other possibilities for the properties of liquid carbon and some issues not raised in the preceding chapters are discussed. A more careful examination of the liquid structure factor is given showing that if the liquid contains a small amount of molecular character, the properties of the liquid are not greatly affected. Rapid resolidification of liquid carbon will be briefly discussed as it pertains to pulsed laser heating and solute trapping. The possibility that liquid carbon may be a semiconducting or semi–metallic liquid is also discussed.

The final chapter presents the low pressure phase diagram suggested by our work. The phase diagram is simple in that we have only observed a single solid phase at high temperatures and a single liquid phase which is metallic. A summary of the properties of liquid carbon is given and the possibilities for future work in laser heating of graphite and liquid carbon are discussed.

References

[1] F.P. Bundy, *Solid State Physics Under Pressure*, edited by S. Minomura, (Terra Scientific Publishing,1985), p1.

[2] F.P. Bundy, *J. Chem. Phys.* 38, 618 (1963).

[3] N.S. Fateeva and L.F. Vereshagin, *Pisma Zh. Eksp. Teor. Fiz.* 13, 157 (1971).

[4] A.C. Mitchell, J.W. Shaner, and R.N. Keeler, *Physica* 140B, 386 (1986).

[5] M.T. Jones, Rep. PRC-3, Nat. Carbon Res. Lab., Parma, OH (1958).

[6] A.G. Whittaker, *Proceedings of the 13th Biennial Conference on Carbon*, (American Carbon Society), 413 (1977).

[7] T. Venkatesan, D.C. Jacobson, J.M. Gibson, B.S. Elman, G.Braunstein, M.S. Dresselhaus, and G. Dresselhaus, *Phys. Rev. Lett.* 53 360, (1984).

[8] J.S. Gold, W.A. Bassett, M.S. Weathers, and J.M. Bird, *Science* 225, 921 (1984).

[9] J. Steinbeck, G. Braunstein, M.S. Dresselhaus, T. Venkatesan, and D.C. Jacobson, *J. Appl. Phys.* 58, 4374 (1985).

[10] A.M. Malvezzi, N. Bloembergen, and C.Y. Huang, *Phys. Rev. Lett.* 57, 146 (1986).

[11] F.P. Bundy, H.P. Bovenkerk, H.M. Strong, and R.H. Wentorf Jr., *J. Chem. Phys.* 35, 383 (1961).

[12] F.D. Rossini and R.S. Jessup, *J. Res. Nat. Bur. Stds. (U.S.)*, 21, 491 (1938).

[13] C.S. Kennedy and G.C. Kennedy, *J. Geophys. Res.* 81, 2467 (1976).

[14] F.P. Bundy, *J. Chem. Phys.* 38, 631 (1963).

[15] F.P. Bundy, *J. Geophys. Res.* 85, 6930 (1980).

[16] J.A. Van Vechtan, *Phys. Rev.* B7, 1479 (1973).

[17] R. Grover, *High Pres. Sci. and Tech., Proc. 7th Internat. AIRAPT Conf.*, Le Creusot, France, 30 Jul. - 3 Aug. 1979, edited by B. Vodar and P. Marteau.

[18] N.A. Gocken, E.T. Chang, T.M. Posten, and D.J. Spencer, *High Temp. Sci.* 8, 81 (1976).

[19] A. Cezairliyan and A.P. Miller, *Proceedings of the March Meeting of the American Physical Society* 16–20 March 1987, New York, New York, p.608.

[20] H.R. Leider, O.H. Krikorian, and D.A. Young, *Carbon* 11, 555 (1973).

[21] R.B. Aust and H.G. Drickamer, *Science* 140, 817 (1963).

[22] F.P. Bundy and J.S. Kasper, *J. Chem. Phys.* 46, 3437 (1967).

[23] M.J. Bassett, *J. Phys. Radium* 10, 217 (1939).

[24] R.B. Heimann, J. Kleinman, and N.M. Salansky, *Nature* 306, 164 (1983).

[25] D.A. Haaland, Rep. 1976, SAND-76-0074, Sandia Nat. Lab., Albequerque, NM (1976).

[26] R.L. Baker and M.A. Covington, Rep. SD-TR-82-19, Office of Naval Research, Arlington, VA, (1982).

[27] A.G. Whittaker, *Science* 165, 589 (1969).

[28] A.G. Whittaker, *Science* 200, 763 (1978).

[29] A.G. Whittaker, E.J. Watts, R.S. Lewis, and E. Anders, *Science* 209, 1512 (1980).

[30] V.I. Kasatochikin, A.M. Sladkov, Y.P. Kudryavtsev, N.M. Popov, and V.V. Korshak, *Dokl. Chem.* 177, 1031 (1967).

[31] P.P.K. Smith and P.R. Buseck, *Science* 216, 984 (1982).

[32] L. Kaufman and H. Nesor, *Treatise on Solid State Chemistry* 5, edited by N.B. Hannay, (Plenum, New York, 1975) p.179.

[33] J. Drowart, R.P. Burns, G. DeMaria, and M.J. Inghram, *J. Chem. Phys.* 31, 113 (1959).

[34] T.A. Milne, J.E. Beachey, and F.T. Greene, *Technical Management Report* No. 2, Midwest Research Inst., Kansas City, MO, (1971).

[35] H.B. Palmer and M. Shelef in "Chemistry and Physics of Carbon" 1, edited by P.L. Walker and P.A Thrower, (Marcel–Dekker, New York, 1965).

[36] E.L. Lee and R.H. Sanborn, Rep. UCRL-74375, Lawrence Livermore Laboratory, (1972).

[37] A.V. Kirillan, S.P. Malyshenko, M.A. Sheindlin, and V.N. Evseev, *Sov. Phys. Doklady* 26, 422 (1981).

[38] R.L. Baker, M.A. Covington, and G.M. Rosenblatt, *J. Appl. Phys.* to be published.

[39] A. Ferraz and N.H. March, *Phys. Chem. Liq.* 8, 289 (1979).

[40] P. Gustafson, *Carbon* 24, 169 (1986).

[41] J.M. Ziman, *Phil. Mag.* 6, 1013 (1961).

[42] H.S. Carslaw and J.C. Jaeger, *Conduction of Heat in Solids*, (Oxford University Press, New York 1959).

Chapter 2

Properties of Carbon

2.1 Introduction

The properties of graphite is the subject of a book by Kelly[1]. This chapter will give a brief review of the overall properties of graphite and concentrate on the properties in the high temperature regime which is the subject of this work.

The chapter starts with a discussion of the structural anisotropy in graphite and the consequences of the anisotropy on the thermal, optical and electrical properties. The next section discusses the mechanical properties of graphite and the thermal expansion of the graphite lattice. The following section discusses the thermal properties of graphite, emphasizing the thermal conductivity and the specific heat. A brief discussion of the heat of fusion in graphite is also given.

The fourth section contains a description of the optical properties of graphite with an emphasis on the visible region where this work is concentrated. This section includes a discussion of spectroscopic methods which are useful in characterizing graphitic materials. The final section contains a discussion of the electrical properties in graphite. Included in this final section is a discussion of the photoconductance of disordered carbons which are important when con-

sidering the effects of high intensity pulsed lasers on carbon.

2.2 Structural Properties of Graphite

2.2.1 Polycrystalline Graphite

Graphite is an anisotropic material composed of layered planes of connected honeycomb rings of carbon. A view of the crystal lattice of graphite is shown in Fig. 2.1. The planes of the graphite lattice are composed of carbon atoms joined by strong sp^2 hybridized carbon–carbon bonds. The direction along the planes is referred to as the *a* direction. The intercarbon distance in the planes is 1.42Å. The planes arrange themselves into the lowest energy state where neighboring planes are displaced from each other by a $(\frac{1}{2}a, 0)$. There are two types of stacking arrangements which may fulfill this requirement. In hexagonal graphite, the planes alternate their displacements and this is called AB stacking. In rhombohedral graphite, the unit cell contains three graphite planes where the inplane displacement between the first and the third planes is $(\frac{1}{2}a, \frac{1}{2}a)$. The planes are held together by a Van der Waals attraction (dipole–dipole interaction) with an interplanar spacing of 3.35Å. The direction perpendicular to the graphite planes is referred to as the *c* direction.

The stacking of the graphite planes determines the size of the unit cell. In hexagonal graphite with an AB stacking, the unit cell repeat distance along the c–axis is 6.70Å. In rombahedral graphite, the ABC stacking of the graphite planes increases the size of the unit cell along the c–axis to 10.044Å.

The dotted lines in Fig. 2.1 mark the "channel" through which ions may be projected during ion beam analysis of graphitic materials. The channel is directed parallel to the c–axis in graphite. The existence of a channel in graphite is useful for determining the amount of disorder in graphitic materials[2]. Ion beam analysis techniques are discussed in chapter 3.

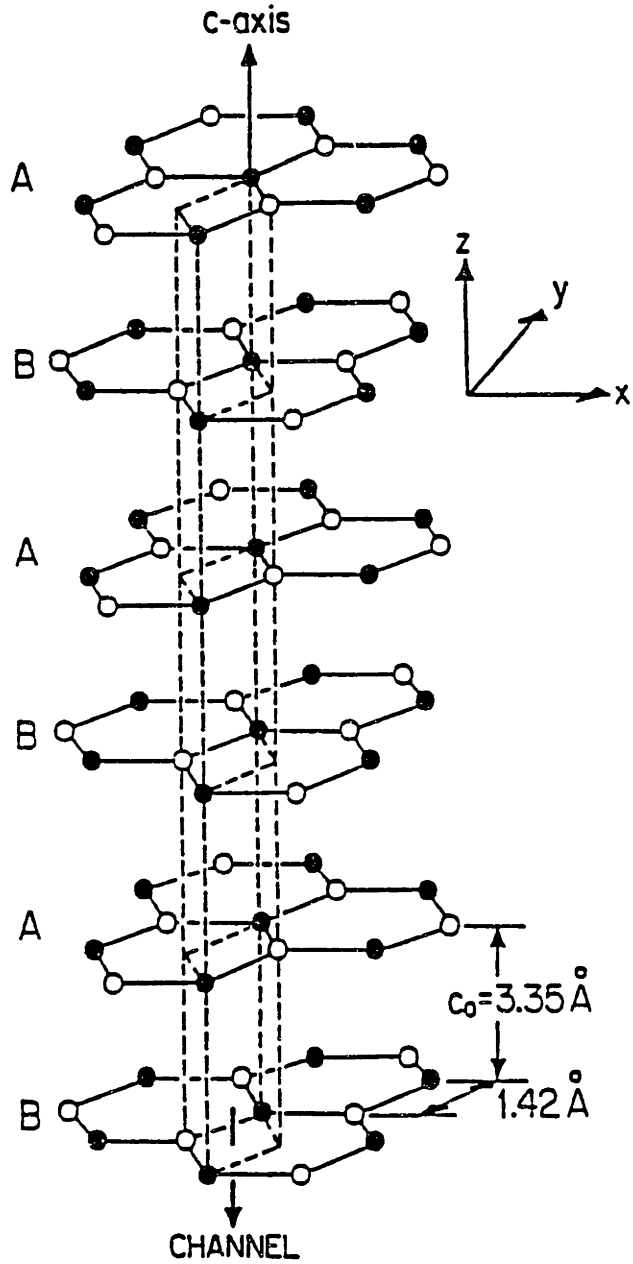

Figure 2.1: The crystal lattice of graphite. Note the alternate stacking of graphene planes. The dotted lines indicate the "channel" through which ions can be passed during ion beam analysis of graphitic materials.

In this work, highly oriented pyrolytic graphite (HOPG) has been used[3] which has the hexagonal structure (AB stacking) shown in Fig. 2.1. This graphitic material was chosen because of its availability and the large size of the polycrystalline pieces which can be manufactured ($\sim 100\text{cm}^2$). The mean crystallite size of the HOPG used in this work is 10μm with a mosaic spread of the c–axis by less than one degree.

The structural anisotropy in graphite leads to large anisotropies in the thermal, electrical, and optical properties of graphite. The effect of the anisotropy of each of these properties will be discussed at length in the following sections. It should be noted that because of the structural anisotropy, the inplane properties of graphite are semi–metallic while the properties perpendicular to the planes are quasi–insulating. The structural anisotropy has consequences in making materials suitable for measurements during pulsed laser heating experiments.

The Van der Waals force holding the layer planes together makes graphite easy to cleave. It is therefore easy to clean the surface of graphite by simply cleaving a portion of the material to form a new clean surface. However, as a consequence, graphite cannot be polished to form good optical surfaces since the graphite planes will peal when using conventional polishing techniques.

The effect of the polycrystalline nature of the material used in our measurements is minimal. The large crystallite size and high degree of orientation of the crystallites in HOPG does not have a large effect on the bulk properties of graphite. This is confirmed by the good agreement between experimentally measured quantities and theoretically predicted quantities, where theoretical calculations are almost always made for a perfect graphite lattice.

2.2.2 Graphite Fibers

Graphite fibers have also been used in a number of pulsed laser and pulsed current heating studies. The graphite fibers used in this work were all grown by chemical vapor deposition techniques[4,5]. A pictorial view of the fiber structures is given in Fig. 2.2. The graphite planes are parallel to the axis of the fibers and the c–axis is radially outward from the fiber axis. The cross–section of the graphite fibers resembles the rings in a tree, where the concentric graphite planes form the rings.

The structure of these graphite fibers is dependent on the heat treatment the fiber receives. As grown graphite fibers are mirocrystalline with small inplane correlation lengths and no c–axis registry. Fibers heat treated to 2500K have larger inplane correlation lengths, but still lack the 3 dimensional structure of graphite. Heat treatment temperatures above 3000K give three dimensional ordering in these fibers.

2.3 Thermal Properties of Graphite

The specific heat and the thermal conductivity of graphite are reviewed in this section for temperatures in the range $300 < T < 3000$K. A knowledge of the thermal properties below 3000K is important for investigating the thermal properties at higher temperatures for the following reasons:

1. The temperature dependence of the thermal properties at temperatures to $\sim$ 3000K can be extrapolated to construct a model for the thermal properties of solid graphite at temperatures $3000 < T < 5000$K (section 2.8).

2. The interpretation of experimental results during pulsed heating (chapter 3) can be compared with the properties of graphite at lower ($T <$

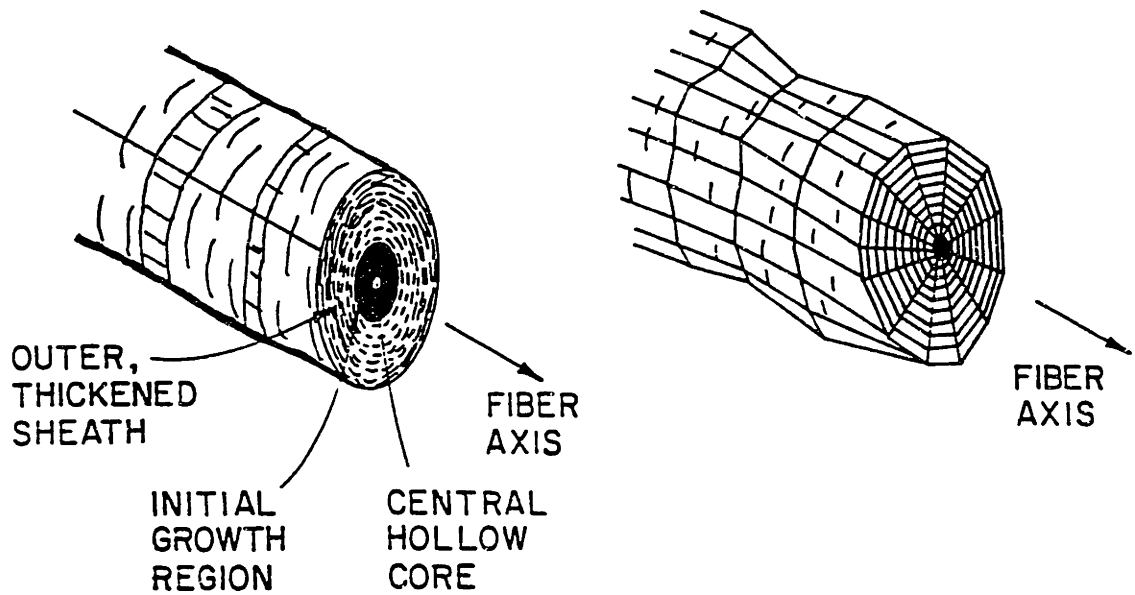

Figure 2.2: A pictorial view of the structure of graphite fibers used in pulsed laser and pulsed current heating experiments and in the photoconductivity studies.

3000K) temperatures.

3. Calculations of heat flow in graphite at high temperature (chapter 5) require a knowledge of the thermal properties at lower ($T < 3000$K) temperatures.

This section begins with a discussion of the specific heat of graphite. The section includes the experimental results of other researchers on the specific heat of graphite up to temperatures $\sim$ 3800K. The following section discusses the inplane and c–axis components of the thermal conductivity of graphite. Thermal conductivity data of other researchers will be shown for both the inplane and c–axis thermal conductivities in graphite and a polynomial fit of the thermal conductivity as a function of temperature is presented.

2.3.1 Specific Heat

The specific heat of pyrolytic graphite at high temperatures and constant pressure has been studied by several researchers[6,7,8]. These researchers usually used natural and pyrolytic graphites in their measurements. A compilation of their work is shown in Fig. 2.3. Since the specific heat is an orientation independent quantity, there are few differences between these graphites and the HOPG used in this work.

The low temperature data ($T < 300$K) are of interest in determining the lattice vibration spectrum. In the temperature range of interest in this work ($300 < T < 5000$K), the specific heat of graphite has a nearly linear temperature dependence as is seen in the experimental data shown in Fig. 2.3 in the range $1500 < T < 3000$. At high temperatures ($T > 3400$K) there is an anomalous increase in the specific heat. The increase in the specific heat above 3400K is reproducible and has been shown to correspond to an activation energy of 7eV[8]. The high temperature data have been explained by Hove[8] and later

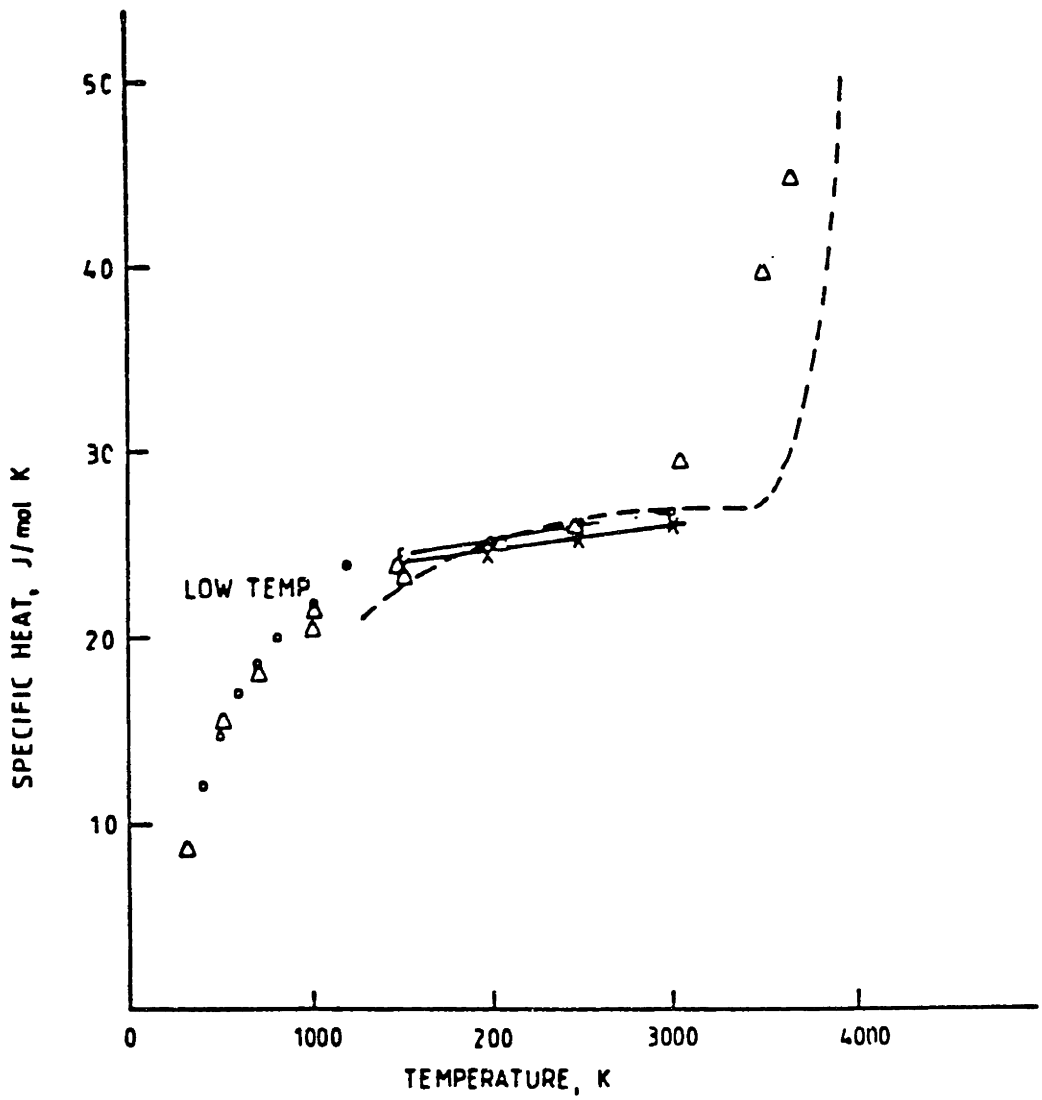

Figure 2.3: Experimental measurements of the specific heat of graphite. The data are due to Cezairliyan[6], Sheindlin[7], and Hove[8]. This figure was compiled by Kelly[1].

confirmed by Rasor and McClelland[9] to be due to the vacancies which exist in the material being measured. The vacancy contribution to the measurement cannot be separated from the measurement. Therefore, in the forthcoming analyses of the specific heat of graphite, the vacancy contribution to the data has been ignored. This assumption is valid since the effect of vacancy formation on the specific heat of the graphite lattice has been shown to be negligible by Hennig[10] since the vacancy concentration will only be 10^{-8}/atom at 3800K.

The specific heat, C_p, for pyrolytic graphite in the temperature range ($1000 < T < 3400$K) has been fit to a line by Cezairliyan and Righini[6] given by

$$C_p = 21.60 + 1.534 \times 10^{-3} T \text{J/mole} - \text{K}. \tag{2.1}$$

The specific heat of graphite at temperatures $1200 < T < 10000$K has also been fit by Leider *et. al.*[11] with a function that neglects the vacancy contribution to the specific heat. The expression for the specific heat is given by[11]

$$C_p = 3R + 4.89 \times 10^{-4} T + 5.86 \times 10^{-8} T^2 - \frac{71.15}{T} - \frac{3.64 \times 10^6}{T^2} \text{J/mole} - \text{K} \tag{2.2}$$

where the units in Eq. 2.2 have been changed to match the units used in this work.

A comparison of Eqs. 2.1 and 2.2 with the experimental data in Fig. 2.3 is given in table 2.1. From the results in table 2.1, the two polynomial functions used to calculate the specific heat are in good agreement with each other and with experimental data for temperatures ($T > 2000$K). For temperatures $T <$ 2000K, the expression given by Leider *et. al.*[11] fits the experimental data better than the expression given by Cezairliyan and Righini[6]. Therefore, Eq. 2.2 has been used in the remainder of this work to calculate the specific heat for pyrolytic graphite.

	C_pJ/mole–K		
Temp. (K)	(Eq. 2.1)	(Eq. 2.2)	(Fig. 2.3)
1200	23.4	22.8	22.5
2000	24.6	26.1	25
3000	26.2	26.3	26.5
4000	27.7	27.7	-
5000	29.3	28.8	-

Table 2.1: A comparison of polynomial representation of the specific heat with each other and with experimental data. The lowest temperature (1200K) in the table is the lowest temperature at which Eq. 2.2 is considered valid[11].

2.3.2 Thermal Conductivity

The thermal conductivity of graphite is different from the specific heat in that the thermal conductivity is affected by the structural anisotropy in graphite. Because of the strong carbon–carbon bonding in graphite and the low carrier density, the thermal conductivity in graphite is dominated by the lattice contribution for both the inplane and c–axis components. The experimentally measured inplane and c–axis thermal conductivities for graphite appear in Figs. 2.4 and 2.5, respectively. In Fig. 2.4 the experimentally measured inplane thermal conductivity for pyrolytic graphite is shown for the temperature range from $10 < T < 2000$K. The characteristic shape of the curve comes from a competition of scattering mechanisms contributing to the dominant lattice component of the thermal conductivity. Boundary scattering from the finite size of the crystallites in the graphite dominates the thermal conductivity at temperatures below the measured maximum in the thermal conductivity. Above the thermal conductivity maximum, phonon–phonon scattering dominates the lattice contribution and causes the thermal conductivity to decrease. Since this is the temperature range of interest in this work, the temperature dependence of the thermal conductivity for temperatures above 1000K would be useful.

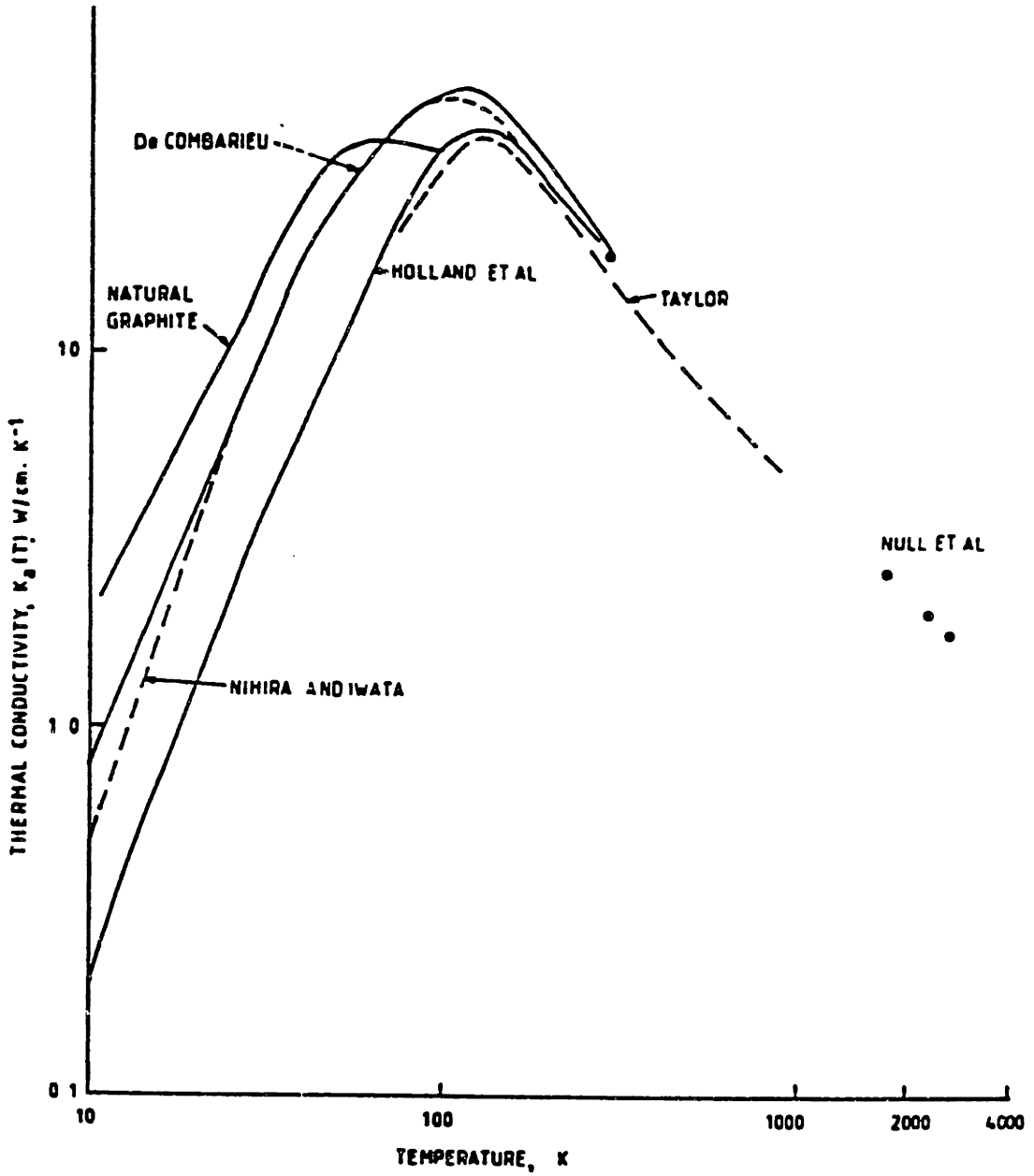

Figure 2.4: The inplane thermal conductivity of pyrolytic graphite. The measurements were made by DeCombarieu[12], Nihira and Iwata[13], Holland *et. al.*[14], Hooker *et. al.*[15], and Taylor[16]. This figure was compiled by Kelly[1].

Unfortunately, a proper theoretical treatment is as yet unknown[1]. The experimental data at temperatures above 1000K have been fit with a $A\exp(B/T)$ relation by Taylor[16]. Lutcov *et. al.*[17] have made high temperature thermal conductivity measurements on a number of graphites and have found good agreement between their data and Taylor's[16] exponential relation.

The inplane thermal conductivity in graphite is generally two orders of magnitude larger than the c–axis thermal conductivity. The reason for the large difference between the inplane thermal conductivity and the c–axis thermal conductivity is the higher velocity of sound and the longer phonon mean free path in the graphite planes.

The thermal conductivity parallel to the c–axis in graphite is more difficult to measure because a small degree of disorder in the material being measured will allow the inplane component of the thermal conductivity to dominate the measurement. The temperature dependence of the c–axis thermal conductivity is similar to the temperature dependence of the inplane component of the thermal conductivity and is shown in Fig. 2.5. The c–axis thermal conductivity increases as the temperature is raised from 10K until a maximum is reached at $\sim$ 80K. The c–axis thermal conductivity then decreases as the temperature is further raised above $\sim$ 80K. The scattering mechanisms for thermal conductivity along the c–axis are the same as the mechanisms for the inplane thermal conductivity. At low temperatures, the thermal conductivity is dominated by boundary scattering while at high temperatures, phonon–phonon scattering dominates the lattice contribution.

There have been several studies of the high temperature thermal conductivity in graphite by Null *et. al.*[18], Tanaka and Suzuki[19], and by Lutcov *et. al.*[17]. The experimental measurements by Null *et. al.* of the inplane thermal conductivity up to 2700K appear in Fig. 2.4. The experimental points

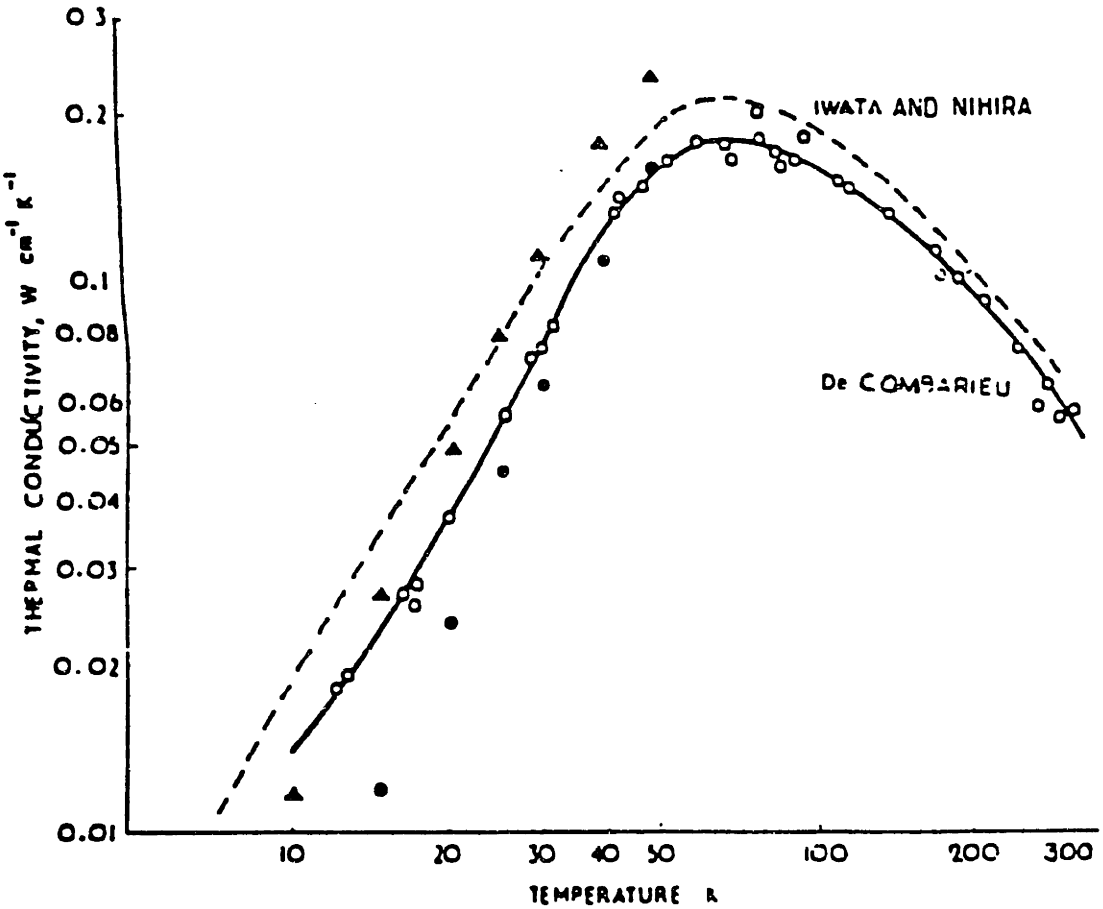

Figure 2.5: The experimentally measured c–axis thermal conductivity in pyrolytic graphite. The data presented are from DeCombarieu[12] and from Nihira and Iwata[13]. This figure was taken from Kelly[1].

fall close to the Taylor exponential relation ($A\exp(B/T)$) which is similar to the behavior found in the measurements of the inplane thermal conductivity at lower temperatures $1000 < T < 1500$K. As mentioned above, the high temperature thermal conductivity measurements by Lutcov *et. al.*[17] have been fit with the Taylor's[16] exponential, $A\exp(B/T)$, relation where the constant $B = 1440$K is used for pyrolytic graphite.

The measurements of Tanaka and Suzuki[19] of the thermal diffusivity in graphite at high temperature are summarized in Fig. 2.6. In Fig. 2.6a the inplane thermal diffusivity is plotted versus temperature. A fit to the data shows that the thermal diffusivity has a $1/T$ dependence. The thermal diffusivity, D, is given by

$$D = \frac{K}{C_p \rho} \tag{2.3}$$

where K is the thermal conductivity, C_p is the specific heat, and ρ is the density. In the previous section, the specific heat was shown to be a nearly linear function of T in the temperature range where Tanaka and Suzuki[19] have made their measurements. By using Eq. 2.3 we note that the inplane thermal conductivity then has a T^{-2} dependence, in qualitative agreement with the data of Null *et. al.*[18] and the data of Lutcov *et. al.*[17] when the constant $B = 1440$K in the Taylor exponential relation. The c–axis thermal diffusivity data from Tanaka and Suzuki[19] are shown in Fig. 2.6b. From the data in Fig. 2.6b, there is no temperature dependence in the c–axis thermal diffusivity, implying a $1/T$ dependence of the thermal conductivity over the temperature range $1300 < T < 2000$K. The temperature dependence of the thermal conductivity from these measurements also agrees with the thermal conductivity measured by Null *et. al.*[18].

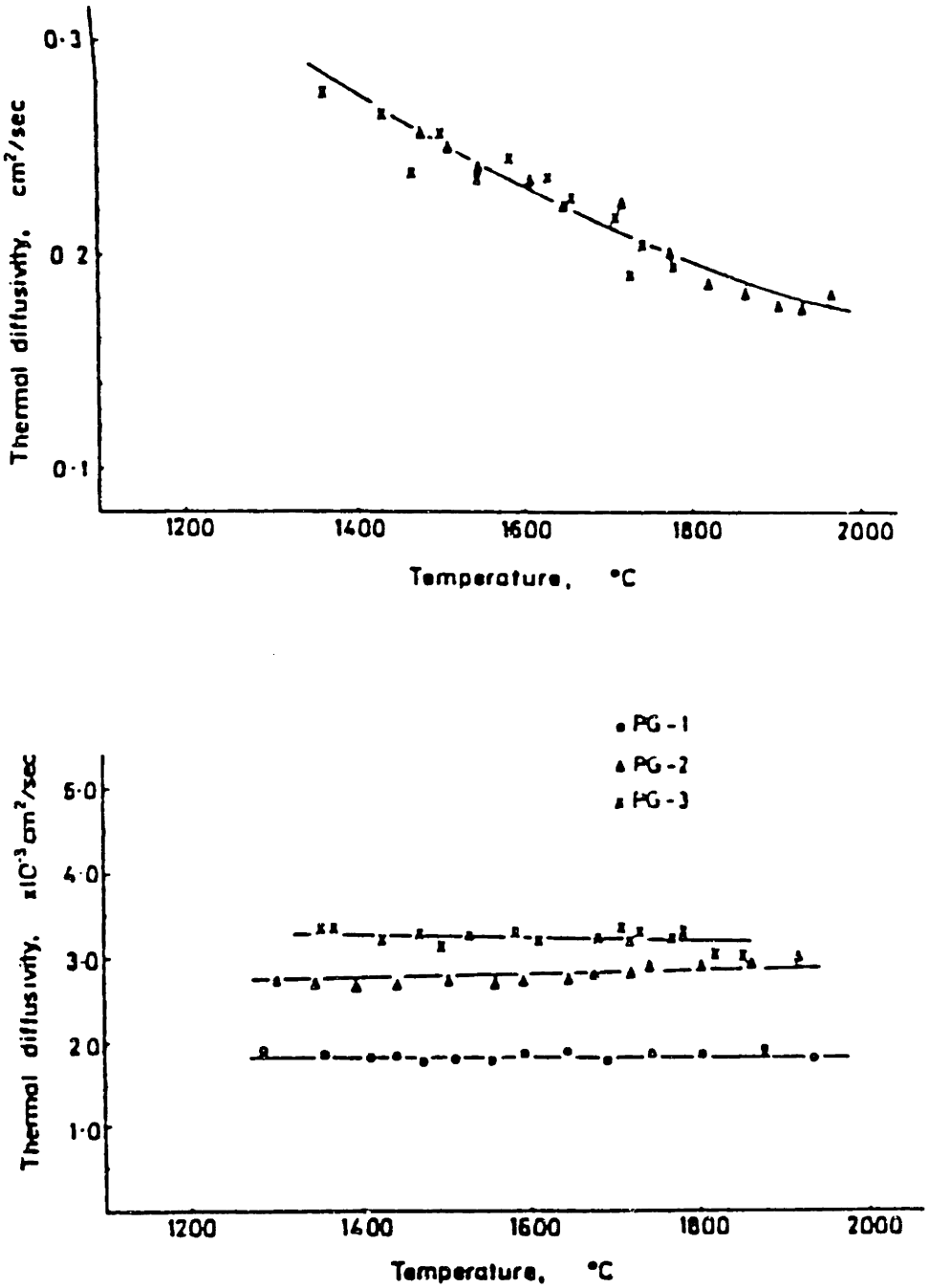

Figure 2.6: Experimental measurements of the thermal diffusivity by Tanaka and Suzuki[19]. The inplane thermal diffusivity is shown in (a) while the c--axis thermal diffusivity is shown in (b).

2.4 The Optical Properties of Graphite

The optical properties of graphite are also sensitive to the structural anisotropy of the graphite lattice. The optical constants, n and k, are dependent upon the direction of the electric field of the light incident on the graphite surface. Graphite is optically uniaxial with the optic axis parallel to the c–axis of graphite. When the light is directed along the optic axis, the optical properties will be determined by the polarizability parallel to the basal planes. When light is directed perpendicular to the optic axis, the optical properties are dependent on the polarization of the incident light. Light polarized parallel to the basal planes will show the same optical constants as light directed along the c–axis. Light polarized perpendicular to the basal planes will have very different properties.

This section on the optical properties of graphite is divided into two parts. The first part describes the optical properties for light polarized in the basal planes of graphite. Information on these properties is needed for pulsed laser heating experiments so that the total energy absorbed from the incident laser pulses can be determined. The optical properties of the basal planes are also important for understanding experiments which probe the surface optically during pulsed laser heating. The second part of this section discusses the lattice modes of graphite which are optically active and how the optically active lattice modes can be used in analyzing disordered graphite.

2.4.1 Optical Properties Along the Optic Axis

The optical constants of graphite for light directed along the optic axis have been measured directly by Ergun *et. al.*[20]. The results of their measurements are shown in Fig. 2.7. The measurements were carried out by measuring the transmission through graphite single crystals.

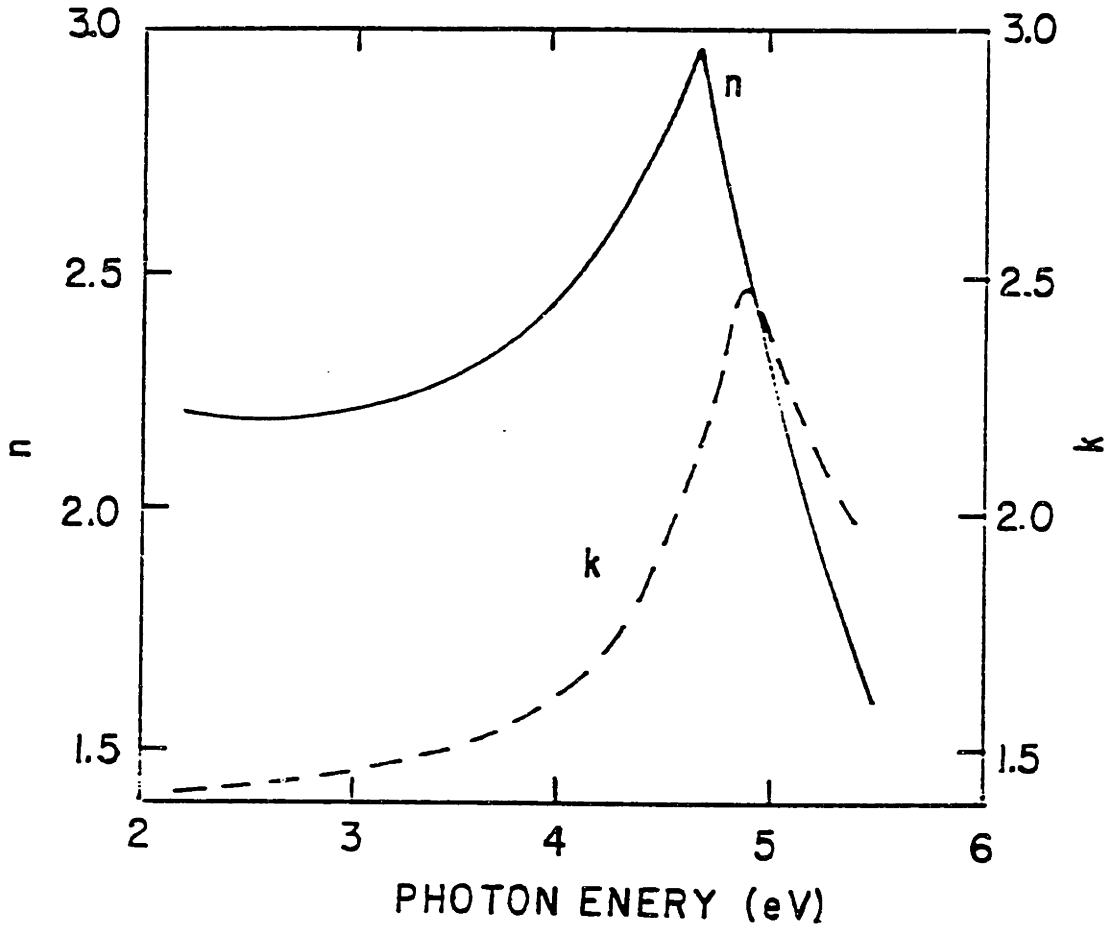

Figure 2.7: The optical constants, n and k, of graphite for light directed parallel to the optic axis as measured by Ergun *et. al.*[20] in the visible and the ultra–violet.

Laser	λ (nm)	n	k	R	α ($\times 10^{-5}$ cm^{-1})
ruby	694	2.25	1.45	0.29	2.6
KrF	248	2.4	2.45	0.45	12.4
Nd:YaG	532	2.2	1.45	0.28	2.6
Ar^+	514.5	2.2	1.45	0.28	2.6
Ar^+	488	2.2	1.47	0.3	2.6

Table 2.2: Optical properties of graphite for lasers used in this work.

Measurements of the reflectance of the basal planes in pyrolytic graphite have been carried out by Carter *et. al.*[21] and by Taft and Phillipp[22]. There is good agreement between the two sets of independent measurements. The results from Taft and Phillipp[22] for the basal plane reflectance are shown in Fig. 2.8. The reflectance of graphite at small energies is dominated by free electron effects[22]. The minimum in the reflectance in Fig. 2.8 between 7 and 10eV is due to surface contamination from the atmosphere.

The important optical information needed for pulsed laser heating experiments can be extracted from the experimental results shown in Figs. 2.7 and 2.8. The optical properties of graphite for the lasers in this work are primarily due to interband transitions of the graphite π electrons[22,23]. The reflectance, R, and the absorption coefficients, α, for the pulsed lasers used to heat graphite and the lasers used to probe the surface of graphite during pulsed laser heating are given in table 2.2. All of the lasers used in this work have normal incidence reflectivities near 0.3 except for the KrF laser where the reflectivity is higher at 0.45; this is in part due to surface contamination effects as described above. The absorption coefficient, α, for all of the lasers shown in table 2.2 was calculated directly from

$$\alpha = \frac{4\pi k}{\lambda}. \tag{2.4}$$

The Ar^+ lasers were used to probe the surface of graphite during pulsed laser

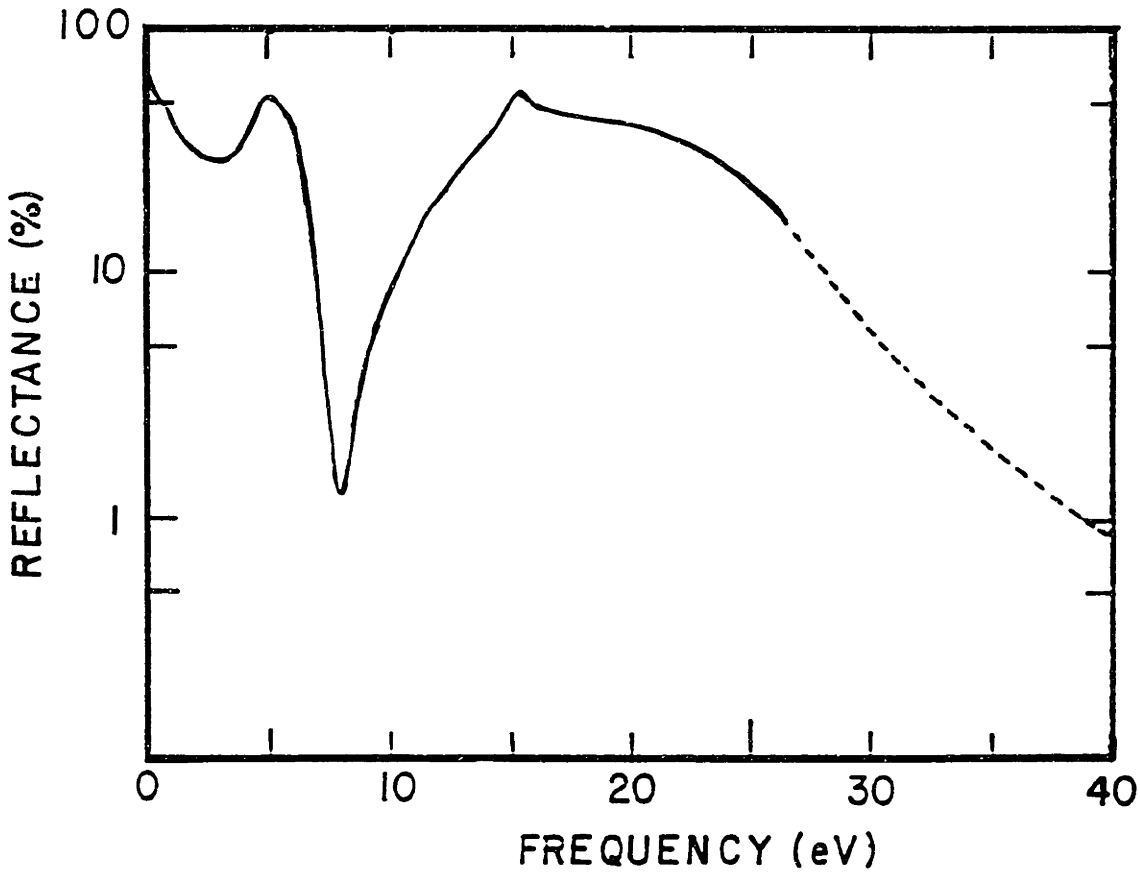

Figure 2.8: The results of reflectance measurements by Taft and Phillipp[22]. The dashed part of the curve is an extrapolation to experimental data.

heating.

2.4.2 Optically Active Lattice Modes

The lattice modes of graphite and their group theoretical designations are shown in Fig. 2.9. There are twelve lattice modes in graphite, since there are four atoms per unit cell, of which three are inactive acoustic modes, three are optically active infra–red modes, four are optically active Raman modes, and the remaining two are silent optical modes. The four Raman active modes are actually comprised of two sets of doubly degenerate modes.

The optically active lattice modes which are of interest in determining the size of the crystallites in polycrystalline graphite are the Raman active modes at $\sim 1580\text{cm}^{-1}$. Measurements of the Raman spectrum of graphite by Tuinstra and Koenig[24] have demonstrated that the crystallite size in polycrystalline graphite can be determined by the ratio of the intensity of the $\sim 1580\text{cm}^{-1}$ zone center Raman active mode, I_{1580}, and a disorder mode which appears at $\sim 1360\text{cm}^{-1}$, I_{1360}. By correlating the Raman intensity ratio, I_{1360}/I_{1580}, with x–ray diffraction measurements of the average crystallite size, the Raman measurements become a method for characterizing the degree of structural order in graphites. The results of the measurements by Tuinstra and Koenig[24] are shown in Fig. 2.10. Tuinstra and Koenig found that the average crystallite size decreases as the intensity ratio of the Raman active modes increases. The Raman intensity ratio can then be used to determine the average crystallite size in polycrystalline graphite.

2.5 The Electrical Properties of Graphite

In this work, the temperature dependence of the electrical resistivity of the semi–metallic basal planes is important for interpreting the results of transient

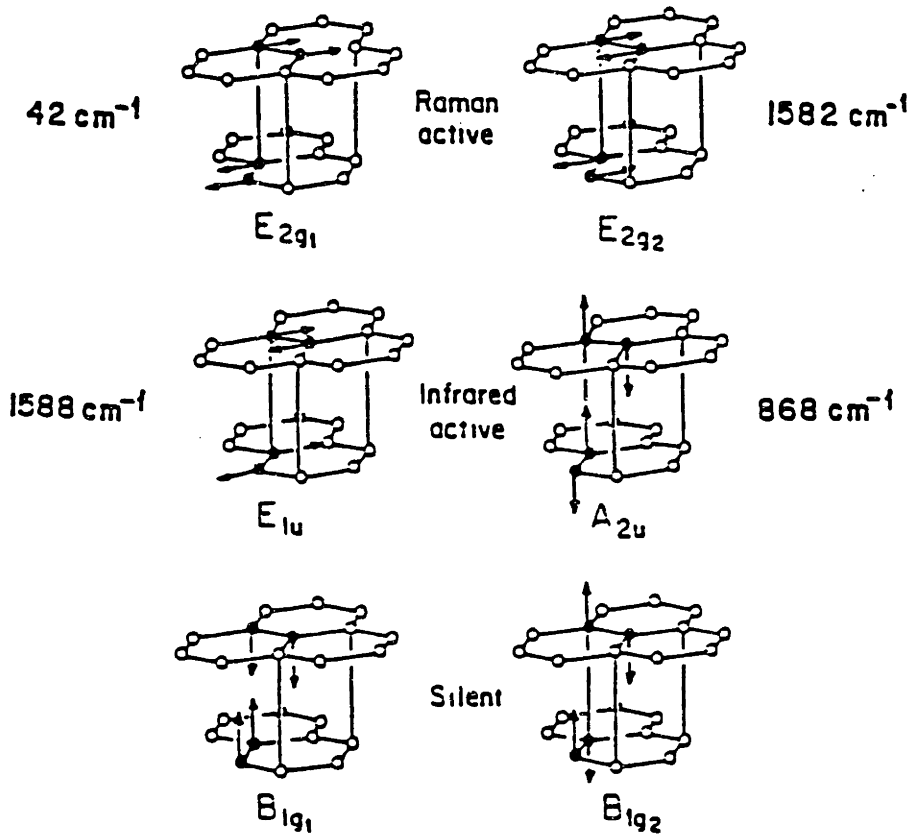

Figure 2.9: Zone center lattice modes of graphite, their group theoretical designations, and their frequencies.

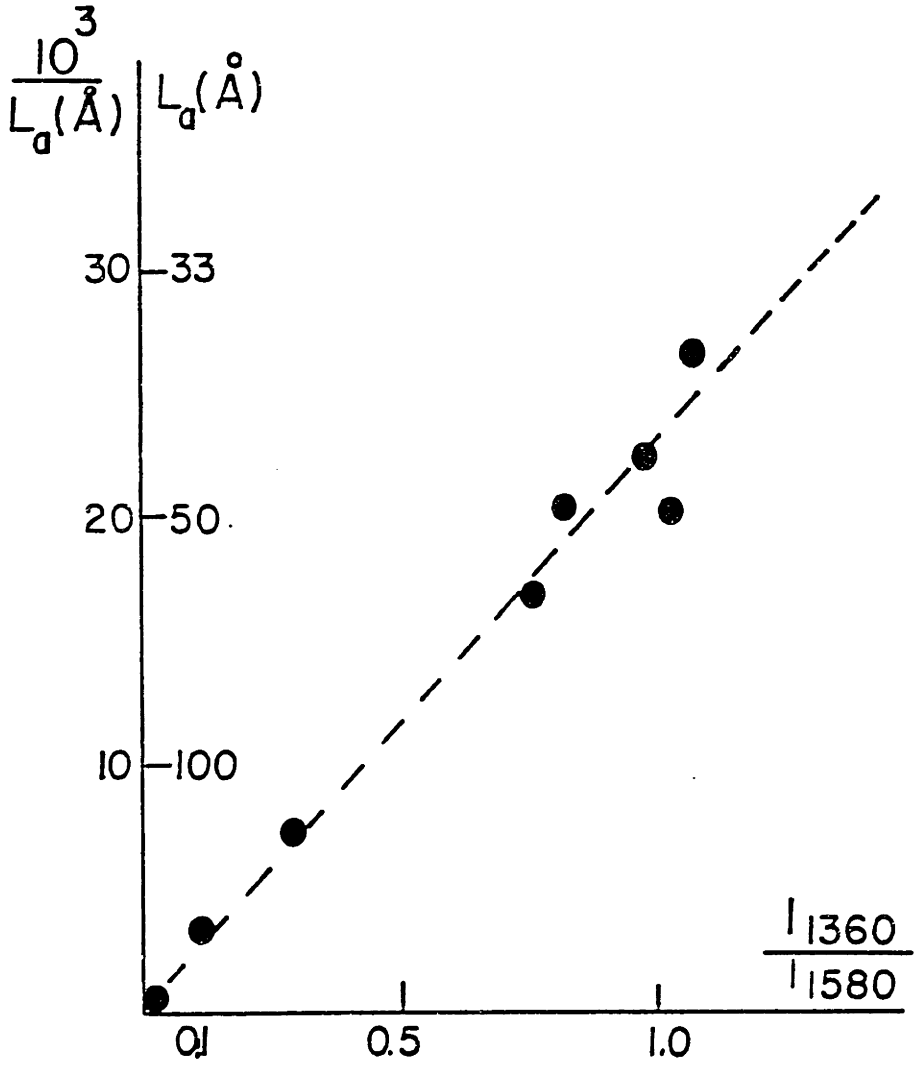

Figure 2.10: The average crystallite size in polycrystalline graphite versus the Raman intensity ratio, I_{1360}/I_{1580}. This figure is taken from Tuinstra and Koenig[24].

electrical resistivity measurements during pulsed laser and pulsed current heating of graphite. The electrical properties of graphite have been measured by numerous researchers[1]. However, most of the studies of the electrical properties are concerned with the electrical resistivity of graphite in the temperature range $0 < T < 300$K.

The electrical resistivity of graphite at high temperature has been studied by Lutcov *et. al.*[17]. The results of the high temperature resistivity measurements of Lutcov *et. al.*[17] are shown in Fig. 2.11. The traces in Fig. 2.11 show the electrical resistivity of graphites with densities in the range $1.0 < \rho < 2.3\text{g/cm}^3$. In graphites with $\rho < 2.1\text{g/cm}^3$ (traces 1–6), the electrical resistivity is seen to decrease with increasing temperature in the temperature range $0 < T < 500$K. The electrical resistivities of the low density graphites then increase nearly linearly with temperature for temperatures $500 < T < 3000$K. The electrical resistivity of pyrolytic graphite (trace 7) is increasing with a metallic temperature dependence over the entire temperature range. The electrical resistivity, ρ_s, data for pyrolytic graphite of Lutcov *et.al.* may be fitted with a line by

$$\rho_s(T) = 36.0 + 0.114T \ \mu\Omega\text{–cm}. \tag{2.5}$$

The electrical resistivity of graphite parallel to the c–axis is more complicated than in the basal planes. There is a large disagreement about the ratio of the electrical resistivity parallel to the c–axis to the electrical resistivity in the basal planes. In natural graphites the resistivity ratio is $\sim 10^2$ while for pyrolytic graphites values as high as $\sim 10^5$ have been reported. Since the experiments carried out in this work only consider the electrical resistivity in the basal planes, the reader is reffered to Kelly[1] for a discussion of the electrical resistivity parallel to the c–axis.

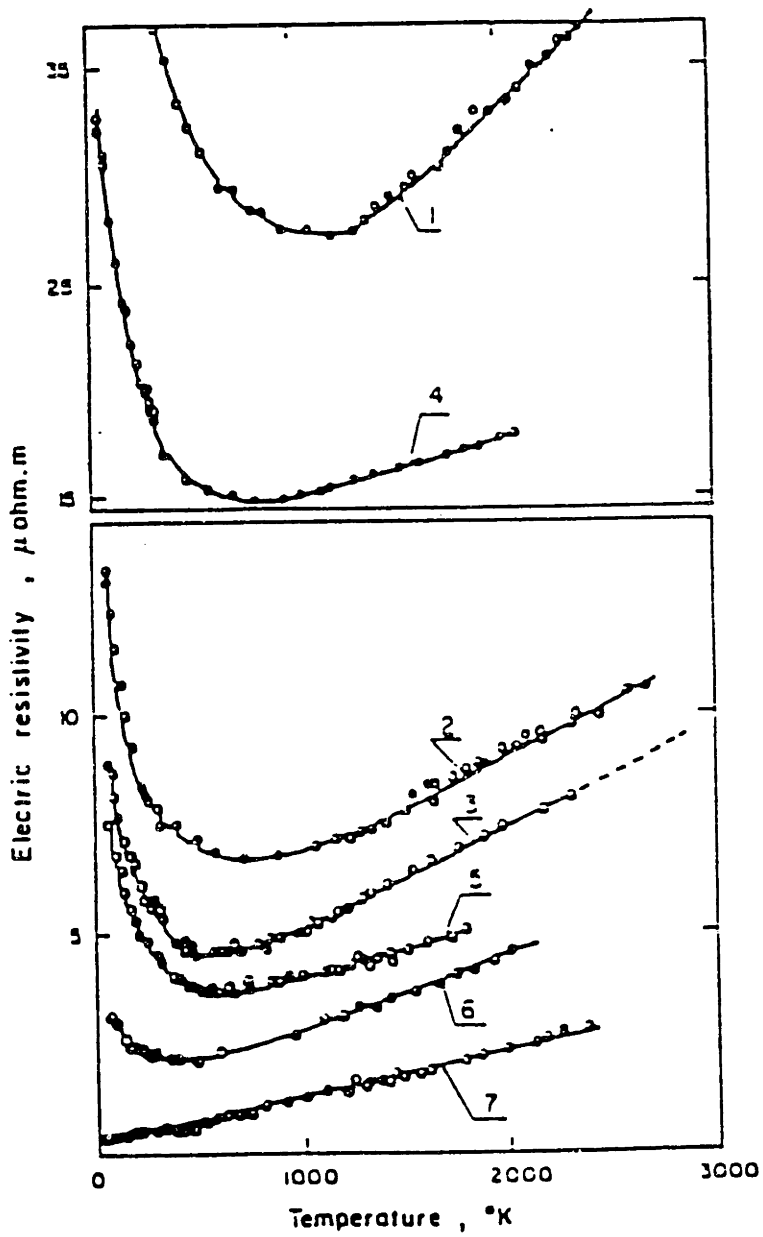

Figure 2.11: The high temperature resistivity of graphite from Lutcov *et. al.*[17]. Trace number 7 is for the basal plane electrical resistivity of pyrolytic graphite. Note the metallic behavior of the electrical resistivity above 1000K.

2.6 Photoconductance in Disordered Carbons

Photoconductivity in disordered carbon must be a consideration when pulsed laser heating is used to heat graphite and to determine the electrical properties of the liquid carbon. In chapter 3 the role of photoconductivity during transient electrical conductivity measurements will be discussed at great length. This section will review the work on the photoconductance in amorphous carbon and present new work on the photoconductance in disordered graphite fibers.

2.6.1 Review of Previous Work

Photoconductivity in amorphous carbon was first reported by MacFarlane *et. al.*[25]. The photocurrent versus radiation intensity and the rise and fall times of the photocurrent are shown in Fig. 2.12. The photoconductance versus the square root of the illumination intensity is plotted in Fig. 2.12a. From this plot, the photoconductance is seen to be related to the incident illumination intensity by the $I^{\frac{1}{2}}$ relation of a simple photoconductor[26]. The measured rise and fall times of the photocurrent are shown in Fig. 2.12b. The rise and fall times of the photoconductance are of comparable magnitudes and on the order of several seconds.

The relative change in the electrical conductivity of illuminated carbon films was also measured by MacFarlane *et. al.*[25]. In some cases, the electrical conductivity of amorphous carbon films could be increased by as much as 40 percent under illumination. Heat treating the amorphous carbon films decreases the photoconductance while increasing the graphitic character of the films.

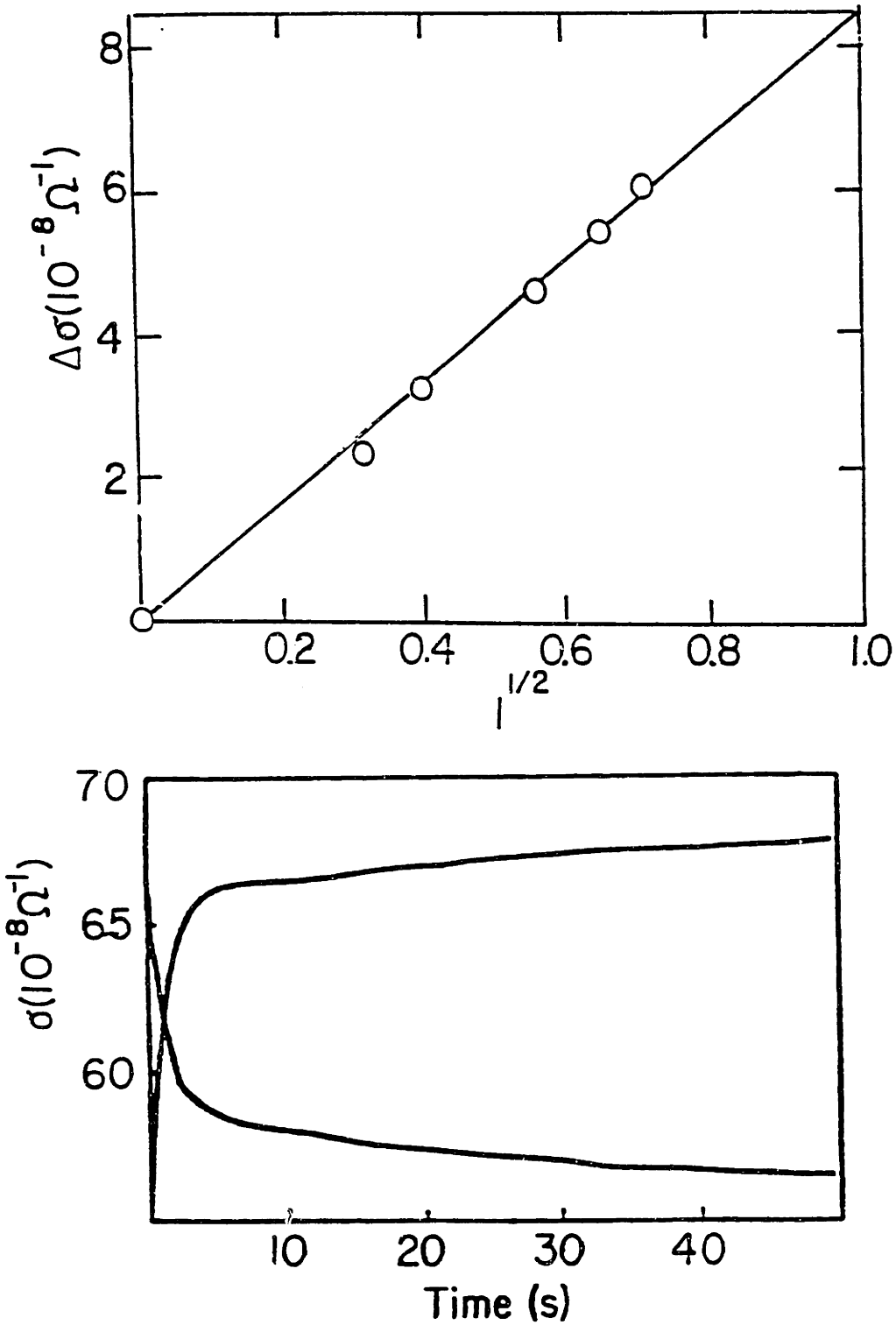

Figure 2.12: The measured photoconductance versus the square root of the illumination intensity is shown in (a) while the rise and fall time of the photocurrent is shown in (b). These data were taken from MacFarlane *et. al.*[25].

2.6.2 Photoconductance in Graphite Fibers

The discovery of photoconductivity in graphite fibers is noteworthy as an example where the absorption of light by an electrical conductor significantly changes the electrical transport properties of the material.

Measurements of the photocurrent in vapor grown graphite fibers are reported as a function of the illumination intensity I, for heat treatment temperatures $T_{HT} \leq 3000$K. Measurements have also been made of the temperature dependence of the photocurrent and the growth and decay time of the photocurrent. The results suggest that the observed photocurrent in graphite fibers is directly related to hopping conduction between shallow localized defect states. The trapping of carriers by deep defect states provides an alternate decay mechanism to phonon scattering where the trapped carriers may contribute to enhancements of the electrical conductivity of the graphite fiber on a time scale considerably longer than the phonon scattering time.

2.6.3 Experimental Overview

The photoconductivity measurements in this work have been done with vapor grown graphite fibers[4]. Fiber diameters ranged from 8 to 12μm. The transport properties of the fibers are dependent upon the heat treatment temperature, T_{HT}. The transport properties of the fibers used in this work are given in table 2.3. The fibers were mounted on a mica substrate and connected to electrical leads in a four point probe configuration. The electrical leads were attached to the fiber by means of Epo–tek H20E silver epoxy and cured at 373K.

The illumination source was an Ar^+ laser operated at several wavelengths in the range $4550 \leq \lambda \leq 5145$Å and in the intensity range $6 \leq I \leq 200$mW. The maximum power density at the surface was 500W/cm^2. The laser was

Table 2.3: Transport properties as a function of T_{HT}. The mobility at $T = 4$K was done by Rahim *et. al.*[?].

T_{HT} (K)	$\rho_{dark}(\Omega-\text{cm})$ $T = 300$K	$\mu_{dark}(\text{cm}^2/\text{V-s})$ $T = 4$K	$\mu_{dark}(\text{cm}^2/\text{V-s})$ $T = 300$K
300	9.3×10^{-4}	≤ 10	≤ 10
1000	7.9×10^{-4}	–	≤ 10
1500	5.1×10^{-4}	7.1×10^{3}	–
2000	2.3×10^{-4}	1.1×10^{4}	1.8×10^{2}
3000	9.9×10^{-5}	2.0×10^{4}	1.8×10^{2}

directed through focusing optics and a glass window in a dewar containing the electrical assembly. The beam was focused to a spot size $\sim 200\mu$m on the fiber surface. The experimental arrangement is shown in Fig. 2.13.

An electric field was applied to the fiber using a 1.5V battery connected in series with the fiber and a 100kΩ potentiometer. The dark current in the fiber was varied from 10 to 200μA to produce potential drops up to 300mV between the fiber electrodes.

Preliminary results indicated that the adsorption of air or He gas on the graphite fiber surface decreases the photocurrent by an order of magnitude. The adsorption of gas on graphite fiber surfaces is well known[27] and the decrease of the photocurrent due to gas adsorption at the surface of a photoconductor has been reported previously[26]. To eliminate this surface effect, all measurements were conducted on samples mounted in a dewar in a vacuum of 10^{-5} Torr.

The photocurrent was measured using a Tektronix differential amplifier and 4904A oscilloscope. The growth and the decay times of the photocurrent were also measured as a function of temperature T and illumination intensity I using the same experimental arrangement. For low temperature measurements, a nichrome–gold thermocouple was used, with the temperature being displayed by an Air Products temperature controller.

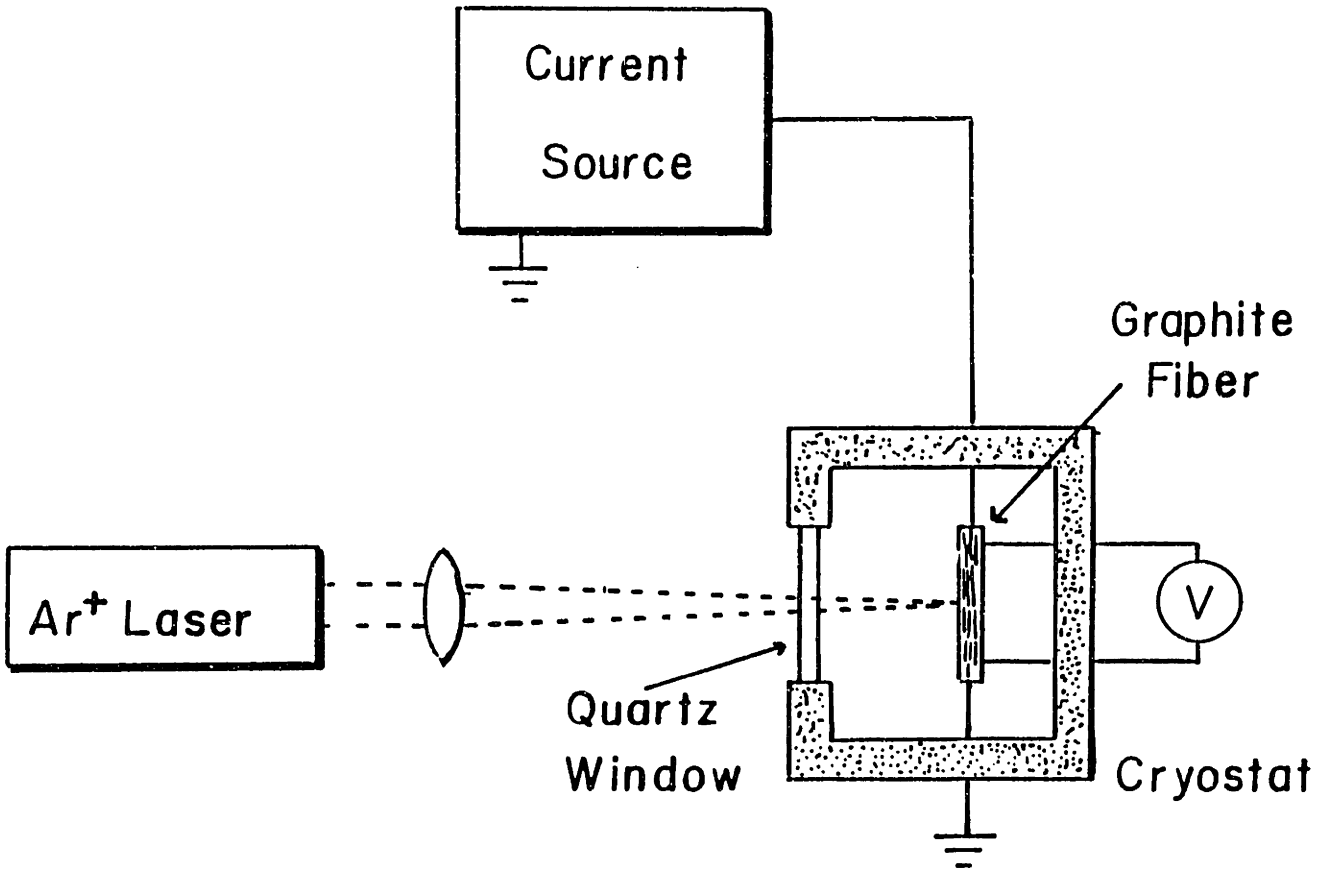

Figure 2.13: The experimental set–up for photoconductivity measurements on graphite fibers.

2.6.4 Experimental Results

The measured photocurrent, i, versus the illumination intensity, I, for an as–grown graphite fiber with the illumination source at $\lambda = 4880\text{Å}$ is presented as a log–log plot in Fig. 2.14. The figure also contains a fit of the photocurrent data with a line representing a $i = AI^{\frac{1}{2}}$ relationship between the photocurrent and the illumination intensity. This relation is characteristic of a photoconduction mechanism due to traps lying near the Fermi level[26]. This can easily be seen by balancing the photo–carrier generation rate with the recombination rate of decaying carriers

$$f = (n_0 + \Delta n)\nu SN \tag{2.6}$$

where f is the photo–carrier generation rate, n_0 is the intrinsic carrier density, Δn is the photocarrier density, S is the capture cross–section and N is the recombination center number density. For disordered graphite fibers illuminated under these conditions, the relation $\Delta n \gg n_0$ is obeyed, since the intrinsic carrier density is low ($< 10^{19}\text{cm}^{-3}$). Since most of the recombination centers will then be holes left behind by excited electrons, $N \sim \Delta n$. Rearranging terms, we have

$$\Delta n = \left(\frac{f}{\nu S}\right)^{\frac{1}{2}} \tag{2.7}$$

which is the experimentally observed relationship for graphite fibers.

Measurements of the growth and decay times of the photocurrent as functions of both fiber temperature, T, and the illumination intensity, I, show that the growth and decay times are independent of the fiber temperature and illumination intensity as T and I are varied over the range $10 \leq T \leq 300\text{K}$ for intensities in the range $0 \leq I \leq 200\text{mW}$. The growth and decay times of the photocurrent are 50 and 100msec, respectively.

A sharp decrease in the photo–enhanced conductivity is found when T_{HT} is

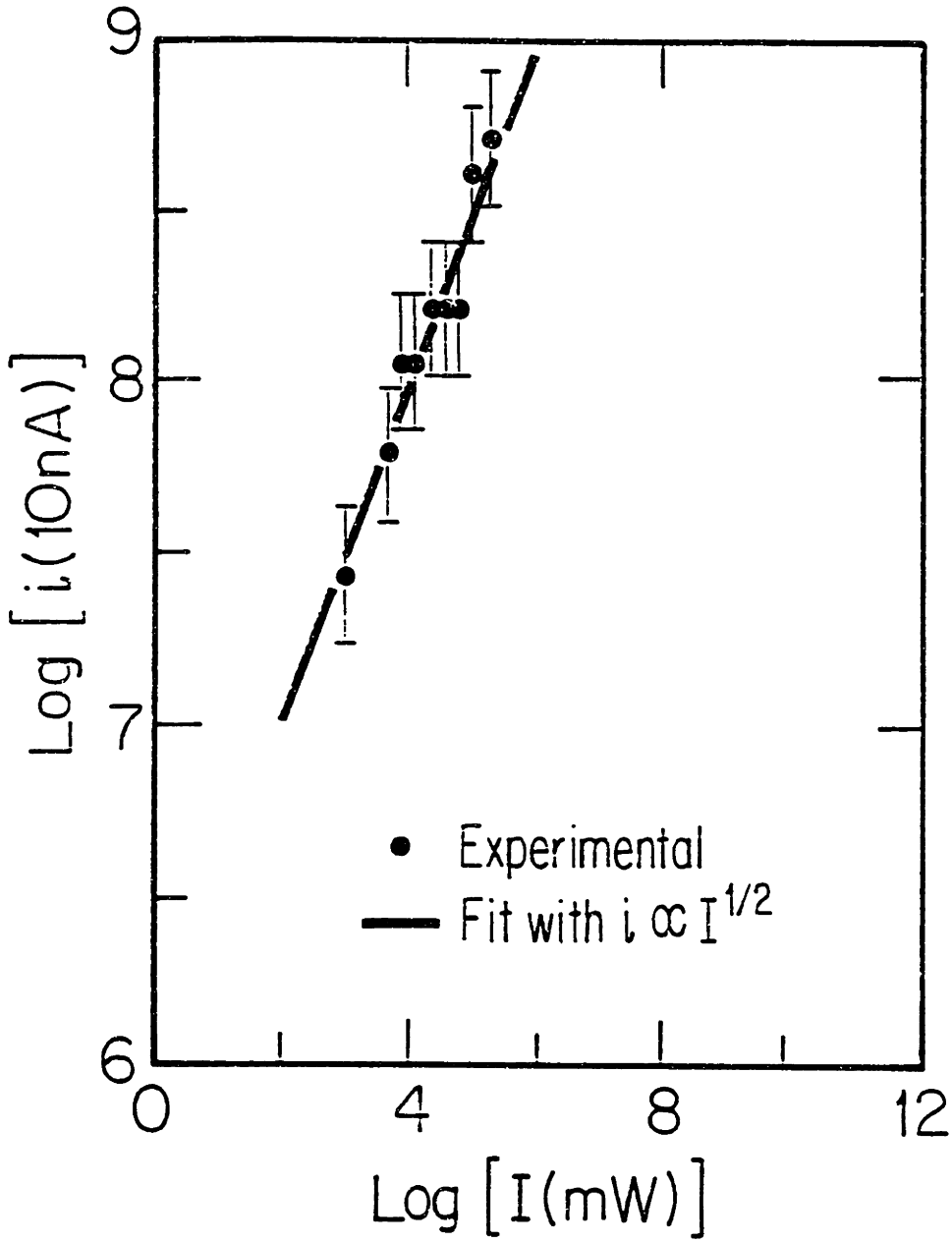

Figure 2.14: Log–log plot of the induced photocurrent, i, versus the illumination intensity, I. The wavelength used was 4880Å. Note the good fit of a line of slope 0.5 to the experimental points showing the $i = AI^{\frac{1}{2}}$ relationship.

raised above 1500K (see Fig. 2.15). The decrease in photo–enhanced conductivity is correlated with the increase in L_a, the in–plane coherence length of the graphite fiber resulting from heat treatment. As T_{HT} is raised above 1500K, defects are expelled, decreasing the density of localized states, reducing the density of traps, and consequently reducing the photogenerated enhancement to the conductivity. This would be expected since the graphite fibers used in this work were prepared at 1400K. Therefore, fibers with T_{HT}'s less than 1400K would not be expected to vary with T_{HT}.

2.6.5 Discussion of Photoconductance in Graphite Fibers

To identify the mechanism by which photoconductivity occurs in graphite fibers, several possibilities were considered. Thermal carrier generation by a laser heating mechanism was ruled out for the following reasons: (1) The growth and decay of the observed photocurrent are independent of I. If the enhanced electrical conductivity were due to thermal effects, then a larger I should decrease the growth time due to an increased heating rate. There should also be a corresponding increase in the decay time of the electrical conductivity enhancement since more heat must be transported away from the illuminated region. Changes in both the growth and decay time should clearly be seen since I was varied by more than an order of magnitude in these experiments. Experimentally, the rise and fall times of the photocurrent are intensity independent. (2) For a train of illumination pulses, the conductivity enhancement was found to maintain a characteristic "sawtooth" shape. If thermal effects were dominant, illumination pulse widths much smaller than the rise and fall times (e.g. $\leq$ 1msec) should make the changes in the electrical conductivity smoothly varying, contrary to observations. (3) The behavior of the photo–enhanced electrical conductivity in graphite fibers is consistent with previously

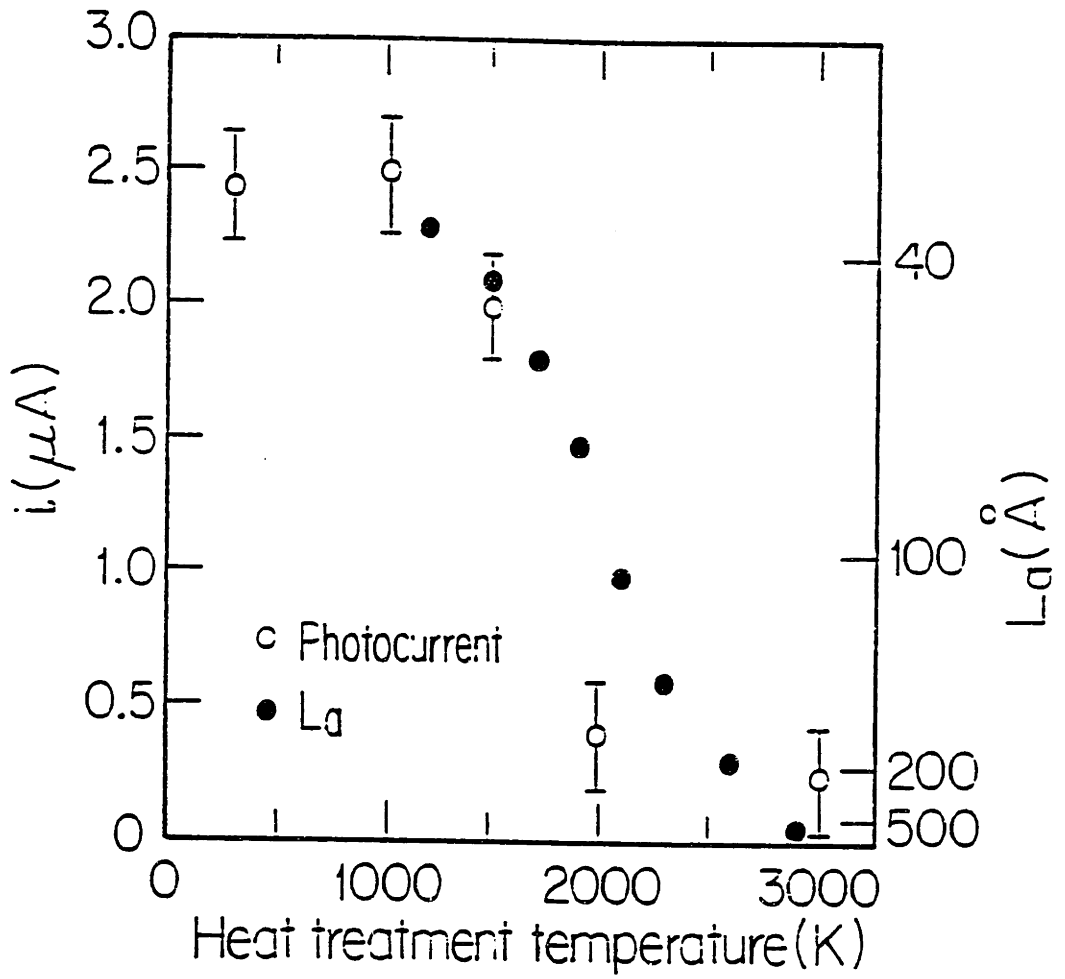

Figure 2.15: Dependence of the photocurrent on heat treatment temperature for an incident power density of $\sim 40 W/cm^2$ with the Ar^+ laser source at 4880Å. Comparison of the in-plane coherence length, L_a, in graphite fibers with the photocurrent. Note the strong correlation between the photocurrent and the onset of long range two dimensional order in graphite through the temperature range 1000K to 2000K.

reported observations of photoconductance in evaporated carbon films[25]. The magnitude of both the rise and fall times for the photocurrent as functions of illumination intensity and temperature as well as the $I^{\frac{1}{2}}$ response of the photocurrent to illumination intensity are found for both graphite fibers and evaporated carbon films[25].

Previous measurements of the temperature dependence of the conductivity in vapor grown graphite fibers[29,30] have shown that in the low heat treatment temperature range ($T_{HT} < 1800$ K), the electrical conductivity is due to an activated or hopping process. It is only for the highest heat treatment temperatures ($T_{HT} > 3000$ K) that band conductivity is observed.

The hopping conductivity given by

$$\sigma = Ne\mu = Ne^2\nu \exp(-E_a/kT) \tag{2.8}$$

where N is the density of active carriers, ν is the attempt frequency and E_a is the activation energy. Of these factors, it is the carrier density that is most sensitive to the optical absorption. The incident photons produce electron–hole pairs with unit quantum efficiency. The photon energies used suggest that most of the carriers are excited to band states far from the Fermi level E_F, indicated in Fig. 2.16a for two–dimensional graphite bands. These excited carriers quickly (< 1 picosecond) relax, via the electron–phonon interaction, to available states near the Fermi level. Here they can either rapidly recombine and give a negligible contribution to the photocurrent, or alternatively, the electron and hole can be separately trapped into the relatively large localized density of states indicated in Fig. 2.16a. The continuous distribution of the localized states is suggested by the temperature insensitivity of the photocurrent. The trapping retards recombination, so that either the electron or hole can be transported to the appropriate collection electrode before recombination and photoconductivity is observed. When the fibers are heat treated, the localized

density of states decreases so that the density of conduction hopping states decreases. In the limit of high heat treatment temperatures ($T_{HT} \sim 3000$ K) the density of states becomes 3-dimensional as indicated in Fig. 2.16b. In this limit, one would not expect any significant photoconductance because of the rapid electron-hole recombination through band states[30,31].

The difference in the growth and decay times for the photocurrent may be understood in terms of the increased phonon scattering rate of the highly excited carriers during illumination, while the decay process only involves the emptying of filled trap states. The insensitivity of the rise and fall times to external conditions is most likely due to photon energies which are much larger than the energy changes associated with carrier recombination processes.

2.6.6 Summary of Photoconduction in Carbon

The observed photo–enhanced electrical conductivity in vapor grown graphite fibers has been shown to be a photoconduction effect. The graphite fiber photocurrent increases as $I^{\frac{1}{2}}$ and has a growth and decay time insensitive to variations of T and I. The photoconductivity observed in graphite fibers is similar to the photoconductivity effect previously reported in evaporated carbon films[25]. The photoconduction in vapor grown graphite fibers is attributed to the activation of localized defect states by populating them with photoexcited carriers. The enhancement in the electrical conductivity comes directly from increased hopping among the defect states. Photo–enhanced conductivity has also been observed in PAN[32] and pitch[33] based carbon fibers, but has not been studied in detail.

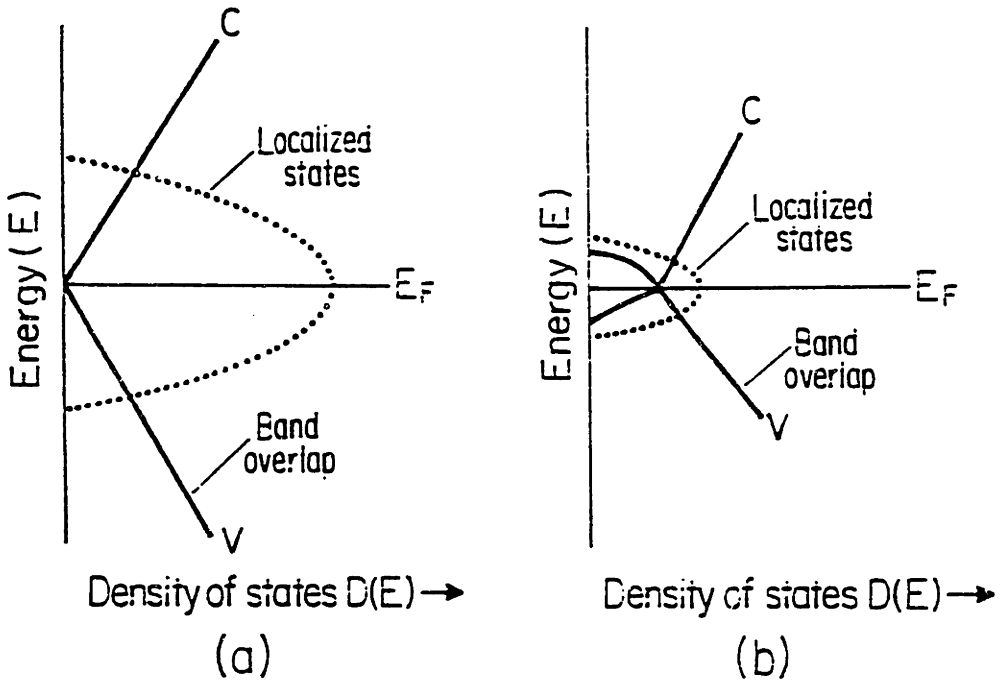

Figure 2.16: Proposed density of states diagram for photoconductivity in vapor grown graphite fibers. Both band states and localized states are shown separately. In *a*) the density of states for an as–grown graphite fiber is shown while *b*) presents the density of states for heat treated vapor grown graphite fibers. The reduction in the density of localized states for heat treated graphite fibers is due to the reduction of defects through heat treatment.

2.7 Mechanical Properties

2.7.1 Introduction

The structural anisotropy in graphite is directly related to the anisotropy in the mechanical properties of graphite. Two mechanical properties which are important in high temperature studies of graphite are the thermal expansion coefficient and the elastic modulus. The thermal expansion coefficients are important in determining the density of graphite as a function of temperature. The density is important because the thermal diffusivity, D_s, is given by

$$D_s = \frac{K}{\rho C_p} \tag{2.9}$$

where ρ is the density and K and C_p are the thermal conductivity and the specific heat, respectively.

A knowledge of the elastic modulus is important for determining the effects of rapid heating on the graphite lattice. If the lattice can be heated more rapidly than it can mechanically relax by expansion, pressure will build in the lattice. An increase in the pressure due to differential thermal expansion is particularly important for pulsed laser and pulsed current heating of graphite fibers where the concentric graphite planes form a closed geometry.

2.7.2 Thermal Expansion

The thermal expansion coefficients of graphite are important for studying the high temperature properties of graphite because of the large thermal expansion which is expected parallel to the c–axis. A summary of the measurements made on the thermal expansion coefficients in graphite is given in Fig. 2.17. Figure 2.17 shows the measured thermal expansion coefficients for both the c–axis (top traces) and the inplane (bottom traces) thermal expansion coefficients. The thermal expansion along the c–axis is always positive indicating that the

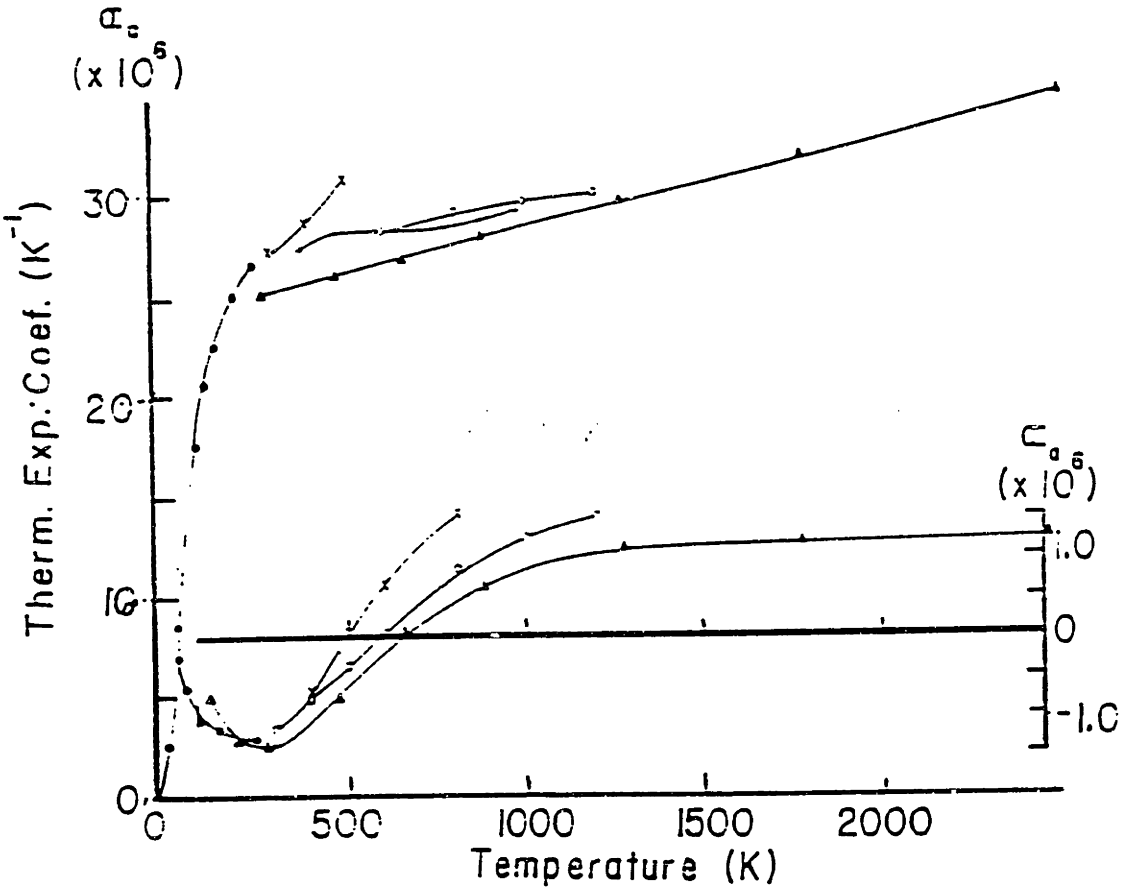

Figure 2.17: A summary of the measurements of the thermal expansion coefficients in graphite. The data shown is from Bailey and Yates[34], Yates *et. al.*[35], Harrison[36], Steward *et. al.*[37] and Nelson and Riley[38]. This figure was taken from Kelly[1].

graphite planes will always move further apart when the temperature of the lattice is increased. The thermal expansion coefficient along the c–axis increases linearly at temperatures above $\sim$ 500K.

The inplane thermal expansion coefficient in the graphite has a more complicated behavior. The inplane thermal expansion coefficient is negative for temperatures below $\sim$ 750K, implying that the lattice contracts in this temperature range. At temperatures above $\sim$ 750K, the inplane thermal expansion coefficient becomes positive and increases nearly linearly with T.

The magnitude of the thermal expansion along the c–axis is twenty times larger than the thermal expansion coefficient in the graphite planes. This means that the thermal expansion perpendicular to the graphite planes will be much larger than the inplane thermal expansion in graphite at all temperatures. Therefore, the temperature dependence of the density of graphite will be primarily dependent on the c–axis lattice spacing. The inplane lattice expansion will be a second order effect.

The c–axis lattice spacing as a function of temperature has been fitted by many authors for several different graphites[37,39,40,41,42]. Steward *et. al.*[37] have determined the c–axis spacing in pyrolytic graphite up to 2900K. The c–axis spacing as a function of temperature, $d_c(T)$, determined by Steward *et. al.*[37] is given by

$$d_c(T) = d_0 + 9.19 \times 10^{-5}(T - 273) + 5.3 \times 10^{-9}(T - 273)^2 \text{Å} \qquad (2.10)$$

where the c–axis spacing at 273K is $d_0 = 3.357$Å.

The density of graphite as a function of temperature, $\rho(T)$, is then given by

$$\rho(T) = \frac{\rho_0 d_0}{d_c(T)} \qquad (2.11)$$

where ρ_0 is the density of graphite at 273K, $\rho_0 = 2.25\text{g/cm}^3$.

2.7.3 The Elastic Modulus

The rapid heating of graphite during pulsed laser and electric current heating may increase the lattice temperature of graphite faster than the lattice can relax by thermal expansion. If the lattice cannot relax fast enough, the increase in the lattice temperature will cause thermal stress which can increase the pressure on the graphite. The thermal stress may also become large enough to cause a permanent plastic deformation of the lattice. In order to check this possibility, it is necessary to know the Young's modulus for graphite.

A calculation by Kelly[1] shows that the Young's modulus varies with the angle relative to the c–axis. The results of Kelly's calculations are shown in Fig. 2.18, where the inverse Young's modulus is plotted against the angle relative to the c–axis in graphite. In Fig. 2.18, Young's modulus is largest for directions parallel to the graphite planes while the modulus is nearly thirty times smaller parallel to the c–axis. The minimum in Young's modulus is not parallel to the c–axis, however, meaning that graphite is weakest when stress is applied at 45° to the c–axis.

The effect of thermal stress on pulsed laser heated polycrystalline graphite is minimal since only the region near the surface of graphite is heated by the rapid energy deposition from the laser pulse. The material that lies below the surface is heated by thermal diffusion. However, the effects of thermal stress are probably important during pulsed laser heating and pulsed current heating of graphite fibers where the graphite planes are confined to an enclosed geometry. As the planes try to become further apart by expanding along the c–axis, the rate at which the planes themselves must expand will be larger than the thermal expansion. The inability of the planes to expand will increase the pressure on the fibers. The increased pressure due to differential thermal expansion can be partially alleviated by heat treating the fibers before using them in pulsed

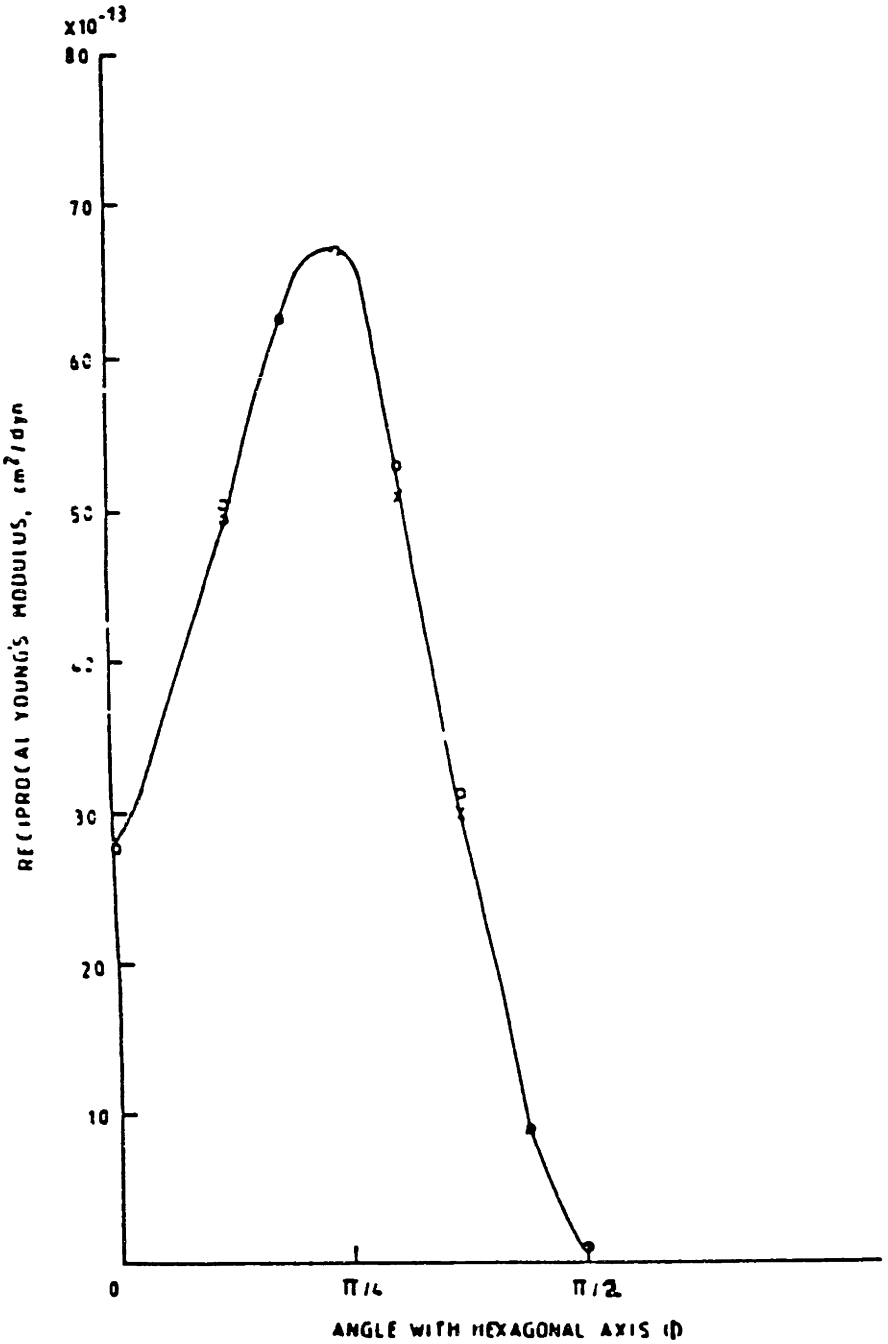

Figure 2.18: The results of calculations by Kelly for the dependence of the inverse of Young's modulus as a function of the angle from the c–axis. Note that the minimum in Young's modulus is not in the direction parallel to the c–axis.

heating experiments[43].

2.8 High Temperature Properties of Graphite

Measurements of the high temperature properties ($T > 3000$K) of graphite are generally inaccessible experimentally because most conventional experimental apparatus cannot be used at temperatures exceeding 3000K. However, high temperature specific heat measurements (section 2.3) strongly suggest that the properties of high temperature graphite can be taken as an extension of the properties at lower temperatures. Leider *et. al.*[11] have used the extension model to determine the specific heat of high temperature graphite and extended their analysis to include liquid carbon. Gustafson[44] has adopted the same extension model for theoretical calculations of the carbon phase diagram.

The extension model for the properties of high temperature graphite has been applied for pulsed laser and pulsed current heating in this work. The acceptance of the model by other researchers[11,44] studying the high temperature properties of graphite makes it worthy of serious consideration. The thermal and electrical properties of graphite at high temperatures are therefore calculated using the temperature dependence determined at lower temperatures.

The temperature dependence of the optical properties of graphite has not been investigated. Since the electrical properties indicate that graphite has metallic behavior at high temperature, the absorption coefficient, α has been taken to have a temperature dependence of[45]

$$\alpha = \alpha(300)\left(\frac{\rho(300)}{\rho(T)}\right)^{\frac{1}{2}} \tag{2.12}$$

where ρ is the temperature dependent electrical resistivity.

References

[1] B.T. Kelly, "Physics of Graphite", (Applied Science Publishers Ltd., London) (1981).

[2] B.S. Elman, G. Braunstein, M.S. Dresselhaus, G. Dresselhaus, T. Venkatesan, and B. Wilkens, *J. Appl. Phys.* 56, 360 (1984).

[3] A.W. Moore, private communication.

[4] M. Endo, *Synthetic Metals* 3, 177 (1981).

[5] G.G. Tibbetts, *Appl. Phys. Lett.* 42, 666 (1983).

[6] A. Cezairliyan and F. Righini, *Rev. Int. Hautes Temp. et Refract.* 12, 124 (1975).

[7] A.Y. Sheindlin, I.S. Belevich, and I.G. Kozhevnikov, *Physics of Heat at High Temperatures* 10, 907 (1972).

[8] J.E. Hove, *Proc. First SCI Conf. on Ind. Carbons and Graphites*, SCI, London, (1958).

[9] N.S. Rasor and J.D. McClelland, *J. Phys. Chem. Solids* 15, 17 (1960).

[10] G. Hennig, *J. Appl. Phys.* 36, 1482 (1965).

[11] H.L. Leider, O.H. Krikorian, and D.A. Young, *Carbon* 11, 555 (1973).

[12] A. DeCombarieu, *J. Phys. (France)* 28, 931 (1968).

[13] T. Nihira and T. Iwata, *Japanese J. Appl. Phys.* 14, 1099 (1975).

[14] M.G. Holland, C.A. Klein, and W.D. Straub, *J. Phys. Chem. Solids* 27, 903 (1975).

[15] C.N. Hooker, A.R. Ubbelohde, and D.A. Young, *Proc. Roy. Soc.* 276, 83 (1963).

[16] R.E. Taylor, *Phil. Mag.* 13, 157 (1966).

[17] A.I. Lutcov, V.I. Volga, and B.K. Dymov, *Carbon* 8, 753 (1970).

[18] M.R. Null, W.W. Lozier, and A.W. Moore, *Carbon* 11 81 (1973).

[19] T. Tanaka and H. Suzuki, *Carbon* 10, 253 (1972).

[20] S. Ergun, J.B. Yasinsky, and J.R. Townsend, *Carbon* 5, 403 (1967).

[21] J.G. Carter, R.H. Huebner, R.N. Hamm, and R.D. Birkoff, *Phys. Rev.* 137A, 639 (1965).

[22] E.A. Taft and H.R. Phillipp, *Phys. Rev.* 138A, 197 (1965).

[23] H. Ehrenreich, H.R. Phillipp, and J.C. Phillips, *Phys. Rev. Lett.* 8, 59 (1962).

[24] F. Tuinstra and J.L. Koenig, *Chem. Phys.* 53, 1126 (1970).

[25] J.M. MacFarlane, I.S. McLintock, and J.C. Orr, *Phys. Stat. Sol. a*, 3, K239 (1970).

[26] R.H. Bube, *Photoconductivity of Solids*, (John Wiley & Sons, New York,1960).

[27] P.L. Walker, and P.A. Thrower, *Physics and Chemistry of Carbon, Vol. 8*, (Marcel Dekker, New York), 1973 p. 232.

[28] I. Rahim, K. Sugihara, and M.S. Dresselhaus, *Carbon* 24, 663 (1986).

[29] J. Heremans, *Carbon* 23, 258 (1985).

[30] T.C. Chieu, M.S. Dresselhaus, and M. Endo, *Phys. Rev. B* 26, 5867 (1982).

[31] M.S. Dresselhaus, G. Dresselhaus, and J.E. Fischer, *Phys. Rev. B* 15, 3180 (1977).

[32] H. Goldberg, private communication.

[33] R. Bacon, private communication.

[34] A. Bailey and B. Yates, *L. Appl. Phys.* 41, 5088 (1970).

[35] B. Yates, Q. Pirgon, and B.T. Kelly, *Proc. Fourth SCI Conf. on Indust. Carbons and Graphites*, SCI, London 1976.

[36] J. Harrison, High-Temperatures–High–Pressures 9, 211 (1977).

[37] E.G. Steward, B.P. Cook, and E. Kellet, *Nature* 187, 1015 (1960).

[38] J.B. Nelson and D.P. Riley, *Proc. Roy. Soc.* A57, 477 (1945).

[39] P. Walker II, H.A. McKinstry, and C. Wright, *Ind. Eng. Chem.* 45, 1711 (1953).

[40] E. Matuyama, *J. Sci. Inst.* 32, 229 (1955).

[41] Y. Baskin and L. Mayer, *Phys. Rev.* 100, 544 (1955).

[42] E.G. Steward and B.P. Cook, *Nature* 187, 1015 (1960).

[43] J. Heremans, C.H. Olk, G. Eesley, J. Steinbeck, and G. Dresselhaus, *Phys. Rev. Lett.* , (1987).

[44] P. Gustafson, *Carbon* 24, 169 (1986).

[45] G. Bekefi and A. Barrett, "Electromagnetic Vibrations, Waves, and Radiation" (MIT Press, Cambridge, MA) 1977, p.442.

Chapter 3

Laser–Materials Interactions

3.1 Introduction

Laser heating involves the transfer of energy from an electromagnetic field into the lattice of a solid. The ability to focus large amounts of energy on small areas with lasers has been of great interest for both science and industry. In particular, the ability to melt materials quickly, efficiently, and cleanly using high power lasers makes laser heating an ideal mechanism for welding and annealing of high purity materials. The mechanisms by which the energy from the electromagnetic field of the laser beam is transferred to the lattice of a solid depends on the optical properties of the material being heated and on the characteristics (pulsed, continuous wave, wavelength, etc.) of the laser being used.

This chapter will focus on the processes occurring during the interaction of a laser beam with materials and on the effects of laser heating in solids. The chapter begins with a discussion of laser heating mechanisms in solids. The following section then discusses phase transitions which occur as a result of laser heating, primarily melting and vaporization. Included in the section is a description of the experimental techniques used to detect phase transitions during pulsed laser heating. The next sections describe the redistribution of

impurities, and mechanical effects caused by the rapid heating and subsequent cooling of laser heated materials. Each section begins with a summary of the effects of laser heating on solids and ends with a description of the observed effects of laser heating on graphite and evaporated carbon films.

Picosecond pulse laser heating in graphite and the current pulse heating of graphite fibers are then discussed. These experiments were done in order to try to overcome some of the difficulties which arise in nanosecond pulsed laser heating experiments. Picosecond pulse laser heating was used to try to overcome difficulties during transient optical measurements caused by carbon vaporization by trying to probe the surface of the hot graphite before vaporization can interfere with the measurements. Current pulse heating of graphite fibers was employed to melt large volumes of liquid in order to obtain information about the electrical resistivity of liquid carbon directly. These experiments are unique in that the graphite fibers used in the experiments are highly ordered.

3.2 Mechanisms of Laser Heating

The mechanisms which govern laser heating are the optical absorption properties of the material being heated and the efficiency of the energy transfer from the incident laser beam to the lattice of the heated material. The energy in an incident laser beam may be transferred to the lattice directly through the photon–phonon interaction, or indirectly through the carrier system of the material. Because of the high frequency of lasers typically used in laser heating experiments, the indirect transfer of energy to the lattice via the carrier system is usually dominant.

3.2.1 General Considerations

The absorption of the energy by the carrier system depends on the properties of the material. Optical absorption excites electrons in materials into higher energy states. The principal absorption and decay mechanisms involved in laser heating are shown in Fig. 3.1. For metals, incident photons cause electrons in the conduction band to undergo intraband transitions between free electron states. The excited electrons may then radiate a new photon (reflection) or, through phonon scattering, transfer their absorbed energy to the lattice. The process is more complicated for semiconductors and insulators where incident photons may cause interband transitions, taking carriers from the valence band to the conduction band. For indirect gap materials, the excitation of carriers across the band gap will be accompanied by the emission or absorption of a phonon for momentum conservation. The decay of excited carriers in semiconductors and insulators occurs through a combination of carrier–phonon, carrier–carrier, and multiple carrier scattering events which transfer the absorbed energy into the lattice.

The incident photons may also cause intraband transitions for free carriers in the conduction band of semiconductors and insulators similar to free carrier absorption in metals, though these effects are often small due to the small free carrier densities in semiconductors and insulators. Similarly, incident photons may cause interband transitions in metals during laser heating. However, interband excitations in metals are often much less important than free carrier absorption.

In addition to these possibilities, amorphous semiconductors have states which lie in the forbidden energy gap which may also be occupied by excited carriers and contribute to the carrier decay processes. Impurities in the material may also introduce states which lie within the forbidden energy gap which may

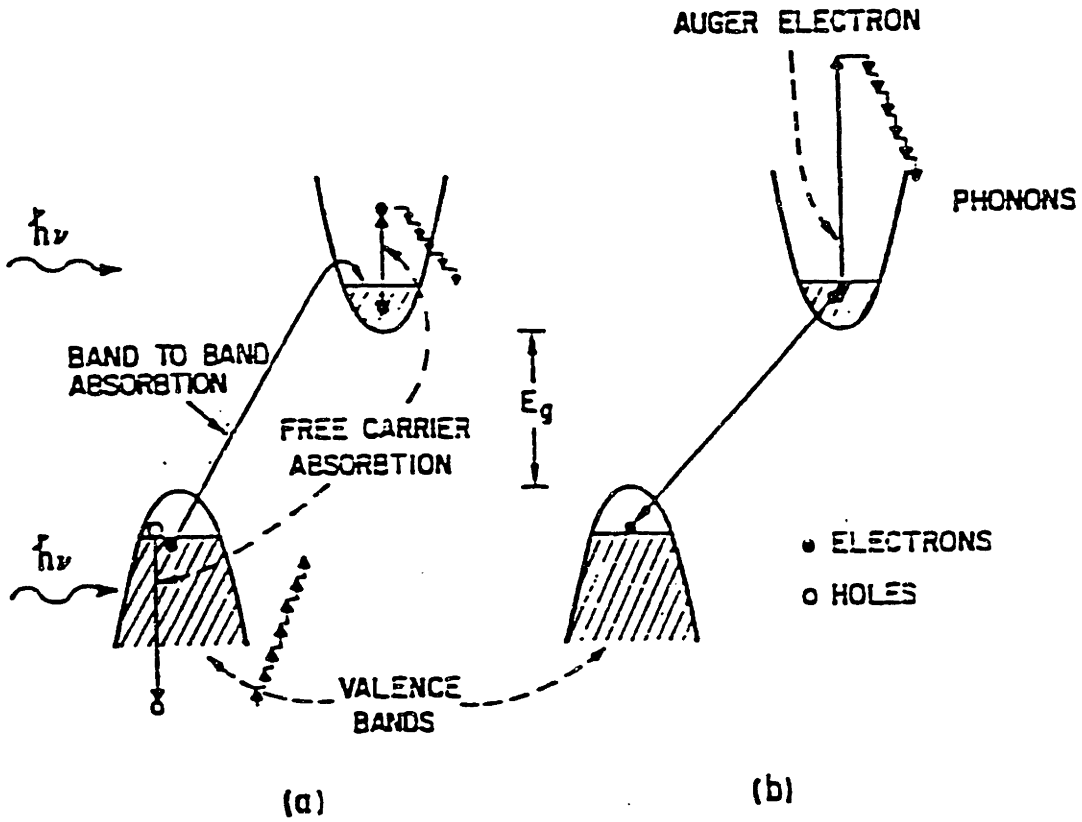

Figure 3.1: Absorption and decay mechanisms during laser heating: (a) the schematic shows the mechanisms of carrier excitation. Note that in metals free carrier absorption dominates. (b) This figure shows the decay mechanisms by which excited carriers transfer their energy to the lattice. This figure was taken from Ref. [1]

be occupied as well.

During laser irradiation, the primary absorption mechanism in semiconductors and insulators may change. Initially, electrons will be excited across the band gap and an electron–hole pair will be created. As the number of electron–hole pairs increase, free carrier absorption will become more significant. Free carrier absorption can dominate the absorption processes in semiconductors and insulators if the incident power density in the laser pulse is large enough[2].

The generation of free carriers in semiconductors may enhance the absorption processes if the decay time of the carriers is not much shorter than the laser pulse duration[1]. The increased absorption is a direct result of increasing the absorption coefficient due to an increase in the free carrier concentration. The increased absorption coefficient will increase the absorbed energy density near the surface which will improve the coupling between the laser and the material.

While there is general agreement about the photon absorption processes in solids, only recently has evidence been given to prove that the energy absorbed by a solid from an incident laser pulse may be treated by a simple thermal model[3] rather than by plasma models[4,5]. The thermal model for laser heating is a model in which the absorbed energy from the incident laser pulse is transferred from the carrier system to the lattice via carrier–phonon scattering processes. The thermal properties of the lattice will then dictate the flow of heat. The heating of the lattice may then cause the material to undergo phase transitions, such as melting and/or vaporization. The plasma model for laser heating considers the electron–hole plasma created by the absorption of incident photons as being shielded from electron–phonon interactions for times up to 100nsec. The target is then left in a "plasma" state as a result of the ionization of lattice atoms.

Only recently has mounting experimental evidence from transient optical and electrical techniques been able to determine that the thermal model is the correct description for laser heating. The plasma model originally had support from Raman measurements which indicated that the lattice temperature of laser irradiated solids did not increase significantly[4,5] However, re–evaluation of the Raman data used to support the plasma model showed that the measurement was not a true measure of the lattice temperature as was first thought[6]. The inability of the plasma model to account for the experimental observations from transient optical and electrical measurements, along with the good fit of the experimental data by calculations using thermal models, has given full support to the thermal model for laser heating.

The thermal model has several intermediate steps before the absorbed energy actually reaches the lattice. Once the carriers are excited by incident photons, the energy contained in the carrier system is transferred to the lattice through carrier de–excitation processes. A series of collisions between the excited carriers and the lattice will result in the emission of phonons which heat the lattice. A simple model for carrier relaxation can be used with a single time constant τ_{e0} representing the decay time of an excited carrier. Typically, τ_{e0} is on the order of 10^{-11}sec[1].

If the excited carrier density is very large in semiconductors, an electron–hole plasma may be formed[1]. The electron–hole plasma is an analog to an electron–ion plasma in the gaseous state, where holes play the role of ions. If an electron–hole plasma forms, the Coulomb interaction between the carriers will be partially screened and the transfer of energy to the lattice will be decreased. The decrease in the energy transfer rate is in part due to the carrier system thermalizing through carrier–carrier scattering and through carrier–plasmon scattering where the energy will be distributed through the carrier system be-

fore it is transferred to the lattice.

The decrease in the energy transfer rate can again be represented by a time constant given by[7]

$$\tau_e = \tau_{e0}\left(1 + \left[\frac{n}{n_c}\right]^2\right) \tag{3.1}$$

where n_c is a critical carrier density for the screening of the Coulomb interaction between the carriers. Calculations by Yoffa[2] show that the critical carrier density for silicon is $n_c \sim 2 \times 10^{21}\text{cm}^{-3}$.

The rate of carrier de–excitation in semiconductors is described by a simple differential equation:[1]

$$-\frac{dn}{dt} = \gamma_1 n + \gamma_2 n^2 + \gamma_3 n^3, \tag{3.2}$$

in which the different terms will dominate in different carrier density regimes. The $1/\gamma_1$ term is the minority carrier lifetime. The second term in eq. 3.2 represents band to band transitions and radiative decay. For materials with an indirect gap, such as silicon, the second term of eq. 3.2 is negligible. The third term in eq. 3.2 represents the decay of excited carriers via the Auger process. The Auger process is the recombination between an electron and a hole with the band gap energy being transferred to a third carrier in the valence band. The energy given to the third carrier is then transferred to the lattice via phonon emission. The Auger constant, γ_3, has an order of magnitude of $10^{-31}\text{cm}^6/\text{s}$[8]. The Auger process can also be described by a lifetime τ_A which is given by

$$\tau_A = \frac{1}{\gamma_3 n^2} \tag{3.3}$$

when the electron and hole concentrations are equal. Auger processes are the dominant decay mechanisms in typical pulsed laser heating[9] experiments in semiconductors.

At sufficiently high incident energies, a dense plasma of electrons and holes will be created which results in a partial screening of the Coulomb interac-

tion between carriers in the plasma. The screening is not significant until the plasma density reaches $\sim 10^{21}\text{cm}^{-3}$[2,10]. However, the Auger recombination time τ_A decreases with increasing carrier concentration and may decrease to $\sim 10^{-12}$s when the density of the electron–hole plasma is on the order of the critical density for the screening to be effective. The increase in the Auger recombination rate from increased carrier densities will inhibit plasma densities from exceeding the screening threshold for laser pulses on the nanosecond time scale[11].

A final consideration is the effect of carrier diffusion during laser heating. When large densities of "hot" carriers are generated during the laser heating process, they may diffuse out of the volume being irradiated by the laser. The carriers will diffuse as an electron–hole pair to preserve space charge and the diffusion of the pair will be governed by an ambipolar diffusion coefficient on the order of $\sim 100\text{cm}^2/\text{s}$[2]. The diffusion of "hot" carriers causes the effective absorption length of the material to be increased as a result of a decrease in the plasma density. Effectively, the diffusion of hot carriers out of the irradiated volume increases the volume which is heated. The consequences of carrier diffusion are that the temperature of the lattice in the laser irradiated region will be lower and hence coupling of the laser energy to the lattice will be less efficient[12].

3.2.2 Laser Heating Mechanisms in Carbon

As described in chapter 2 graphite is a semi–metal with an overlap of the valence and conduction bands occurring at the K point in the Brillouin zone. The primary absorption mechanism in graphite for the photon energies used in the laser heating experiments is interband transitions taking electrons from the valence band up into the conduction band, creating an electron–hole pair

for each absorbed photon. Since graphite does not have a direct band gap, radiative decay of excited electrons will be negligible. Because there is a band overlap in graphite, both Auger recombination *and* carrier–phonon scattering will keep the density of the electron–hole plasma formed during irradiation below the critical density for screening of the Coulomb interaction between carriers. Hot carrier diffusion in graphite will not be significant for the power densities used, since the band overlap will allow carrier–phonon scattering to be a dominant recombination process.

The absorption mechanism in evaporated carbon films is also an interband absorption process as discussed in chapter 2. In addition to the interband transitions, there will also be excitations to states within the band gap which will decay solely by carrier–phonon scattering. Hot carrier diffusion may play a role in evaporated carbon films for high power density laser pulses due to the band gap in the films which will retard carrier recombination. However, the hot carrier diffusion may be partially attenuated by recombination from the states within the band gap with carriers in the valence and conduction bands.

As described in the previous section, the mechanisms of laser heating will depend on the optical properties of the material used and the characteristics of the irradiating laser. The experiments described in this work have used pulsed lasers in both the nanosecond and picosecond time scales. On the nanosecond time scale, laser heating was done with laser pulses with the pulse power density in the range $0 \leq P \leq 1.5 \times 10^8 \mathrm{W/cm^2}$ with pulsed ruby and excimer lasers. On the picosecond time scale, the laser pulses used were from a frequency doubled Nd:YaG laser with pulse power densities in the range $0 \leq P \leq 5.0 \times 10^{10}\ \mathrm{W/cm^2}$. Table 3.1 describes the characteristics of the lasers used. The maximum carrier generation rate, g, may be calculated from

$$g = \frac{\alpha P_{max}}{h\nu} \tag{3.4}$$

Type	λ(nm)	$h\nu$(eV)	t_{pulse}(nsec)	P_{max}(W/cm^2)
ruby	694	1.78	30	1.5×10^8
KrF (excimer)	248	4.98	25	1.0×10^8
ArF (excimer)	192	6.43	25	1.0×10^8
Nd:YaG	532	2.32	20psec	5.0×10^{10}

Table 3.1: Pulsed lasers used for laser heating experiments in carbon.

where α is the absorption coefficient for the laser wavelength used. By using table 3.1, the maximum carrier generation rate, g, during laser heating for pulses on the nanosecond time scale will be $g \sim 5 \times 10^{31} \mathrm{cm}^{-3}\mathrm{s}^{-1}$ and for the picosecond time scale $g \sim 1.35 \times 10^{34} \mathrm{cm}^{-3}\mathrm{s}^{-1}$. Even though this carrier generation rate is sufficient to generate electron–hole plasmas in semiconductors, carrier–phonon scattering will be a dominant decay mechanism and keep the density of carriers well below the critical density for the effects of the creation electron–hole to be significant. For evaporated carbon films, the large carrier generation rate may be important since these materials have a band gap making the Auger process the dominant decay mechanism for exited carriers.

3.3 Phase Transitions in Laser Heated Materials

3.3.1 Melting

Melting, induced by laser heating, has been studied in many materials. Melting during laser heating is a first order phase transition which occurs at or near the equilibrium melting temperature, T_M. Once the material is heated to the melting temperature, the latent heat of fusion, H_f, must be supplied by the incident laser pulse to put the material into the liquid state. Overheating of the solid beyond the equilibrium melting temperature may occur for very high

power density pulses, but overheating of the solid generally does not occur because of the high speed with which energy is transferred to the lattice atoms via phonon scattering. A more thorough discussion of overheating and associated effect of undercooling, during laser heating is deferred until chapter 6 where rapid resolidification is discussed.

The melting phase transition may easily be observed in real time for some materials, such as silicon, which undergo an insulator–metal transition upon melting using transient optical techniques. Transient optical reflectivity and transmission may be used to observe the melting phase transition and to determine the optical constants of the liquid. However, the usefulness of optical techniques in determining the amount of material which has been melted is limited by the optical properties of the molten material. In many cases, the penetration of the liquid by optical methods is no more than a few hundred angstroms due to the metallic properties of the liquid. Transient electrical conductivity measurements are used to complement the optical measurements and provide melt penetration information as a function of time and additional information about the electrical properties of the liquid.

In addition to *in–situ* techniques, post heating studies of laser–melted materials are useful in determining the degree of crystallization of the resolidified melt as well as determining the maximum penetration of the melt into the solid. These techniques include ion beam channeling, and Rutherford backscattering spectrometry which can be used to measure the maximum penetration of the melt front nondestructively. Raman scattering and electron microscopy can also be used to investigate the microscopic structure of resolidified melts created by laser heating.

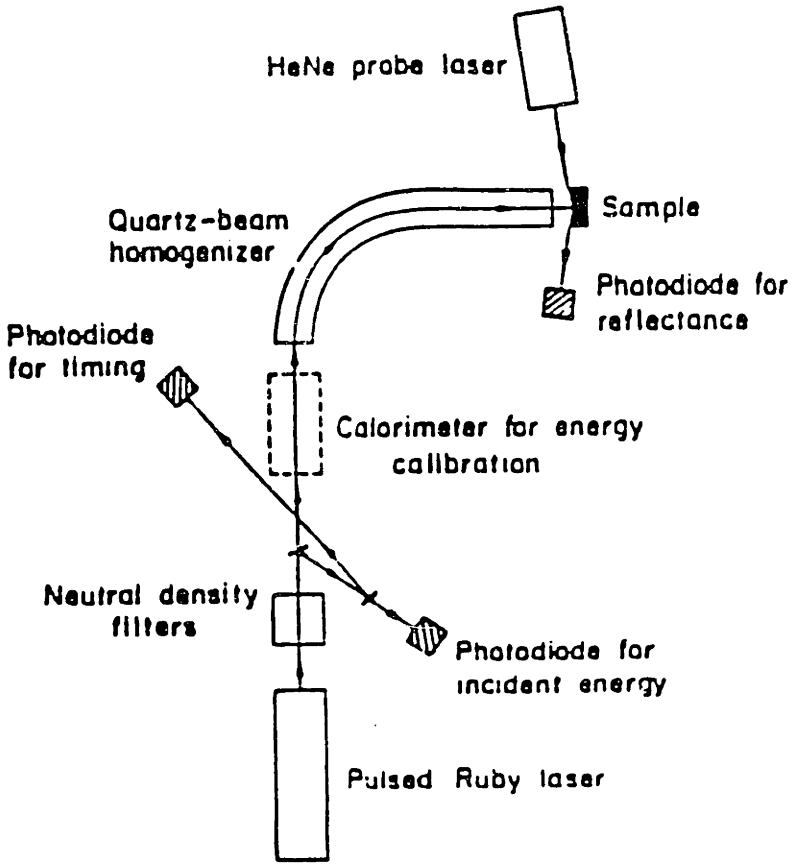

Figure 3.2: Experimental arrangement for transient measurements of the reflectivity of a laser–heated surface. A continuous–wave laser is used as a reflectivity probe. This figure was taken from Ref. [13]

Transient Reflectivity Measurements

One of the first *in situ* measurements made during laser heating was the monitoring of the reflectivity of a laser heated surface[1]. The experimental arrangement is shown in Fig. 3.2. A continuous wave laser probe is reflected off the surface of interest with the reflected intensity being measured by a photodetector. By monitoring the changes in the reflectivity during and after laser heating, the melting phase transition can be observed.

Early measurements of the transient reflectivity on silicon during pulsed laser heating by Khailbullin *et. al.*[14] show an increase in the reflectivity from 0.35 for solid silicon to 0.72 during the laser heating pulse. It was noted by Khailbullin *et. al.*[14] that the increase in the reflectivity corresponded to the reflectivity of liquid silicon. However, these early results were not able to make the distinction between the thermal model for laser heating which predicts the existence of the liquid phase and plasma model for laser heating which suggests that increases in the reflectivity are due to a large free carrier density in the solid state.

Later, more accurate measurements of the transient reflectivity made in many laboratories showed that the doubling of the reflectivity in silicon occurs at a threshold power density. Below the power density threshold for the doubling of the reflectivity, a smaller reflectivity increase can be observed which is ascribed to an increase in the carrier concentration from heating the silicon lattice. The appearance of a sharp increase in the reflectivity following the increases in the reflectivity due to lattice heating suggest that the silicon has undergone a change in phase from solid to liquid. If the plasma model for laser heating were correct, a continuous increase in the reflectivity from the steady increase in the excited carrier concentrations would be expected. These data gave strong support to the thermal model for laser heating and indicated that the doubling of the reflectivity was actually the melting of solid silicon into the liquid phase.

Transient reflectivity measurements are also useful for determining the duration of the existence of the liquid phase. For materials which undergo an insulator–metal transition upon melting, the abrupt changes in the reflectivity as these materials melt and resolidify may be used as an accurate indicator of the melting or condensing phase transition. Many investigators have used this

technique to measure the duration of the melt in materials. An example of this measurement from Galvin *et. al.*[13] for the laser melting of silicon is given in Fig. 3.3. The duration of the melt is measured from the onset of the increase in the reflectivity to the point tc where the reflectivity assumes values at or below that of the original solid phase. The final reflectivity may be lower than the original reflectivity due to the roughening of the surface.

Similar transient reflectivity measurements have been attempted in metals. In general, the correct interpretation of the results of the measurements is difficult to make due to the formation of an electron–ion plasma near the surface of laser heated metals. The formation of an electron–ion plasma above the laser heated surface changes the optical properties above the surface and, if the density of the plasma becomes large enough, may shield the surface from additional heating. A more detailed discussion of electron–ion plasma formation is metals is given in section 3.3.3.

Transient Electrical Conductivity

While transient reflectivity measurements can provide a probe to monitor possible phase changes in the target material, specific information about the extent of melting and the rates of melting and resolidification cannot be monitored using optical techniques due to limited optical penetration of the surface. By measuring the transient electrical conductivity of laser heated materials, this difficultly is overcome since this technique is not restricted by optical penetration depths.

The transient electrical conductivity measurements were first carried out by White *et. al.*[15] and Young *et. al.*[16]. A typical experimental arrangement for transient conductivity measurements in semiconductors is given in Fig. 3.4. The current passing through a semiconducting target is monitored during and

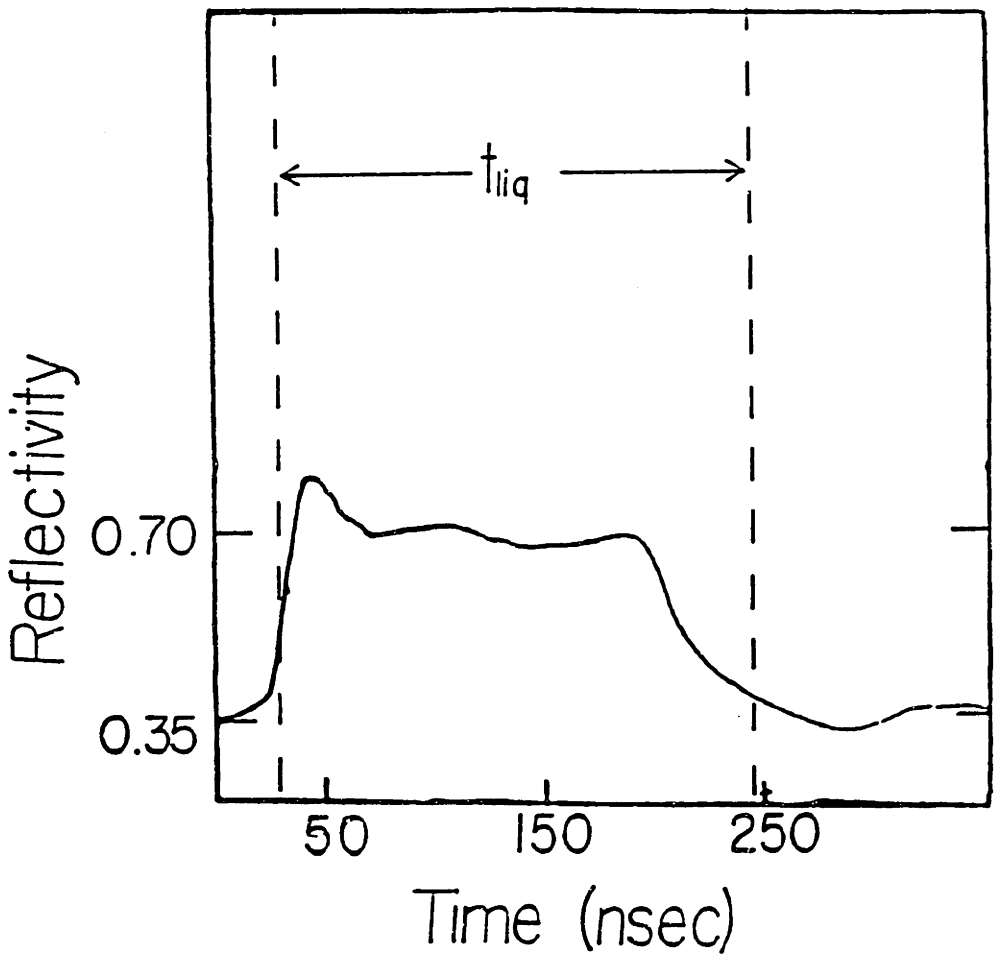

Figure 3.3: The duration of the melt in pulsed ruby laser melted silicon measured using the transient reflectivity technique[13].

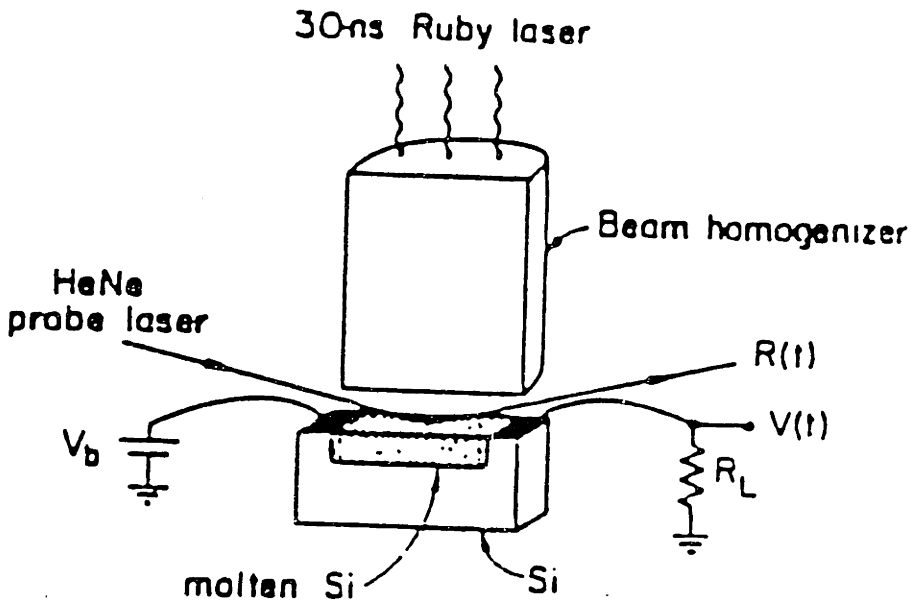

Figure 3.4: Experimental apparatus for measuring the transient electrical conductivity of laser heated semiconductors. (Taken from Galvin *et. al.*[13]).

after laser heating of the target material. Changes in the measured current can be related to changes in the electrical conductivity of the material being heated. Using this technique, both White *et. al.* and Young *et. al.* showed that there is an increase in the conductivity of silicon during pulsed laser heating. Unfortunately, these early measurements were complicated by the photoconductance of silicon.

Refinements to the transient electrical conductivity technique by Galvin *et. al.*[13] were able to partially overcome the problem of the silicon photoconductance by using silicon wafers doped with Au to reduce the photoconductivity signal. By uniting the transient reflectivity technique with transient conductivity measurements, Galvin *et. al.*[13] showed that the thermal model for laser heating accounts for the observed changes in the optical and transport properties of laser heated silicon. They showed that the thermal model is correct by demonstrating that the changes in the electrical conductivity during laser heating are identical to the changes expected during a solid to liquid phase change in silicon. In addition, the changes in the electrical conductivity were shown to correspond exactly to changes observed during transient reflectivity measurements.

The measurements were also able to yield direct information about the rate of resolidification of the molten silicon. Previously, only estimates of the resolidification front velocity from heat flow calculations were available. The data obtained by Galvin *et. al.* is shown in Fig. 3.5. From this figure the rate of solidification of the molten silicon is seen to be on the order of meters per second and confirms the validity of heat flow calculations for laser heated materials. This rapid solidification rate of molten silicon can lead to undercooling of the molten silicon. Rapid resolidification processes will be discussed at length in chapter 6.

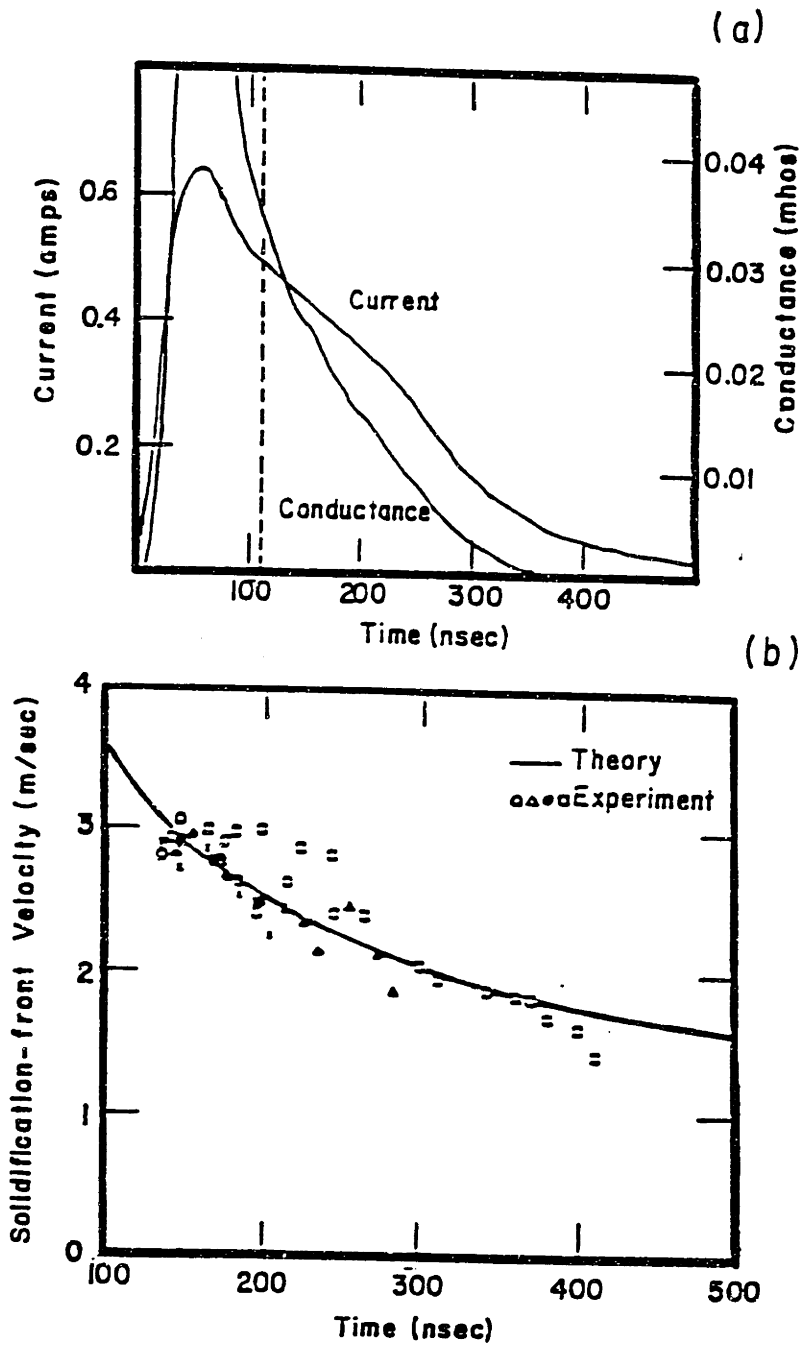

Figure 3.5: Results of transient electrical conductivity experiments in silicon. (a) Representative trace of current through the sample as a function of time and the corresponding conductance. The dashed line denotes the duration of the photoconductance. (b) The resolidification front velocity versus time determined directly from measurements and compared to calculated velocities[13].

The use of a similar transient conductivity techniques for laser heating studies of metals is complicated by several factors. First, the low electrical resistivity of metals increases the difficulty of obtaining useful signals. Second, the liquid phase of most metals is *more* resistive than the solid phase[17] meaning that the contribution of a liquid layer to the electrical resistance will be very small compared to the solid portions of the sample being heated. Third, the formation of an electron–ion plasma above the surface may cause arcing which cannot be easily accounted for in a rigorous analysis of data. Some of these difficulties can be overcome by using thin metal films. Experiments on Al by Tsao *et. al.*[18] show that transient conductivity measurements can be made on metals which can be deposited as thin films.

Post Heating Studies

Post heating analysis of laser heated materials is also useful for the analysis of the melting phase transition. Post heating studies are generally used to determine the structure of resolidified material, but they can provide useful information about the molten phase and its evolution during laser heating.

Two techniques which have been used extensively in the analysis of laser heated materials are Rutherford backscattering (RBS) and ion beam channeling[19]. Both techniques project light ions, usually H or He, at a target material in the MeV range. Since the ions used in these techniques are usually light compared with the mass of the atoms in the target material, the technique is generally nondestructive. For an extensive treatment of RBS and ion channeling spectroscopy, the reader is referred to Ref. [19].

As the ions pass through the material, they lose energy due to collisions with both electrons and the atomic nuclei in the lattice. By measuring the energies of backscattered particles, a depth profile can be established for the

material. For collisions between the incoming ion and the lattice atoms, the energy transferred to the atoms in the lattice will depend on the mass of the target atom. Heavier atoms will have a smaller amount of energy transferred to them than light atoms, so that the energy of ions backscattered from heavy atoms will be more energetic than ions scattered from light atoms. Using this information, RBS is also useful for monitoring impurity distributions in materials.

The concentration of atoms in the target material can be determined from the backscattered yield (i.e. the number of particles detected at a particular energy) by knowing the scattering cross–section for a target atom and the energy loss incurred by the incoming ion from both electron and nuclear scattering. In general, the backscattering yield is proportional to the square of the target atom mass. By using this fact, the relative concentration of elements in a target material may be determined.

By directing the incoming ion beam along a crystallographic direction, the cross–section for backscattering will be decreased since the atoms in the material will appear to be lined up one after another. In addition, the collisions which the ions make with lattice atoms will be at glancing angles so as to steer the ion along the "channel" on the crystallographic axis. This has been termed ion beam channeling[20]. The ion beam channeling technique is useful in determining the crystalline order in materials since atoms that block the channels will increase the backscattering cross–section of the material and hence increase the backscattering yield. Like Rutherford backscattering, ion beam channeling is sensitive to both the depth from the surface and the mass of constituent atoms in the target.

Rutherford backscattering–ion channeling studies on laser heated materials show that resolidified materials are disordered by laser heating. This is particu-

larly true for materials which have been melted at power densities which lie just above the melting transition threshold. When the power density in the laser radiation is increased further some materials, such as silicon, can be annealed by the laser radiation back to their original crystalline state by an epitaxical regrowth from the liquid state. The ion channeling studies also show that defects and interstitials introduced by the implantation of constituents of the material can be annealed such that the implanted species occupy substitutional sites in the cold lattice for small ion concentrations.

Electron microscopy has also been a useful tool in the analysis of materials melted by laser heating. Transmission electron microscopy has been used to show that the microcrystallites remaining after laser heating may randomly orient themselves as a result of rapid solidification from a melt[21,22]. Additional studies of the interface between the melted region and the bulk material show that the region near the solid–liquid interface contains a higher density of defects relative to the rest of the resolidified material[23]. The formation of these regions was further shown to result from the high velocity of regrowth[23]. A description of the stratification observed in the resolidified material is deferred to the discussion of rapid regrowth in chapter 6.

Raman spectroscopy has also been used as a tool to study the effects of laser heating on materials. Originally, transient Raman techniques were used to determine the lattice temperature of laser heated materials[4,5,24]. The results of the transient Raman measurement formed the basis for the plasma model of laser heating. As a technique for post heating studies, Raman spectroscopy is useful for determining the mean crystallite size in resolidified materials near the surface in some materials.

Other Techniques

Several other experimental techniques have been employed in the analysis of materials melted by laser heating. Two these are optical pyrometry and x–ray scattering[25,26]. Optical pyrometry was originally employed to try to determine whether the thermal model or the plasma model was a correct description of laser heating. The use of optical pyrometry is limited, however, by the short time scales over which laser heating takes place. The use of x–ray scattering during pulsed laser heating is useful for determining the temperature gradients below the liquid layer, while x–rays used as a post–heating technique may be used to study the resolidification of the liquid.

3.3.2 Vaporization

Vaporization is also important in studying the effects of laser heating on materials. In many materials the vaporization phase transition is identical with melting: the material (solid or liquid) is heated up to its vaporization temperature, T_v, and once the latent heat of vaporization, H_v, is supplied, material leaves the surface in gaseous form. The vaporized material generally leaves the surface at the thermal velocity, but other processes, such as the formation of an electron–ion plasma, may affect the velocity of the vaporized material.

In some materials, such as carbon, the material has a significant vapor pressure over a range of temperatures. In this case, the vaporization process is best described by an activated process where the activation energy is given by the difference in the free energy of the solid, or liquid, phase and the vapor phase plus the heat of formation for the particular vapor species. The vaporized material again leaves the surface at the thermal velocity unless it is acted upon by a non–thermal mechanism.

Vaporization during the laser heating of materials has been studied by sev-

eral complementary techniques. Time of flight measurements have been the primary method by which gas species determinations have been made, while ion implanted markers and weighing have been used to measure the total amount of removed material.

Time of Flight Measurements

The time of flight technique is useful for determining the species which are evolved from the surface of laser heated materials. The technique is comprised of two phases. The first collects the vapor evolved from the laser heated surface and strips a single electronic charge from each molecule. The charged molecules are then accelerated electrostatically to velocities larger than the thermal velocity and the number of charges striking a collection electrode are counted as a function of time. Since the final velocity of the accelerated particles will be inversely proportional to the square root of the mass of the particles, the mass distribution of the vapor species will be measured directly by the collection electrode.

Time of flight measurements in the analysis of vapor species have been carried out for several materials. For laser heated GaAs and Si, time of flight measurements were done by Pospieszczyk *et. al.*[27] to show that the distribution of the evolved species is a thermal distribution. Work by Kasuya and Nishina[28] on both silicon and carbon show that the mass distribution of charged clusters emitted during pulsed laser heating changes with time from large clusters to smaller clusters. The cluster emission from laser heated carbon surfaces have also been studied by Kasuya and Nishina[29] showing that large carbon clusters ($\sim C_{30}$) are emitted from the laser irradiated surface and these clusters also break up into smaller units with time.

Ion Implanted Markers

An ion implanted marker is a useful tool for determining the total amount of material removed from the surface of laser heated materials. The depth of the removed layer of material can be measured from the shift in the position of the ion implanted impurity distribution using Rutherford backscattering. An example of the ion implanted marker technique appears in Fig. 3.6 for laser irradiation of graphite with a $1.5 J/cm^2$ ruby laser pulse. The figure shows the original distribution of implanted As impurities in graphite and the distribution of As impurities after the graphite has been laser irradiated with a 30nsec ruby laser. The change in the impurity distribution is caused by two effects: the removal of material from the surface due to impurity segregation with solute trapping and vaporization.

Solute segregation and trapping is known to occur in this particular case since some of the implanted As is seen on the surface of the sample. The detailed mechanisms of impurity segregation will be discussed at length in section 3.5. The shift of the impurity distribution toward the surface which is due to vaporization is therefore measured from the back edge (farther from the surface) of the impurity distribution. The measurement is taken from the back side of the distribution, so that the effects of impurity segregation, which redistribute impurities, do not distort the vaporization measurement. The total amount of removed material can then be calculated by knowing the area which was irradiated by the laser pulse.

3.3.3 Plasma Formation

During laser irradiation, plasmas may be formed both inside and outside of a condensed phase target. While the melting and vaporization phase transformations are straight forward, the study of laser induced plasmas is not because

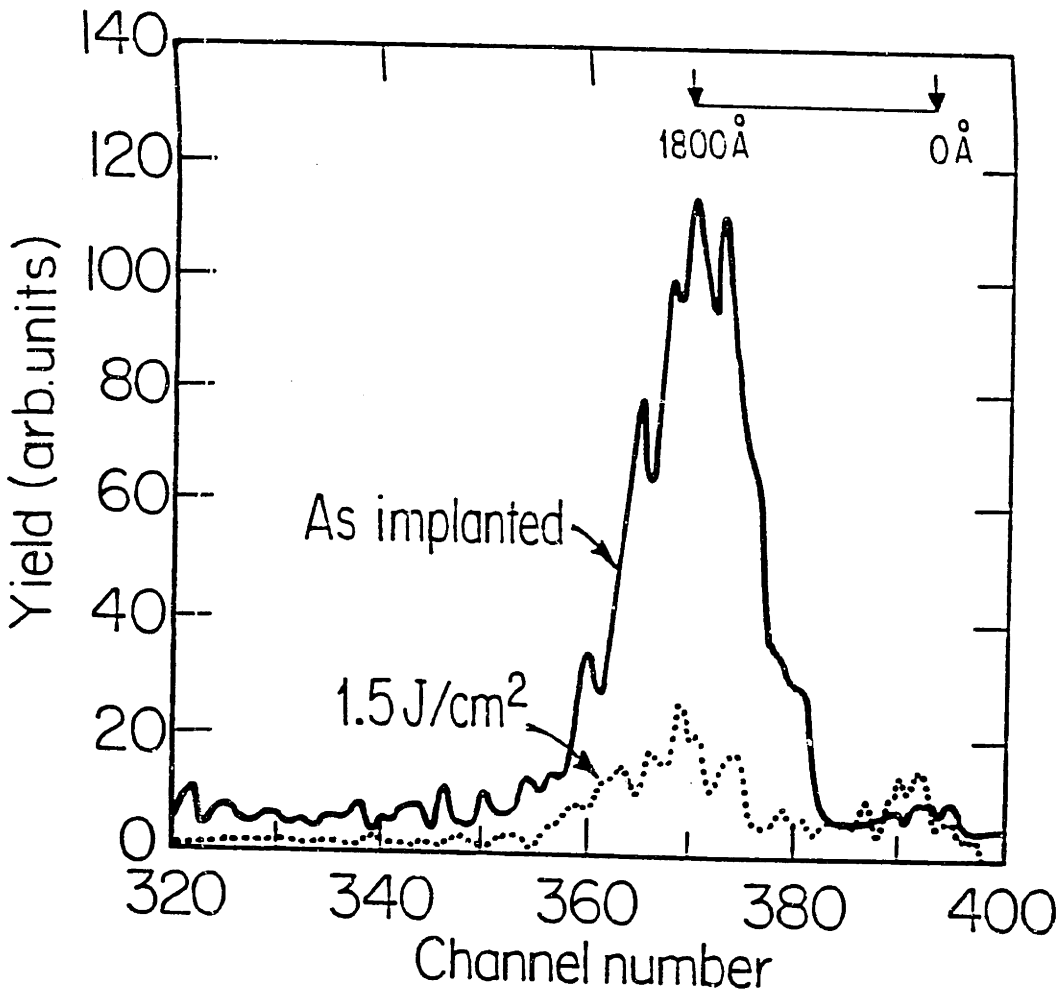

Figure 3.6: An example of how material loss can be measured using ion implanted markers. The solid line shows the original distribution of As implanted in graphite. The dotted line shows the distribution of the As after irradiation with a 1.5J/cm^2 ruby laser pulse. The shift in the position of the distribution determines the depth of removed layer of material. The appearance of a peak in the As distribution near the surface after laser irradiation is due to segregation of As.

of the complex interactions between the laser pulse, evolved vapor species, and alterations in the optical properties of solids caused by the high excitation rate of the laser pulse. Two kinds of plasmas may be formed by laser heating. The first is a traditional electron–ion plasma formed when gaseous species evolved from the laser heated surface are ionized by photons in the laser pulse. The electron–ion plasma is typically formed during laser irradiation of metals and can usually be observed using interferometric and recombination emission techniques. The second kind of plasma is unique to the laser heating of solids known as an electron–hole plasma and is usually formed during laser irradiation of semiconductors. The electron–hole plasma is created when incident photons create electron–hole pairs at rates faster than the excited pairs can decay back to their original state. Electron–hole plasmas may be observed experimentally using transient reflectivity techniques on a subnanosecond time scale.

Electron–Ion Plasmas

Electron–ion plasmas may be formed during pulsed laser heating of materials when some of the material evaporated from the surface becomes ionized. When surfaces are heated by an intense light pulse, charged species will be ejected from the surface. Initially, the concentration of the charged species will be small. If no vaporization occurs, then the low density plasma will dissipate as electrons recombine with positively charge ions.

If there is vaporization, energetic free electrons may collide neutral atoms in the vapor and ionize them. The electrons freed by the impact ionization may then absorb incident photons and cause more ionizations in an avalanche fashion. The process will continue until the plasma carrier density reaches the critical density after which *all* of the incident light in the laser pulse will be reflected. This process is known as inverse bremsstrahlung and is particularly

prominent in metals where the vaporization temperature is easily reached at moderate laser power densities due to a large absorption coefficient.

The density of laser induced electron–ion plasmas may be measured using an interferometric technique illustrated in Fig. 3.7 and used by David *et. al.*[30] to measure the density of laser generated carbon plasmas. A visible laser probe is used by dividing it up into two beams and measuring their relative phases as a function of time during laser irradiation. By using several different wavelengths to probe the space above the laser–irradiated region the electron density, N_e, and neutral particle density, N_0, can be obtained from the phase shifts observed using a set of equations

$$\Delta S \lambda_n = 2R(AN_0 - B_n N_e) \tag{3.5}$$

where ΔS is the number of phase shifts by 2π, while λ_n is the n^{th} wavelength used to probe the plasma, A is the neutral particle polarizibility, and B_n is the electron polarizibility at the n^{th} wavelength.

Using this technique, David *et. al.*[30,31,32] found that plasmas with densities as high as 10^{19}cm^{-3} could be generated 1mm above a laser–irradiated carbon surface at power densities of $\sim 10^{10}\text{W/cm}^2$. Similar techniques may be used to determine the densities of plasmas generated in other materials.

Electron–Hole Plasmas

Electron–hole plasmas are a solid state analog to the electron–ion plasma with a hole taking the role of the ion. The electron–hole plasma is created by the formation of electron–hole pairs through interband absorption of incident photons. The characteristics of these plasmas were discussed earlier with the mechanisms of laser heating in section 3.2.1.

The electron–hole plasma may be observed directly on a subnanosecond time scale during the early portions of the heating of a semiconductor, such as

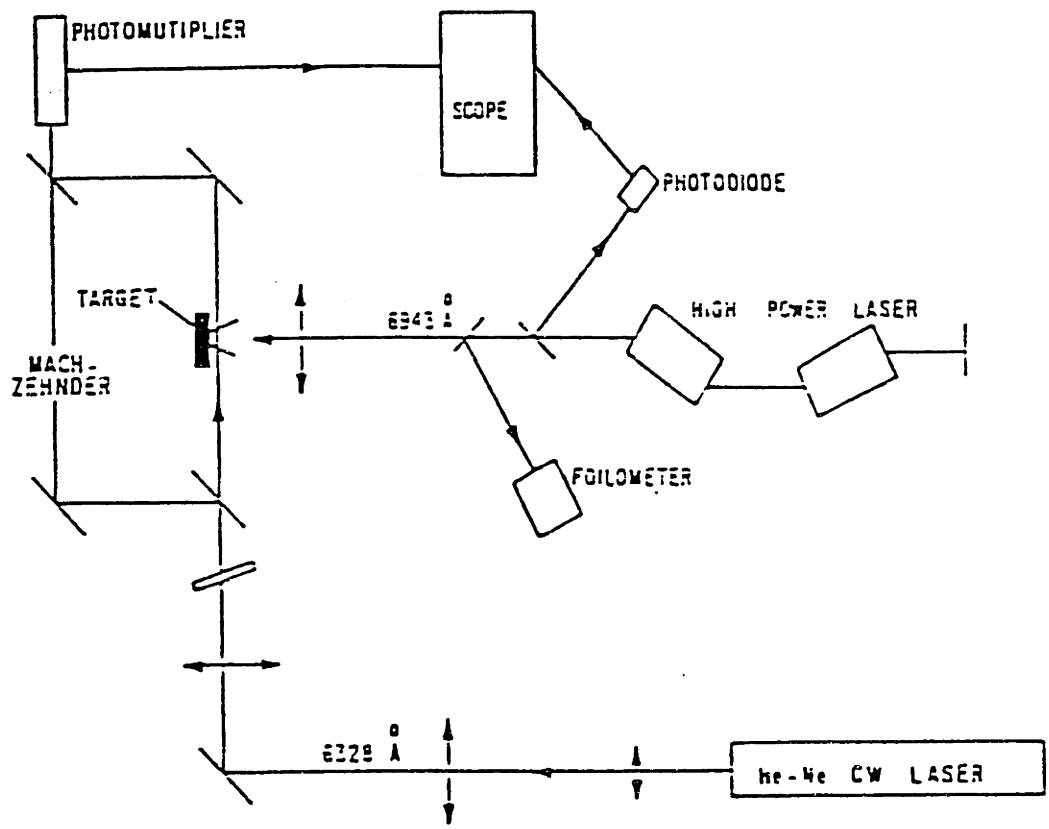

Figure 3.7: Experimental set–up for measuring the density of laser–induced electron–ion plasmas above a laser heated surface from[30].

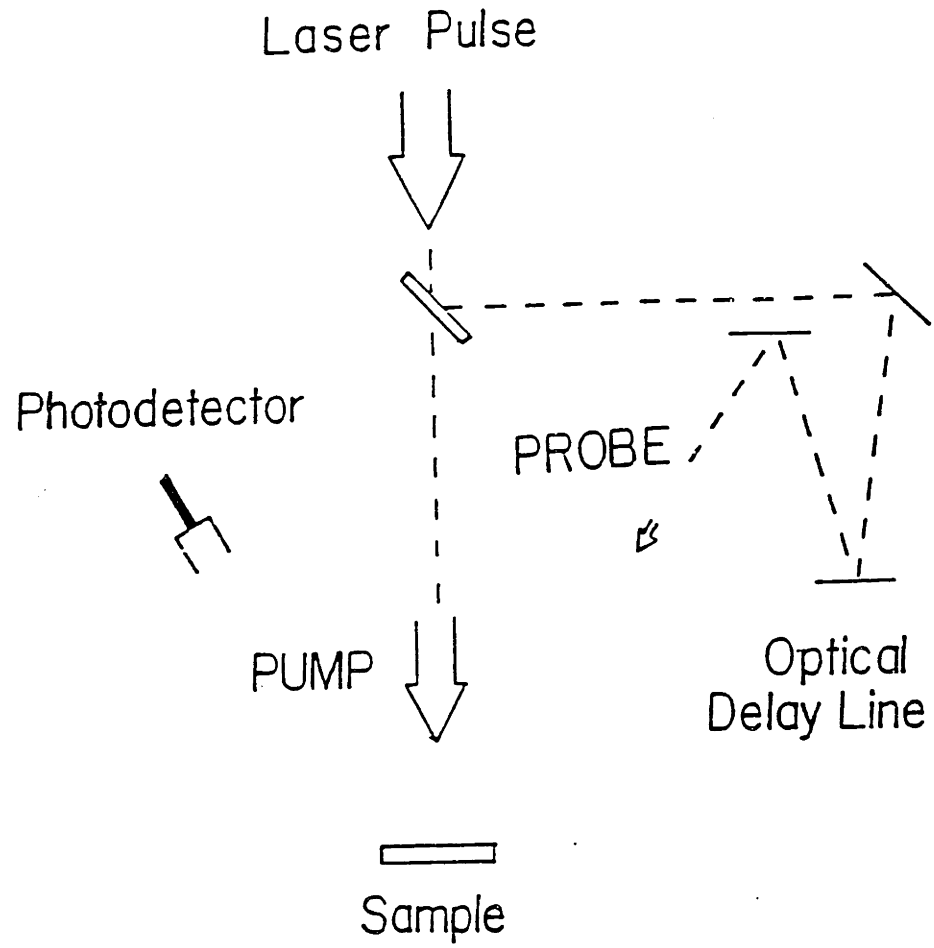

Figure 3.8: Experimental arrangement for the pump and probe technique used to measure optical reflectivity on the picosecond and femtosecond time scales.

silicon, using a pump and probe transient reflectivity technique. The experimental arrangement for the pump and probe technique is given in Fig. 3.8. The laser pulse coming from the laser is divided into two pulses: one of high intensity used to "pump" the sample and the other a low intensity pulse used to "probe" the optical properties. The probe pulse is usually detected by a photomultiplier and the intensity of the probe is integrated to obtain the reflectivity at a particular point in time. Time resolution is obtained by using an optical delay line to vary the time it takes for the probe to reach the sample relative to the pump. The transient reflectivity is then obtained by using a number of measurements at various delay times to generate a reflectivity versus time profile.

The pump and probe technique has been used successfully by Liu *et. al.*[33,34] to show the existence of the electron–hole in laser–heated silicon and laser–heated gallium arsenide at times concurrent with the laser heating pulse.

3.4 Phase Transitions in Carbon

Pulsed laser heating has been used to induce phase transitions in graphite and other forms of carbon. The usefulness of pulsed laser heating in melting graphite is that the high temperature required to melt graphite can be readily attained and that the graphite will form its own crucible so that contamination from a molten container will not affect the melting temperature or heat of fusion. The initial part of the section will show that carbon can be melted by pulsed laser heating using several complementary post–heating techniques.

The following section will discuss the vaporization and material loss of carbon during pulsed laser heating using ion implanted markers. The final sections will discuss our transient optical and electrical measurements during pulsed laser heating. Also discussed are possible mechanisms for the formation of dense electron–ion plasmas at the surface of graphite which impede optical measurements.

3.4.1 Evidence for the Formation of Liquid Carbon

A suggestion that graphite can be melted using pulsed laser heating came from Rutherford backscattering and ion beam channeling experiments[21] on laser heated graphite. A series of ion channeling spectra for 30nsec pulsed ruby (694nm) laser irradiated graphite parallel to the c-axis appear in Fig. 3.9. For incident laser pulses with energy densities less than $0.6 J/cm^2$, the ion channeling spectrum appears the same as for graphite. For laser pulses with energy densities above $\sim 0.6 J/cm^2$ a layer of disordered carbon is formed on the

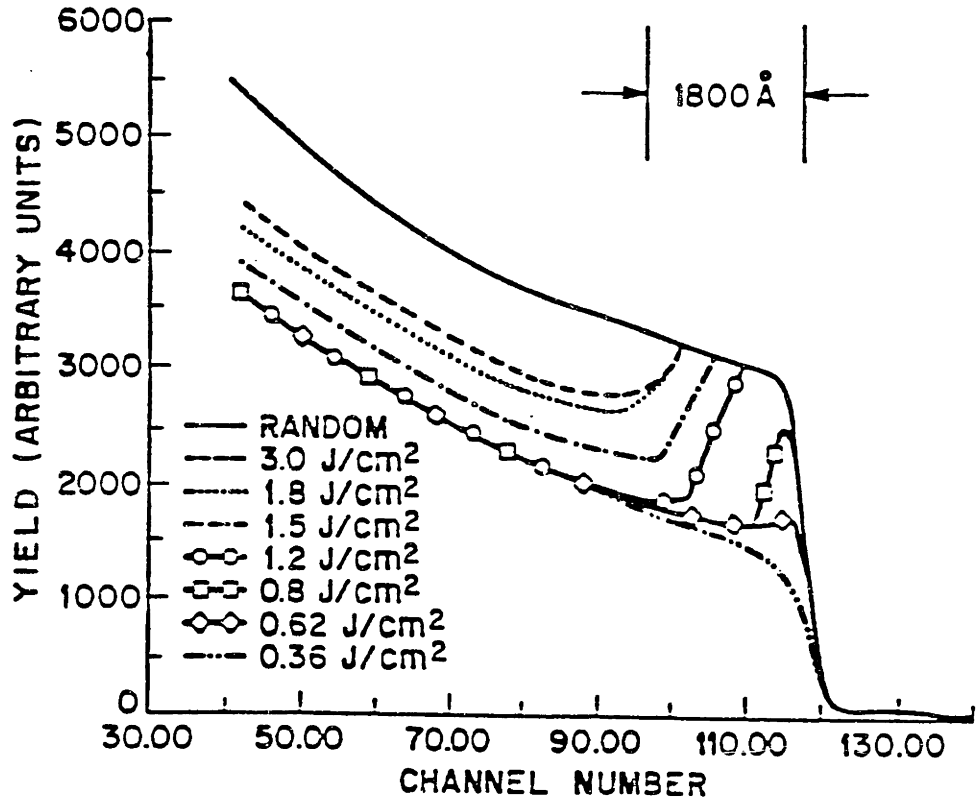

Figure 3.9: Ion channeling spectra for 30nsec pulsed ruby laser irradiated graphite. The onset of a disorder layer occurs for an energy density $0.6 J/cm^2$. The disorder depth appears to saturate for energy densities above $1.8 J/cm^2$. (Taken from Venkatesan *et. al.*[21])

graphite surface. This is indicated in the figure by the increase in the backscattering yield above the level of the backscattering yield for graphite (trace for $0.36 J/cm^2$ in Fig. 3.9). The thickness of the disorder layer, measured by the thickness of the high RBS yield region, grows nearly linearly with increasing laser pulse energy density until the energy density reaches $\sim 1.8 J/cm^2$. For energy densities above $1.8 J/cm^2$, the disorder layer thickness appears to saturate at ~ 1800Å.

Melting is suggested from the ion channeling spectra for the following reasons: First, the back edge of the disorder layer peak is sharp compared to damage caused by radiation such as ion implantation. An ion channeling spectrum for ion–implanted graphite appears in Fig. 3.10 for comparison. Note that the back edge of the disorder peak falls off more gradually than in the laser heating case. The more gradual fall off of the disorder peak is due to the nonuniform distribution of implanted ions. If the graphite were simply damaged by the laser radiation, then a similar disorder pattern would be expected. The sharp back edge is indicative of a sharp interface between two distinct regions of different degrees of order in the material.

Second, melting is suggested by the threshold energy density needed for creating disorder and the nearly linear growth of the disorder layer thickness with increasing energy density. Since more energy is introduced for larger laser pulse energy densities, it is reasonable that the amount of liquid created by the laser pulse will increase. A summary of the pulsed ruby laser results appears in Fig. 3.11. From the slope of the line drawn for the energy density versus disorder layer thickness, an order of magnitude estimate of the heat of fusion can be made. The slope of the line in Fig. 3.11 determines the amount of energy needed to raise the temperature of graphite to the melting temperature and supply the heat of fusion to melt the graphite. By multiplying the slope

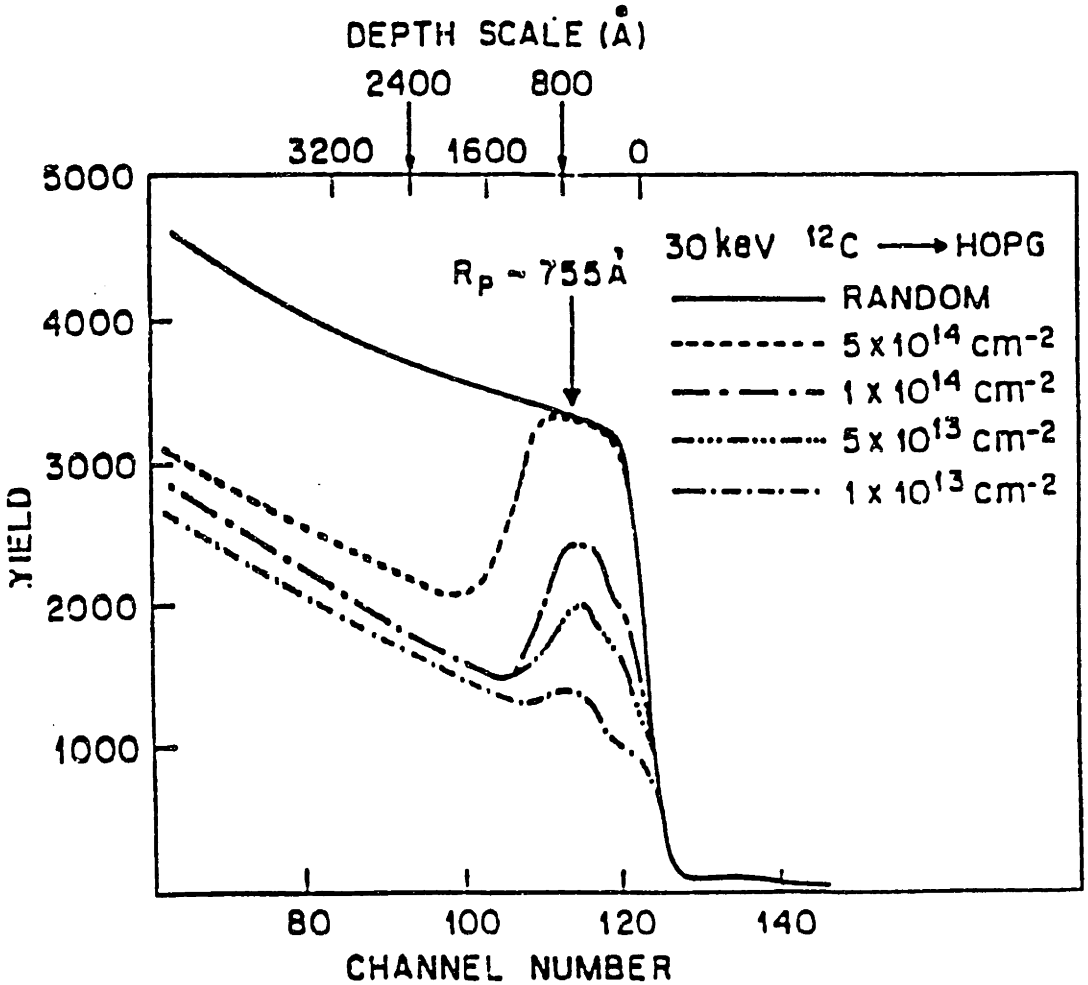

Figure 3.10: Ion channeling spectra for ion implanted graphite taken from Elman *et. al.*[35]

by the fraction of the energy absorbed from the laser pulse (one minus the reflectivity), and using the specific heat for graphite (chapter 2) to calculate the energy needed to heat graphite up to the melting temperature, the heat of fusion can be estimated. The heat of fusion estimated in this way is 140kJ/mole for pulsed ruby laser irradiated graphite. This value is in good agreement with the accepted value of $\sim$ 105kJ/mole[36,37] since our estimate does not account for thermal diffusion and vaporization.

The effects of thermal diffusion and vaporization are important when trying to calculate the heat of fusion. Accounting for the effects of thermal diffusion will decrease the estimated heat of fusion because some of the energy introduced into the sample diffuses away from the laser–irradiated region and would therefore not be counted for in the above analysis. Accounting for vaporization would also decrease the estimate of the heat of fusion since a portion of the energy introduced into graphite is removed from the sample by the vapor species. Since thermal diffusion and vaporization are not accounted for in the above analysis, the high estimate of the heat of fusion can be explained.

In addition to the pulsed ruby laser results, the ion channeling results are reproducible using other pulsed laser sources. A series of ion channeling spectra for 25nsec pulsed KrF (248nm) laser irradiated graphite shows a similar behavior of the disordered layer as in Fig. 3.9. In the series of ion channeling spectra for KrF laser–irradiated graphite, the back edge of the disorder peak is sharp and the disorder layer thickness saturates at large laser pulse energy densities. The differences between the results of the ion channeling studies for pulsed ruby laser and pulsed KrF laser are that the threshold energy density for the creation of a disordered layer is greater for the KrF irradiated graphite and the thickness at which the disorder layer thickness saturates for KrF irradiated graphite is smaller than for the ruby laser case.

The differences between the results for pulsed ruby and pulsed KrF are attributed to the differences in the optical properties of graphite at the irradiating laser wavelength. The higher reflectivity of graphite at 248nm (KrF laser) than at 694nm (ruby laser) would account for the higher melting threshold of the KrF laser. The reason that the maximum disorder layer thickness is smaller for the pulsed KrF laser is due to the optical properties of liquid carbon. If the liquid is metallic (chapter 4) then the liquid will absorb strongly and there will be an increase in the vaporization of carbon relative to the pulsed ruby laser case. If the liquid is molecular, there is a strong absorption near 248nm which will again increase vaporization relative to the pulsed ruby laser case.

By plotting the disorder layer thickness, measured using ion channeling, as a function of the incident pulse energy density in Fig. 3.11, one can see the near linear relationship between the incident energy density and the disorder layer thickness. From the results for pulsed KrF laser irradiated graphite, the heat of fusion, calculated from the slope of the line as above, is $\sim$ 290kJ/mole, again neglecting thermal diffusion and vaporization. The doubling of the estimate for the heat of fusion is due to the smaller rate at which the disorder layer thickness grows.

Although ion channeling results suggest that melting has occurred, the ion channeling results by themselves are not a sufficient proof that graphite has melted. The saturation of the disorder layer thickness may be related to the optical penetration of the incident laser pulse into the solid graphite. Since the optical penetration of the lasers used is comparable to the measured disorder layer thickness, the disorder may still be created as a result of the laser damaging the graphite due to the high heating rate associated laser heating.

Additional evidence for melting is supplied by Raman spectroscopy and electron microscopy. A series of Raman spectra for pulsed ruby laser irradiated

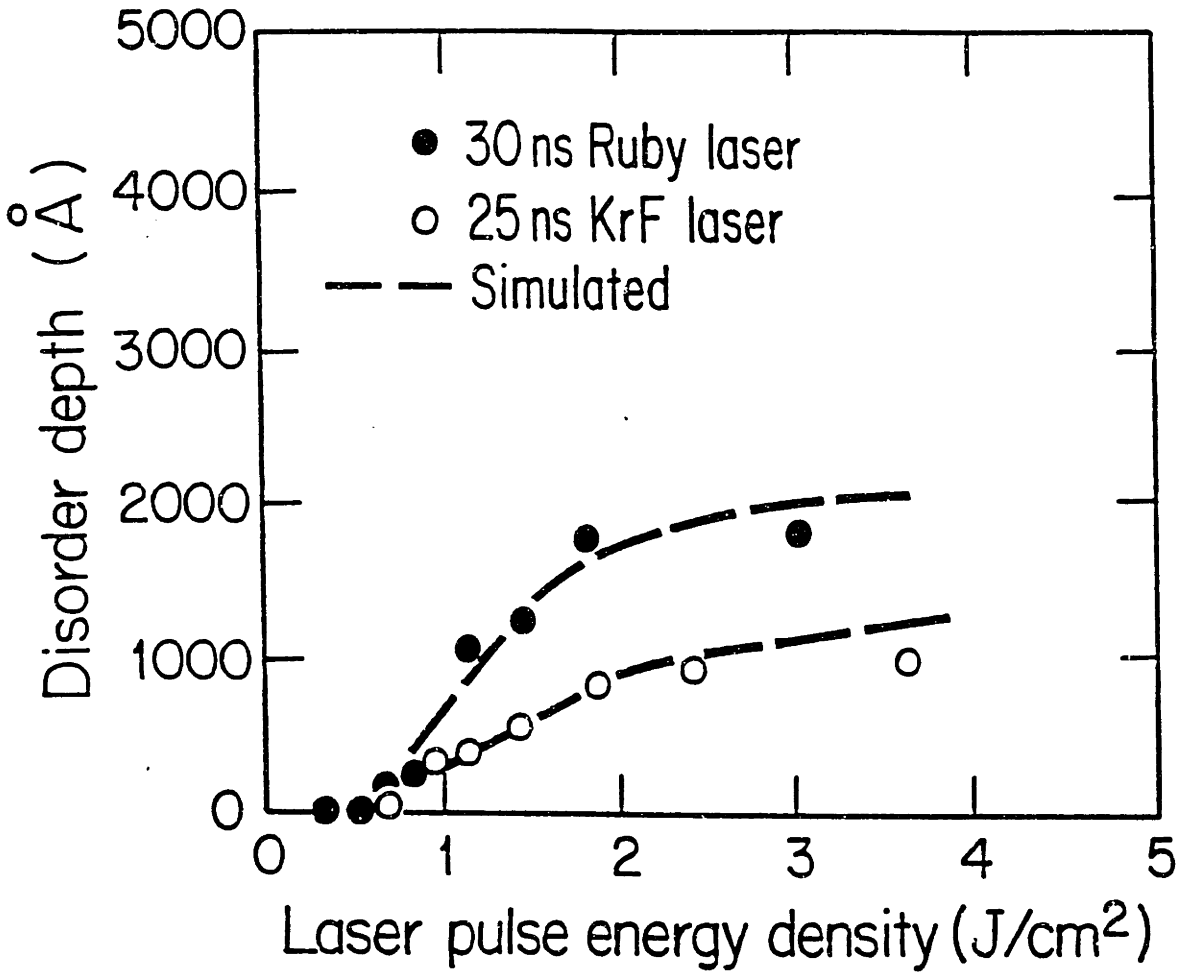

Figure 3.11: Summary of the results of ion channeling spectra in 30nsec pulsed ruby (694nm) laser irradiated graphite and 25nsec pulsed KrF (248nm) laser irradiated graphite. Note the nearly linear dependence of the disorder layer thickness with energy density for pulses with energy densities just above the melt threshold.

graphite appear in Fig. 3.12. As shown in Fig. 3.12 in the first order Raman spectrum, the intensity of the disorder induced mode at 1360cm^{-1} increases relative to the intensity of the zone–center Raman–allowed mode at 1582cm^{-1} as the laser pulse energy density increases above the threshold value measured with ion channeling. However, for the largest energy density pulses, the trend reverses and the intensity of the disorder–induced mode at 1360cm^{-1} deceases relative to the intensity of the Raman allowed mode at 1582cm^{-1}. The second order Raman spectra show similar behavior. When the energy density of the laser is a somewhat larger than the threshold value for creating a disordered layer, the second order Raman spectrum for graphite almost disappears (Fig. 3.12b). However, for very large laser pulse energy densities, the second order spectrum returns, but the second order peaks are not as sharp as for graphite (Fig. 3.12c).

A comparison of these spectra with a Raman spectrum for glassy carbon, a disordered graphite, shows that the material in the disordered layer is a highly disordered graphite. However, the disordered layer created by pulsed laser irradiation is not glassy carbon since the ratios of the intensities in the Raman peaks are not the same as in glassy carbon. The results of Raman measurements on pulsed KrF laser–irradiated graphite are similar.

A summary of the first order Raman measurements for pulsed laser heated graphite with pulsed ruby and pulsed KrF lasers appears in Fig. 3.13 and shows the increase in the intensity ratio, I_{1360}/I_{1582}, of the disorder–induced mode to the Raman–allowed mode for irradiating pulses with energy densities increasing above the threshold value. Figure 3.13 also shows that the intensity ratio reaches a maximum value for both pulsed lasers and that for higher energy densities, the intensity ratio decreases, as explained below.

The intensity ratio, I_{1360}/I_{1582}, has been related to the average crystallite

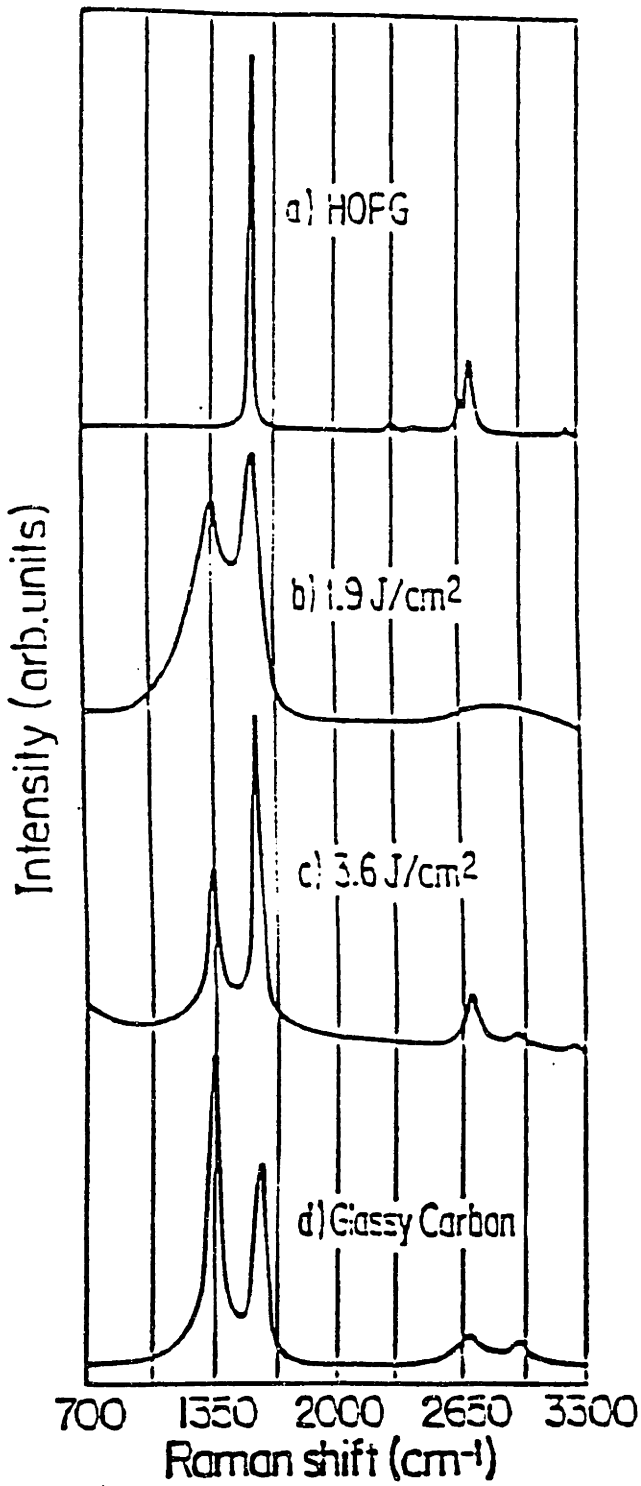

Figure 3.12: Raman spectra for pulsed laser irradiated graphite. The spectrum in (a) is for the first and second order Raman peaks in graphite. The spectra in (b) and (c) are the first and second order Raman spectra for graphite irradiated with 1.9J/cm^2 and 3.6J/cm^2 from a 30nsec pulsed ruby laser, respectively. The spectrum in (d) is for glassy carbon, a disordered graphite, for comparison.

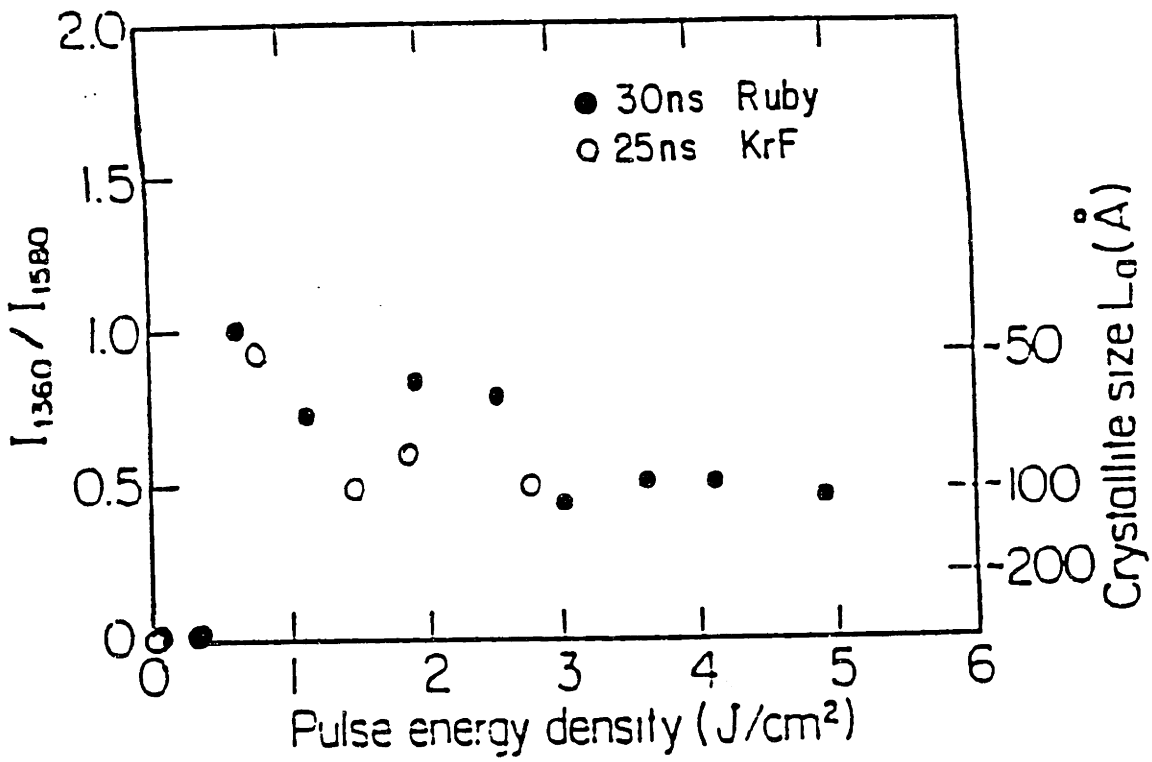

Figure 3.13: Summary of the results from Raman spectroscopy. Note the increase in the ratio of the intensity of the disorder–induced mode at 1360cm^{-1} to the intensity of the Raman–allowed mode 1582cm^{-1} for energy densities just above the melting threshold. At very large energy densities, the ratio decreases. The right hand ordinate was calibrated by the work of Tuinstra and Koenig[38].

size in graphite by Tuinstra and Koenig[38] and their calibration appears on the right hand ordinate in Fig. 3.13. Using this calibration, laser pulses with energy densities just above the threshold energy density have average crystallite sizes which decrease with increasing energy density. This would be expected if the graphite were simply damaged by the incident laser pulse. However, after the crystallite size reaches a minimum, it begins to increase with increasing laser pulse energy density until it reaches a saturation value at about 10nm. These results cannot be explained solely on the basis of a damage model since increasing the laser pulse energy density would be expected to increase the degree of damage in the graphite. Higher degrees of damage would show up in the Raman spectra as increases in the intensity ratio. Since the intensity ratio reaches a maximum value (the average crystallite size reaches a minimum value), this means that either the heating of the surface is causing self annealing, or, since a liquid would be expected to last longer for larger laser pulse energy densities, the liquid is resolidifying in larger crystallite sizes.

Transmission electron microscopic studies of the laser irradiated region confirm the Raman results regarding the trend in the crystallite size and add new information about the microstructure of the resolidified melt. As observed with Raman spectroscopy, laser pulses with energy densities just above the damage threshold produce a disorder layer with an average crystallite size which decreases with increasing energy density. For laser pulses with energy densities large compared to the damage threshold, the average crystallite size increases until a saturation value $\sim$ 10nm is reached in accordance with the Raman results.

The additional information provided by TEM about the orientation of the crystallites in the microstructure provides another piece of evidence for laser melting of graphite. Studies of radiation damaged graphite[39] show that while

the graphite planes are disordered as a result of the radiation, the orientation of the graphite planes relative to the c–axis of the starting material does not change. In laser irradiated graphite, the orientation of the graphite planes in all of the crystallites in the disordered region do not remain perpendicular to the c–axis after heating with a laser pulse with an energy density greater than the threshold for creating the disordered layer. This is shown in TEM diffraction patterns of pulse ruby laser irradiated graphite in Fig. 3.14. In Fig. 3.14a the micrograph for a region irradiated with a $1.2J/cm^2$, 30nsec ruby laser pulse is displayed. The ($hk0$) rings in the micrograph are diffuse and are indicative of the damaged graphite planes oriented perpendicular to the graphite c–axis with a small coherence length. The appearance of ($00l$) rings in the micrograph means that some of the crystallites are oriented with their graphite planes parallel to the c–axis of the graphite substrate. In Fig. 3.14b a diffraction pattern for a region irradiated with a $3.0J/cm^2$ ruby laser pulse shows sharp rings. The sharp rings in Fig. 3.14b are indicative of an average crystallite size of 10nm. In addition to the ($hk0$) rings, ($00l$) rings also appear indicating that there are crystallites with their graphite planes oriented along the c-axis direction. The orientation of graphite planes along the c–axis is uncharacteristic of graphite damaged by radiation whereas melting and resolidification can readily explain the orientation of some graphite crystallites along the c—axis direction.

Scanning electron photographs of the surface region of the irradiated areas show that there are many places where graphite planes appear to be torn and uplifted. In addition, there are tiny spheres scattered about the surface as shown in Fig. 3.15. The small spheres which are scattered on the surface are reminiscent of the spheres observed by Kelly *et. al.*[40,41,42] on the surface of resolidified metals which have been pulsed laser melted. The spheres on the graphite surface are up to 0.2 microns in diameter which is also similar to the

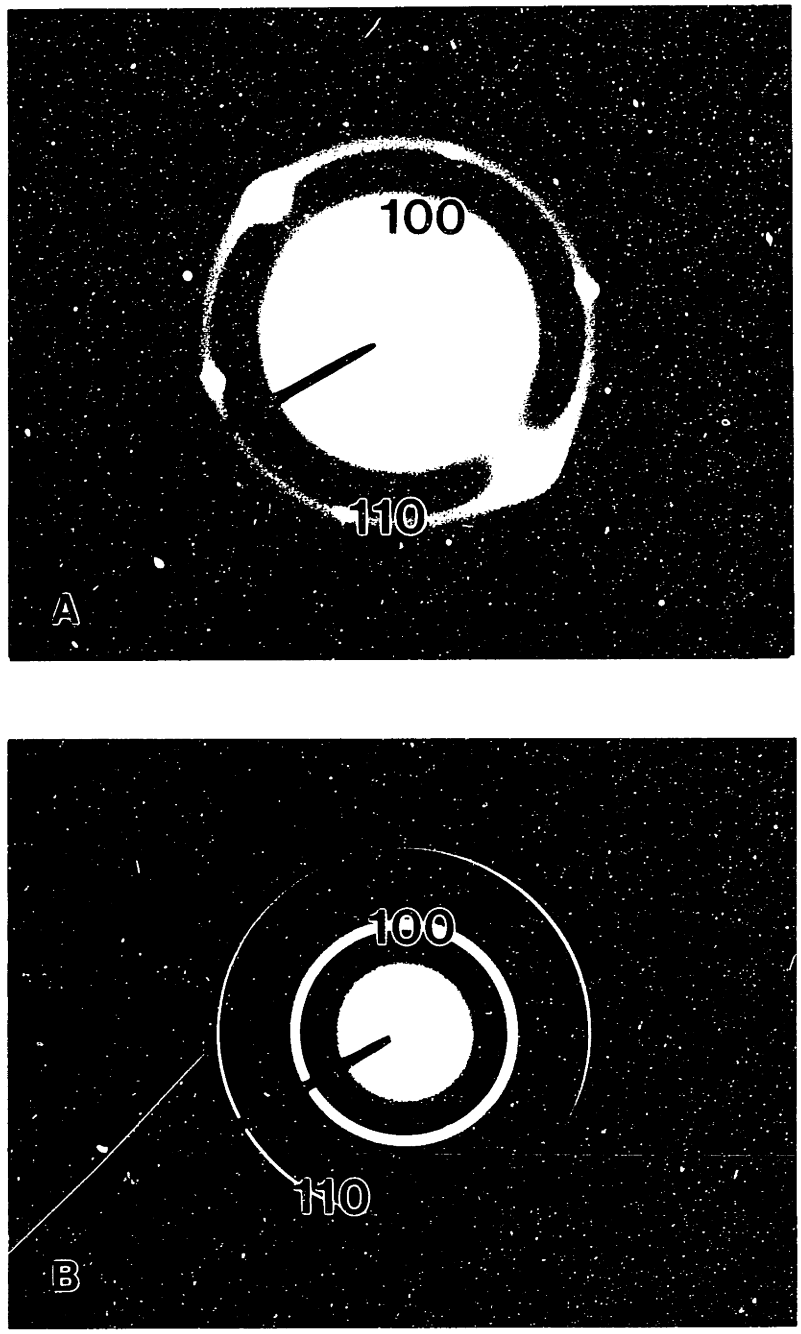

Figure 3.14: Selected area diffraction pattern from pulsed ruby laser irradiated graphite. In (a) a region irradiated with a 1.2J/cm^2 30nsec pulsed ruby laser and in (b) a region irradiated with a 3.0J/cm^2 pulsed ruby laser. Note the diffuse rings in (a) and the sharp rings in (b). (Taken from Speck *et. al.*[22])

Figure 3.15: Scanning electron photograph of a pulsed ruby laser irradiated graphite surface. Note the uplifted graphite planes and the spheres of material scattered across the surface. The spheres are thought to form from the surface tension on the surface of the liquid[40]. (Taken from Speck *et. al.*[22])

observations of Kelly *et. al.*[40,41,42] for pulsed laser melted metals. These spheres are probably formed as a result of hydrodynamic effects on the liquid to minimize its free surface energy. These will be discussed in chapter 6.

The fourth experiment which suggests that pulsed laser irradiated graphite melts is the segregation of ion implanted impurities. Segregation and solute trapping of impurities in graphite will be discussed in section 3.5. However, to show that solid state effects cannot account for the observed changes in the impurity profiles in graphite after pulsed laser–irradiation, it is sufficient to show that the diffusion coefficient, D_{cc}, for impurities in graphite along the c-axis must be much larger than its normal value of $D_{cc} \sim 10^{-10}\text{cm}^2\text{s}^{-1}$. This can be done by placing impurities in graphite by ion implantation and measuring the change in the impurity distribution using Rutherford backscattering. Figure 3.16 shows the results of Rutherford backscattering measurements on the distribution of implanted germanium impurities in graphite before and after pulsed ruby laser irradiation. In Fig. 3.16, the zero for the depth scale corresponds to the surface of the graphite. When graphite is laser–irradiated with pulses which have energy densities above the threshold for creating the disorder layer on the surface, the germanium impurities are redistributed. This can be seen in Fig. 3.16 by the changes in the backscattering yield and by observing the changes in the depth of the germanium from the surface in the spectra for samples irradiated with 1.5, 2.0 and 3.0J/cm^2.

The impurities which appear on the surface after pulsed laser irradiation must move more than 1000Å. In order for this to occur on the time scale of $\sim$ 100nsec, the diffusion coefficient must be $D_{cc} \sim 2.5 \times 10^{-4}\text{cm}^2\text{s}^{-1}$ where D_{cc} is given by

$$D_{cc} = \frac{d^2}{4t} \tag{3.6}$$

where d is the diffusion length and t is a relevant time scale for heating

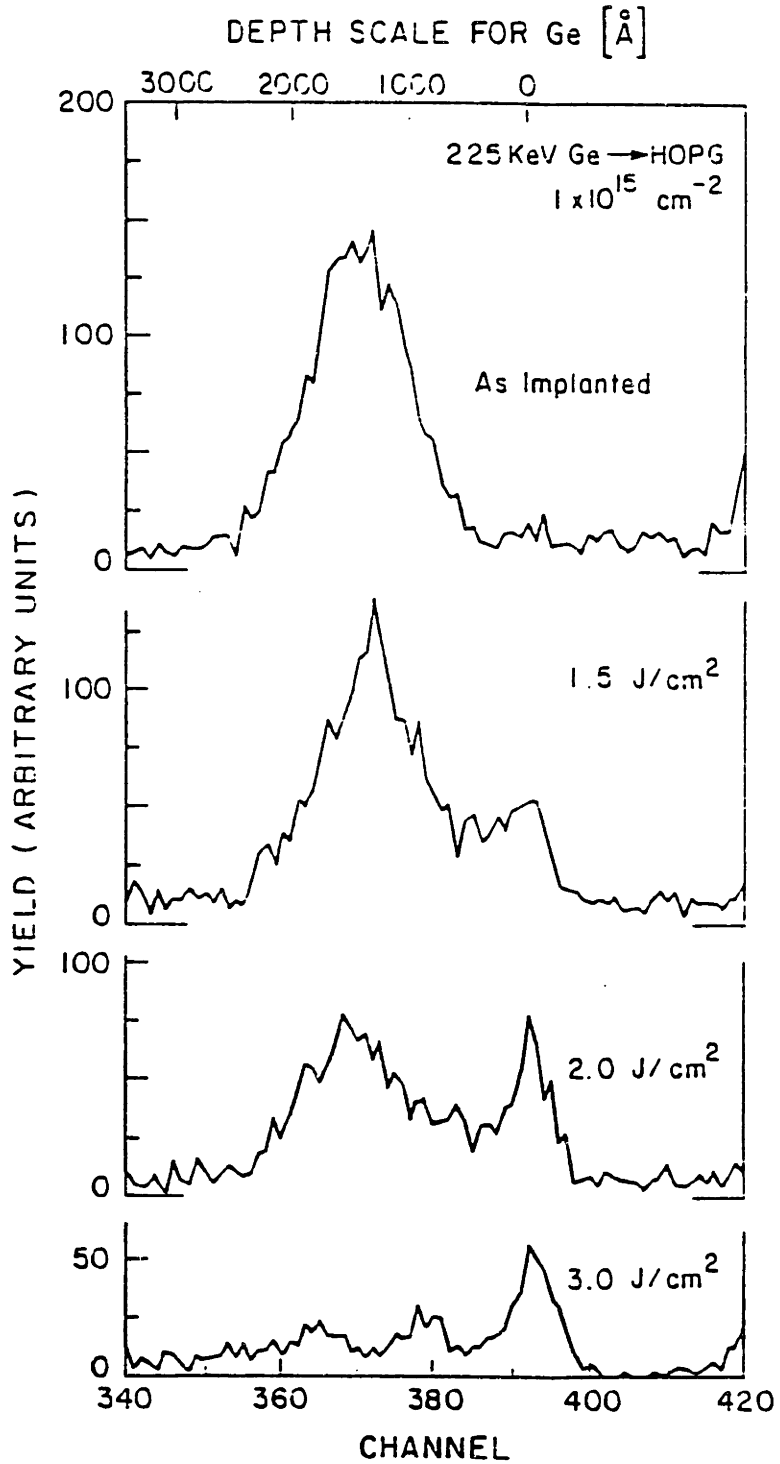

Figure 3.16: Plot of the RBS yield versus depth (channel number) showing the redistribution of ion implanted germanium in pulsed laser irradiated graphite. Note the movement of impurities to the surface. The impurity redistribution cannot be explained by solid state diffusion.

(100nsec). Since D_{cc} must be large enough to accommodate the diffusion of impurities to the surface, liquid carbon must have been present to allow for the diffusion. In fact, the diffusion coefficients for both liquid silicon and liquid germanium are $\sim 10^{-4}\text{cm}^2\text{s}^{-1}$ so that the estimated diffusion coefficient for liquid carbon is the right order of magnitude.

From a culmination of these experimental results, the only conclusion which can be drawn is that graphite is melted by pulsed laser radiation if the incident energy density in the laser pulse is high enough. The magnitude of the energy density threshold for melting as well as the amount of liquid created will depend on the optical properties of graphite for the wavelength of the irradiating laser pulse and the thermal properties of graphite (chapter 2).

3.4.2 Material Loss in Pulsed Laser Heated Carbon

The loss of carbon due to vaporization and sublimation during pulsed laser heating of graphite has been shown in section 3.3.2 while discussing the ion implanted marker method for determining the total amount of material removed from a laser heated surface. For pulsed ruby laser heated graphite, the amount of removed material increases linearly with increasing laser pulse energy density for energy densities above the threshold for melting. Our experimental results are plotted in Fig. 3.17, which shows that the onset of material loss via vaporization and sublimation occurs at or near the pulse energy density threshold for melting at 0.6J/cm^2. This is the energy density at which tne distribution of implanted As impurities is seen to shift by the minimum detectable amount ($\sim$ 100Å) using RBS. The shift in the As distribution grows nearly linearly as the incident pulse energy density is increased. By drawing a line through the experimental points, the amount of material lost per unit energy above the threshold is $\simeq 400\text{Å/J}$.

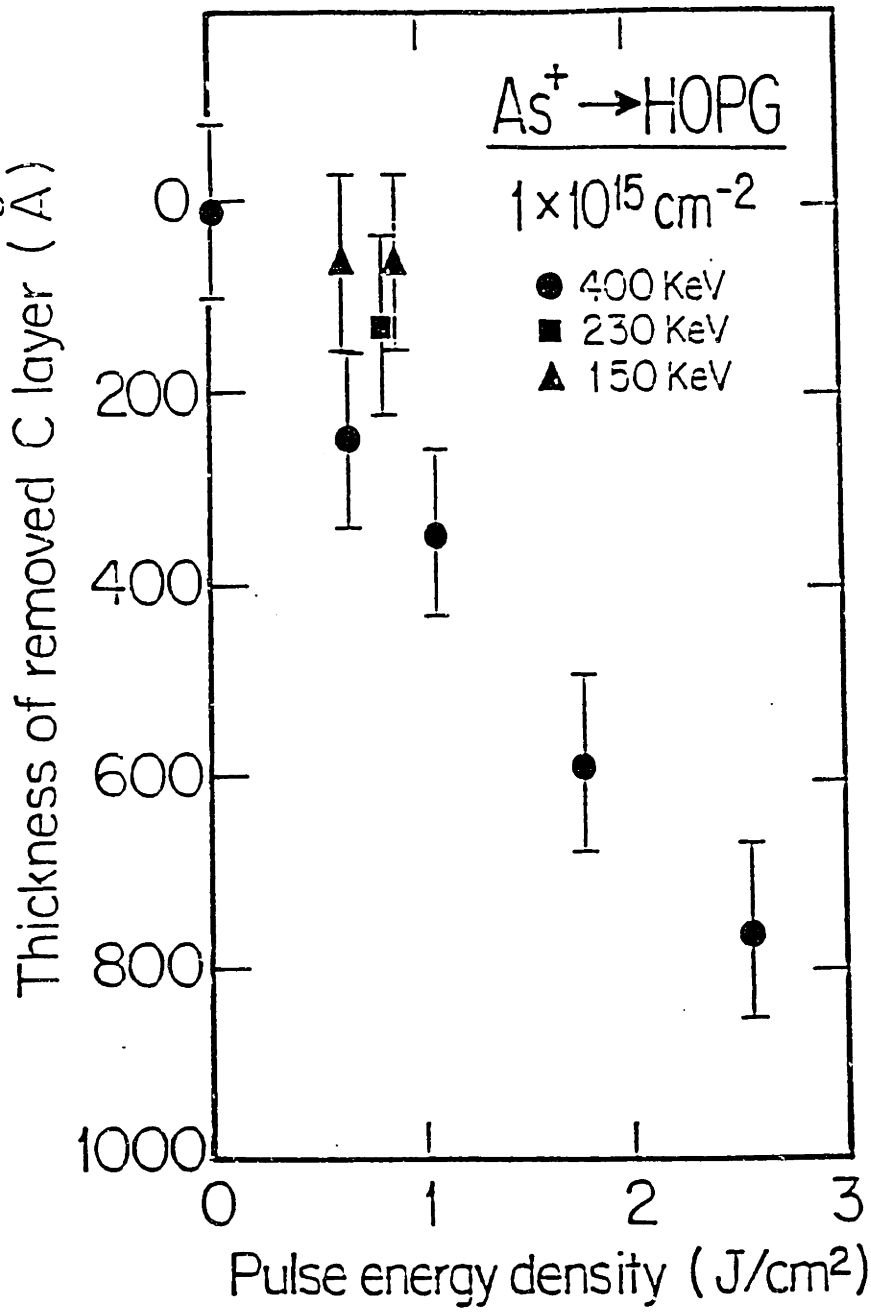

Figure 3.17: The amount of material removed from graphite as a function of pulsed ruby laser energy density. Note the nearly linear relationship for energy densities above the melt threshold.

Kelly *et. al.* have shown, using emission spectroscopy, that for pulsed KrF laser irradiation the loss of material from graphite targets occurs predominantly by equilibrium processes[43]. Therefore, the loss of material by pulsed ruby laser irradiation must also occur by equilibrium processes. This conclusion may be drawn since the photon energy of the ruby laser is smaller than that for the KrF laser so that nonequilibrium ejection of material from the surface is less likely for ruby laser irradiation since there is a lower probability that carbon atoms will be ionized.

The data for material loss can be used to obtain a better estimate for the heat of fusion for pulsed ruby laser melted graphite. If we consider the material lost to have been first melted, then the thickness of the molten layer created is the sum of the thickness of the layer of material lost in Fig. 3.17 and the disorder layer thickness in Fig. 3.11. Applying the same method described earlier, the estimate for the heat of fusion for pulsed ruby laser melted graphite becomes $H_f = 125$kJ/mole, which is in better agreement with the accepted value of $H_f = 105$kJ/mole[36,37] than our previous estimate.

Evaporated carbon films also show material loss for energy densities comparable to and above the threshold energy density for melting in graphite. The material loss in evaporated carbon films can be measured using Rutherford backscattering by measuring the thickness of a carbon film both before and after laser irradiation. The results obtained for a 3000Å evaporated carbon film appear in Fig. 3.18. The RBS spectra for evaporated carbon films in Fig. 3.18 show the backscattering yield from the carbon film sitting on top of the backscattered yield from both silicon and oxygen which comprise the quartz substrate on which the film sits. The carbon film thickness is measured in a similar fashion to the disorder layer thickness in graphite by measuring the thickness of the backscattered yield solely due to carbon.

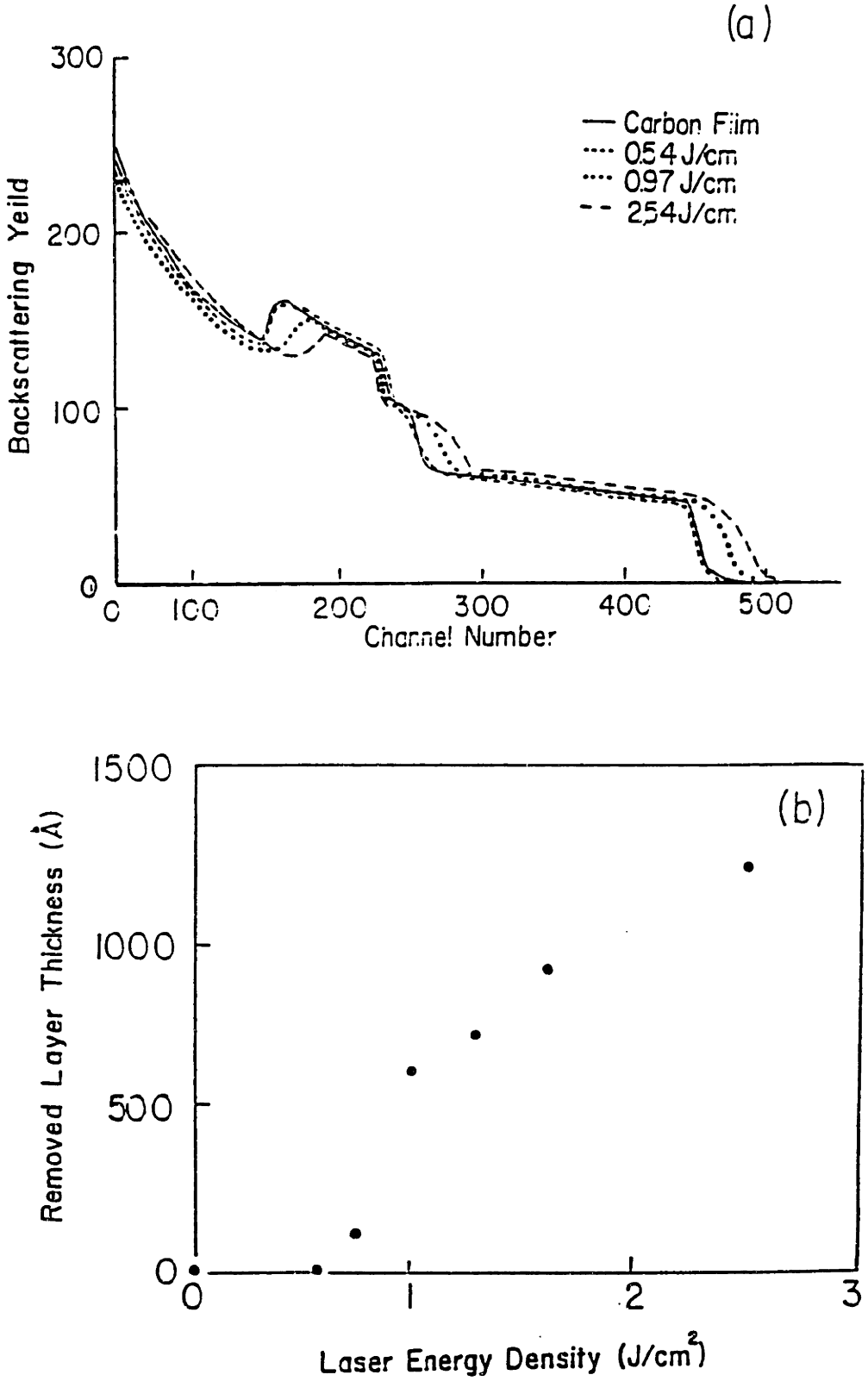

Figure 3.18: The material loss in evaporated carbon films. In (a) a series of RBS spectra as a function of KrF laser pulse energy density. In (b) a summary of the spectra of (a) showing the material loss as a function of incident pulse laser energy density.

For small pulse laser energy densities, there is no loss of carbon from the films. When the pulse energy density becomes comparable to the pulse energy densities required to melt graphite, the thickness of the carbon films decrease, indicative of material losses due to vaporization. Since the onset of significant material loss in the evaporated carbon films occurs at energy densities comparable to the melt threshold in graphite, the temperature at the surface of the films will be comparable to the surface temperatures in graphite during pulsed laser heating.

The material loss versus laser pulse energy density for evaporated carbon films is shown in Fig. 3.18b which is similar to Fig. 3.17. In Fig. 3.18 the slope of the line joining the data points is $\simeq 800$Å/J showing that the temperatures reached in the evaporated carbon films are comparable to those reached in graphite during pulsed laser heating. The larger rate of material loss in the evaporated carbon films is consistent with the rate of material loss in graphite since the binding energy in the carbon films will be lower than in graphite. It is also noteworthy that significant material loss does not occur until the pulse laser energy density is sufficient to cause melting in graphite.

3.4.3 Transient Reflectivity and Electrical Conductivity Measurements

Transient measurements are the best way to directly determine the properties of liquid carbon generated by pulsed laser heating. The transient measurements techniques that are used during pulsed laser heating have been previously described in section 3.3 as they have been applied to other materials. The application of transient measurement techniques to pulsed laser melted graphite is described in this section. Also presented are attempts to overcome the problems encountered during the measurements.

The results of transient reflectivity measurements are discussed for graphite melted with pulsed ruby and KrF lasers. A discussion of transient reflectivity measurements on evaporated carbon films is also included. The discussion of transient reflectivity measurements made on a subnanosecond scale is deferred until section 3.8. A discussion of transient electrical conductivity measurements on pulsed laser melted graphite fibers follows the discussion of the nanosecond transient reflectivity measurements. Measurements of the transient electrical conductivity during pulsed current heating of graphite fibers are discussed in section 3.7.

Transient Reflectivity Measurements

Transient reflectivity measurements were carried out on pulsed laser melted graphite using the same experimental arrangement shown in Fig. 3.2. A continuous wave HeNe laser and a continuous wave Ar^+ laser were used to probe the reflectivity in the laser irradiated region. A typical measurement of the reflectivity versus time is shown in Fig. 3.19. The trace in Fig. 3.19 shows that the reflectivity of the laser irradiated region sharply decreases during the laser pulse. The reflectivity reaches a minimum value which is close to zero. The reflectivity then increases until it saturates at a value which is smaller than the reflectivity before laser irradiation. The smaller post irradiation reflectivity is attributed to the nonuniform surface resulting from the rapid solidification of the liquid.

In silicon and germanium, the reflectivity sharply increases during the irradiating laser pulse because of a semiconductor to metal transition which accompanies the melting of those elements. The decrease in the reflectivity observed in laser melted graphite would suggest that liquid carbon has a substantially smaller electrical conductivity than graphite. If the electrical conductivity of

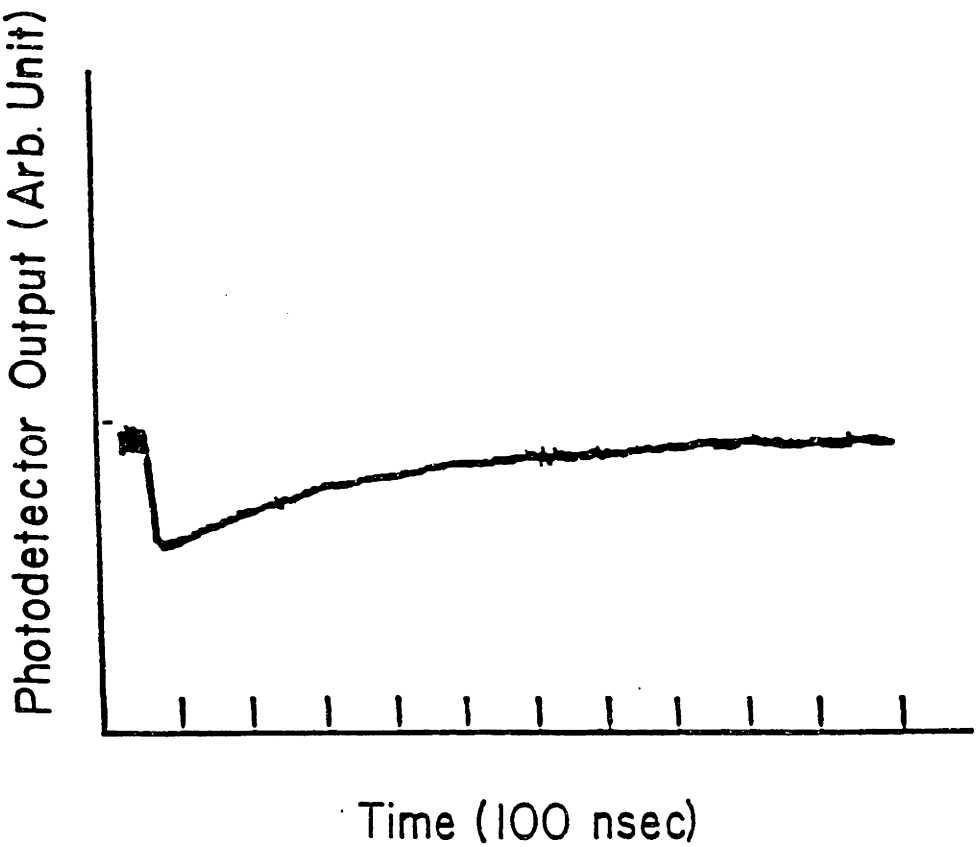

Figure 3.19: A typical transient reflectivity trace for pulsed laser melted graphite. A 30nsec ruby laser pulse with energy density 2.0J/cm^2 was used to melt the graphite.

liquid carbon is much smaller than the electrical conductivity of graphite, then the absorption depth for optical wavelengths should be much larger.

The liquid layer thickness can be estimated from the disorder depth remaining after laser irradiation and the thickness of the vaporized material, measured by RBS and ion channeling. Using the ion channeling and RBS measurements described earlier, the thickness of the liquid carbon layer is known not to exceed 3000Å for a 2.0J/cm^2 30nsec ruby laser pulse. However, if the absorption depth for the liquid is large, then the reflectivity signal will be from both the liquid layer and the underlying graphite. The reflectivity of graphite is $R \sim 0.3$ for the wavelength of the probing HeNe laser so that it is unlikely that the observed signal is due to reflectivity from the laser irradiated region since the reflectivity becomes nearly zero during the laser pulse. The long recovery time ($>$ 200nsec) of the reflectivity also suggests that the observed signal is not due to liquid carbon on the surface of graphite.

By directing the probing laser parallel to the surface of the graphite, the optical properties of the space *above* the laser heated region may be monitored. The experiment is done by using a photodiode to monitor the intensity of the probe beam *transmitted* through the space above the laser heated region. The experimental arrangement is shown in the inset of Fig. 3.20 which shows the transient transmission through argon gas above a laser heated graphite surface for a 1.5J/cm^2 25nsec pulsed KrF laser pulse. As seen in Fig. 3.20, the transmission through the space above the laser irradiated graphite is similar to the reflectivity measurements of the surface. There is a sharp decrease in the transmission which is followed by a slow recovery lasting several hundred nanoseconds. This shows that the optical properties in the medium above the surface change during pulsed laser melting of graphite so that optical probing of the surface is not possible for laser heating of graphite on the nanosecond

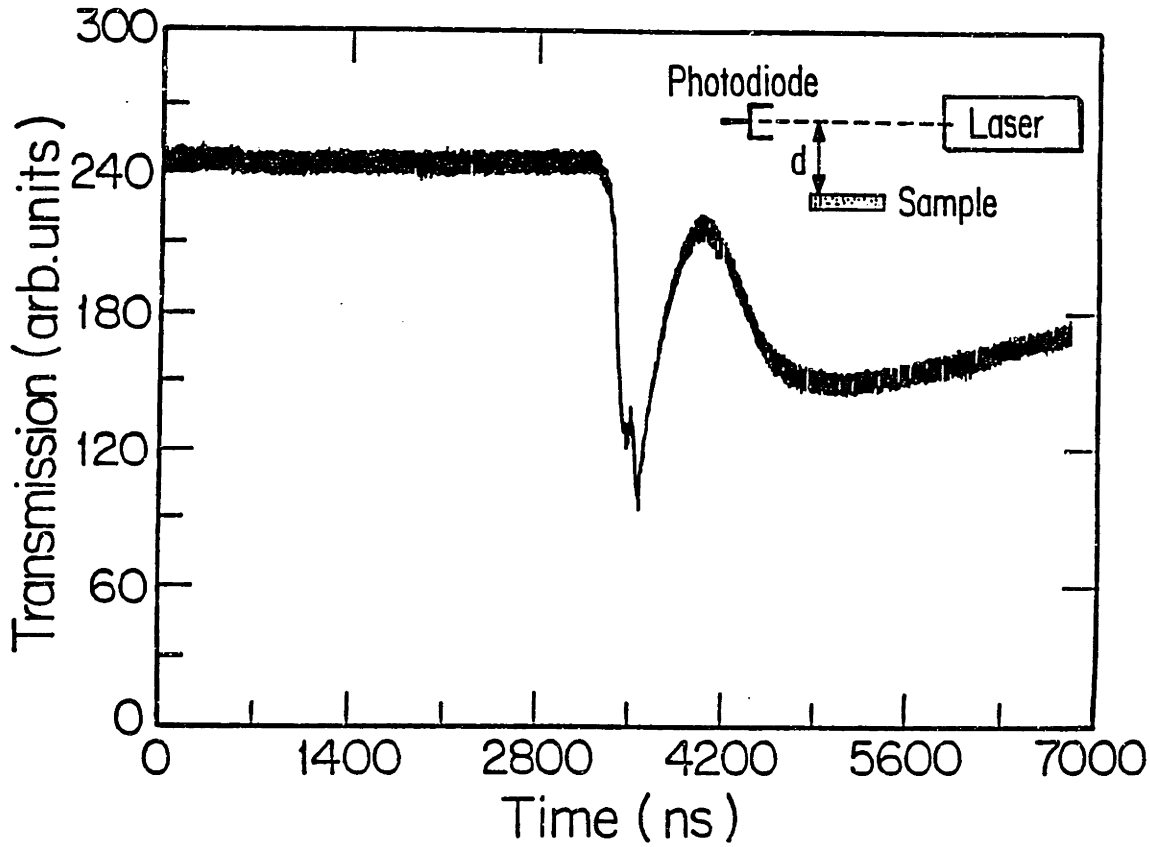

Figure 3.20: The transmission through air above a laser-melted graphite surface. This particular trace was taken for a 1.5J/cm^2, 25nsec KrF laser pulse.

time scale. The details of the origin of the decrease in the optical transmission are discussed in section 3.6.

The transient transmission experiment was also tried in vacuum to determine whether material loss from the hot graphite and liquid carbon play a role in changing the optical properties above the surface. Figure 3.21 shows a trace for the transient transmission experiment in vacuum. The trace in Fig. 3.21 is similar to the trace in Fig. 3.20. There is again a sharp drop in the transmitted intensity followed by a slow recovery of several hundred nanoseconds. This means that material being evolved from the surface alters the optical properties of the space above the surface of the heated graphite. The major difference between the two traces is that for the transmission through air (Fig. 3.20) there is a second decrease in the intensity at later times which is attributed to carbon vapor and is discussed in section 3.6.

In all cases, the results are qualitatively the same. There is a sharp decrease in the transmission followed by a slow recovery. This means that the changes in the optical properties above the surface are due to the expulsion of material from the hot graphite surface. A possible way to defeat the problem of emitted material is to create liquid carbon at lower temperatures, since the vaporization properties of carbon have a strong temperature dependence.

Experiments with amorphous silicon show that it has a lower melting threshold than crystalline silicon. One way to lower the melting temperature in carbon is to try to laser–melt amorphous carbon. Another reason for using amorphous carbon films is that they can be deposited on transparent media through which a probe beam can be passed. One can thereby eliminate the effects of vaporization on optical probes by probing the back side of an amorphous carbon film, provided the film does not become detached from the substrate. The experimental arrangement for back side reflectivity is shown in Fig. 3.22.

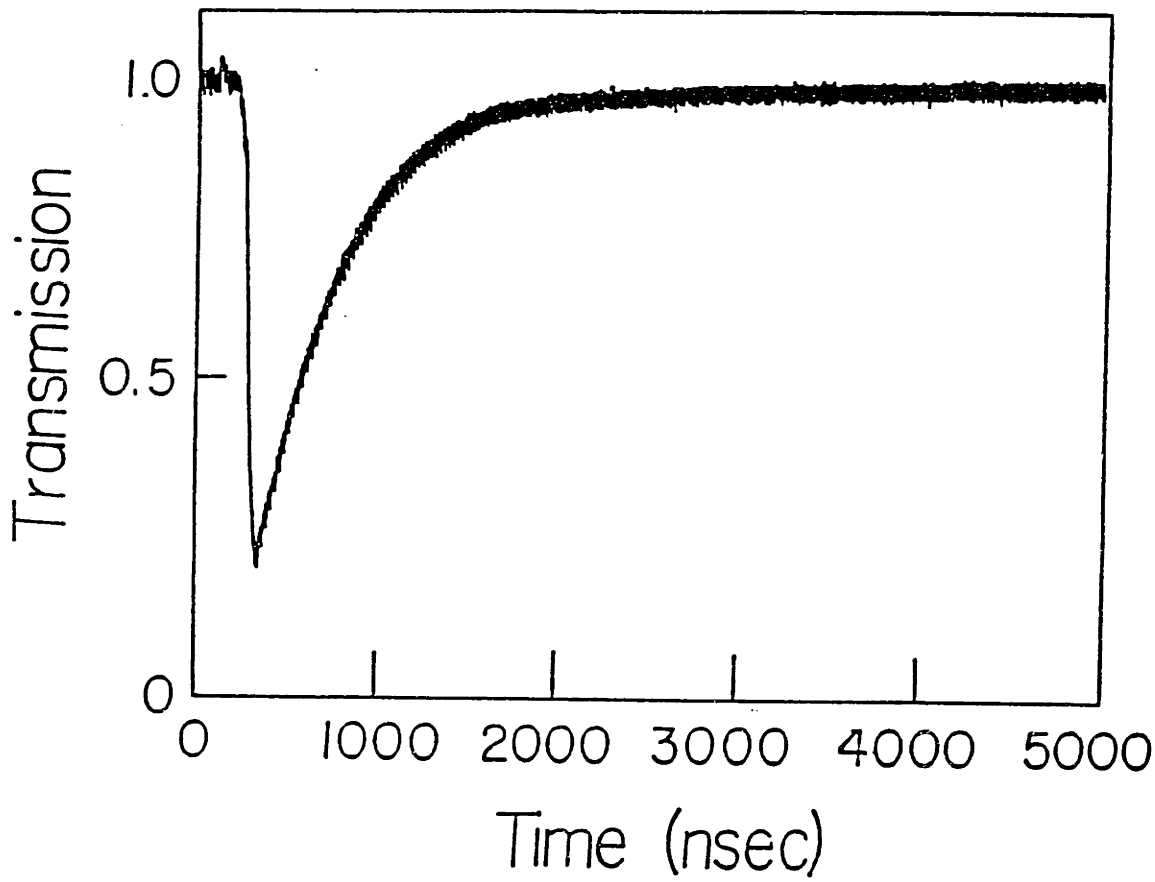

Figure 3.21: The transmission through vacuum above a laser heated graphite surface. The graphite was irradiated with a 1.5J/cm^2, 25nsec KrF laser pulse.

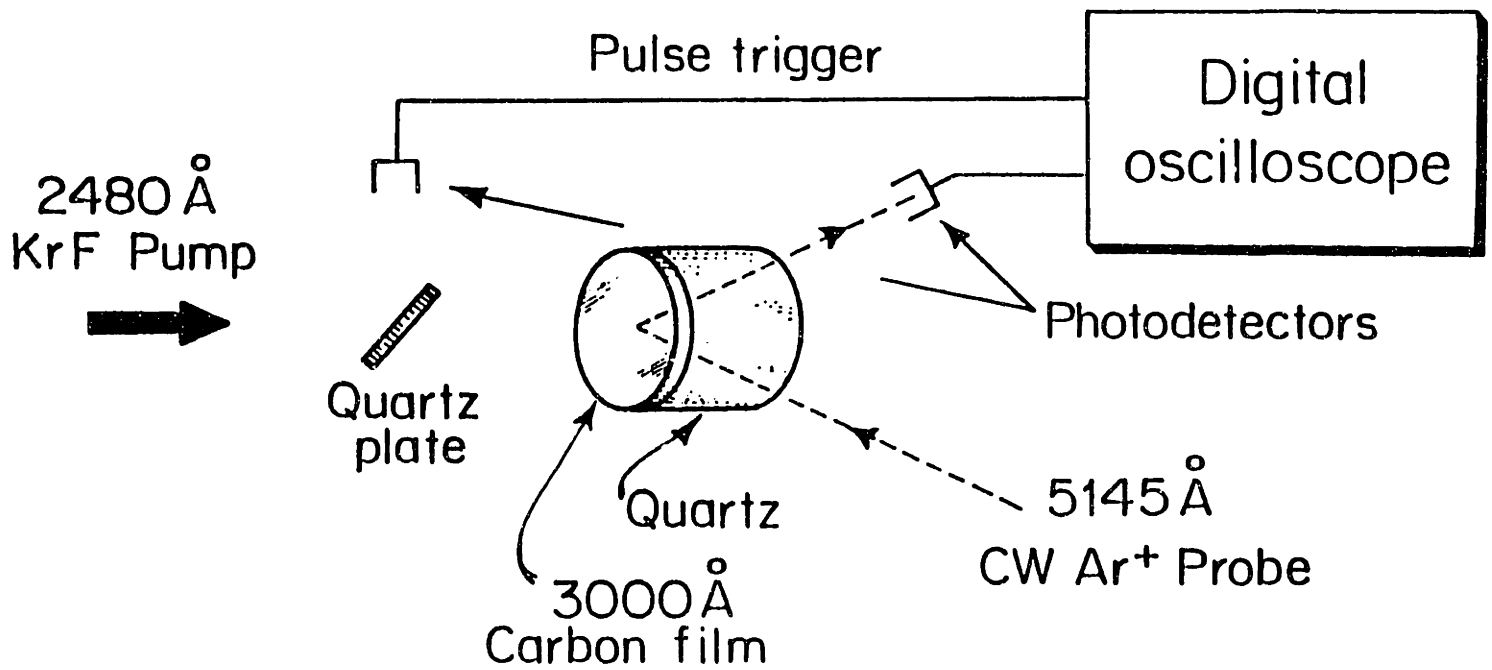

Figure 3.22: The experimental arrangement used for back side reflectivity measurements. The probe beam is passed through a transparent substrate and reflected off the back side of an amorphous carbon film.

When both front and back side transient reflectivity measurements are tried on amorphous carbon films at pulse energy densities near the melting threshold for graphite, the results are qualitatively the same as those for laser melted graphite. There is a sharp decrease in the reflectivity followed either by a slow recovery to a saturation level, or by no recovery due to the film being completely vaporized in the irradiated region.

For pulse laser energy densities smaller than the threshold value for graphite melting, several new results are obtained. The results obtained for three different pulse laser energy densities from front and back side transient reflectivity measurements are shown in Figs. 3.23 and 3.24, respectively. The traces in Figs. 3.23 and 3.24 represent the reflectivity from three different pulse laser energy densities in three distinct energy ranges. First, for energy densities comparable to the energy densities required to melt graphite, the transient reflectivity for the amorphous carbon films is qualitatively similar to graphite. The only difference between measurements for amorphous carbon films and graphite is that the reflectivity of the carbon films does not recover to any saturation value. This is due to the entire film vaporizing in the laser irradiated region. Second, for laser pulse energy densities somewhat smaller than required for melting graphite, there is a decrease in the reflectivity on the front side, attributed to vaporization, but a small increase in the reflectivity on the back side of the film as would be expected from a melt front moving toward the back side of the film. At later times, however, the reflectivity signal vanishes as the film vaporizes. Finally, for pulse laser energy densities which are very small compared to the energy density needed to melt graphite, the reflectivity on both sides of the film increases, but at later times, the films vaporize and the reflectivity vanishes. It should also be noted that the increase in the back side reflectivity is delayed with respect to the front side reflectivity, indicative

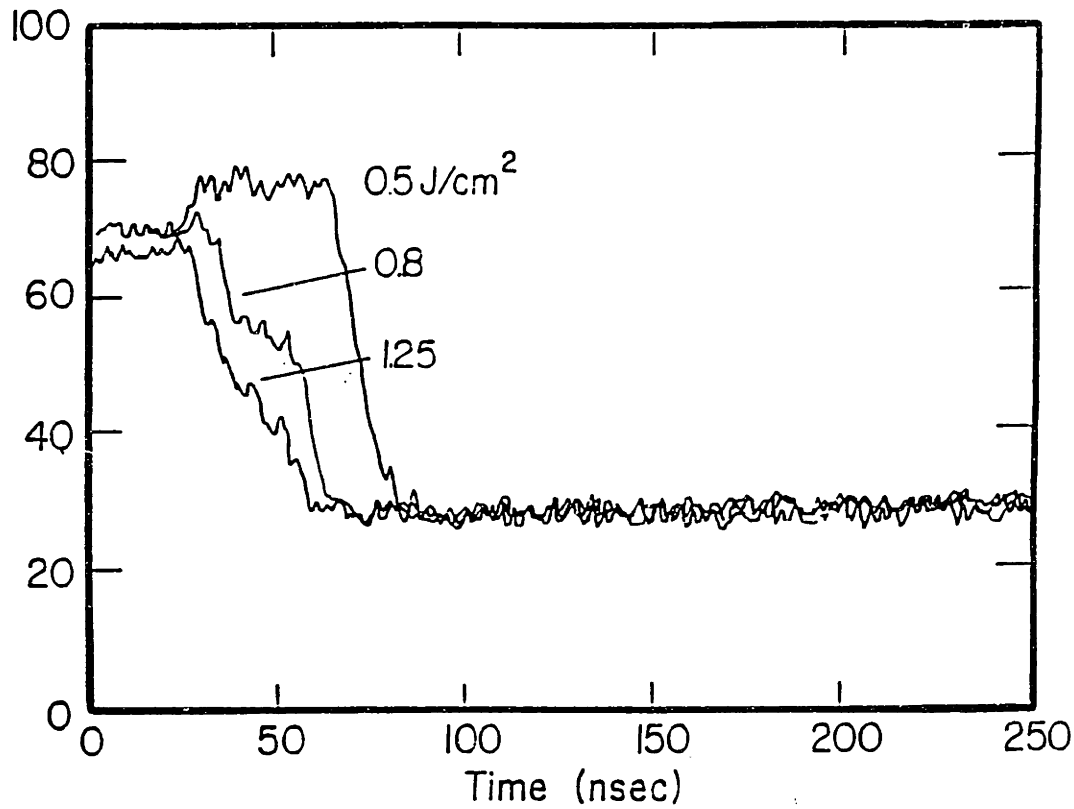

Figure 3.23: The results of transient reflectivity measurements made on the front side of amorphous carbon films. The traces are for pulse laser energy densities of 0.5, 0.8 and 1.25 J/cm^2 pulses from a 25nsec KrF excimer laser.

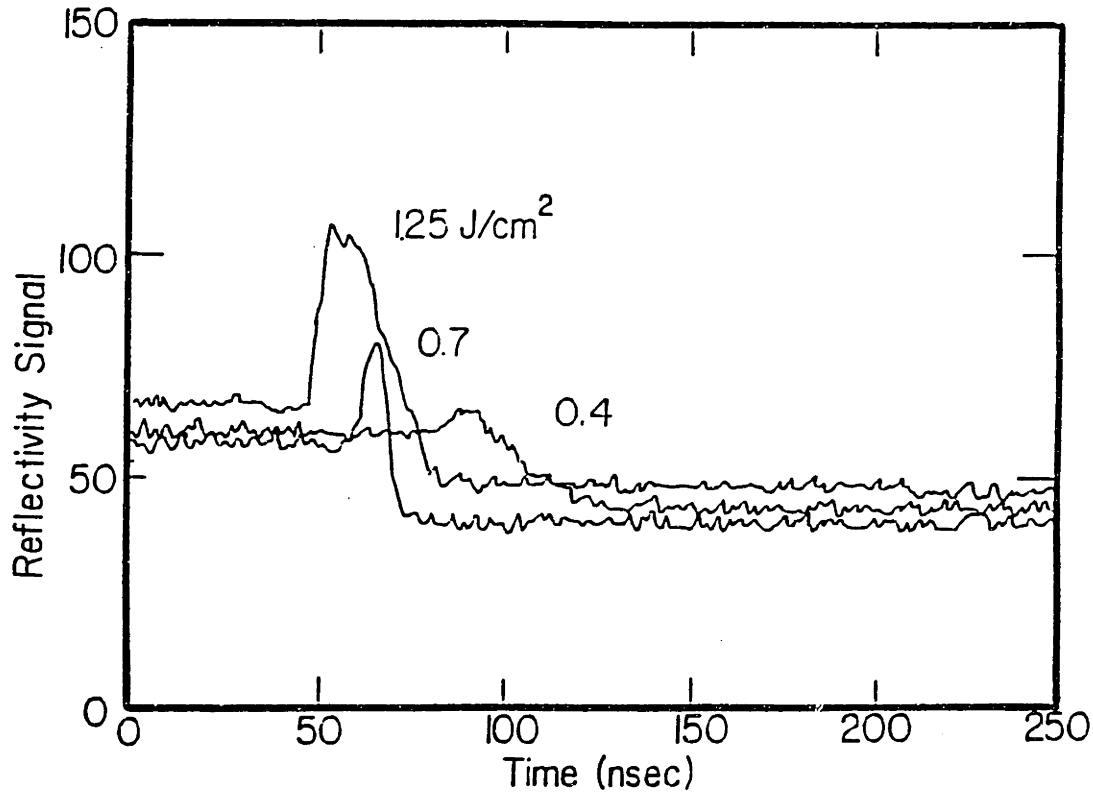

Figure 3.24: The results of transient reflectivity measurements made on the back side of amorphous carbon films. The traces are for pulse laser energy densities of 0.4, 0.7, and 1.25J/cm^2 pulses from a 25nsec KrF excimer laser.

of a melt front starting at the surface of the film and then moving through the film.

These results would immediately suggest that liquid carbon has a reflectivity comparable to the solid graphite reflectivity parallel to the c–axis. However, ion marker experiments carried out on the amorphous carbon films are not consistent with a melting hypothesis. If the carbon films had melted, then the ion implanted impurities should segregate as they did when graphite was melted by the pulsed laser. The segregation of the implanted impurities was not observed in the films irradiated with small energy density laser pulses. This suggests that the observed increase in the reflectivity of the laser irradiated carbon films is due to a rapid pregraphitization of the carbon films rather than melting.

A rapid pregraphitization process with an activation energy of $E_a \simeq 0.15$eV has been observed during annealing of ion implanted graphite[44]. Evaporated carbon films are also known to graphitize at low (800K) temperatures[45]. From these two experimental facts, it is likely that pulsed laser heating could cause the rapid pregraphitization of amorphous carbon films.

The use of transient optical measurements to determine the properties of liquid carbon created by pulsed laser heating on the nanosecond time scale is difficult for two reasons. First, the inability to control the surface temperature during pulse laser heating of graphite inevitably leads to carbon vaporization which hinders optical probing of the surface. Second, when amorphous carbon films are used in an effort to reduce the temperature needed to create liquid carbon, a rapid graphitization process negates the advantages of using amorphous carbon. Optical probing of the properties of liquid carbon may be possible if the liquid can be created on a time scale which is short compared to the time which is required by the vapor to change the optical properties of

the space above the irradiated surface. A discussion of picosecond pulse laser heating used to take advantage of this is discussed in section 3.8.

Transient Electrical Conductivity Measurements

The other transient technique which is readily used during pulsed laser melting is the measurement of the transient electrical conductivity. As discussed earlier, transient electrical conductivity measurements on metals requires the use of thin films. Since no thin films of well oriented graphite exist, well ordered graphite fibers were used for the transient electrical conductivity measurements. The experimental arrangement is similar to the arrangement used for measuring the transient electrical conductivity in pulsed laser melted silicon shown in Fig. 3.4.

For transient electrical conductivity measurements in graphite fibers, the silicon wafer in Fig. 3.4 is replaced by a graphite fiber with the graphite planes oriented along the fiber axis. The fibers used were typically $\sim 10\mu$m in diameter and the distance between the electrodes was $\sim$ 5mm. The typical resistance of the fibers used was $\sim 1k\Omega$. Typical results of the transient electrical conductivity measurements appears in Fig. 3.25 for graphite fibers irradiated with a 30nsec pulsed ruby laser at energy densities of 0.14, 0.6, and 2.7J/cm^2, respectively. For all pulsed laser energy densities in Fig. 3.25 there is a sharp decrease in the electrical resistance of the graphite fiber during the laser pulse. The resistance then slowly recovers to the original resistance of the fiber after several milliseconds. The decrease in the electrical resistance during the laser pulse is proportional to the energy density of the laser pulse while the recovery time of the resistance is the same for all pulsed laser energy densities.

The observed decrease in the electrical conductivity for a 0.14J/cm^2 laser pulse is due to the photoconductance of disordered graphite. The long recovery

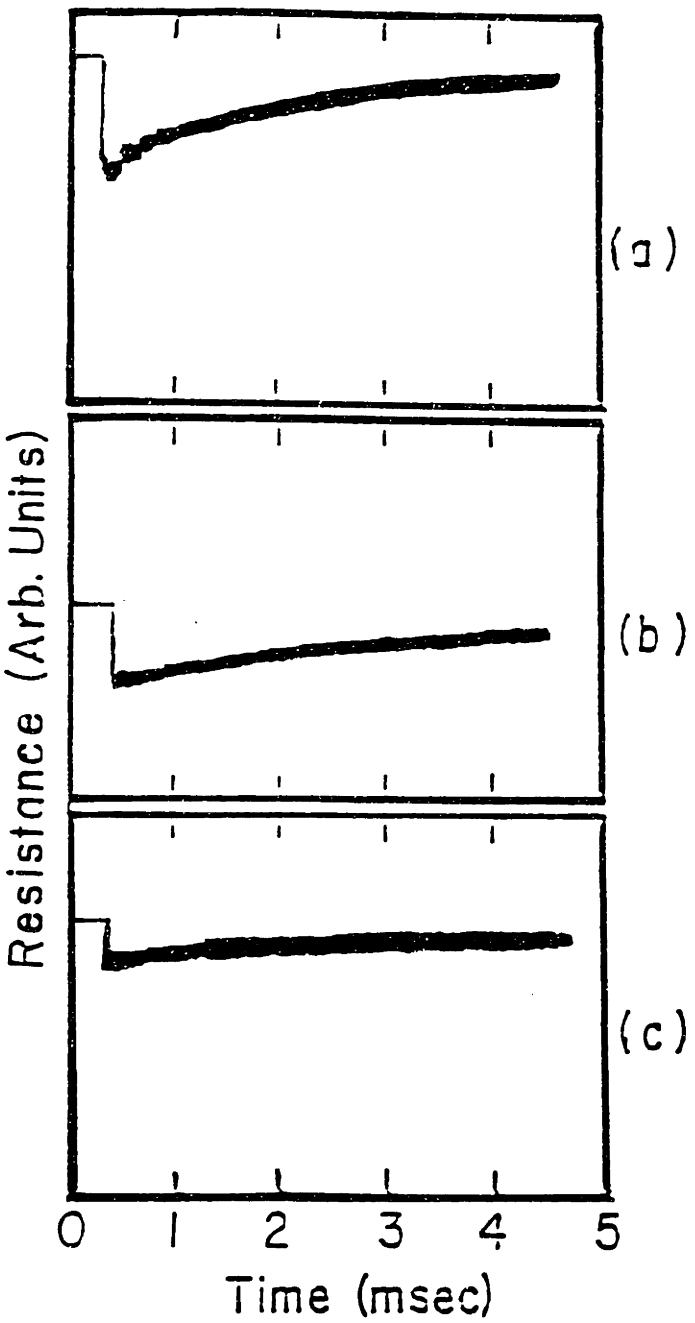

Figure 3.25: The results of transient electrical conductivity measurements in graphite fibers. In (a) the graphite fiber was irradiated with $2.7J/cm^2$, in (b) $0.6J/cm^2$ and in (c) $0.14J/cm^2$. Note that in all cases the resistance of the fiber decreases sharply and then recovers slowly to it original value.

time of the resistance is also comparable to the photocurrent decay time in chapter 2. Although the photoconductance of disordered graphite is small, the high intensity of pulsed laser irradiation can excite a very large density of carriers which will give a much larger contribution to the electrical conductivity than the small volume of molten carbon near the fiber surface.

3.5 Impurity Segregation and Solute Trapping

3.5.1 Introduction

Laser heating may induce phase transitions in materials as described in section 3.3. Once materials have been melted, impurities in the material are subject to the kinetics at the phase boundaries created by the incident laser pulse. The effects of the phase boundary equilibria manifest themselves in the redistribution of impurities in the laser heated material. The redistribution of impurities in laser melted materials can be put to use in determining the kinetics at the liquid–solid interface. The new distribution of impurities after solidification will be a function of the diffusion coefficient in the liquid material as well as the free energy of the impurity in both the liquid and solid phases. This information can then be used to determine the equilibrium concentrations of the impurity in both the liquid and solid phases of the material.

The rapid melting and resolidification velocities that may be achieved using pulsed laser heating are of use in creating materials with impurity concentrations that are much greater than can be achieved at equilibrium. This is termed *solute trapping* and occurs when a layer of molten material solidifies faster than the impurity can diffuse out of the region. Solute trapping has been reviewed extensively by Cahn *et. al.*[46] showing thermodynamically that this process can occur in laser melted materials.

Dopant	k_0	k	$v_D = D_s/d_{100}$ cm/sec
B	0.8	1.0	3.7×10^{-5}
P	0.35	1.0	3.7×10^{-5}
As	0.3	1.0	5.0×10^{-6}
Sb	0.23	0.7	6.6×10^{-6}
Ga	0.008	0.2	7.4×10^{-5}
Bi	0.0007	0.4	1.1×10^{-5}
In	0.0004	0.15	2.8×10^{-5}
Cu	< 0.0001	< 0.01	184
Fe			11
Zn			6

Table 3.2: The segregation properties of impurities in silicon (Refs.[47,49]). The k_0 are the equilibrium segregation coefficients, k are the velocity dependent (2 to 4m/sec) segregation coefficients, and v_D is the solid state diffusive speed along the (100) direction.

3.5.2 General Considerations

Solute trapping occurs when the partition coefficient of a material–impurity combination, k, departs from its equilibrium value given by

$$k = \frac{C_s}{C_l} \tag{3.7}$$

where C_s and C_l are the equilibrium concentrations of the impurity in the solidus and liquidus of the material. The magnitude of the segregation coefficient is dependent on both the temperature and the crystallographic orientation of the resolidifying material. An example of solute trapping and impurity redistribution is shown in Fig. 3.26 for arsenic implanted into silicon taken from White *et. al.*[47]. Additional work by White[47,48]and Baeri[49,50] showed that many different impurities can be "trapped" in silicon in concentrations much higher than the equilibrium concentration in the host silicon. Table 3.2 summarizes the results of White and Baeri for solute trapping in silicon. Not surprisingly, the impurities which were trapped in the highest concentrations

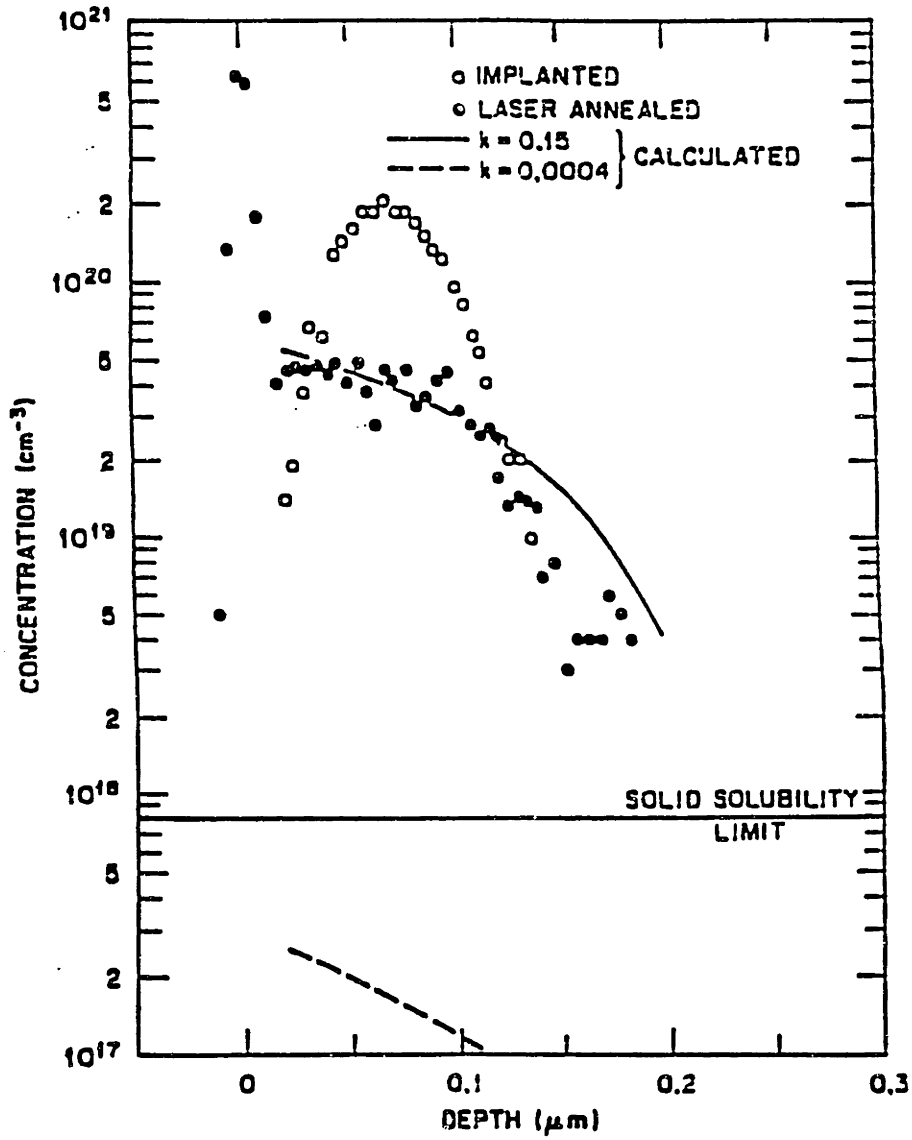

Figure 3.26: Solute trapping for arsenic in silicon after pulse laser heating. The arsenic is redistributed, during solidification of the molten silicon, at concentrations higher than is possible under equilibrium conditions. (This figure was taken from Ref. [1])

were those which occupied substitutional lattice sites upon solidification, such as As and B. The metals (Cu, Fe, and Zn) are not trapped by the rapidly moving liquid–solid interface so that their diffusive speed is much greater than that for the elements which have a high segregation coefficient.

3.5.3 Models for Solute Trapping

Several models have been developed to describe solute trapping as the result of a moving interface. The models are based on the solution of a set of four equations, a model relating the compositional growth of a solid from a liquid, an expression relating the growth velocity to the local conditions at the liquid–solid interface, an equation describing the transport of rejected solute at the interface, and finally, an equation describing the flow of heat in the system. For the case of laser melted materials, the growth velocity of the solid is very rapid (~m/sec) so that the solution to all four of the equations is important in determining the solute trapping resulting from the moving liquid–solid interface. The velocity dependent composition of the growing solid is determined by solving the one–dimensional diffusion equation, and in turn this determines the driving force for the transformation at the interface.

The models used to describe solute trapping all treat the solute atoms as trying to avoid trapping by diffusion at the interface. Since solidification only involves short range atomic rearrangement from the liquid state and no long range diffusive motion, the liquid–solid interface can proceed far more rapidly than solute diffusion in the liquid. As a result, for liquid–solid interface speeds, u, which exceed the solute diffusive speed, D_l/w, where D_l is the liquid diffusivity and w is the interatomic spacing, solute atoms will be engulfed by the advancing liquid–solid interface and trapped in the solid. The details of how solute atoms are trapped depends on how the liquid–solid interface is thought to

advance. The models which have been proposed to describe the solute trapping process consider several types of interfaces.

A molecular dynamics calculation by Wood[51] tries to calculate the trapping of solute atoms on an atomic level using the change in the energy of solute atoms upon trapping. The calculations are tedious and are not able to provide a broad picture of solute trapping in a wide variety of materials. The other models for solute trapping consider planar liquid–solid interfaces. However, each of these models is different in the way in which it treats the trapping of atoms in the solid across the interface.

The Baker model[52] treats a planar liquid–solid interface as a continuum. The energy of a solute atom is constant in both the liquid (E_l) and solid (E_s) states and is described by a single value at the center of the interface (E_i). The energy of the solute atom everywhere else is dependent on the position of the atom in the interface and is considered to vary linearly across the interface between E_l, E_i, and E_s. The diffusion equation is solved in a reference frame where the interface is fixed and velocity of the reference frame is u. The ratio of the steady state compositions on both sides of the interface, the segregation coefficient k, is given from this model as

$$k = \frac{C_s}{C_l} = \frac{\beta + \ln k_e}{\beta + \frac{1}{k_e} \ln k_e \exp(-\beta)} \tag{3.8}$$

where β is the ratio of the interface speed to the solute diffusive speed at the interface $\beta = wu/D_l$.

Another model which treats a planar liquid–solid interface is a model proposed by Jackson, Gilmer and Leamy (JGL)[53]. The JGL model uses rate equations to calculate the hopping of solute atoms across the liquid–solid interface going both from the liquid to the solid and from the solid back into the liquid. The rate equations are used to describe both crystallization and solute redistribution, but ignore the basic differences between the two processes. The

interface velocity is determined from the net fluxes of the solute atoms and the atoms of the host liquid moving into the interface. An additional trapping flux is added to the model to account for the trapping of solute atoms in the solid phase. The segregation coefficient derived from this model is given as

$$k = \frac{\alpha V + \gamma_s k_e \exp\left(\frac{\Delta h_A^0 - \Delta h_B^0}{RT_i} - \frac{\Delta s_B^0}{R}\right)}{V + \gamma_s \exp\left(\frac{\Delta h_A^0 - \Delta h_B^0}{RT_i} - \frac{\Delta s_B^0}{R}\right)} \tag{3.9}$$

where γ_s is the activity coefficient of the solute in the solid, h is the partial molar enthalpy, s is the entropy, and V is a dimensionless velocity

$$V = \frac{uC_l^A}{J_{l\to s}^A} \tag{3.10}$$

where $J_{l\to s}$ is the atomic flux from the liquid to the solid and the superscripts A and B refer to the atoms of the liquid and the solute, respectively.

Two models for solute trapping have been proposed by Aziz[54,55] which treat the liquid–solid interface as planar, but treat the solidification of the liquid as either stepwise or continuous. The stepwise growth model proposes that a finite thickness of liquid at the liquid–solid interface freezes at the same time. The advance of the liquid–solid interface results from many layers freezing sequentially. The segregation coefficient predicted by the stepwise growth model is

$$k = k_e + (1 - k_e)\exp\left(\frac{-D_i}{uw}\right) \tag{3.11}$$

where D_i is the diffusivity through the interface and is typically taken as $D_i = D_l$.

The second model proposed by Aziz[55] is a continuous growth model for the solid from the liquid. The continuous growth model considers the solute to jump across an atomically thin liquid–solid interface. The flux of solute atoms is considered to be steady–state and there is a finite activation energy

for a solute atom to make a jump. The segregation coefficient derived from the simultaneous solution of the rate equations and the diffusion equation is

$$k = \frac{\beta + k_e}{\beta + 1} \tag{3.12}$$

where β is as defined before.

Comparisons of the different models for solute segregation and trapping appear to be quite different at first glance. However, a more careful analysis shows that several of the models predict the same general behavior. The models all predict that for slowly moving interfaces, the segregation coefficient reduces to its equilibrium value at the interface temperature, k_e. The major differences in the models are the predictions for fast moving interfaces and the transient between the two extremes of interface velocity. The Baker model and the Aziz models both predict that all of the solute will be trapped for very fast moving liquid–solid interfaces (i.e. $k = 1$). The JGL model, however, predicts that there will be an upper limit to the amount of solute which may be trapped by a rapidly moving interface. The upper limit predicted by the JGL model is

$$k_{max} = \frac{1 + k_e}{2}. \tag{3.13}$$

The restriction on k in the JGL model is a direct result of assuming diffusion limited growth which is limited by the diffusive speed of the interface. In addition, it has been shown by Aziz *et. al.*[56] that the JGL model fails to properly predict the solute trapping at both ends of the phase diagram for solute–solvent mixing.

The functional form of the segregation coefficient as a function of the interface speed is the other major difference between the models. Some of the differences are explained by the approximations used to solve the four simultaneous equations governing the segregation. The Baker model linearizes the

differential equations, whereas Aziz solves them directly using numerical techniques; this accounts for the differences between the Baker model and the Aziz continuous growth model. Comparison of the models with experimental results by Aziz *et. al.*[57] has shown that for the case of laser–melted silicon, the continuous growth model describes the segregation and solute trapping behavior better than the Baker model or the stepwise growth model. Since the original analysis which led to the derivation of the segregation coefficient in the continuous growth model is general, this model should apply to all systems where solute trapping can occur.

3.5.4 Segregation and Solute Trapping in Laser Melted Graphite

Solute segregation and trapping have been observed in laser melted graphite as explained in section 3.4, but at that time the description of the segregation of implanted impurities focused on showing that graphite can be melted using pulsed laser heating. The focus in this section is on the experimental determination of the diffusivity of liquid carbon and the segregation coefficient. In this experiment, graphite was implanted with ^{73}Ge and ^{75}As at several energies at a fluence of $1.0 \times 10^{15}\text{cm}^{-2}$ and then laser irradiated with a 30nsec pulsed ruby laser. The energy densities used were above the melt threshold of 0.6J/cm^2. The distribution of the impurities both before and after laser irradiation was measured using RBS. Our results for ^{73}Ge implanted at 225KeV are illustrated in Fig. 3.27. The top portion of Fig. 3.27 shows the original implanted Ge distribution. A depth scale from the surface of the graphite appears on the top abscissa in Fig. 3.27 while the lower abscissa refers to the channel number of the multichannel analyzer used in RBS measurements.

When the laser pulse energy density is above the melt threshold, a small

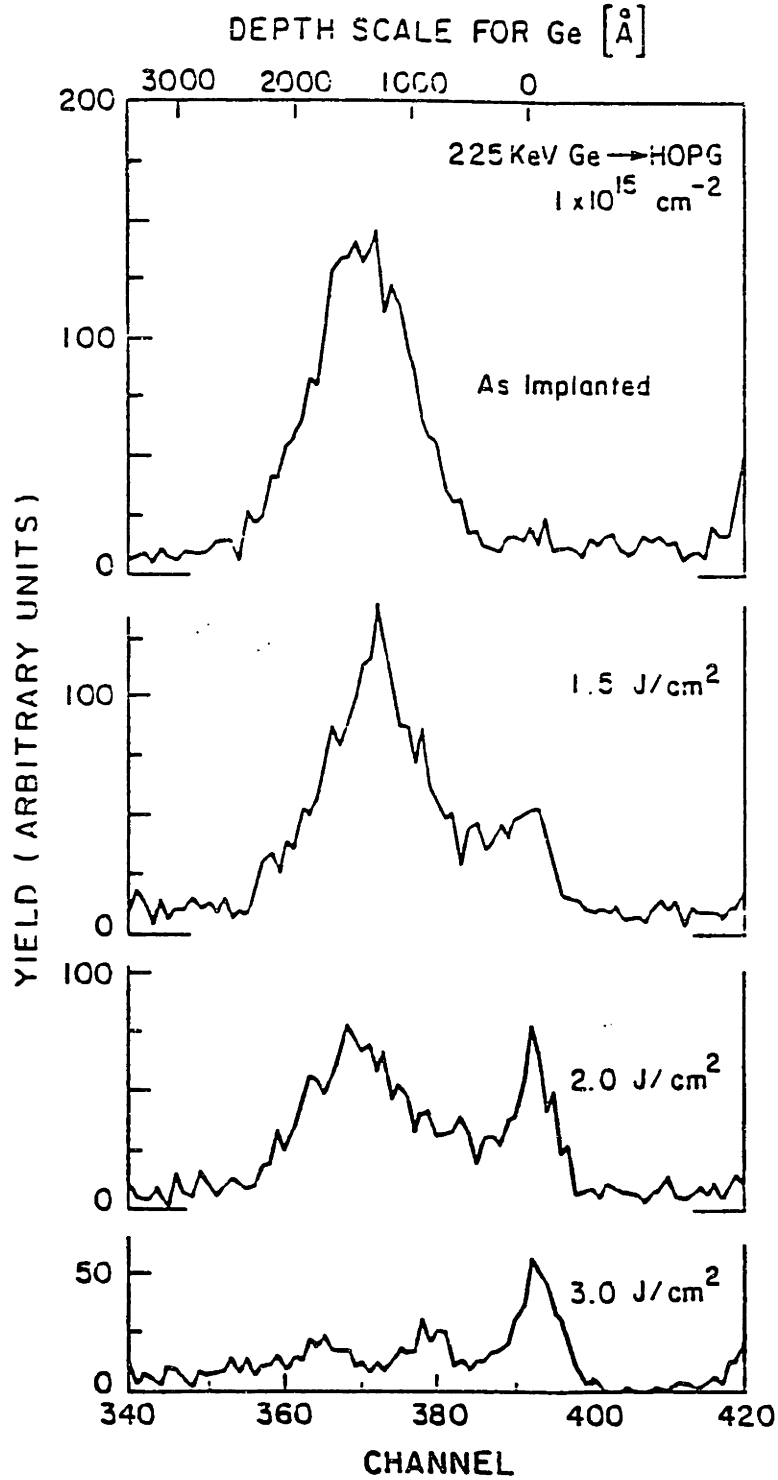

Figure 3.27: The distribution of Ge impurities in graphite before and after laser irradiation with a range of pulse energy densities from a 30nsec pulsed ruby laser. The top portion of the figure shows the original impurity distribution. These measurements were made using RBS.

layer of liquid carbon will be generated on the sample surface. As the laser pulse energy density is increased, the melt front penetrates deeper into the solid. Eventually, the melt front penetrates into the implanted impurity distribution as shown in the second trace of Fig. 3.27. The impurities which are between the liquid–solid interface and the surface are then free to diffuse in the liquid carbon. The solidification of the liquid results in segregation behavior pushing some of the Ge to the surface. However, as described earlier, the velocity of the liquid–solid interface in laser heating experiments is typically meters per second, so that the segregation coefficient during rapid solidification will be significantly larger than the equilibrium segregation coefficient and will allow some of the Ge to be trapped before it can diffuse with the interface.

As the laser pulse energy density is increased further, the melt front penetrates deeper into the Ge distribution and eventually the penetration goes beyond the original implanted Ge distribution as shown in the lower two panels of Fig. 3.27. Again, the solidifying liquid segregates impurities toward the surface. Since the segregation coefficient will be larger than the equilibrium value, some of the impurities will be trapped in the solid. One note to make is that the amount of the trapped impurities appears to decrease as the pulse laser energy density is increased. In Fig. 3.27 this is seen as a reduction in the backscattering yield on the ordinate. The reason for this is that the initial velocity of the liquid–solid interface during solidification is usually smaller when the volume of liquid is large. The thermal gradients are smaller because the longer lifetime of the liquid allows thermal diffusion to reduce them.

The total amount of Ge in the resolidified material is seen to be dramatically less than in the original implanted distribution. The loss of Ge may be accounted for by the vaporization of hot liquid carbon containing impurities from diffusion, *and* by the loss of Ge due to Ge vaporization at the surface of

the hot graphite immediately after resolidification. The loss of impurities at the surface of the hot graphite must be taken into account since the melting temperature of carbon is far higher than the boiling point for *all* impurities which may be placed into carbon. The amount of Ge lost due to each of these vaporization mechanisms depends on the penetration of the melt front into the graphite since this will determine the amount of Ge which may diffuse through the liquid. A model used to calculate the effect impurity of vaporization is presented in chapter 5.

Segregation and solute trapping have also been observed for ^{75}As in graphite. The same general segregation behavior is observed as is shown in Fig. 3.28 for ^{75}As implanted into graphite at 100KeV and 230KeV at a fluence of 1.0×10^{15}cm^{-2}. The figure illustrates that the As is segregated toward the surface by the resolidifying liquid carbon after graphite has been melted by a 30nsec pulsed ruby laser with pulse energy densities of 1.5J/cm^2. In Fig. 3.28a, the As was implanted with at an energy of 100KeV as shown by the solid trace. The dotted trace shows the distribution of the As after resolidification. Note that some of the impurities are pushed to the surface.

In Fig. 3.28b, the original As distribution is from an implant at 230KeV. The original distribution of implanted As is given by the solid trace while the dotted trace represents the distribution of the As after resolidification. Again, some of the impurities are segregated toward the surface. The only difference between the 100KeV implant and the 230KeV implant is the depth of the original impurity distribution. In the case of the 100KeV implant, the melt front penetration goes beyond the depth of the implant causing all of the impurities to diffuse in the liquid and be subject to segregation and solute trapping effects. For the implant at 230KeV, only part of the impurity distribution is affected by segregation and solute trapping since the melt front only penetrates part of

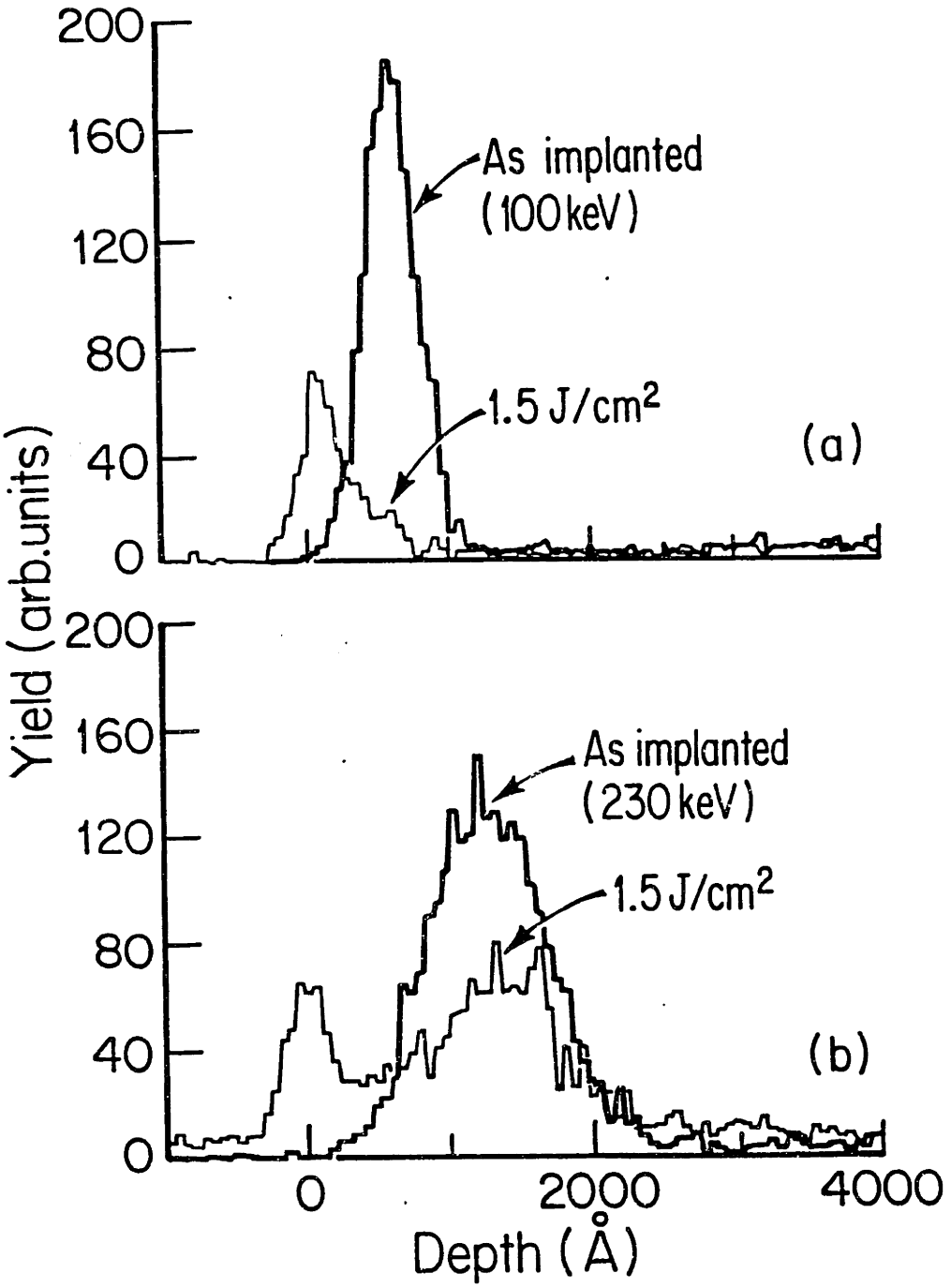

Figure 3.28: The segregation of As in graphite. The As in the (a) was originally implanted at 100KeV and in (b) 230KeV at a fluence of $1.0 \times 10^{15}\text{cm}^{-2}$. In both cases the pulse laser energy density was 1.5J/cm^2. The segregation of the impurities is seen to be nearly the same as in the case for Ge.

the impurity distribution.

There are many similarities for the segregation behavior of ^{75}As and ^{73}Ge. Figure 3.28 shows that for As there is again a significant loss of impurities due to vaporization. This is seen by the decrease in the yield of the RBS data by comparing the traces for before and after laser melting. The loss of As is again attributed to the vaporization of both the liquid carbon containing As and to the loss of As at the surface of the hot graphite due to As vaporization in similar fashion to Ge.

Another similarity between the Ge and As segregation behavior can be seen by comparing the second panel in Fig. 3.27 and the lower panel in Fig. 3.28 which are both for a laser pulse energy density of 1.5J/cm^2. In both cases, the melt front penetrates the impurity distribution and causes some of the impurities to segregate while leaving the rest in their original positions. In both cases, impurities are piled up on the surface forming the peak in the backscattering spectrum. In between the peaks created by the impurities on the surface and the impurities which have not been disturbed, there is a plateau in the impurity distribution caused by the trapping of some of the impurities. Since the initial implantation fluence of the impurities is the same for the Ge and the As and the masses of As and Ge are almost the same, the magnitude of the plateau in the segregated distributions suggest that the segregation coefficients of Ge and As in graphite are nearly the same.

A general analysis of these experiments using simple diffusion theory shows that the impurities in liquid carbon must be able to diffuse to the surface from depths $d \sim 1000$Å in times on the order of $t_l \sim 100$nsec. This would mean that the liquid diffusivity of liquid carbon would be on the order of

$$D_l \sim \frac{d^2}{4t_l} = 2.5 \times 10^{-4}\text{cm}^2/\text{sec} \qquad (3.14)$$

for both Ge and As in liquid carbon. This liquid diffusivity is on the same

order as the liquid diffusivity of liquid silicon (2.0×10^{-4}cm^2/sec) determined by Aziz *et. al.*[57].

The determination of the segregation coefficient is more complex since it has an explicit dependence on the velocity of the liquid–solid interface. However, our heat flow calculations described in chapter 5 show that melt velocity of the liquid–solid interface during resolidification is typically on the order of 5 m/sec. By using the formula for the segregation coefficient from the continuous growth model of Aziz[55] in Eq. 3.12 and by using the gross estimate of the liquid diffusivity in Eq. 3.14, a rough estimate of the segregation coefficient, k, for liquid carbon can be obtained as $k = 0.17$, where we have assumes that the equilibrium segregation coefficient is $k_e = 0$.

A better estimate for the segregation coefficient and for the liquid diffusivity is made in chapter 5 where a solution to the one dimensional diffusion equation is employed following along the same lines as the calculation by Aziz *et. al.* for silicon. The major addition to this calculation is a model for the vaporization of impurities on the surface of hot graphite after the liquid carbon has resolidified which is unnecessary in the case of silicon.

3.6 Laser Induced Shock Waves

Because pulsed laser heating is used to rapidly heat materials with energy pulses of very short duration, pulsed laser heating is a form of shock heating. The generation of shock waves both inside and outside of the heated material results from rapid thermal expansion and material ejection during pulsed laser heating. The magnitude of the shock waves generated will depend upon both the laser heating geometry, and the mechanical and optical properties of the material being heated. The generation of the shock waves within the material may change the thermodynamic conditions under which the material is being heated,

while the generation of shock waves external to the material may complicate optical measurements of the near surface properties of the heated material due to changes in the optical properties of the medium above the material surface.

3.6.1 Shock Waves Above a Laser Heated Surface

The rapid heating rate (10^{11} K/s) of laser heating combined with the vaporization properties of some materials may give rise to the production of shock waves in the gaseous medium above the material surface. The shock waves form as a result of the gaseous medium above the laser heated surface interacting with material being evolved from the heated surface. The generated shock waves travel normal to the surface being heated with velocities as high as 10^6cm/s[58,59,60,61]. This is more than an order of magnitude greater than the speed of sound in air and also far greater than the expected thermal velocity of particles emitted from the heated surface.

The formation of a shock wave above a laser heated surface is dependent on the power density of the incident heating pulse. If the power density of the incident laser pulse is large enough, the material evolved from the hot surface may form an electron–ion plasma and generate a shock wave from the ionization of the gas above the surface[59,60,62]. For smaller power densities, a shock wave may be formed mechanically if a large amount of material is ejected from the surface during laser heating, similar to an explosion occurring in the laser heated region of the surface with the material leaving the surface at the thermal velocity[61].

A model for the formation of shock waves above a laser heated surface has been proposed by Emmony and Irving from laser heating experiments on carbon done with a Q–switched laser with pulse durations $\sim$ 40nsec[62]. An

empirical relation

$$r \propto t^N \tag{3.15}$$

was determined to describe the distance the shock front has moved from the surface as a function of time t, where r is the distance from the surface and N is a parameter which describes the decay of the shock wave. The exponent N assumes two ranges of values in the Emmony and Irving model. A value of $0.6 < N < 0.7$ is assumed for times coincident with the laser pulse while for times greater than 400nsec, N assumes values ~ 0.4. The former values of N describe the case where the material ejected during laser heating is dense and, through collisions, ionizes the gas above the surface of the material to form an electron–ion plasma above the surface. The latter values for N describe the shock wave generated by material which is less dense; the ions ejected out of the plasma and material that was emitted from the surface has separated over time due to the velocity distribution of the emitted material. This transition from large values of N to small values of N reflects the change in the nature of the wave from being a supported blast wave (large N) to an unsupported blast wave (small N).

The model also predicts the amount of material removed from a target, by simple thermodynamic considerations, and the amount of energy needed to produce the shock, based on blast wave theory[63,64]. The relation derived for the total mass, m, of material removed is

$$m = \frac{3}{2.2c}\sigma\epsilon A t T^3 \tag{3.16}$$

where T is the final temperature of the gas in the shock wave, c is the specific heat of the material, t is the time of the exchange of energy to the shocked gas, A is the area of the shock front at time t, σ is Stefan's constant, and ϵ is the emissivity of the evolved material. The values for the mass loss obtained using

this theory agree on an order of magnitude basis with experimental measurements of the mass loss in carbon and silicon[62].

The relation used to calculate the energy, E, contained in the shock wave is given by[64]

$$E = \rho\alpha(\gamma)\frac{r^5}{t^2} \tag{3.17}$$

where ρ is the ambient gas density, and α is a function of the adiabatic index γ[64]. Using this model to calculate the energy of the shock wave, the energy in the wave is up to fifty percent of the incident laser energy for large ($> 10^{11}\mathrm{W/cm^2}$) power density laser pulses[62].

Because the generated shock wave is the result of material being ejected into the medium above the surface and the shock wave generates a density compression of the medium above the surface, the optical properties of the medium change. The change in the optical properties in the gas above the surface results in the formation of layers of gases with different refractive indices. The change in the optical properties may be large enough to disrupt the optical path through the gas so that optical techniques for probing the heated surface can become complicated. Measurements of the transient reflectivity and optical determination of the surface temperature of the heated material through the shock fronts are particularly difficult.

3.6.2 Shock Pressure on a Laser Heated Surface

The evolution of material during laser heating, either thermally or nonthermally, will induce an additional pressure onto the heated surface by conservation of momentum. For sufficiently high energy densities, or for very short ($< 10^{-9}$s) pulses, the induced pressure may be on the order of a megabar as was shown by experiments done in the mid 1960's by Neuman[65] and by Gregg and Thomas[66].

Neuman showed that pulsed laser heating of materials does indeed transfer momentum to the heated material from the recoil of ejected material[65]. Gregg and Thomas extended Neuman's work by determining the relationship between the incident energy density and the momentum transferred to a material heated by a pulsed laser. From their experiments, Gregg and Thomas arrived at an empirical formula for the momentum transferred to the laser heated material, M, as

$$M = Cp^{-n}E_p \tag{3.18}$$

where p is the average incident power intensity, E_p is the total energy in the laser pulse, and C and n are fitted parameters for the target material.

Equation 3.18 covers a range of incident power densities, $5.0 \times 10^8 < p < 4.0 \times 10^{10}\text{W/cm}^2$. For power densities below $5.0 \times 10^8\text{W/cm}^2$, there are too few data points to determine a generalized relation.

The momentum transferred to the target may be simply related to an induced surface shock pressure by

$$P = \frac{M}{A\Delta t} \tag{3.19}$$

where P is the shock pressure, A is the area of irradiation, and Δt is the time over which material is ejected off of the surface. By using eq. 3.19, the additional pressure on a laser heated surface may be determined.

The validity of eq. 3.19 will be restricted to laser heating conditions which allow the material to remain in thermal equilibrium. For laser pulses with durations shorter than the electron–phonon scattering time, the energy from the incoming pulse will be transferred to the lattice in a time longer than the laser pulse duration. The momentum transfer for ultra–short pulses will be smaller than predicted by eq. 3.18, since vaporization occurs on the same time scale as the transfer of energy to the lattice. The rate of energy transfer from

the laser pulse to the lattice will become important for laser pulses of durations $\sim 10^{-12}$s and shorter, since the electron–phonon scattering time is $\sim 10^{-11}$s[1]. Therefore, the shock pressure predicted by eq. 3.19 for ultra–short laser pulses will be greatly overestimated since the transfer of energy, and hence momentum, occurs on time scales longer than the laser pulse duration. However, by using the electron–phonon scattering time as an upper limit to the rate of momentum transfer to the lattice of a laser–heated material, an upper bound to the shock pressure may be determined by

$$P = \frac{CE_p^{1-n}}{At_{e-p}^{1-n}} \tag{3.20}$$

where t_{e-p} is the electron–phonon scattering time.

Since the pressure on the surface is only applied for a short duration, a shock wave will develop in the material. The generated wave travels through the material and may cause mechanical deformations of the material if the pressure is much greater than the elastic limit.

3.6.3 Shock Waves in Graphite Due to Pulsed Laser Heating

During pulsed laser heating in graphite, shock waves may develop externally to the heated surface as well as within the graphite target. The shocks external to the graphite are generated by a large expulsion of material during heating and the ionization of the gas above the surface by the hot evolved material from the surface.

Shock waves develop in gaseous media above a pulsed laser heated graphite surface when heated by laser radiation with power densities in the range $\sim 10^8$W/cm^2[61,67]. There is a power density threshold for the formation of shock waves in the gaseous medium which lies close to the threshold for melting. The coincidence of the threshold for shock wave formation and melting may

be unique to graphite since the temperatures are very high and there is a significant vapor pressure near the melting temperature. No distinction could be made between the threshold for shock wave formation and melting due to poor power density resolution.

The shock waves can be detected optically and the displacement of these waves from the surface has been measured using the transmitted intensity through the gas of a continuous wave laser directed parallel to the graphite surface as shown in Fig. 3.29. The graphite target was placed in a chamber which could be either evacuated or filled with gas. A laser pulse is directed through a quartz plate to take a small portion of the laser pulse for electronic timing. The rest of the laser pulse is then directed through a window in the chamber before hitting the target. A continuous wave laser probe is set parallel to the target surface and may be adjusted to any height above the surface. The transmitted intensity of the continuous wave laser probe was measured using a photodiode and displayed on an oscilloscope output. By adjusting the height of the probe above the surface, the displacement of particles or shock fronts can be measured. A plot of the transmission through the shocked Ar gas appears in Fig. 3.30. As can be seen in Fig. 3.30, measurements of the optical transmission through an argon medium above the laser heated graphite reveal that there are two distinct broad decreases in the transmitted intensity through the gas above the surface. The first is associated with the shock wave produced in the gas by the hot carbon gas and carbon particles evolved from the surface. The additional structure on this decrease is most likely from density fluctuations in the shock wave.

The second front is associated with the evolved carbon from the heated surface and the broadening of the distribution occurs as a result of collisions with the argon gas, causing the velocity distribution of the carbon vapor to

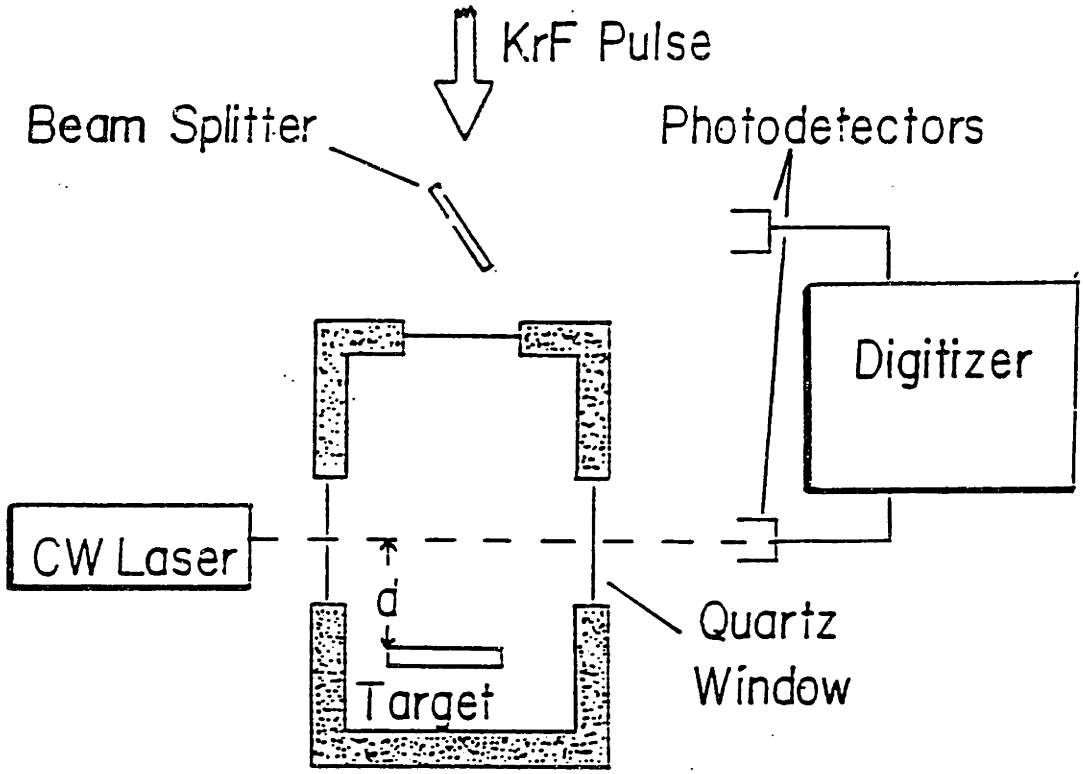

Figure 3.29: Experimental set–up used to measure the transmission through the medium above the laser heated graphite surface.

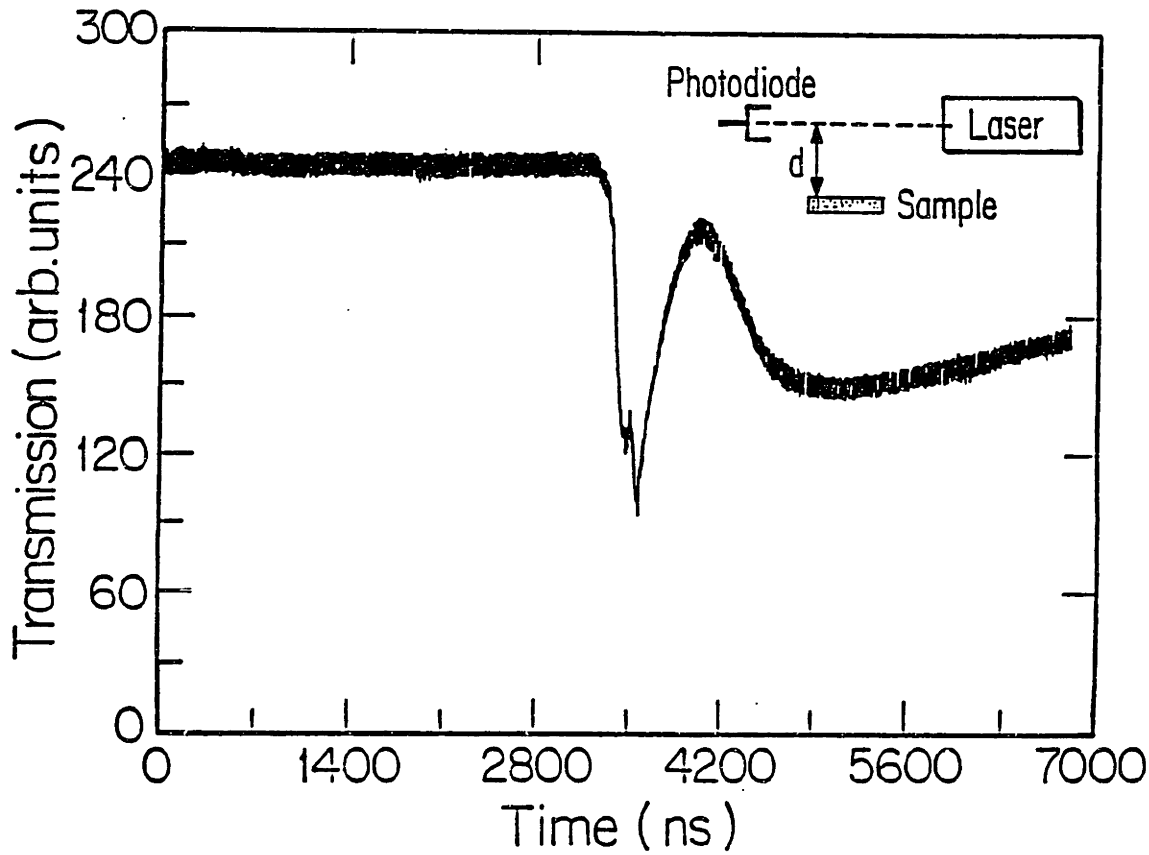

Figure 3.30: The transmission through an Ar atmosphere 5000μm above a graphite surface heated by a 25nsec KrF laser pulse. The two distinct decreases in the transmitted intensity are associated with a shock wave in the Ar and hot carbon particles, respectively.

broaden. This is confirmed by doing the same experiment in vacuum (Fig. 3.31) where only a single decrease in the transmitted intensity is observed. A third front can be observed at much later times (2μs later) and is due to the gas refilling the region behind the shock front.

All fronts are attenuated as they move away from the heated surface and were no longer optically detectable beyond three centimeters above the surface. The shock front position was taken as the half height of the transmitted intensity drop. The half height method is appropriate due to the finite thickness of the probe laser beam ($\sim 100\mu$m). A log–log plot of the shock front position versus time for the measurements that were made appears in Fig. 3.32. The fitted curves for the shock front position and the carbon particle positions show that for both, the shock front position may be given by eq. 3.15 with $N = 0.6$. These relations are characteristic of the shock front model proposed by Emmony and Irving in the regime where the shock in the gas is associated with a supported blast wave. When graphite is heated in vacuum, the carbon emitted from the surface does not collide with a gas above the surface, so that the carbon vapor is not slowed except by collisions with other carbon vapor species. The supported blast wave is never slowed and thus the distance traveled by the wave is proportional to the time (slope = 1).

There are several mechanisms which may account for the alteration of the transmission through the medium above the irradiated region. One mechanism by which the transmission of light through the gas may be disrupted is by absorption. However, in order for absorption to make a major contribution to the disruption of light transmission, the carbon particle size must be $\sim 10^5$ carbon atoms[68]. If absorption by particles were solely responsible for the decrease in light transmission, then the total number of carbon clusters required to account for the decrease in the transmission would be much larger than the

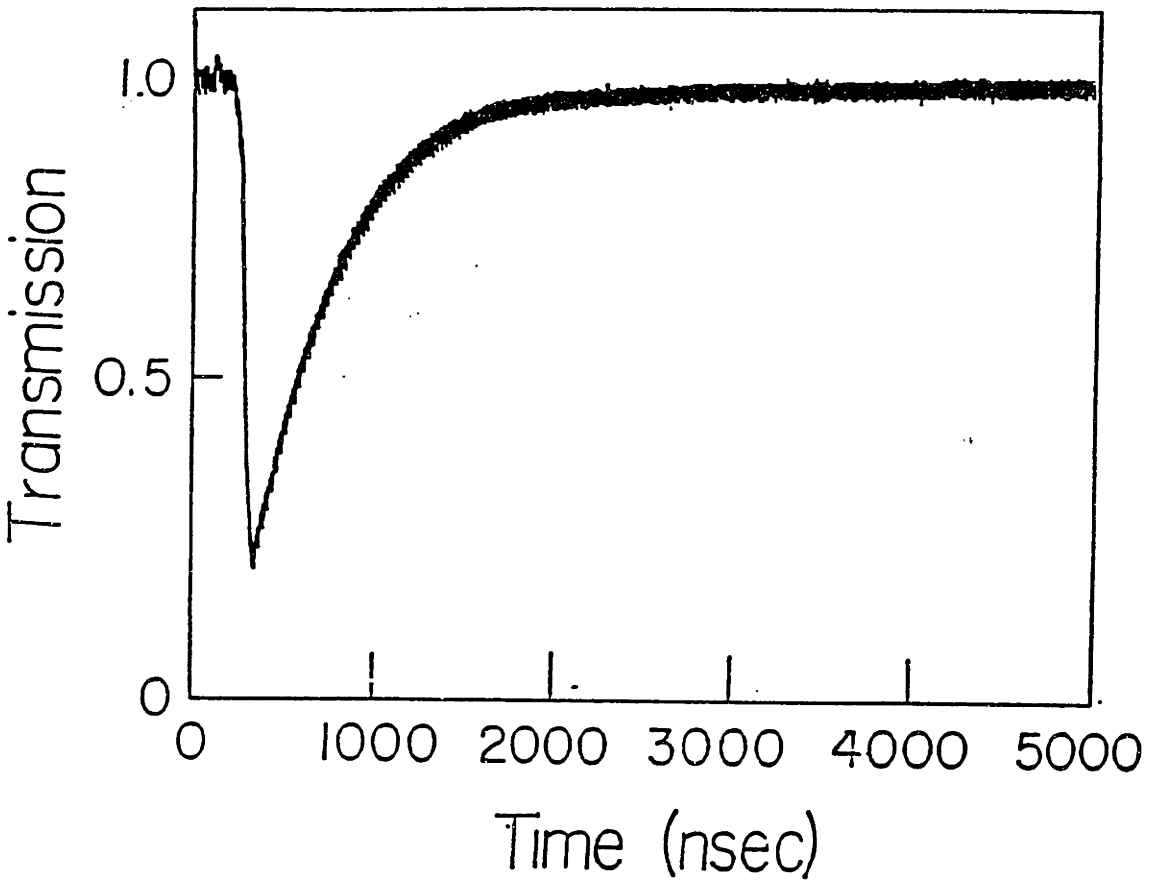

Figure 3.31: The transient transmission trace for pulsed laser heated graphite in vacuum. Note that there is only a single decrease in the transmitted intensity which must be due to the evolution of carbon from the surface.

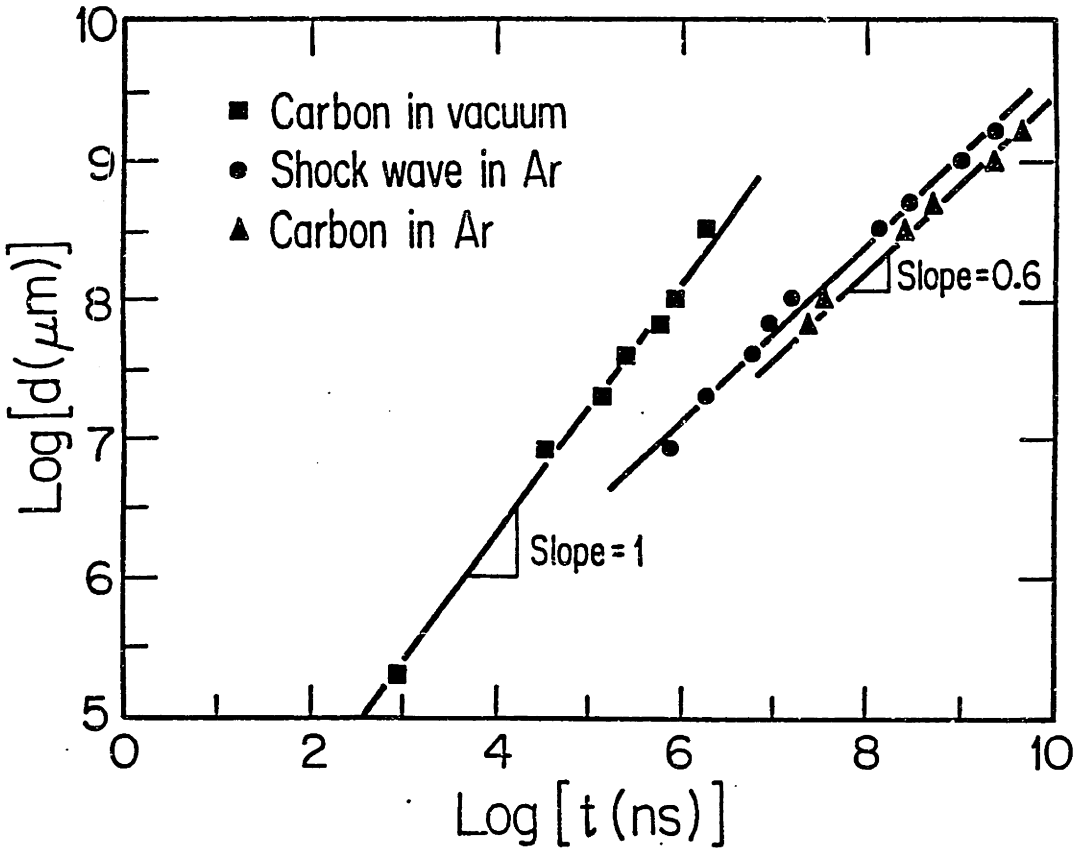

Figure 3.32: The optically measured shock front position versus time in both vacuum and 1 bar Ar gas. The $t = 0$ was taken as the initial half maximum of the incident laser pulse. The points in the figure are experimentally measured while the lines are a fit of the Emmony and Irving model[62].

measured amount of vaporized material.

The absorption coefficient for carbon particles containing 10^5 carbon atoms is $\sim 10^5 cm^{-1}$[68] for light at the probe wavelengths. If the carbon clusters were packed together, the dimensions of the volume containing the carbon clusters would have to be at least: 4.6×10^{-5}cm (1 percent transmission) by 0.4cm (to account for the length of time the transmission is disrupted) by 1cm (the diameter of the laser irradiated region). If the mean carbon–carbon distance in the volume is 2Å, then the total number of carbon atoms required to fill this volume is 2.5×10^{18}, or equivalently, a layer of graphite 2000Å thick, which is much more than is evolved from graphite, as shown in section 3.4.

Another possibility is the formation of an electron–ion plasma in the region near the irradiated surface. While it is unlikely that the density of the plasma would reach the critical density for optical wavelength transmission[58], the optical properties of the space above the irradiated region may be changed sufficiently to cause refractory effects which would deflect the probe beam. Refraction would be important in this experiment because the interface between the plasma and the gas surrounding the plasma will not be infinitely sharp or uniform[59,58].

The shock pressure induced as a result of the carbon leaving the surface may be estimated from the data of Gregg and Thomas[66] for the momentum transfer, M, for graphite in the energy density range around $1.5 \times 10^8 W/cm^2$, which is the power density range where most of the present work has been carried out. Using the simple shock pressure formula in eq. 3.19 for a carbon evolution time of 100nsec and a power density of $1.5 \times 10^8 W/cm^2$, the induced shock pressure on the graphite surface is $\sim$ 200bars.

The addition of 200bars of pressure on the surface from a shock wave during pulsed laser heating will not critically alter the properties of graphite. The

additional pressure on the surface may however be critical in determining the properties of liquid carbon according to the model for liquid carbon proposed by Ferraz and March[69] discussed in chapter 1. According to the Ferraz–March model, the addition of 200bars of pressure to the surface during heating, could cause graphite to melt into a metallic phase of liquid carbon and, as the pressure falls during cooling, the liquid will undergo a phase transformation into an insulating phase of liquid carbon. However, measurements of the transient electrical conductivity during pulsed current heating at low pressure do not indicate the presence of an insulating liquid phase[70]. These observations thus provide no support for the the Ferraz–March model. Therefore, the additional pressure on the surface due to shock pressure for power densities used in this work does not significantly alter the properties of liquid carbon.

For the power densities used in these experiments, the shock wave produced in the graphite as a result of the applied pressure from the ejected material is far too small to cause permanent deformations of the graphite lattice. Therefore, the effects of these waves may effectively be ignored in considering the thermal evolution of pulsed laser heating experiments in graphite for the power density range used in this work.

For laser pulses on the picosecond time scale, the shock pressure may be estimated using either eq. 3.19 or eq. 3.20. Pulsed laser heating of graphite in the picosecond regime has been carried out by Malvezzi *et. al.*[71] with 20psec duration pulses from a Nd:YaG laser operated at 532nm. The shock pressure induced for this case may be as high as 10^4 bar predicted by eq. 3.19 and will remain at that pressure for times much longer than the laser pulse since vaporization will occur as long as the liquid phase is present. This pressure is still much less than the graphite–diamond–liquid carbon triple point pressure ($\sim$ 100kbar) and is not significant except in the Ferraz–March model for liquid

carbon where the pressure on the liquid will determine whether the liquid is metallic or insulating. However, no evidence for two liquid carbon phases was provided from transient reflectivity measurements[71] so that again no support is lent to the Ferraz–March model.

3.7 Electric Current Pulse Heating

The traditional approach to creating liquid carbon is to melt macroscopic quantities of carbon by passing a large current through carbon as described in chapter 1. Pulsed electric current heating has been employed to determine the electrical conductivity of liquid carbon and high temperature graphite in order to overcome the difficulties encountered in transient electrical conductivity measurements during pulsed laser heating. There are two advantages in using pulsed current heating. First, electric pulse heating is not affected by the photoconductance of disordered carbon. Measurements of the transient electrical conductivity during pulsed laser heating reveal that the photoconductance of disordered carbon is important in analyzing the pulsed laser heating data as described in section 3.4. Second, large volumes of liquid may be created during pulsed current heating whereas pulsed laser heating is only able to create small pools of liquid near the surface.

As stated in chapter 1, there are difficulties in applying the pulsed current technique. The major difficulty is the pressure changes which occur as the result of the rapid expansion of carbon during heating. The other major problem with past experiments[36,72,73] using pulsed current heating is that the material used in those experiments is a disordered carbon or graphite. The reason disordered carbons and graphites have been used in the past is that graphite is a good conductor along the graphite planes so that in order for a large fraction of the dissipated power to be placed in the graphite during pulsed current

heating, the resistance of the graphite had to be raised by using disordered carbons and graphites.

In the present experiments, highly oriented graphite fibers have been used. The graphite planes in the fibers are oriented parallel to the fiber axis. The small diameter of the graphite fibers used ($\sim 10\mu$m) makes the resistance of the fibers large ($\sim 100\Omega$) before heating. The good crystalline orientation of the fibers eliminates the complications in the measurements which may introduced by the different thermal expansion coefficients of the graphite planes and c–axis when graphite is heated.

3.7.1 Experimental Technique

In this work, the pulsed current heating technique has been used to melt graphite fibers with diameters $\sim 10\mu$m and of lengths of $\sim$ 5mm. The graphite fibers were prepared by a chemical vapor deposition process[74] and were heat treated at temperatures in the range $1700 < T_{HT} < 2850$°C prior to being melted by the current pulse. The fibers have an onion skin type structure with the graphite planes parallel to the axis of the fiber.

The experimental arrangement used to electrically melt the fibers is shown in Fig. 3.33. A pulsed current source is in series with the graphite fiber to be melted. The current through the fiber is measured as a function of time by an oscilloscope through a 2.2Ω shunt resistor while the voltage across the fiber and the shunt resistor is measured by an oscilloscope with a 50Ω termination. Measurements are triggered by the rising edge of the current pulse. In order to suppress arcing between the electrodes, the fibers were placed in a steady flow of a N_2 and SF_6 gas mixture.

Several optical measurements were made during pulsed current heating to discount results which arise from carbon arcing and to obtain an *estimate* of the

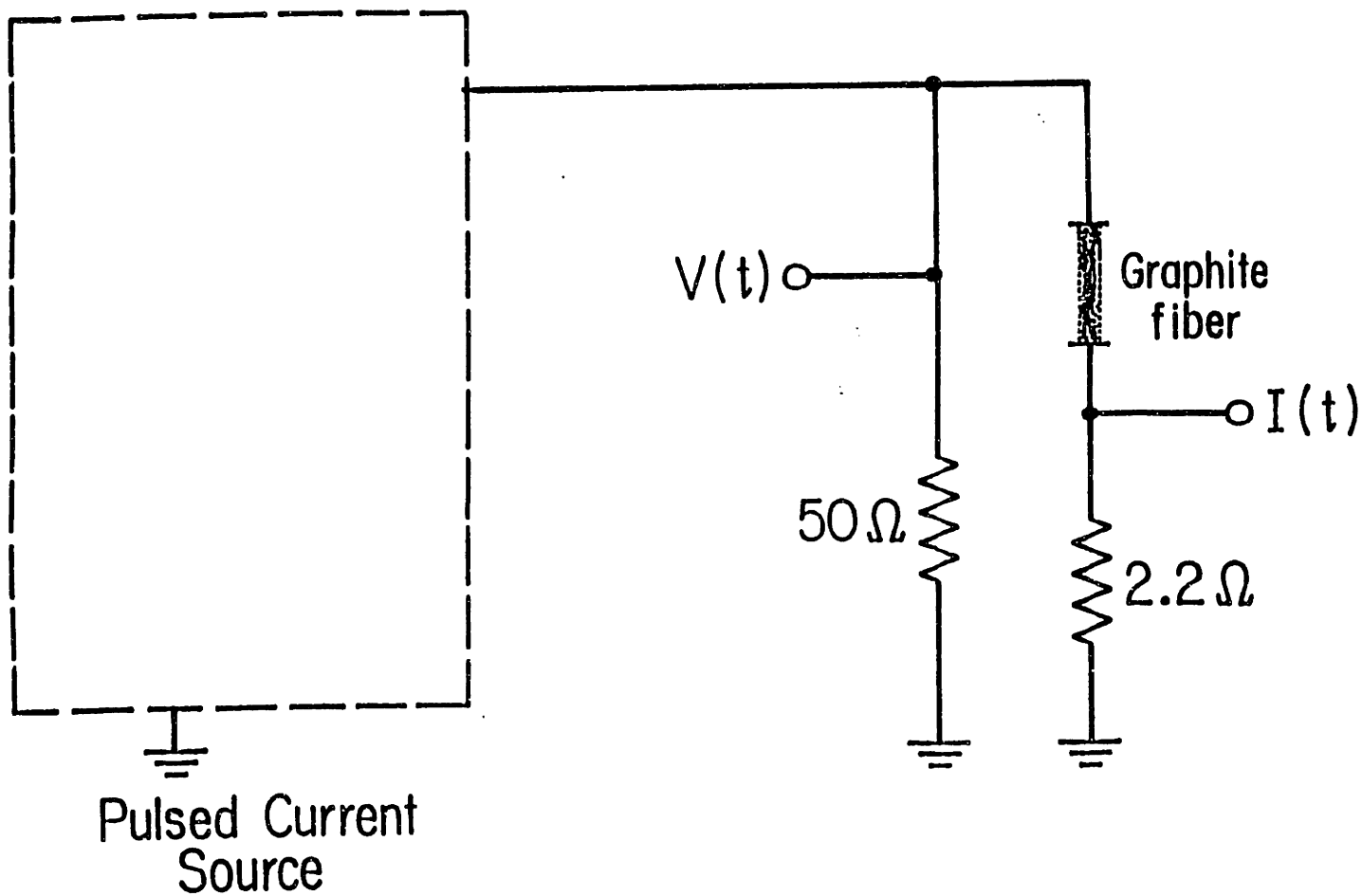

Figure 3.33: The experimental arrangement used to electrically heat and melt graphite fibers.

maximum fiber temperature. A photomultiplier tube (PMT) was used to detect ultraviolet emissions from the fiber during heating and a silicon photodiode with a UV filter was used to detect visible radiation from the fiber during heating. For all conditions, the visible signal maintains the same magnitude. During good runs, UV emissions are an order of magnitude smaller than the visible light emissions and track the shape of the visible emissions. When arcing occurs during pulsed current heating, a strong UV signal results from the recombination of ionized carbon and cyanogen molecules in the gas mixture.

In a second set of experiments, the light emitted from the fiber during pulsed current heating was directed into a spectrometer and analyzed by a photodiode array. The spectrum was first analyzed in the range of $237 < \lambda < 263$nm, centered about the carbon emission line at 247.8nm. These measurements showed that there was not a strong emission at 247.8nm so that the electrical measurements were not being made on conduction paths associated with a carbon arc or carbon plasma.

By looking at the spectrum centered about 600nm, a rough temperature measurement can be made. The intensity of the collected light is seen to steadily increase as the wavelength decreases. This means that the temperature of the fiber must be greater than 5000K during pulsed current heating since the maximum in the blackbody radiation for 5000K occurs $\sim$ 600nm.

3.7.2 Experimental Results

The results for electric current pulse heating of graphite appear in Figs. 3.34, 3.35, and 3.36. In Fig. 3.34 the measured current and voltage traces are shown for a fiber with $T_{HT} = 2850$°C. The combination of the increase in the voltage and the decrease in the current during the early stages of the current pulse are characteristic of the rising fiber temperature and an increase in the electrical

resistivity of the solid fiber at high temperatures[75]. The sharp transition that occurs at $\sim 5\mu$sec is attributed to the melting of the graphite fiber since arcing and plasma formation are known not to occur from the optical measurements. The voltage across the liquid column and the current through the column remain essentially constant for the remaining duration of the current pulse. Since the temperature of the fiber is still rising during the latter portions of the current pulse, the electrical resistivity of liquid carbon appears to be temperature independent for temperatures near the melting temperature at $\sim 30\mu\Omega$–cm.

The voltage and current traces for a graphite fiber with $T_{HT} = 1700°$C are shown in Fig. 3.35. The voltage and current traces for the graphite fibers with $T_{HT} = 1700°$C also undergo an abrupt change between 10 and 15μsec which is attributed to the fiber melting. The electrical resistivity of the fiber falls to $\sim 50\mu\Omega$–cm after the transition and remains at $\sim 50\mu\Omega$–cm for the remaining duration of the current pulse. In fact, the general behavior of the voltage and current traces is the same for fibers with different T_{HT}'s between 1700 and 2850°C. The early stages of the traces are characterized by the resistivity changes in the solid fiber as it is heated. At a later time, there is a sharp transition, attributed to melting, after which the electrical resistivity becomes nearly constant at $\sim 40\mu\Omega$–cm.

The resistance of the fibers can be calculated from the voltage and current traces and appears in Fig. 3.36. Note that the melting transition is again sharp in the case of the fiber with $T_{HT} = 2850°$C while the transition is broadened for the fiber with $T_{HT} = 1700°$C.

The resistance trace for the graphite fiber with $T_{HT} = 1700°$C in Fig. 3.36 is distinctly different from the resistance trace for the fiber with $T_{HT} = 2850°$C during the early stages of the current pulse. This is due to the different mechanisms of electrical conduction in the fibers. The fibers with $T_{HT} = 1700°$C

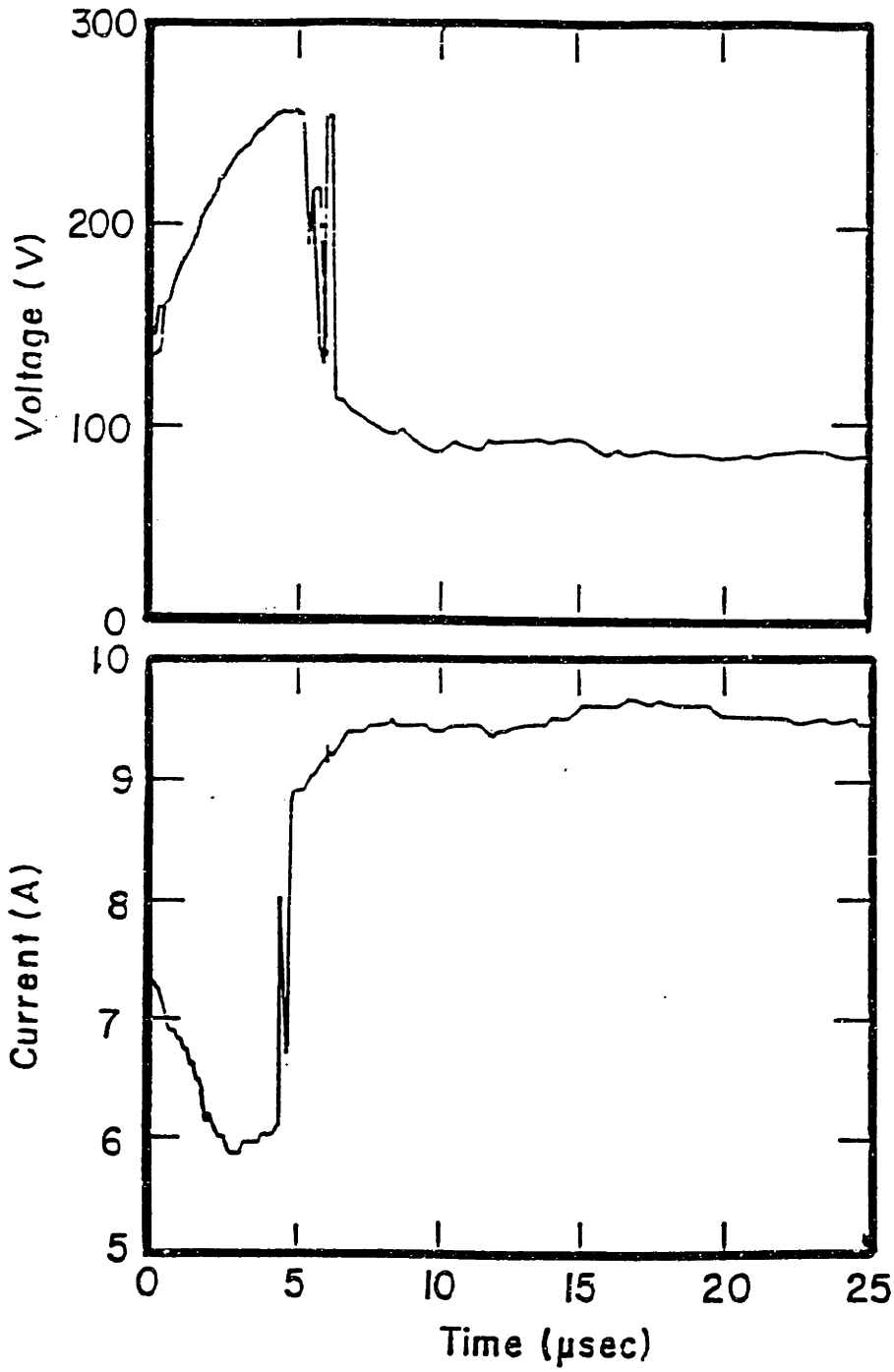

Figure 3.34: The voltage across and the current through a graphite fiber during pulsed current heating ($T_{HT} = 2850°C$). The sharp transition in both traces is attributed to the melting of the fiber.

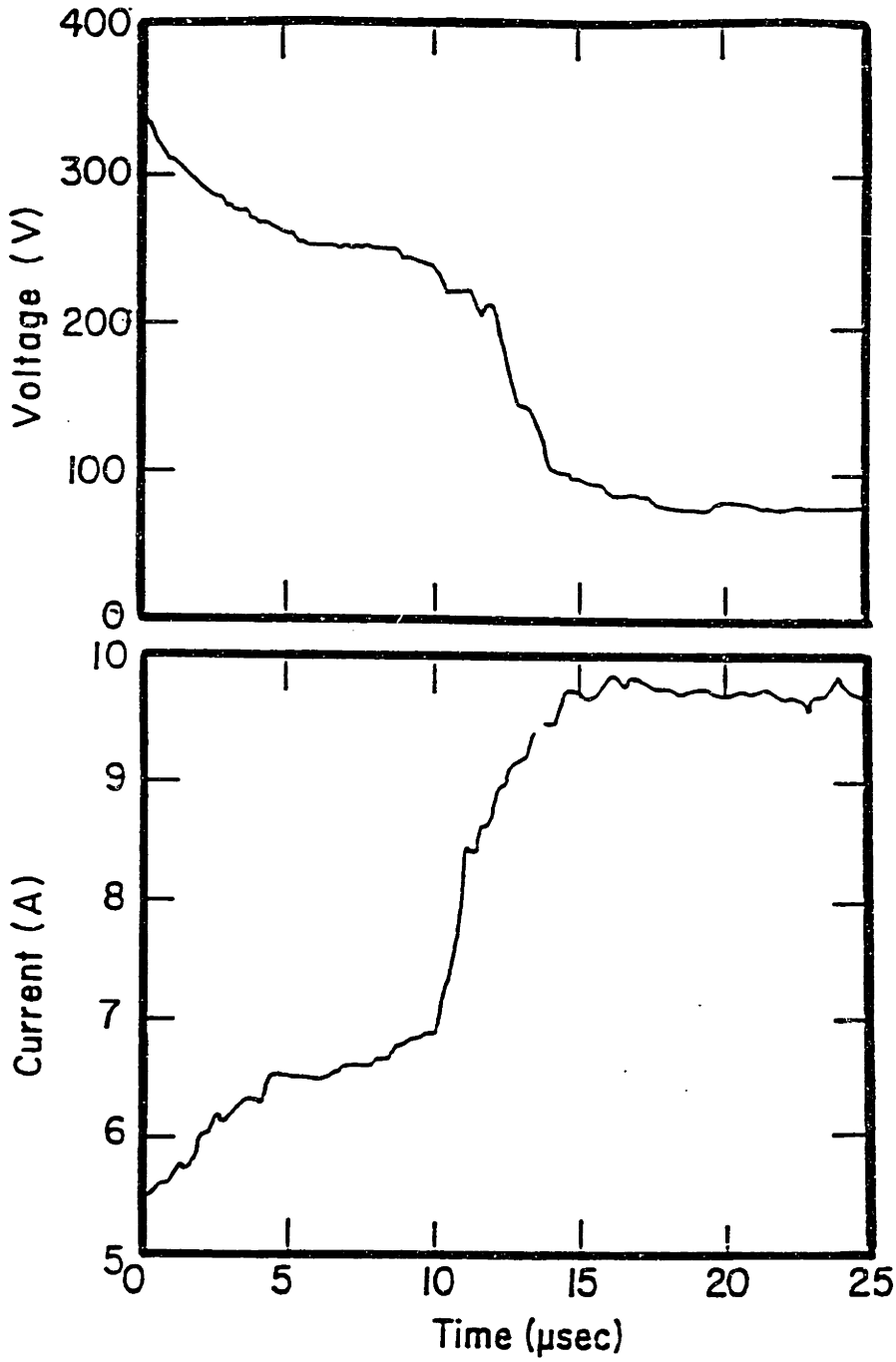

Figure 3.35: The voltage and current traces for a graphite fiber with T_{HT} = 1700°C. The initial decrease in the voltage trace and the initial increase in current trace are due to a decrease in the electrical resistivity of the solid fiber.

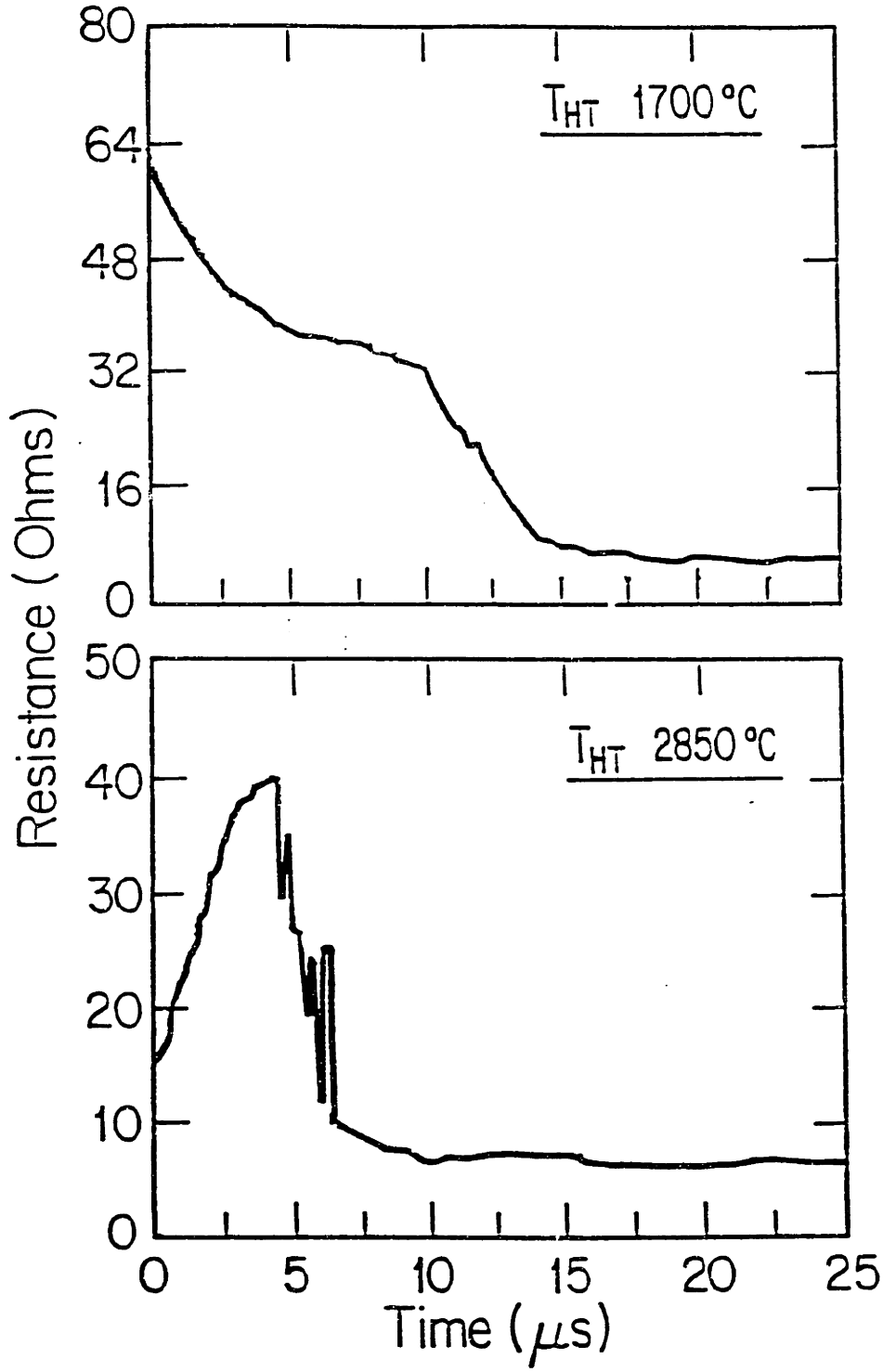

Figure 3.36: The resistance versus time for pulsed current heated graphite fibers. The difference in the traces during the early stages of heating reflect the different electrical conduction mechanisms.

have activated electrical conduction, dominated by defect scattering, in which the electrical resistivity decreases as the temperature of the fiber increases. The graphite fibers with $T_{HT} = 2850°C$ have a metallic conductivity which decreases with increasing temperature due to increased phonon scattering. All the graphite fibers are of comparable dimensions so that the difference in the initial resistance of the fibers is also attributed to the different conduction mechanisms.

The other major difference between the resistance traces in Fig. 3.36 is the time at which the fibers melt. The time difference between the melt transitions can be attributed to the power density which is heating the fiber during the current pulse. From Fig. 3.34 and 3.35 the current in the fiber with $T_{HT} = 1700°C$ is smaller than the current for the fiber with $T_{HT} = 2850°C$. The power, P, absorbed by the fiber is

$$P = I^2 R \tag{3.21}$$

where I is the current through the fiber and R is the fiber resistance. The smaller current in the fiber with $T_{HT} = 1700°C$ then heats that fiber more slowly than the larger current in the fiber with $T_{HT} = 2850°C$.

The other difference between the two fibers is the width of the transition as the fiber melts. This difference can also be explained in terms of the difference in the absorbed power since the time required to transform the fiber from the solid state to the liquid state will depend on the time required for the fiber to absorb the heat of fusion. The lower power in the case for $T_{HT} = 1700°C$ means that it will take longer for the current to supply the heat of fusion to the fiber, hence, the time required to go from the solid to liquid state is longer.

The temperature dependence of the electrical resistivity for the solid fibers can be estimated from the resistance traces in Fig. 3.36 by using the known dimensions of the fibers, the room temperature electrical resistivity, and by

assuming that the temperature increases linearly with time for $300 < T < T_M$ where T_M is the melting temperature known to be close to $T_M \simeq 4500$K. The justification for this assumption is that numerical heat flow calculations (chapter 5) show that the mean temperature of the fiber versus time increases nearly linearly with time when the time dependence of the input power and the thermal properties are accounted for. The electrical resistivity of the solid fibers, ρ_s, can be fit with an expression

$$\rho_s = a + bT + cT^2 \tag{3.22}$$

where a, b, and c, are constants.

By mapping a temperature scale on to the time scale, the electrical resistivity versus time is determined and shown in Fig. 3.37. In Fig. 3.37, the electrical resistivity versus temperature has been determined for graphite fibers with T_{HT}'s of 1700, 2100, 2300, and 2800°C using pulse current heating. Note that only the temperature dependence of the electrical resistivity for the fiber with $T_{HT} = 1700$°C is characteristic of an activated process. The electrical conductivity for fibers with $T_{HT} = 2300$ and 2800°C have a temperature dependence characteristic of semimetallic graphite while the temperature dependence of the electrical resistivity for the fiber with $T_{HT} = 2100$K is probably a combination of both the metallic and activated conduction processes.

Table 3.3 contains the constants a, b, and c for the electrical resistivity of graphite fibers with $T_{HT} = 1700$, 2100, 2300, and 2800°C. The constants were derived by fitting the electrical resistivity in Fig. 3.37 with Eq. 3.22. The point at which the fiber was assumed to reach the melting temperature, T_M, was taken to be the point where the resistance begins to decrease due to melting.

Since there are no abrupt changes in the electrical conductivity until the fibers melt, the properties of graphite between 3000K and the melting temperature at $\sim$ 4500K may be approximated by extrapolating experimental data

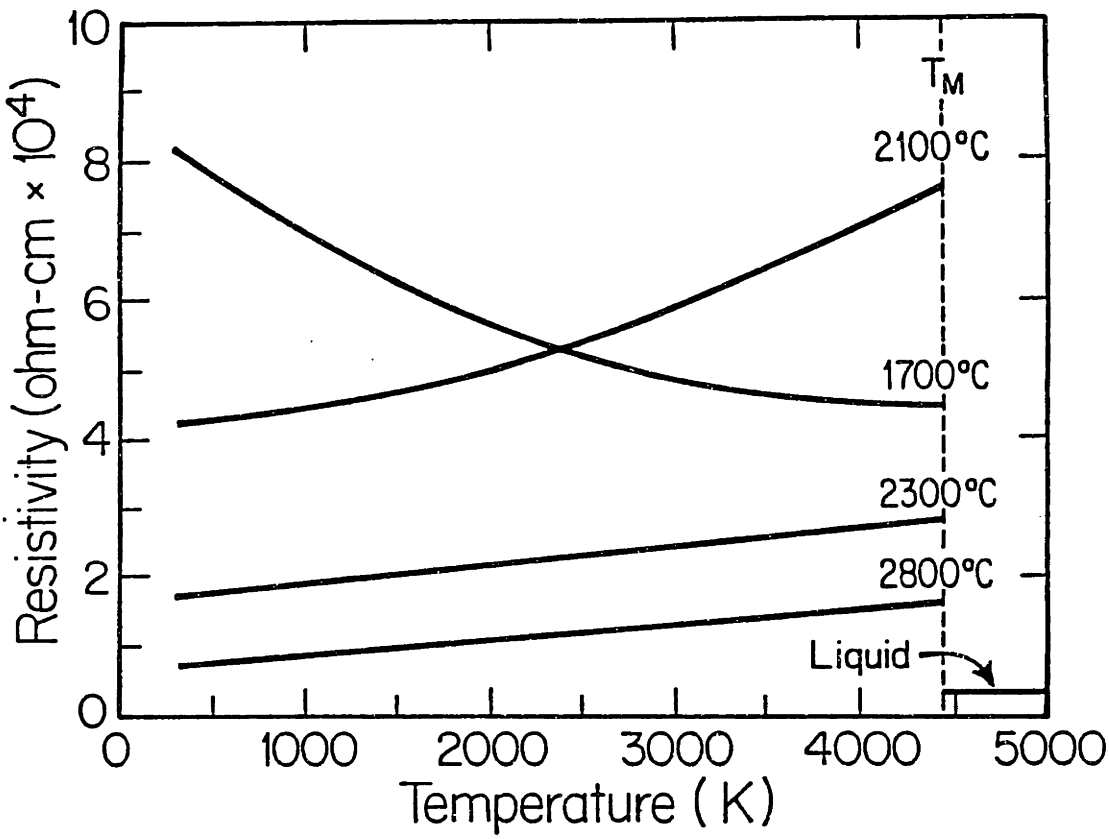

Figure 3.37: The electrical resistivity versus temperature for graphite fibers with T_{HT} = 1700, 2100, 2300, and 2800°C, respectively. The measured electrical resistivity for liquid carbon is shown at the right of the figure. Note that the electrical resistivity for the fiber with T_{HT} = 1700°C is the only one characteristic of an activated conductivity.

T_{HT} (°C)	a ($\mu\Omega$-cm)	b ($\times 10^2 \mu\Omega$-cm K^{-1})	c ($\times 10^4 \mu\Omega$-cm K^{-2})
1700	871	-20.3	0.24
2100	424	0.37	0.16
2300	166	2.71	0
2800	63	2.33	0

Table 3.3: The constants a, b, and c used in Eq. 3.22 for graphite fibers for $300 < T < 4500$K.

for $T < 2850$°C up to the melting temperature without incurring a large error. Previously, this approximation has been used by many author in attempts to determine the properties of liquid carbon[76,77] without any experimental verification of this assumption. Since the electrical conductivity is an indicator for the predominant scattering mechanisms in materials, the lack of deviations from the expected behavior in graphite at temperatures above 3000K strongly suggests that there are no additional scattering mechanisms at high temperature which would cause the thermal conductivity or the specific heat of graphite at high temperature to deviate significantly from extrapolations from data at lower temperatures.

3.7.3 Pressure Generated During Pulsed Current Heating

A discussion of the properties of liquid carbon requires a careful consideration of the pressure under which the liquid carbon has been created. This is necessary because the properties of liquid carbon are thought to be sensitive to pressure as shown in the phase diagrams in chapter 1. In other pulsed current melting studies on carbon, the pressure on the surface of the carbon is known to be several hundred kilobars[36,72,73]. The pressure is generally applied by external source to the carbon, but a portion of the pressure comes from inter-

nal sources such as the rapid thermal expansion of carbon during heating. The internal pressure is generated when the temperature of the graphite increases faster than the graphite can mechanically adjust to it. Since graphite expands as it is heated, rapid heating applies a compressive stress on graphite.

The internally generated pressure on the graphite fibers which have been melted by the pulse current technique in this work is not large. This is proven directly in our experiments since the electrical resistivity of the liquid is nearly the same for fibers with very different T_{HT}'s. If an internal pressure were generated from the rapid thermal expansion of the graphite, then the pressure generated in fibers with $T_{HT} = 1700°C$ should be much larger than the pressure generated in fibers with $T_{HT} = 2850°C$. The reason for this is that the heat treatment performed prior to the pulsed current experiments allows the relaxation of the compressional stresses from thermal expansion up to the heat treatment temperature. Upon cooling, there is differential thermal contraction which leads to the formation of buckles in the fiber surface. Since there is no piezoelectric effect observed in our resistivity data at temperatures above T_{HT} for the fibers, and since the measured electrical conductivity of liquid carbon is the same, within experimental error, for all T_{HT}'s, the internal pressure in the fibers must be nearly the same and is probably not much greater than atmospheric pressure.

Since the vaporization temperature is close to the melting temperature, as shown by laser heating experiments, the vaporization of carbon may also apply a pressure to the surface of the fiber during heating. However, the dynamic vapor pressure generated by pulsed current heating must be less than the vapor pressure generated by pulsed laser heating for the following reason: the induced vapor pressure on the surface of the fiber will be dependent on the velocity of the material as it leaves the surface. For pulsed current heating, the carbon

vapor is known not to be influenced by plasma effects. The carbon vapor leaves the surface at the thermal velocity at $\sim 2.5 \times 10^5$cm/sec for carbon atoms at 4500K. Since this velocity is four times smaller than the velocity of carbon leaving the surface during pulsed laser heating, the vapor pressure induced by pulsed current heating is much smaller than the vapor pressure induced by pulsed laser heating.

3.8 Picosecond Pulse Laser Heating

Picosecond pulse laser heating has been done on graphite in order to overcome some of the difficulties encountered in doing transient optical measurements during nanosecond pulse laser heating due to the vaporization of carbon. Laser heating on the picosecond time scale may alleviate the problems with carbon vaporization by melting graphite *before* carbon vaporization can interfere with optical measurements.

Laser irradiation of graphite on the picosecond time scale is somewhat different than for pulsed laser heating on the nanosecond time scale. On the picosecond time scale, the energy in the laser pulse is put into graphite on a time scale such that thermal diffusion will only play a small role in determining the melting threshold for graphite. Another difference is geometric in that the area of irradiation by picosecond pulse lasers is much smaller than in the nanosecond case. The small area of irradiation is an artifact of having to focus picosecond laser pulses in order to obtain power densities sufficient for melting.

3.8.1 Liquid Carbon Created by Picosecond Pulse Laser Heating

The pressure on the surface of the graphite during pulsed laser heating may play an important role in determining the properties of liquid carbon as is illustrated

by the many phase diagrams shown in chapter 1. The pressure may arise from the differences in the vaporization rate and from the internal pressures which may build up as a result of the graphite not being able to expand fast enough. Unfortunately, the geometry of the irradiated area is generally too small to do the extensive post–heating analysis that was done for the nanosecond pulsed laser melted graphite. Two of the post heating techniques which may be applied to picosecond pulsed laser melted graphite are Raman spectroscopy and TEM.

The aim of the post heating studies is to try to determine if the liquid created with picosecond pulse laser heating is significantly different from the liquid created by nanosecond pulse laser heating. This is necessary so that comparisons of the data from transient optical measurements made on the picosecond time scale may be compared with similar measurements on the nanosecond time scale.

Raman microscopy and TEM have been used to study the structural properties of the disordered region remaining after graphite is irradiated with 20psec Nd:YaG laser pulses at 532nm. The results have been compared with the results from similar measurements on the disordered region remaining after irradiation with 30nsec ruby laser pulses at 694nm[22,78].

The results of Raman measurements in both the picosecond and nanosecond regime are given in Fig. 3.38 as a function of the irradiating energy density. Specifically, the intensity of the disorder–induced mode, I_{1360}, in graphite is compared to the intensity of the Raman–active mode, I_{1582}. The abscissas in the figure have been set so that comparisons between the two irradiating conditions can be made easily. The average crystallite size in graphite has been related to the ratio of the intensities, I_{1360}/I_{1582}, by Tuinstra and Koenig[38] and is given on the right hand ordinate. As can be seen from Fig. 3.38, the general trend in both the nanosecond and picosecond regimes is to create a

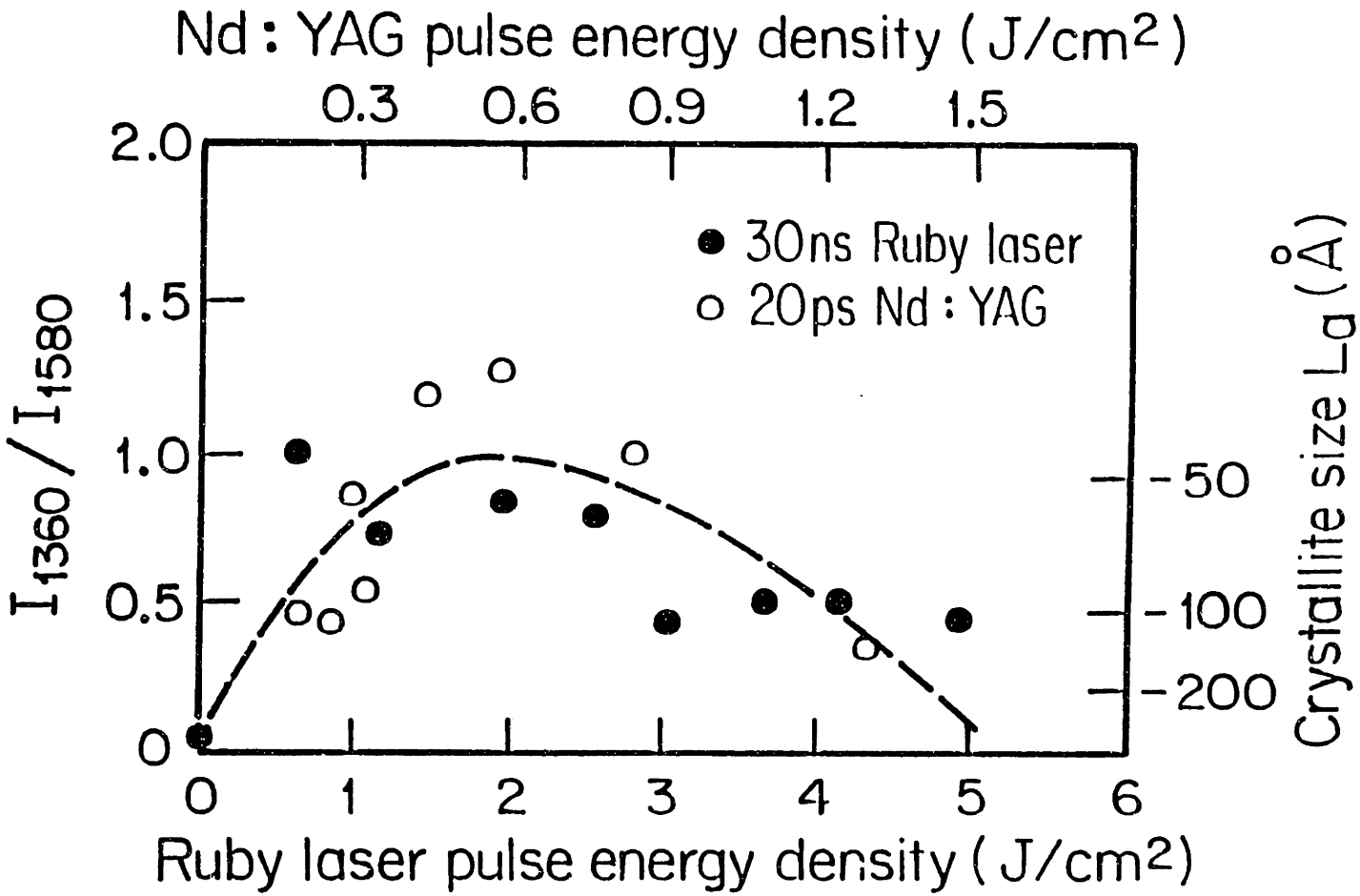

Figure 3.38: A summary of Raman measurements made on 20psec Nd:YaG (532nm) pulsed laser melted graphite and 30nsec pulsed ruby laser melted graphite. Note the similar behavior of the intensity ratio, I_{1360}/I_{1580}, for the two different laser heating conditions.

highly disordered region at irradiating energy densities close to the melt threshold (0.6J/cm^2 for 30nsec ruby laser, 0.14J/cm^2 for 20psec Nd:YaG laser). As the irradiating energy density is increased further, the average crystallite size reaches a minimum and then begins to increase. Some of the samples for 20psec 532nm Nd:YaG irradiation between 0.7 and 0.9J/cm^2 had Raman spectra characteristic of amorphous carbon implying complete disorder.

The similarity in behavior between nanosecond and picosecond irradiation is verified by examining the irradiated region by transmission electron microscopy. Selected area electron diffraction results from samples irradiated in the nanosecond and picosecond regimes display a (001) ring and (hk0) rings, as shown in Fig. 3.39a for samples irradiated with $\sim$ 4J/cm^2 30 nsec ruby laser pulse and in Fig. 3.39b for a sample irradiated with a 1.8 J/cm^2 20 psec Nd:YaG laser pulse. Such diffraction patterns are indicative of a random dispersion of fine turbostratic graphite grains (no 3–dimensional crystallographic correlations).

The widths of rings observed in these electron diffraction patterns are determined by the degree of orientational ordering in the resolidified material *and* by the actual size of the turbostratic graphite grains, so that only qualitative trends can be established. For the case of samples irradiated in the nanosecond regime, we find that the ring widths tend to increase with increasing laser fluence up to 2.2J/cm^2 then decrease at higher energy fluences. This is in qualitative agreement with the Raman microprobe measurements show in Fig. 3.38. The Raman results suggest that longer liquid dwell times leads to a larger average resolidified grain size and more (00l) orientation.

The grain structure in the resolidified material can be directly imaged. A dark field image formed from a small portion of the (001) ring is shown in Fig. 3.40 for a sample irradiated with a 20psec 532nm Nd:YaG laser pulse with an energy density of 1.8J/cm^2. The resolidified grains are clearly visible in the

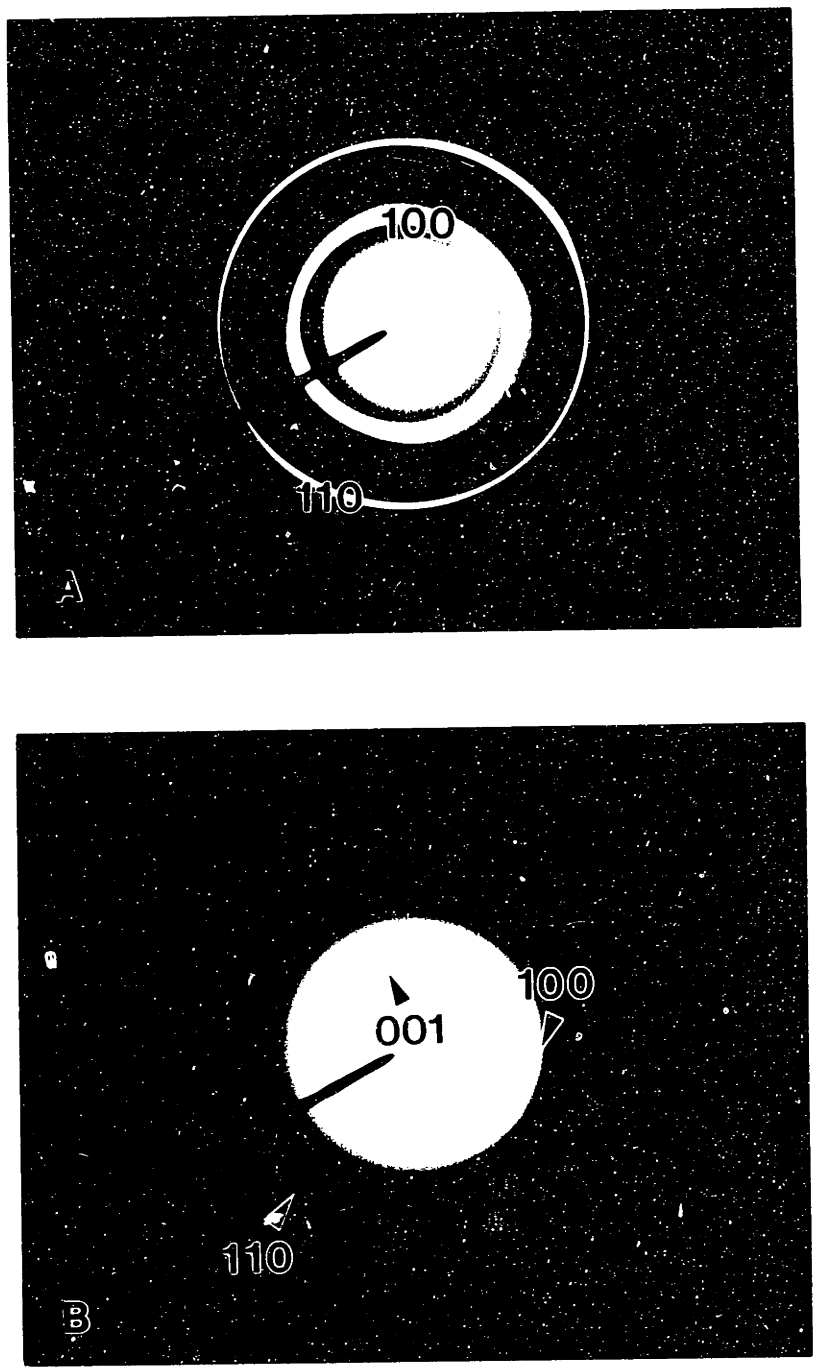

Figure 3.39: Selected area electron diffraction pattern from graphite sample irradiated with (a) ~4 J/cm^2 30 nsec ruby laser pulse and (b) 1.8J/cm^2 psec Nd:YaG pulse.

figure. The turbostratic graphite grains have an a/c aspect ratio of about two. The grain size in the a–direction is ~10nm and in the c–direction is ~5nm. A grain morphology of this nature is consistent with surface energy minimization.

The surfaces of the samples irradiated in both regimes show upheavals and spheres. For the 20psec case, the spheres, shown in Fig. 3.41, measure ~100nm in diameter. This is in good agreement with results published on the surfaces of samples irradiated in the nsec regime [22]. Recent work on laser sputtering suggests that the observed spheres are due to hydrodynamic sputtering of the surface[40]. This interpretation must be investigated more fully for the irradiated graphite systems.

While these results are consistent with the hypothesis that the liquid created from pulsed laser heating on the picosecond time scale is the same as the liquid created by nanosecond pulse laser heating, this is not a direct proof that the liquid created under both heating conditions is the same. However, if the liquids created by in the two pulsed laser heating regimes differed greatly, then one might expect those differences to manifest themselves in the resolidified material because the microstructure of the resolidified material is determined by the velocity of the liquid–solid interface, as discussed in section 3.5, which *is* determined by the thermal properties of the liquid. In particular, the thermal conductivity of the liquid will play a large role in determining the melt front velocity.

If the liquids created were significantly different, in that one is insulating comprised of molecular carbon chains, while the other is a metallic liquid of atomic carbon, then the thermal conductivities of the liquids would be very different which should appear as differences in the microstructure of the resolidified material. The major difference to be expected would be larger crystallite sizes for molecular liquids since the thermal conductivity of a molecular liquid

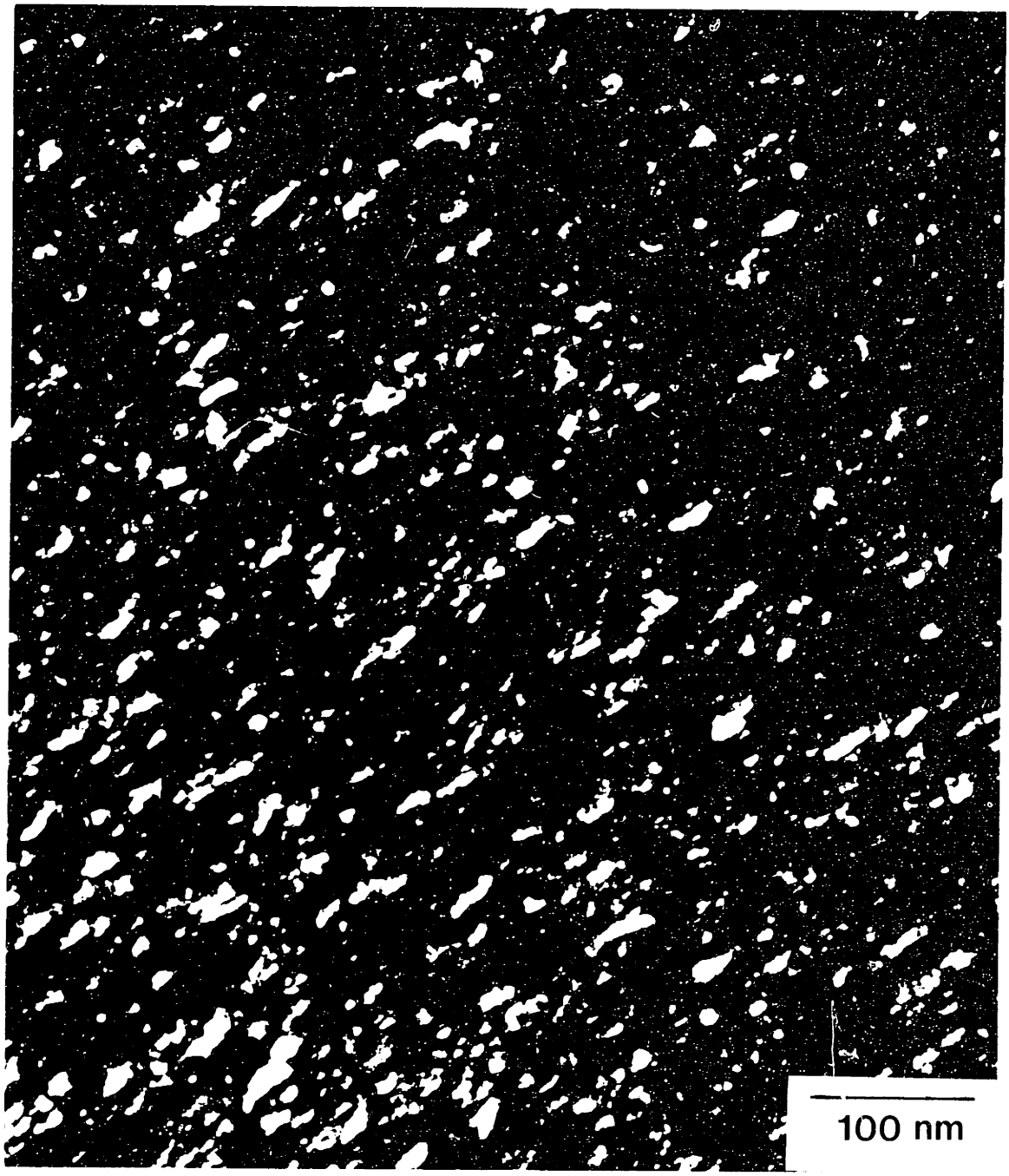

Figure 3.40: (001) dark field image of 20psec Nd:YaG pulsed laser melted graphite. The image was formed using $0.6/2\pi$ of the (001) ring.

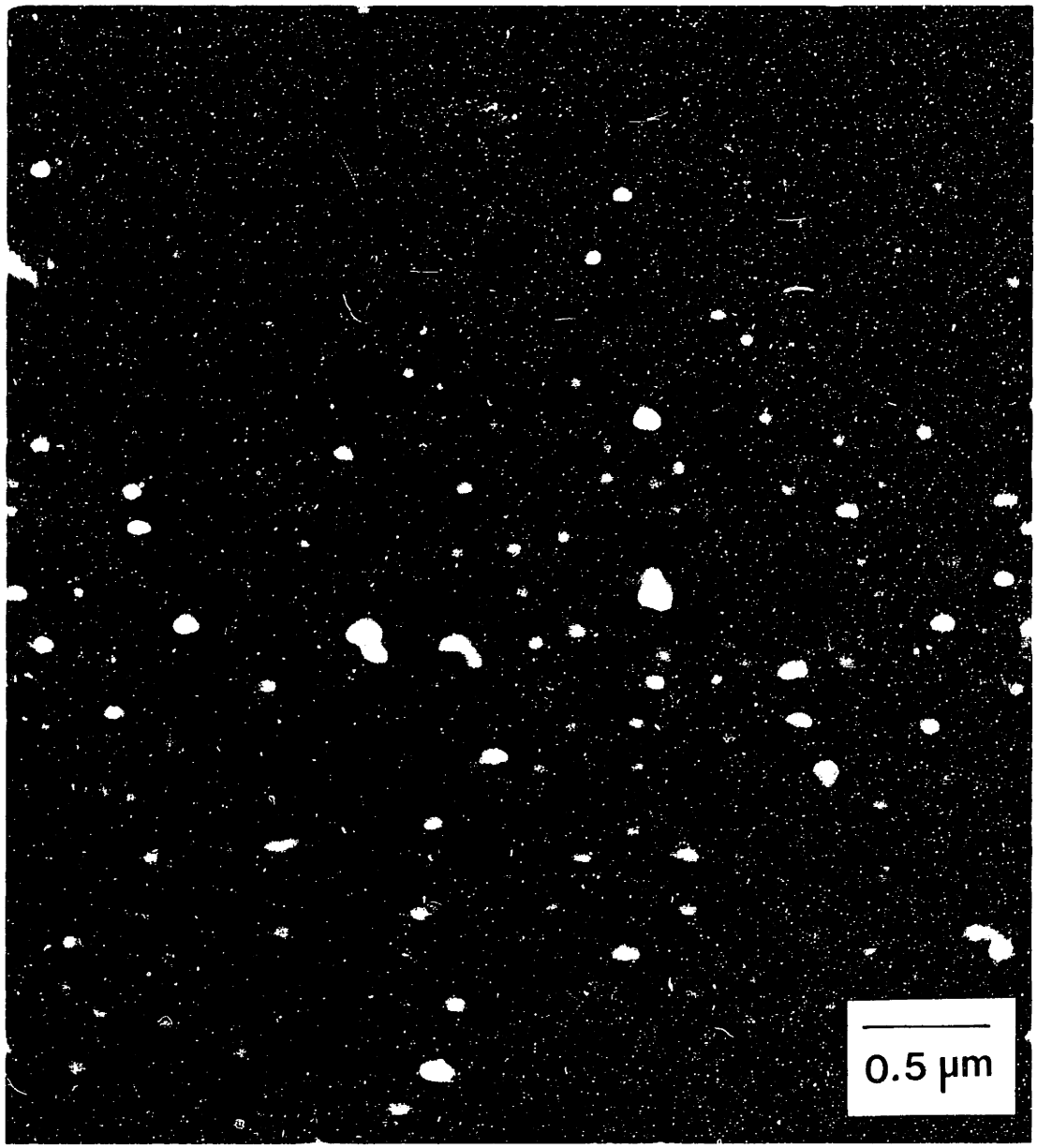

Figure 3.41: Scanning electron micrograph of the boundary region of a psec irradiated sample. The small carbon spheres are common to both psec and nsec laser irradiation structures.

would be smaller than the thermal conductivity in a metallic liquid. The post heating analysis done with Raman spectroscopy and electron microscopy does not reveal a large difference in the size of the crystallites remaining after laser melting by either picosecond or nanosecond laser pulses. This means that the velocity of the liquid–solid interface during resolidification is nearly the same, suggesting that the liquids created by both picosecond and nanosecond laser pulses are the same.

3.8.2 Transient Optical Measurements

Transient optical reflectivity measurements have been done by Malvezzi *et. al.*[71] on graphite using the pump and probe technique described in section 3.3.3. The results of these measurements are shown in Fig. 3.42, and are similar to the transient reflectivity measurements made on the nanosecond time scale. There is an initial sharp drop in the reflectivity once the laser pulse energy density exceeds the melt threshold. The sharp drop in the reflectivity is then followed by a slow increase until the reflectivity saturates at a value which is smaller than the reflectivity of graphite at the probe laser wavelength. The incomplete recovery of the reflectivity is attributed to surface roughening as in the nanosecond case.

The results of Fig. 3.42 have been interpreted by Malvezzi *et. al.*[71] to show that liquid carbon is an insulating phase than graphite. To support this claim, ellipsometric measurements by Malvezzi *et. al.*[79] and transient electrical conductivity measurements by Chauchard *et. al.*[80] also were interpreted to support the claim that liquid carbon is an insulating phase of carbon. However, the transient electrical conductivity results reported by Chauchard *et. al.*[80] account neither for an increase in the electrical resistivity of graphite when heated, nor for the material losses which occur through vaporization. Both

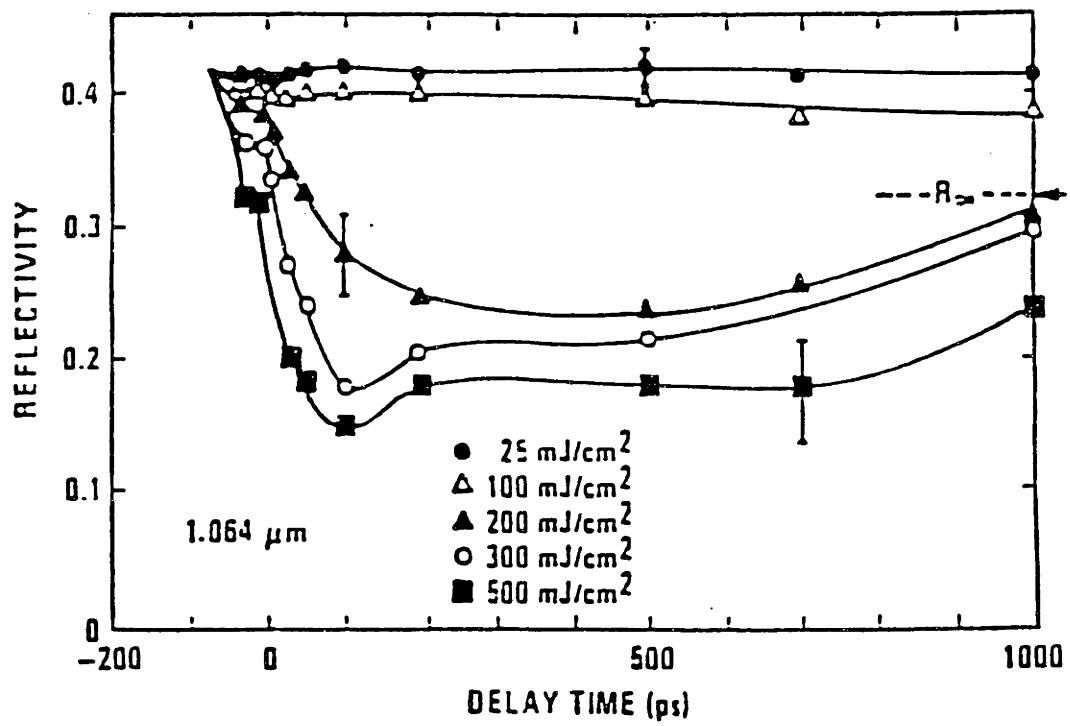

Figure 3.42: The results of transient reflectivity measurements done by Malvezzi *et. al.*[71] using the pump and probe technique. The pump and probe were provided by a 20psec second harmonic (532nm) Nd:YaG laser.

of these effects introduce serious complications to the analysis of the transient electrical conductivity measurements in a metallic material like graphite.

The analysis of transient optical measurements on the picosecond time scale may also be more complicated due to carbon vaporization. While simple vaporization may not produce enough vapor to affect optical measurements, it has been shown that carbon plasmas are formed during pulsed laser heating in graphite using pulses with power densities comparable to those used in the picosecond pulse heating experiments[30]. The formation of a dense electron–ion plasma near the surface in the laser irradiated region during picosecond pulse laser heating could affect optical probing of the surface as it does in the nanosecond case.

To show that the analysis of transient optical measurements is not as straight forward as was originally thought, graphite has been excited by laser pulses 5psec in duration at 632.8nm by Heremans *et. al.*[70] with energy densities which are well below the melt threshold energy density of $0.14 J/cm^2$. Transient reflectivity measurements made with the pump and probe technique appear in Fig. 3.43. The traces in Fig. 3.43 represent transient reflectivity measurements made on graphite with pulse energy densities of 0.02, 0.1, and $0.2 mJ/cm^2$. The change in the reflectivity is plotted against time in Fig. 3.43. These measurements are markedly different in that they show that the reflectivity of graphite *increases* during the pump pulse while for times after the pumping laser pulse, the reflectivity falls sharply to values slightly smaller than the reflectivity of graphite at the probe laser wavelength. The inset in Fig. 3.43 gives a longer time history of the trace for a $0.2 mJ/cm^2$ pump pulse. The reflectivity trace is similar to the transient reflectivity measurements made on longer time scales in that the reflectivity has a slow recovery.

The pumping pulse energy densities for this work are too small to induce

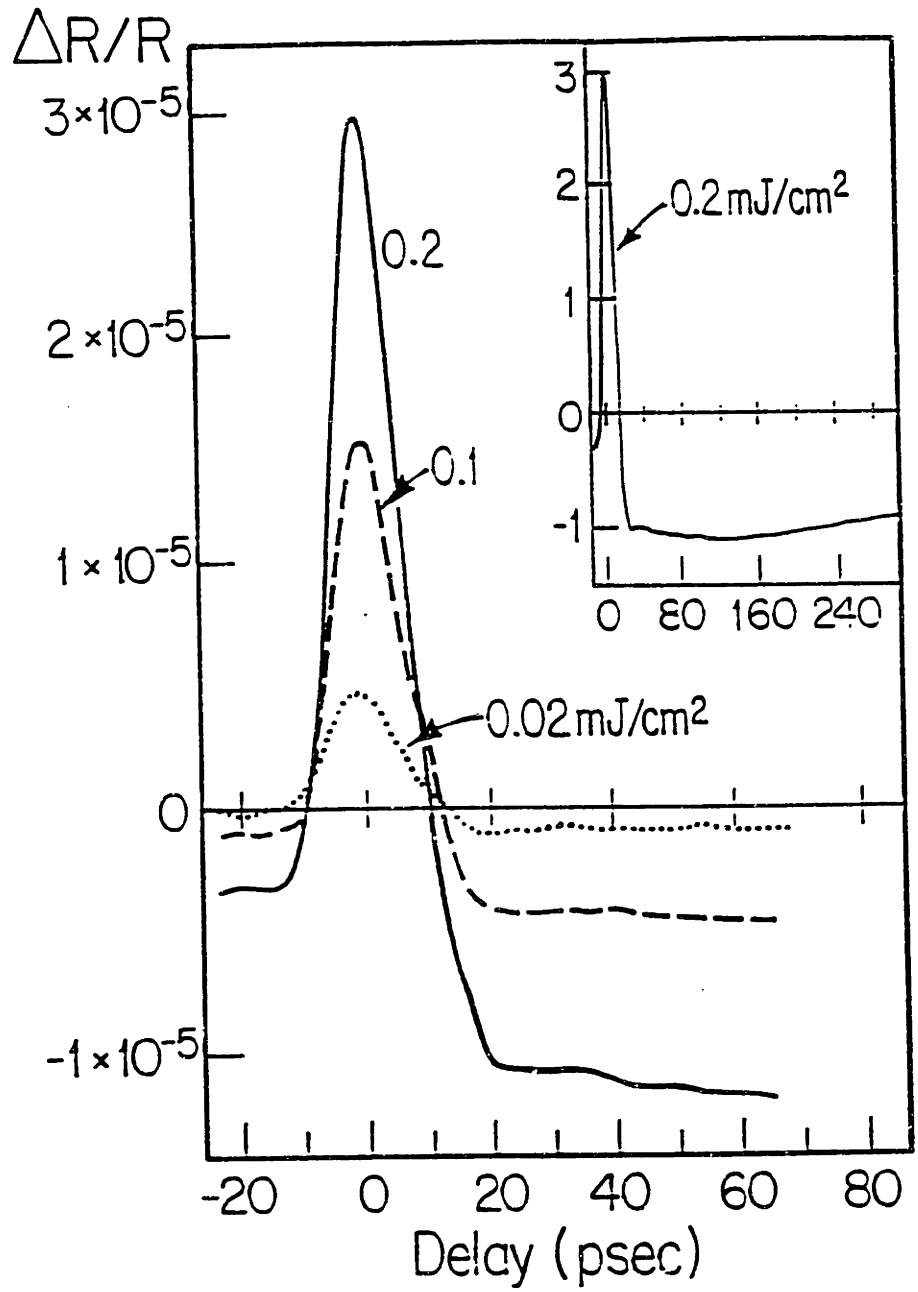

Figure 3.43: The results of transient reflectivity measurements during picosecond pulse laser heating. Shown in the figure are the traces for 0.02, 0.1, and 0.2mJ/cm^2 laser pulses which are well below the melt threshold energy density of $\sim$ 0.14J/cm^2. The inset shows a longer trace for the 0.2mJ/cm^2 laser pulse showing the slow recovery of the reflectivity at long times from the laser pulse. Taken from Heremans *et. al.*[70].

melting on the surface, but the reflectivity nevertheless changes. The changes may be explained by two effects: the creation of an electron–hole plasma during the laser pulse, and the heating of the graphite lattice at later times. During the pumping laser pulse, large numbers of electron–hole pairs are created since the energy of the photons in the pumping pulse cause the electrons to undergo interband transitions. The initial increase in the reflectivity is caused by the increased carrier density from the excited electrons. As the energy is transferred from the carrier system to the lattice, the number of free carriers decreases and the phonon scattering rate increases, which heats the lattice. By comparing the change in the reflectivity with expected changes in the electrical conductivity we find

$$\frac{\Delta\rho}{\rho} = \frac{\Delta R}{R} \simeq -6 \times 10^{-7}\mathrm{K}^{-1} \tag{3.23}$$

which is compatible with the electrical conductivity reported for graphite[81].

These results indicate that transient optical measurements during picosecond pulse laser heating of graphite are far more complex than was originally assumed by Malvezzi *et. al.*[71]. The creation of an electron–hole plasma and the changes in the optical properties as graphite is heated must be taken into account when interpreting transient optical data. As discussed in section 3.3.1, transient electrical conductivity measurements are difficult to make on pulsed laser heated graphite because of the metallic properties of graphite. The high temperature properties of graphite must be accounted for in any interpretation of transient electrical data as well.

3.9 Summary

This chapter has presented experimental results from pulsed laser heating of graphite on the nanosecond time scale. The mechanisms of laser heating were discussed in the opening sections. Phase transitions induced by laser heat-

ing were then discussed and the transient and post–heating techniques used to study laser melted materials were described. An emphasis was placed on transient optical and electrical measurements which directly measure the properties of the molten material.

The post heating analysis of the disordered layer remaining after pulsed laser–irradiation of graphite shows that pulsed laser heating does indeed cause graphite to melt. From the threshold energy density required to create the disorder layer, an estimate of the melting temperature for graphite was obtained at $T_M \simeq 4500$K. The disorder layer thickness remaining after pulsed laser heating can be measured using ion channelling. Material loss is also known to occur and this can be measured using an ion implanted marker and RBS. Using the disorder layer thickness and the thickness of the layer of material removed, the heat of fusion for graphite can be estimated as $H_f \simeq 125$kJ/mole.

Transient optical and electrical measurements on graphite during pulsed laser heating were attempted. However, the material evolved from the surface of graphite during pulsed laser heating changes the optical properties of the space above the surface so that optical probing of the graphite surface during pulsed laser heating is not possible. The transient optical measurements were repeated on evaporated carbon films hoping that the films would melt at a lower temperature than graphite to eliminate the problems caused by vaporization. Unfortunately, the results of these measurements indicate that the films undergo a rapid pregraphitization which cannot be separated from a melting transition. Transient electrical measurements on graphite fibers were attempted, but the photoconductance of disordered carbon dominates the measurement of the electrical resistivity of the fiber during pulsed laser heating.

Studies of the segregation and solute trapping of impurities in graphite were made for ^{73}Ge and ^{75}As implanted into graphite. The results of these

studies show that the diffusivity of liquid carbon must be on the order of $\sim 2.5 \times 10^{-4} \mathrm{cm}^2/\mathrm{sec}$. The segregation coefficient for Ge and As is also estimated to be $k \simeq 0.17$ using the Aziz[54] continuous growth model.

Laser induced shocks are discussed in the following section and estimates for the pressure generated by evolved material are made. The changes in the optical properties above the surface of laser heated graphite may be understood from the formation of an electron–ion plasma. Using the model for the shock pressure of Gregg and Thomas[66], the pressure applied to a graphite surface by the emitted vapor species is $\sim$ 200bar during pulsed laser heating on the nanosecond time scale. Pulsed laser heating on the picosecond time scale has a higher pressure (10^4bar). It was noted that the liquid phase transition proposed by Ferraz and March[69] was not observed during transient optical measurements on the picosecond time scale, suggesting that there is only a single liquid phase.

The final two sections of the chapter described pulsed current heating of graphite fibers and the post heating analysis of picosecond pulse laser–melted graphite. These techniques were used to try to overcome the difficulties encountered during transient measurements with nanosecond pulsed laser heating. Current pulse heating of graphite fibers has several advantages over previous current pulse heating studies of carbon because of the crystalline order associated with graphite fibers. The electrical resistivity of liquid carbon using pulsed current heating was determined to be $\sim 30 \mu\Omega$–cm, suggesting that liquid carbon is a liquid metal. The electrical resistivity of liquid carbon is also shown to be nearly temperature independent.

Current pulse heating was also used to determine the temperature dependence of the electrical resistivity of graphite fiber at high temperature. Graphite fibers with T_{HT}'s greater than 2300°C are shown to have a metallic behavior in

their electrical resistivity. The temperature dependence of the electrical resistivity of graphite fibers with T_{HT}'s below 1700°C is characteristic of an activated conduction process. These measurements suggest that the high temperature properties of graphite can be approximated by extrapolating the properties of graphite at lower temperatures, where measurements are available, into the high temperature regime, where there are no reported measurements.

Picosecond pulse laser heating was attempted to try to optically probe the surface of liquid carbon before vaporization can alter the optical properties of the space above the surface. Transient reflectivity measurements are shown to be difficult on the picosecond time scale because of the conflicting results obtained with different laser pulse power densities. A post–heating analysis of the disordered material remaining after pulsed laser heating shows that the liquid created by picosecond pulse laser heating is the same liquid created by laser heating on the nanosecond time scale.

While many of our measurements do not yield information about high temperature graphite and liquid carbon directly, the information obtained from these measurements is important. Measurements on pulsed laser heated graphite on the nanosecond time scale provide information on the amount of liquid and vapor created during pulsed laser heating. By knowing the total amount of liquid and vapor created, model calculations can be used to determine if a particular liquid model is appropriate for liquid carbon. The fact that the liquids created by laser heating on both the nanosecond and picosecond time scales are the same suggests that there may only be a single liquid phase of carbon.

References

[1] E. Rimini in *Surface Modification by Laser, Ion, and Electron Beams* J.M. Poate, G. Foti, and D.C. Jacobson, eds., Plenum, 1983 p15.

[2] E.J. Yoffa, *Phys. Rev. B* 21, 2415 (1980).

[3] M. Birnbaum and T.L. Stocker, *J. Appl. Phys.* 39, 6032 (1968).

[4] J.A. Van Vechtan in *Laser and Electron Beam Processing of Materials*, edited by C.W. White and P.S. Peercy (Academic Press, New York, 1980) p. 53.

[5] J.A. VanVechtan and M. Watelet, *Phys. Rev. B* 23, 5443 (1981).

[6] D. von de Linde, *Laser–Solid Interactions and Transient Thermal Processing; Proceedings of the Materials Research Society* edited by J. Narayan, W.L. Brown, R.A. Lemons, (North–Holland,New York,1984)

[7] A. Lietoils and J. Gibbons in *Laser and Electron Beam–Solid Interactions and Material Processing*, J.F. Gibbons, L. Hess, and T. Sigmon, eds., 1981, p23.

[8] J. Krausse, *Solid State Electron.* 17, 427 (1974).

[9] A.R. Beattie and P.T. Landesberg, *Proc. R. Soc. London Ser. A* 249, 16 (1959).

[10] A. Haug, *Solid State Electron.* 21, 1281 (1978).

[11] M. Combescot, *Phys. Lett.* 85A, 308 (1981).

[12] E.J. Yoffa, *Appl. Phys. Lett.* 36, 37 (1980).

[13] G.J. Galvin, M.O. Thompson, J.W. Mayer, P.S. Peercy, R.B. Hammond, and N. Paulter, *Phys. Rev. B* 27, 1079 (1983).

[14] I.B. Khaibullin, E.I. Shtrykov, M.M. Zaripov, R.M. Bagizitov, and M.F. Galjauntdinov, *Radiation Effects* 36, 225 (1978).

[15] C.W. White, P.P. Pronko, S.R. Wilson, B.R. Appleton, J. Narayan, and R.T. Young, *J. Appl. Phys.* 50, 3261 (1979).

[16] R.T. Young, C.W. White, G.J. Clark, J. Narayan, W.H. Christie, M. Murakami, P.W. King, and S.D. Kramwer, *Appl. Phys. Lett.* 32, 139 (1979).

[17] J.M. Ziman, *Phil. Mag.* 6, 1013 (1961).

[18] J.Y. Tsao, S.T. Picraux, P.S. Peercy, and M.O. Thompson, *Beam-Solid Interactions and Phase Transformations: Proceedings of the Materials Research Society*, edited by H. Kurz, G.L. Olsen, and J.M. Poate (Materials Research Society, Pittsburgh, 1986) p. 283.

[19] W.K. Chu, J.W. Mayer, and M.A. Nicolet, *Backscattering Spectrometry*, (Academic : New York, 1978).

[20] L.C. Feldman, J.W. Mayer, and S.T. Picraux, "Materials Analysis by Ion Channeling", (Academic, New York, 1982).

[21] T. Venkatesan, D.C. Jacobson, J.M. Gibson, B.S. Elman, G.Braunstein, M.S. Dresselhaus, and G. Dresselhaus, *Phys. Rev. Lett.* 53 360, (1984).

[22] J.S. Speck, J. Steinbeck, G. Braunstein, M.S. Dresselhaus, and T. Venkatesan, *Energy Beam-Solid Interactions and Phase Transformations, Symposium Proceedings of the Materials Research Society* H. Kurz, G.L. Olsen, and J.M. Poate eds., (MRS: Pitssburgh, 1985) p263.

[23] A.G. Cullis, *Energy Beam-Solid Interactions and Transient Thermal Processing, Symposium Proceedings of the Materials Research Society* D.K. Biegelsen, G.A. Rozgonyi, and C.V. Shank eds., (MRS: Pitssburgh, 1984) p15.

[24] A. Compaan, M.C. Lee, H.W. Lo, G.J. Trott, and A. Aydinli, *J. Appl. Phys.* 54, 5950 (1983).

[25] B.C. Larson, C.W. White, T.S. Noggle, J.F. Barhorst, and D. Mills, *Appl. Phys. Lett.* 42, 282 (1983).

[26] J.A. Van Vechtan and M Watelet, *Phys. Rev. B* 23, 5443 (1981).

[27] A. Pospiesczcyk, M.A. Harith, and B. Stritzker, *J. Appl. Phys.* 54, 3176 (1983).

[28] A. Kasuya and Y. Nishina, *Phys. Rev. Lett.* 57, 755 (1986).

[29] A. Kasuya and Y. Nishina, *Phys. Rev. B* 28, 6571 (1983).

[30] C.D. David, *App. Phys. Lett.*, 11 394, (1967).

[31] C. David, P.V. Avizonis, H. Weichel, C. Bruce, and K.D. Pyatt, *J. Quan. Elect.*, QE-2 493, (1966).

[32] C.W. Bruce, J. Deacon, and D.F. Vonderhaar, *Appl. Phys. Lett.* 9, 164 (1966).

[33] J.M. Liu , R. Yen, H. Kurz, and N. Bloembergen, *Appl. Phys. Lett.* 39, 755 (1981).

[34] J.M. Liu, A.M. Malvezzi, and N. Bloembergen, *Beam-Solid Interactions and Phase Transformations* Proceedings of the Materials Research Society 51, edited by H. Kurz, G.L. Olsen, and J.M. Poate, (Materials Research Society, Pittsburgh, 1986) p255.

[35] T. Venkatesan, B.S. Elman, G. Braunstein, M.S. Dresselhaus, and G. Dresselhaus, *Ion Implantation and Ion Beam Processing of Materials, Symposium Proceedings of the Materials Research Society* G.K. Hubler, O.W. Holland, C.R. Clayton and C.W. White eds., (North–Holland: New York, 1983) p567.

[36] F.P. Bundy, *J. Chem. Phys.* 38, 618 (1963).

[37] W.N. Reynolds, "Physical Properties of Graphite", (Elsevier, New York, 1968).

[38] F. Tuinstra and J.L. Koenig, *J. Chem. Phys.*, 53 1126, (1970).

[39] B.S. Elman, G. Braunstein, M.S. Dresselhaus, G. Dresselhaus, T. Venkatesan, and J.M. Gibson, *Phys. Rev.* B 29, 4703 (1984).

[40] R. Kelly ,J.J. Cuomo, P.A. Leary, J.E. Rothenberg, B.E. Braren, and C.F. Aliotta, *Nuc. Instr. and Meth. in Phys. Res.* B9, 329, (1985).

[41] J.E. Rothenberg and R. Kelly, *Nuc. Instr. and Meth. in Phys. Res.* B1, 291, (1984).

[42] R. Kelly and J.E. Rothenberg, *Nuc. Instr. and Meth. in Phys. Res.* B7/8, 755, (1985).

[43] R.W. Dreyfus, R.E. Walkup, R. Kelly, and R. Srinivasan, (to be published) (1987).

[44] T. Venkatesan, B.S. Elman, G. Braunstein, M.S. Dresselhaus, G. Dresselhaus, *J. Appl. Phys.* 56, 3232 (1984).

[45] I.S. Mclintock and J.C. Orr, *Chemistry and Physics of Carbon* 11, edited by P.L. Walker and P.A. Thrower, (Marcel Dekker, New York, 1973), p.243.

[46] J.W. Cahn, S.R. Coriell, and W.J. Boettinger in *Laser–Solid Interactions and Laser Processing–1978* edited by S.D. Ferris, H.J. Leamy, and J.M. Poate (American Institute of Physics, New York, 1979), p89.

[47] C.W. White, S.R. Wilson, B.R. Appleton, and F.W. Young Jr., *J. Appl. Phys.* 51, 738 (1980).

[48] C.W. White, B.R. Appleton, B. Stritzker, D.M. Zehner, S.R. Wilson, in *Laser and Electron–Beam Solid Interactions and Materials Processing* edited by J.F. Gibbons, L.D. Hess, and T.W. Sigman, (North–Holland, Amsterdam, 1981), p59.

[49] P. Baeri, J.M. Poate, U. Campisano, G. Foti, E. Rimini, and A.G. Cullis, *Appl. Phys. Lett.* 37, 912 (1980).

[50] P. Baeri, G. Foti, J.M. Poate, S.U. Campisano, and A.G. Cullis, *Appl. Phys. Lett.* 38, 800 (1981).

[51] R.F. Wood, *Phys. Rev. B* 25, 2786 (1982).

[52] J.W. Cahn, S.R. Coriell, and W.J. Boettinger in *Laser and Electron Beam Processing of Materials*, edited by C.W. White and P.S. Peercy (Academic, New York, 1980), pp.89-103.

[53] K.A. Jackson, G.H. Gilmer, and H.J. Leamy in *Laser and Electron Beam Processing of Materials*, edited by C.W. White and P.S. Peercy (Academic, New York, 1980), pp.104-110.

[54] M.J. Aziz, *J. Appl. Phys.* 53, 1158 (1982).

[55] M.J. Aziz, *Appl. Phys. Lett.* 43, 552 (1983).

[56] M.J. Aziz, J.Y. Tsao, M.O. Thompson, P.S. Peercy, and C.W. White, in *Energy Beam–Solid Interactions and Transient Thermal Processing/1984* edited by D.K. Biegelsen, G.A. Rozgonyi, and C.V. Shank (Materials Research Society, Pittsburgh, Pa., 1985) p.153.

[57] M.J. Aziz, J.Y. Tsao, M.O. Thompson, P.S. Peercy, and C.W. White, *Phys. Rev. Lett.* 56, 2489 (1986).

[58] C. David, P.V. Avionis, H. Weichel, C. Bruce, and K.C. Pyatt, *IEEE Jour. Quan. Elect.* QE-2, 480 (1966).

[59] D.C. Emmony and J. Irving, 8^{th} *International Conference on Phenomena in Ionized Gases*, Vienna, Austria 27 Aug to 2 Sep 1967, (Vienna, Austria : Springer–Verlag, Vienna 1967) p58.

[60] N.G. Basov, O.N. Krokhin, and G.V. Sklizkov,*J.E.P.T. Lett.* 6, 168 (1967).

[61] T. Venkatesan, J. Steinbeck, G. Braunstein, M.S. Dresselhaus, G. Dresselhaus, D.C. Jacobson, and B.S. Elman, *Beam-Solid Interactions and Phase Transformations*, edited by H. Kurz, G.L. Olsen, J.M. Poate, Mat. Res. Soc. Symp. Proc. (1986).

[62] D.C. Emmony and J. Irving, 9^{th} *International Conference on Phenomena in Ionized Gases*, Bucharest, Rumania 1–6 Sep 1969, (Bucharest, Rumania: Ed. Aka. Rep. Soc. Rumania 1969) p334.

[63] G.I. Taylor, *Proc. Roy. Soc. A* 201, 159 (1950).

[64] L.I. Sedov, Similarity and Dimensional Methods in Mechanics, (New York, Academic Press) p.213.

[65] F. Neuman, *Appl. Phys. Lett.* 4, 167 (1967).

[66] D.W. Gregg and J. Thomas, *J. Appl. Phys.* 37, 2787 (1966).

[67] J. Steinbeck, M.S. Dresselhaus, T. Venkatesan, D. Dijkkamp, X. Wu, *Appl. Phys. Lett.*, (1987) (to be published).

[68] D.M. Roessler, D.S.Y. Wang, and M. Kerker, *Appl. Opt.* 22, 3648 (1983).

[69] A. Ferraz and N.H. March, *Phys. Chem. Liq.* 8, 289 (1979).

[70] J. Heremans, C.L. Olk. G. Eesley, J. Steinbeck, and G. Dresselhaus, *Phys. Rev. Lett.* , (1987) (to be published).

[71] A.M. Malvezzi, N. Bloembergen, and C.Y. Huang, *Phys. Rev. Lett.*. 57 146, (1986).

[72] A.C. Mitchell, J.W. Shaner, and R.N. Keeler, *Physica* 140B, 386 (1986).

[73] J.W. Shaner, J.M. Brown, C.A. Swenson, and R.G. McQueen, *J. de Physique* C8, 235 (1984).

[74] G.G. Tibbetts, *Appl. Phys. Lett.* 42, 666 (1983).

[75] J. Heremans, *Carbon* 23, 431 (1985).

[76] J. Abrahamson, *Carbon* 12, 111 (1974).

[77] P. Gustafson, *Carbon* 24, 169 (1986).

[78] J. Steinbeck, G. Braunstein, M.S. Dresselhaus, T. Venkatesan, D.C. Jacobson, *Energy Beam Solid Interactions and Transient Thermal Processing: Proceedings of the Materials Research Society* (Materials Research Society, Pittsburgh) 1984.

[79] A.M. Malvezzi, G. Reverberi, N. Bloembergen, and C.Y. Huang, *Bulletin of the American Physical Society: Program of the March Meeting of the American Physical Society 16–20 March, New York, New York* 1987,p.608.

[80] E.A. Chauchard, C.H. Lee, and C.Y. Huang, *Appl. Phys. Lett.* 50, 812 (1987).

[81] B.T. Kelly, "Physics of Graphite", (Applied Science Pub., London) (1980).

Chapter 4

Liquid Metals

4.1 Introduction

To answer questions about the properties of liquid carbon, our experimental data must be compared to theoretical predictions for the properties of liquid carbon. The experimental results presented in chapter 3 provide strong evidence that liquid carbon is a liquid metal. It is therefore appropriate to apply liquid metal theory to carbon to make a theoretical determination of the thermal, electrical, and optical properties of the liquid. The calculated properties can then be compared with our experimental results.

Liquid metals have been extensively studied for many reasons ranging from their use as coolant for atomic reactors to understanding the semiconductor–metal phase change that occurs for materials such as silicon. Present day liquid metal theory predicts the transport properties of known liquid metals with accuracy to about 20 percent. The largest errors in the theory come for high valence elements whose liquid state may consist of complex units such as the helix structures in liquid Se and Te. The predictions of liquid metal theory for the group IV elements are also in some disagreement with experimental results. The disagreement is also thought to arise from the presence of some small amount of bonding between atoms in the liquid.

The theory describing liquid metals has advanced from its early stages of treating the liquid simply as a free electron gas. Ziman[1] was the first to apply pseudopotentials to adequately describe the transport properties of monovalent liquid metals in 1961 using a structure factor and a pseudopotential describing a single ion in the liquid state. The polyvalent metals were then described using the same general theory by Bradley *et. al.*[2]. As the theory of liquid metals developed, models for the liquid structure factor developed by Percus and Yevick[3,4] and model potentials by Heine *et. al.*[5,6,7,8] were employed in the calculation of the transport properties of liquid metals. The models for the structure factor and ion potentials took into account the effects of dielectric screening, ion correlations and the Coulomb nature of the potential about an ion in the liquid. The potentials calculated for 25 elements were then tested using the Ziman theory and good agreement with experiment was found between experiment and theory by Sundstrom[9] and by Ashcroft and Lekner[10].

In this chapter the general properties of liquid metals will be discussed. The Ziman theory will be reviewed and it will be applied to calculate the transport properties of liquid carbon. The structure factor for liquid carbon will be calculated using the Percus–Yevick model and the pseudopotential will be calculated using the Heine–Abarenkov method. The chapter closes with our calculations of the electrical resistivity of liquid carbon based on these theories and a discussion of the temperature dependence of the electrical resistivity. By using the information needed to calculate the electrical resisitivty, the specific heat, C_p, the thermal conductivity, K, and the optical constants, n and k, will be calculated for liquid carbon. A discussion of other attempts to apply liquid metal theory to liquid carbon by Stevenson and Ashcroft[11] is included in this final section.

4.2 Properties of Liquid Metals

Liquid metals are essentially comprised of ion cores sitting in a sea of free electrons. The number density of the free electrons, n_e, is given simply by

$$n_e = n\frac{N}{V} \tag{4.1}$$

where n is the valency of the metal, and N/V is the atomic number density of the liquid. This simple result has been verified by Hall measurements and by the measurement of the optical properties[2,12,13] in many liquid metals. By using optical measurements, a predicted d.c. conductivity, $\sigma_{opt.}$, and the relaxation time, τ, may be calculated from the Drude theory. When these numbers are compared to the measured d.c. conductivity, $\sigma_{d.c.}$, the ratio $\sigma_{opt.}/\sigma_{d.c.}$ is found to be very close to unity so that the nearly free electron description of polyvalent liquid metals is quite good.

Using the τ calculated from the optical data, and the conductivity of the nearly free electron model, σ_{NFE}, given by

$$\sigma_{NFE} = \frac{4e^2}{3h^2}\tau k^2 \frac{\partial E}{\partial k} \tag{4.2}$$

the $E(k)$ relation may be checked to see if it is close to

$$E = \hbar^2 k^2/2m \tag{4.3}$$

for a spherical Fermi surface. From the data of Hodgson[14] and Schulz[15], it is seen that

$$k^2\frac{\partial E}{\partial k} \propto k^3 \tag{4.4}$$

to within experimental error. The dispersion relation is then given by

$$E(k) = \frac{\hbar^2 k^2}{2m} \tag{4.5}$$

Element	Valence	$\rho_l(\mu\Omega$–cm)	$\rho_s(\mu\Omega$–cm)
Li	1	25	15
Na	1	9.6	6.6
K	1	13.0	8.3
Rb	1	22.0	13.8
Mg	2	27.4	4.5
Cd	2	33.7	6.83
Hg	2	91	
Al	3	24.2	2.7
Ga	3	25.8	17.4
In	3	33.1	8.4
Si	4	86	2.3×10^11
Ge	4	80	4.7×10^7
Sn	4	48	11
Pb	4	95	20.6
Bi	5	128	107

Table 4.1: The electrical resistivities of liquid metals of several different valence states. The last column contains representative values for the electrical resistivity of the solid state for comparison.

to a good approximation, so that the Fermi surface in the liquid metals is nearly spherical. This means that to a good approximation the Fermi energy is given simply by

$$E_f = \frac{\hbar^2 k_f^2}{2m}. \tag{4.6}$$

The electrical resistivity for the liquid metals may be given by the simple formula

$$\rho_l = \frac{m v_f}{n_e e^2 \Lambda} \tag{4.7}$$

where the electron mean free path, Λ, is the only quantity which must now be calculated by theory.

The experimentally measured electrical resistivities of liquid metals for several valence states is given in table 4.1. From the values of the electrical resistivity given in table 4.1 it is clear that the electrical resistivities of liquid metals

are generally greater than the electrical resistivity of the solid state. In fact, of all of the elements listed in table 4.1, only Si and Ge have substantial decreases in their electrical resistivity when they melt. All of the other elements listed in table 4.1 have increases in their electrical resistivity by as much as an order in magnitude (Al). The decrease in the electrical resistivity for Si and Ge may be directly attributed to the large increases in the carrier density when Si and Ge melt.

4.3 Liquid Metal Theory

4.3.1 Basic Formalism

The theoretical treatment of liquid metals starts with the treatment given by Ziman[1]. In his theory, Ziman treats liquid metals as a gas of ions and free electrons whose electrical conductivity may be given by the familiar Drude formula

$$\rho_l = \frac{m^* v_f}{ne^2\Lambda} \tag{4.8}$$

where m^* is the effective mass of the free electrons, n is the number density of free electrons, v_f is the Fermi velocity, and Λ is the carrier mean free path. For Λ we have

$$\frac{1}{\Lambda} = \frac{N_i}{V} 2\pi \int_0^{2\pi} (1 - \cos\theta) T(\theta) \sin\theta d\theta \tag{4.9}$$

where $T(\theta)$ is the differential scattering cross–section between the ions and the electrons.

The differential scattering cross–section may be calculated in the Born approximation as if it were due to a pseudo–potential $U(\vec{r} - \vec{R})$ for each ion at $\vec{R}$. The differential scattering cross–section is then given by[16]

$$U_K = \int U(\vec{r}) \exp(i\vec{k} \cdot \vec{r}) d^3r \tag{4.10}$$

$$T(\theta) = |U_K|^2 \tag{4.11}$$

where K is now the scattering vector $K = 2k_f \sin(\theta/2)$ ranging from 0 to the diameter of the Fermi sphere, $2k_f$. By using Eq. 4.11 in Eq. 4.9 we find the electron mean free path in the gas model is

$$\Lambda_{gas} = \frac{2\sqrt{2}}{3\pi E_f^{1/2}} E_f^2 \frac{1}{|U^2|} \tag{4.12}$$

where the term $|U|^2$ is given by

$$|U|^2 = \frac{1}{4k_f^4} \int_0^{2k_f} |U_K|^2 K^3 dK. \tag{4.13}$$

If the pseudopotential $U(\vec{r} - \vec{R})$ were known, then all of these equations could be easily solved, yielding an electrical resistivity for all liquid metals. When this basic formalism was applied to the liquid state of the alkali metals and several transition metals by Ziman[1], the theoretical mean free path fell far short of the experimental values for all of the alkali metals.

4.3.2 Correlations in the Liquid

The reason the basic formalism does not produce good results for the alkali metals is that it neglects two important differences between a gas and a liquid. The first of these is the effect of correlations between the atoms in the liquid. The liquid state, although highly disordered, is not a truly random arrangement of atoms as is implied by the use of a nearly free electron gas model. There is a maximum packing of atoms which can take place due to the finite size of the atoms. This means that the positions of the atoms will not be independent, but will depend on the positions of all of the atoms in the liquid in a complicated way.

We can account for the effect of correlations in the calculation by writing the pseudo–potential as

$$U(\vec{r}) = \sum_i U(\vec{r} - \vec{R}_i) \tag{4.14}$$

and now calculate the differential scattering cross–section as before

$$U_{k,k'} = \frac{1}{V}\sum_i \int \exp\left[i(\vec{k'}-\vec{k})\cdot\vec{r}\right] U(\vec{r}-\vec{R_i})d\vec{r} \quad (4.15)$$

$$= \frac{1}{V}\sum_i \exp(i\vec{K}\cdot\vec{R_i}) \int \exp\left[i\vec{K}\cdot(\vec{r}-\vec{R_i})\right] U(\vec{r}-\vec{R_i})d\vec{r} \quad (4.16)$$

$$= U_K \frac{1}{N}\sum_i \exp(i\vec{K}\cdot\vec{R_i}) \quad (4.17)$$

where U_K is the same as in Eq. 4.11 and $\vec{K} = \vec{k'} - \vec{k}$.

This sum is generally an irregular function of the scattering vector, $\vec{K}$ of random phase. However, we are interested in the mean value of the square modulus of the matrix element, which can be expressed in terms of a radial distribution function of the atoms in the liquid. From x–ray diffraction theory we know that we can write[17]

$$a(K) = \left|\frac{1}{N}\sum_i \exp(i\vec{K}\cdot\vec{R_i})\right|^2 \quad (4.18)$$

$$= 1 + \frac{N}{V}\int_0^\infty [P(R)-1]\frac{\sin(KR)}{KR} 4\pi R^2 dR \quad (4.19)$$

where $P(R)$ is the pair correlation function.

The pair correlation function for liquids can be calculated using the theory of Percus and Yevick[3,4]. The integral equation for $P(R)$ given by Percus and Yevick for the case of a liquid consisting of hard spheres has been solved numerically by Wertheim[18] and by Thiele[19]. Using the methods of Wertheim or Thiele allows the liquid structure factor, $a(K)$, to be calculated directly. From Ashcroft and Lekner[10] the liquid structure factor may be written as

$$a(K\sigma) = \frac{1}{1+nc(K\sigma)} \quad (4.20)$$

where n is the atomic number density, and $c(K\sigma)$ is given by

$$c(K\sigma) = 4\pi\sigma^3 \int_0^1 ds s^2 \frac{\sin(sK\sigma)}{sK\sigma}(\alpha + \beta s + \gamma s^3) \quad (4.21)$$

where σ is the hard sphere diameter. The α, β, and γ are constants which are functions of σ, but are simplified by writing them in terms of the liquid packing fraction η. This set of constants are given by

$$\begin{aligned} \eta &= \frac{\pi}{6} n\sigma^3 \\ \alpha &= \frac{(1+2\eta)^2}{(1-\eta)^4} \qquad (4.22) \\ \beta &= -6\eta \frac{(1+\eta/2)^2}{(1-\eta)^4} \end{aligned}$$

$$\gamma = \frac{1}{2}\eta\alpha. \qquad (4.23)$$

The integral in Eq. 4.21 can be easily integrated to yield the structure factor for any liquid so long as the packing fraction, η, or the hard sphere diameter, σ, of the liquid is known.

The accuracy with which this theory predicts the structure factor for liquids is illustrated in Fig. 4.1 where the liquid structure factor times the hard sphere diameter, σ, for cesium, measured using neutron diffraction by Gingrich and Heaton[20], is compared to the theoretical predictions of the Percus–Yevick theory. As can be seen in Fig. 4.1 the theoretical prediction is in good agreement with the experimentally measured liquid structure factor. The agreement is particularly good for $0 \leq K\sigma \leq 7$ where the calculation of the electrical resistivity would be carried out using Ziman's integral. The disagreement which occurs for larger $K\sigma$ is due mainly to the ion–ion core interactions which are not well described by the hard sphere model[10].

The structure factor, $a(K)$, has several important features. The structure factor for a gas model would simply be $a(K) = 1$ since the atoms would be randomly arranged. The behavior of the structure factor at large $\vec{K}$ for liquids has the behavior $a(K) \rightarrow 1$ as would be expected. At small $\vec{K}$ however, the structure factor is small, meaning that the density of the atoms far from an

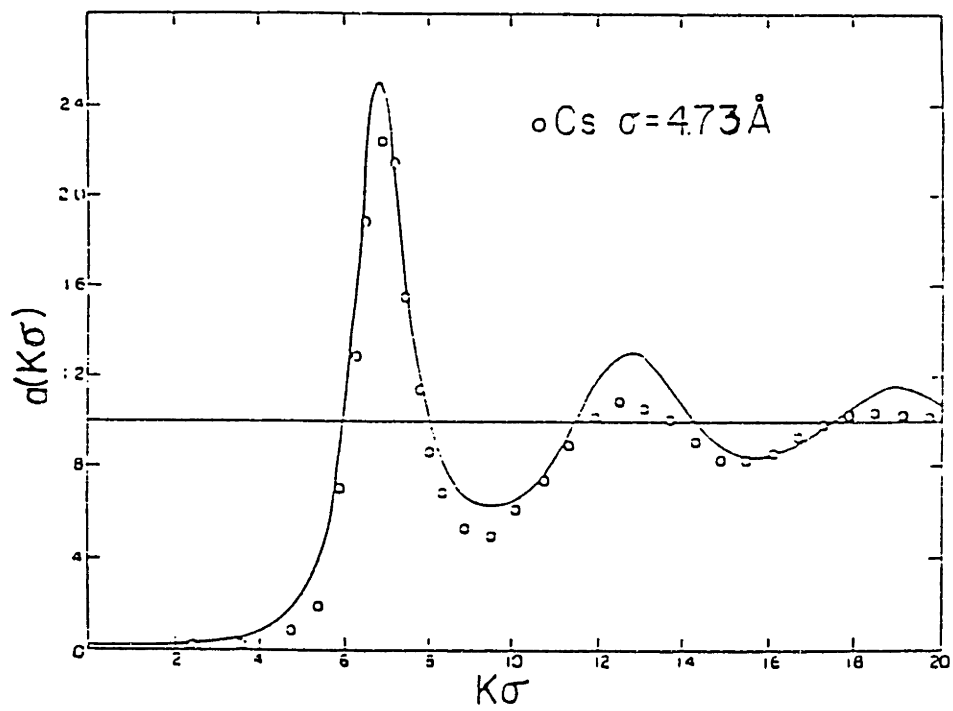

Figure 4.1: A comparison of the liquid structure factor from experiment (circles) as measured by neutron diffraction[20] and the theoretical prediction using the theory of Percus and Yevick (solid line) for a hard sphere model with $\sigma = 4.73$Å, $\eta = 0.45$. The calculation was carried out by Ashcroft and Lekner[10].

atom becomes nearly constant, so that the Fourier components of long wavelength become small. The limiting value of $a(K = 0)$ may be given by a simple classical analysis using the equipartition theorem. The limiting value is then[21]

$$a(0) = k_B T N \beta_C / V \tag{4.24}$$

where k_B is the Boltzmann constant and β_C is the compressibility of the liquid at temperature T.

The short range order in the liquid, which may be inferred from the small structure factor, means that electron scattering will not be important at small $\vec{K}$ where the ion core potentials will be large. The electron mean free path therefore increases since only scattering near $2k_f$ will be important.

The primary peak in the liquid structure factor lies close to the wave vector corresponding to the mean interatomic spacing of the atoms in the liquid. The position of the peak is important since most or all of the electron scattering will occur at wavenumbers close to the peak. The relation of the primary peak in the structure factor to the diameter of the Fermi sphere is most influenced by the valence state, n, of the atoms in the liquid as shown in Fig. 4.2. For valences of two or higher the primary peak is entirely contained within the Fermi sphere diameter as shown in the Fig. 4.2. The structure factor for the alkali metals, however, has the primary peak fall at the diameter of the Fermi sphere ($2k_f$). This makes the calculated electrical resisitivity for the alkali metals particularly sensitive to the *exact* shape of the structure factor near the Fermi surface since the major contribution to the electrical resistivity comes from the scattering near the Fermi surface.

The position of the peak relative to the Fermi surface is also important when considering the temperature dependence of the electrical resistivity of the liquid. The discussion of the temperature dependence is deferred to section 4.5.

The inclusion of the liquid structure in the calculation can be easily included

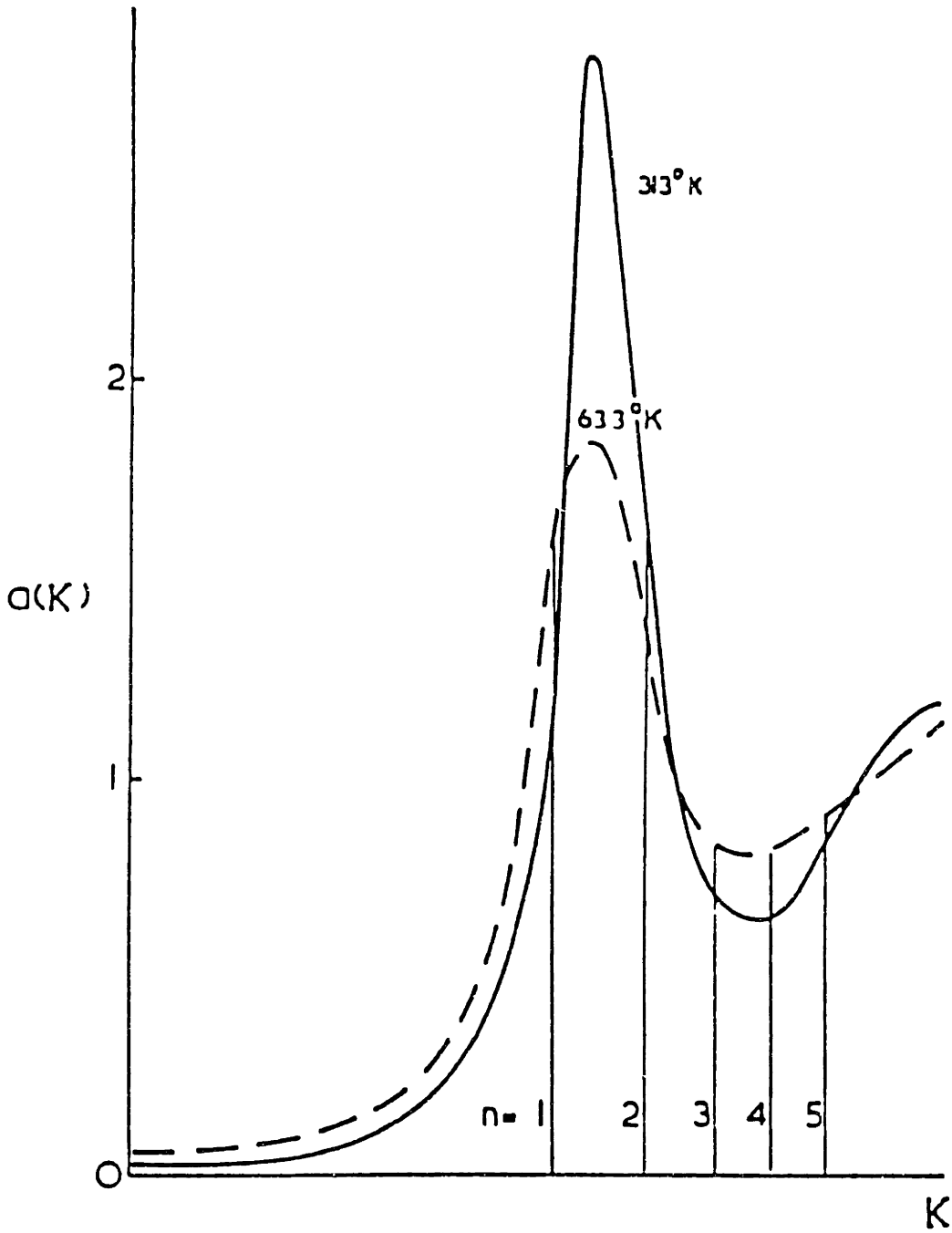

Figure 4.2: The relation of the primary peak in the liquid structure factor to the diameter of the Fermi sphere as a function of the valence state, n, of the atoms in the liquid. Note that for alkali metals the peak is at a wavenumber close to the Fermi sphere diameter. This figure was taken from Bradley *et. al.*[2].

into the previous calculations. The electron mean free path for the liquid metal is now given by

$$\Lambda_{liq} = \frac{2\sqrt{2}}{3\pi E_f^{1/2}} E_f^2 \frac{1}{< a|U|^2 >} \tag{4.25}$$

where

$$< a|U|^2 >= \frac{1}{k_f^4} \int_0^{2k_f} a(K)|U_K|^2 K^3 dK. \tag{4.26}$$

Equations 4.25 and 4.26 are the same as Eqs. 4.12 and 4.13 except for the addition of the $a(K)$ in the integral of Eq. 4.26.

From Eq. 4.25 it is clear that the addition of the liquid structure factor in the calculation improves the basic formalism for the theoretical treatment of liquid metals. The mean free path for liquid metals is increased since the electron scattering becomes confined to a region near the edge of the Fermi sphere. For polyvalent metals, such as carbon, the primary peak lies within the Fermi diameter and most of the electron scattering occurs within the Fermi sphere. The mean free path for polyvalent liquid metals will be smaller than for monovalent metals because of the incresased scattering in the polyvalent metals, assuming that the potential in Eq. 4.25 does not contain a zero near the peak in the structure factor. The good agreement of the theory and experimentally measured liquid structure factors as shown in Fig 4.1 means that the liquid structure factor for carbon calculated from the Percus–Yevick theory will be a reasonable first approximation.

4.3.3 Plasma Scattering

The other major contribution to the electron mean free path which is neglected by the basic formalism is plasma scattering arising from vacancies in the liquid (the reasons for the terminology willbe discussed below). Since vacancies in the liquid possess no charge they are seen by the electrons as having a negative

charge relative to the neighboring ions in the liquid and hence act as repulsive scattering centers.

To account for plasma scattering in the liquid, it is necessary to consider the local density fluctuations in the liquid. The ions and electrons in the liquid are considered to constitute a plasma with an effective potential, W_0, associated with the dilatation[22] of

$$W_0 = \frac{2}{3}E_f \tag{4.27}$$

where this is taken in the long wavelength limit of the matrix element of the potential. In solids the plasma term is the dominant term in determining the electron mean free path, being the major contribution in the Bardeen formula for the electron–phonon interaction. The transition probability for plasma scattering is then

$$|W_0|^2 a(0) = \left(\frac{2}{3}E_f\right)^2 \frac{kTN\beta_C}{V} \tag{4.28}$$

for small scattering angles. For large $\vec{K}$ the precise behavior of W_K is not known. This is in part due to an inability to determine the the screening of the ion cores for short wavelength excitations. However, the function W_K should decrease rapidly with increasing $\vec{K}$. By using the Bardeen formula for the electron–phonon interaction, where the charge for each conduction electron is spread over the volume of a Wigner–Seitz sphere of radius, r_s, we can write

$$W_K \sim \frac{2}{3}E_f G(Kr_s) \tag{4.29}$$

where

$$G(Kr_s) = \frac{3(x\cos x - \sin x)}{x^3}. \tag{4.30}$$

Now by substituting Eq. 4.29 for U_K in Eq. 4.25 we can calculate the electron mean free path due to plasma scattering and find

$$\Lambda_{plasma} = \frac{2\sqrt{2}}{3\pi E_f^{1/2}} \left(\frac{E_f}{\frac{2}{3}E_f}\right)^2 \frac{1}{< aG^2 >} \tag{4.31}$$

where we have again accounted for the liquid structure by using $a(K)$ and $< aG^2 >$ is defined similarly to Eq. 4.26.

The contribution of plasma scattering to the electrical resistivity of liquid metals will depend primarily on the pseudopotential used to describe the ion cores in the liquid. When the plasma contribution is added in the calculation of the electrical resistivity for Na and K, the theoretical result comes into good agreement with the measured electrical resistivity. The contribution made by plasma scattering to the resistivity for the other alkali metals is small due to the magnitude of W_k in these metals near the Fermi surface.

The contribution of plasma scattering in polyvalent metals has been discussed by Bradley *et. al.*[2]. Since the contribution of plasma scattering to the electron mean free path is proportional to $1/r_s$ according to the Bardeen theory, this means that the plasma scattering will also be proportional to $k_f/n^{1/3}$, where n is the valence of the metal. If we assume that $a(K)$ is roughly constant up to this value of $\vec{K}$, then the plasma scattering scales as

$$\beta_C T \frac{E_f^2}{v_f^2 n^{4/3}} \propto \frac{\beta_C T}{V n^{2/3}} \tag{4.32}$$

so that the plasma scattering will decrease as the valence of the atoms in the liquid increases. The contribution of plasma scattering to the electrical resistivity of polyvalent liquid metals was calculated by Bradley *et. al.* and is shown to be a negligible contribution to the electrical resistivity for the polyvalent liquid metals[2]. Therefore, the conribution of plasma scattering to the electrical resistivity of liquid carbon is considered to be negligible.

4.3.4 The Pseudopotential

The final piece of information which is needed to calculate the transport properties of liquid metals is the pseudopotenial U_K in Eq. 4.25. In the initial calculations of Ziman[1] and Bradley *et. al.*[2] the pseudopotential was estimated

from Fermi surface measurements. While this was adequate for developing the theory and comparing the theory to experiment for the monovalent metals, it is inadequate for comparing the theoretical predictions with experiment for the polyvalent metals. The reasons for this are simple. First, in the monovalent metals the electrical resistivity is dominated by the plasma scattering term, so that the pseudopotential of the ion cores in the liquid has little to do with the predicted resisitivity. The contribution to the electrical resistivity by plasma scattering in the polyvalent metals is negligible. Second, the primary peak in the liquid structure factor for the polyvalent metals, such as liquid carbon, is contained within $2k_f$. This means that the magnitude of the pseudopotential for $\vec{K} < 2k_f$ is important for determining the magnitude of Λ, the electron mean free path in liquid carbon.

A model for the pseudopotential for the ion cores in liquid metals has been developed by Heine, Abarenkov, and Animalu[5,6,7,8] where the potential is taken as

$$V(r) = \sum_l A_l P_l \quad r < R_m \tag{4.33}$$

$$V(r) = Z/r \quad r \geq R_m \tag{4.34}$$

where we have taken $e = \hbar = m_e = 1$, the P_l are projection operators on the sub–space Y_{lm}(m = -1 to m = 1), and the A_l are constants calculated from the energy levels of the atoms in the liquid. The subscript l denotes the orbital quantum number. The potential defined by Eqs. 4.33 and 4.34 reflect the locality of the scattering felt by the electron based on its position. Equation 4.33 is the nonlocal part of the potential while the Coulomb contribution to the potential (Eq. 4.34) is the local part.

The nonlocal part of the potential defined in Eqs. 4.33 has been shown to be strongly dependent on the orbital quantum number l while only weakly

dependent on the principal quantum number $\hat{n}$ for levels with the same l. Therefore, it is only necessary to calculate the values A_l for a single n and interpolate the A_l for all other $E_{\hat{n}l}$[5].

The procedure for calculating the A_l is given by Abarenkov and Heine[6] and is sketched below. The A_l are calculated from the Coulomb wave functions for the radial part of the atomic orbitals, $\chi(r)$, given by

$$\chi(r) = P_l(ZR_m) + \gamma(\mathcal{N}, l)Q_l(ZR_m) \tag{4.35}$$

where P_l and Q_l are the Coulomb wave functions which are respectively regular and irregular at the origin. The function $\gamma(\mathcal{N}, l)$ is given by

$$\gamma(\mathcal{N}, l) = \frac{\Gamma(\mathcal{N} - l)\tan(\pi[\mathcal{N} - l - 1])\mathcal{N}^{2l+1}}{\Gamma(\mathcal{N} + l + 1)} \tag{4.36}$$

where N is an energy parameter given by

$$\frac{1}{\mathcal{N}^2} = \frac{2|E|}{Z^2} \tag{4.37}$$

where $2|E|$ is the energy of the atomic level of interest. The constants A_l are then calculated by solving the trancendental equation

$$\frac{Xj_{l-1}(X)}{j_l(X)} = \frac{DP_l(ZR_m) + \gamma(N, l)DQ_l(ZR_m)}{P_l(ZR_m) + \gamma(N, l)Q_l(ZR_m)} \tag{4.38}$$

where

$$X = [2(A_l - |E|)]^{\frac{1}{2}}R_m \tag{4.39}$$

the operator D is

$$D = r\frac{\partial}{\partial r}. \tag{4.40}$$

and the j_m are Bessel functions.

The pseudopotential may then be calculated in the Born approximation

$$V(k) = \int_0^\infty \exp(ikr)V(r)r^2dr \tag{4.41}$$

so that the bare potential of the ion in the liquid is

$$V(k) = G(k) + F(k, k_f, k_f) \tag{4.42}$$

where $G(k)$ is the local part of the potential given by

$$G(k) = -\frac{8\pi A_2}{\Omega k^3}\left[\sin(kR_m) - kR_m\cos(kR_m)\right] - \frac{8\pi Z}{\Omega k^3}\cos(kR_m) \tag{4.43}$$

and $F(k, k_f, k_f)$ is the nonlocal part of the potential given by

$$\begin{aligned} F(k, k_f, k_f) \;=\; & -\frac{4\pi R_m^3(A_0 - A_2)}{\Omega}\left[j_0(k_f R_m)^2 - \frac{1}{k_f R_m}\cos(k_f R_m) j_1(k_f R_m)\right] \\ & - \frac{12\pi R_m^3(A_1 - A_2)}{\Omega} \times \\ & \left(1 - \frac{k^2}{4k_f^2}\right)\left[j_1(k_f R_m)^2 - j_0(k_f R_m) j_2(k_f R_m)\right] \end{aligned} \tag{4.44}$$

where the functions j_n are Bessel functions.

The model pseudopotential given in Eqs. 4.33 and 4.34 is a basis for calculating the transport properties of any liquid metal, including liquid carbon. However, the potential given in Eqs. 4.43 and 4.44 must also account for the screening of the ion potential due to the electron gas which surrounds the ion cores. The screening of the local part of the potential (Eq. 4.43) may be accounted for by dielectric screening. The dielectric function $\epsilon(k)$ is given by[7]

$$\epsilon(k) = 1 + \mathcal{X}(k) m^*(1 + \alpha)\left(1 - \frac{0.5k^2}{k^2 + k_f^2 + k_s^2}\right) \tag{4.45}$$

where the susceptibility $\mathcal{X}$ is

$$\mathcal{X}(k) = \frac{4\pi e^2 Z}{\Omega k^2}\left(\frac{2}{3}E_f\right)^{-1}\left(\frac{1}{2} + \frac{4k_f^2 - k^2}{8kk_f}\log\left|\frac{2k_f - k}{2k_f + k}\right|\right) \tag{4.46}$$

and the screening factor $k_s^2 = \frac{1}{2}(k_{TF})^2$ where k_{TF} is the Thomas–Fermi screening wavevector. The constant α in Eq. 4.45 is used to preserve the normalization of the wave functions.

The screening of the nonlocal part of the potential (Eq. 4.44) has been derived by Animalu[7] and is given by

$$I(k) = \frac{32m^*[1-f(k)]}{\pi\Omega k^2\epsilon(k)}\left[(A_0 - A_2)L_0 + 3(A_1 - A_2)L_1\right]R_m^2 \qquad (4.47)$$

where the L_n are integral terms.

The model potential can now be written in terms of the above equations as

$$V(k) = \frac{G(k)}{\epsilon(k)} + F(k, k_f, k_f) - I(k). \qquad (4.48)$$

The potential produced by this formula are illustrated in Fig. 4.3 for several metals including several group IV elements. The salient feature of these potentials is the oscillatory behavior unlike other potentials such as the screened Thomas–Fermi potential. The zero which occurs at wavevectors near the maximum in the structure factor reduces the contribution of scattering at this point and hence lowers the electrical resistivity of the liquid as calculated using Eq. 4.25.

The electrical resistivities of liquid metals have been calculated by Sundstrom[9] and by Ashcroft and Lekner[10] using the Heine–Abarenkov potentials for 25 elements with a metallic liquid state. A summary of the results of the calculations appears in table 4.2. The agreement between experimental results and the prediction by the liquid metal theory is quite good when the structure factor for the liquid is known. The general trend of the calculations is that the electrical resistivity predicted by theory is somewhat smaller than the measured electrical resistivity. The disagreement is attributed to the uncertainty in the liquid structure factor. When the liquid structure factor is not well known, as in the case of Ge and Si, the predictions of the theory are well below the experimental values. The large disagreement between the theory and the calculations has been attributed to the partial molecular nature of liquid Si and Ge which gives a larger contribution to the structure factor at small k.

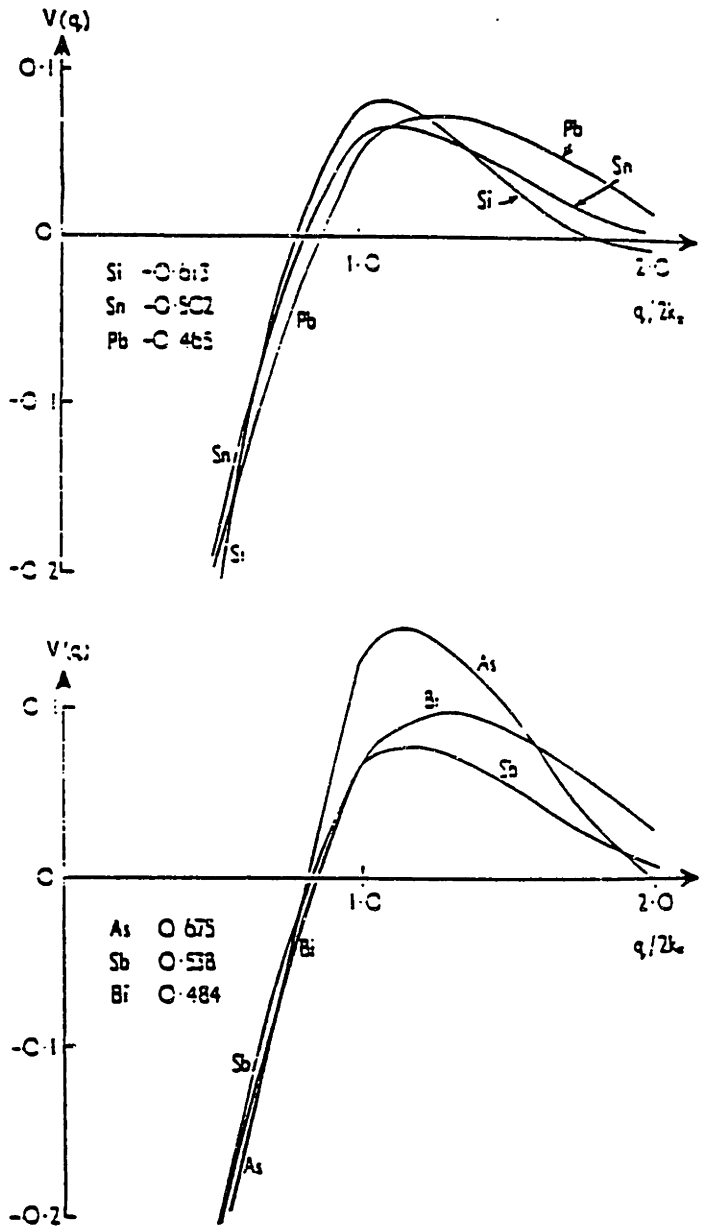

Figure 4.3: The calculated potentials taken from Animalu and Heine[8] for several ions using the Heine and Abarenkov theory. The salient feature of the potential is the zero which occurs near the wavevector where the structure factor becomes a maximum near $2k_f$.

Element	ρ_{exp}	ρ_{calc}
Li	25	15.7
Na	9.6	9.5
K	13.0	16.2
Rb	22.0	27.2
Cs	36.0	36.0
Mg	27.4	25.1
Zn	37.4	18.6
Al	24.2	20.6
Si	86	27
Ge	80	20
Pb	95	73.5

Table 4.2: The experimental electrical resistivity of liquid metals compared to the theoretical prediction using the Heine–Abarenkov model potential. The results were taken from Sundstrom[9] and Ashcroft and Lekner[10]

The Heine–Abarenkov model potential can be calculated for carbon since the energy levels of atomic carbon have been determined. The electrical resistivity of liquid carbon can then be calculated from the Ziman integral (Eq. 4.25) and the structure factor calculated from the Percus–Yevick model.

4.4 Fermi Surface Blurring

The transport properties of liquid metals have been considered to depend entirely upon the liquid structure factor and the potential of the ion cores for scattering occurring for $0 < k < 2k_f$. However, when the mean free path of the electrons in the metals becomes comparable to the interatomic spacing of the ion cores in the liquid, the blurring of the Fermi surface becomes a significant factor in determining the electron mean free path. A simplified treatment of Fermi surface blurring is given by Ferraz and March[23] and will be summarized here.

The Ferraz–March theory is actually an extension to the Ziman theory by considering the Fourier transform of the square modulus of the derivative of the Dirac density matrix, $\bar{\sigma}_D$, evaluated at the Fermi energy, E_f. The Dirac density matrix is incorporated into the calculation of the electron mean free path through the force–force correlation formula for the electrical resistivity by

$$\rho \propto \int dr_1 dr_2 \frac{\partial V(r_1)}{\partial r_1} \frac{\partial V(r_2)}{\partial dr_2} |\bar{\sigma}_D(r_1, r_2, E_f)|^2 \tag{4.49}$$

where r_1 and r_2 are the scattering vectors. The Ziman theory, as presented, uses the free electron approximation for $\bar{\sigma}_D$ so that the Fourier transform of $\bar{\sigma}_D$ results in

$$\begin{aligned} \Gamma_0(k, k_f) = &\ \tfrac{1}{k} \quad \text{for } k < 2k_f \\ = &\ 0 \quad \text{for } k > 2k_f \end{aligned} \tag{4.50}$$

where the cut–off at $2k_f$ comes as a direct result of the undamped oscillatory form of $\sin(k_f R)/k_f R$ with $R = |r_1 - r_2|$ at large R. By using this form of $\bar{\sigma}_D$ we retrieve the Ziman formula for the electrical resistivity, Eq. 4.12.

Ferraz and March use the Bardeen approximation whereby the Dirac density matrix may be taken as

$$\bar{\sigma}_D(r_1, r_2, E_f) = \bar{\sigma}_{D0}(r_1, r_2, E_f) \exp\left(-\frac{R}{2l}\right) \tag{4.51}$$

where l is the electron mean free path. The Fourier transform of this may then be carried out directly with the result

$$\Gamma(k, k_f, l) = \int \exp(ikr) |\bar{\sigma}_{D0}(R)|^2 \exp(-R/l) dR. \tag{4.52}$$

By substitution of $\bar{\sigma}_{D0}$ into Eq. 4.52 and carrying out the integration we have

$$\begin{aligned} \Gamma(k, k_f, l) = &\ \frac{2}{\pi^3 k} \left[\arctan(kl) - \frac{1}{2} \arctan \frac{2kl}{1 + (2k_f)^2 - (kl)^2} \right. \\ &\left. - \frac{\pi}{2} \theta \left(k - \sqrt{\frac{1}{l^2} + (2k_f)^2} \right) \right] \end{aligned} \tag{4.53}$$

where θ is the step function. In the limit $l \rightarrow \infty$, Γ reduces to Γ_0 in Eq. 4.50.

Adding Fermi surface blurring into the calculation of the electron mean free path in liquid metals makes Eq. 4.25 become

$$\frac{1}{\Lambda_{liq}} = \int_0^\infty k^4 a(k) |U_k|^2 \Gamma(k, k_f, l) dk \tag{4.54}$$

where the limits now reflect the fact that the Fermi surface has no cutoff. Of course by taking $l \rightarrow \infty$ Eq. 4.54 reduces back to the original Ziman form in Eq. 4.25.

From Eq. 4.54, only when l is comparable to the mean interatomic spacing given by

$$a = \frac{(3\pi^2)^{\frac{1}{3}}}{k_f n} \tag{4.55}$$

where n is the valence of the atom, will the blurring of the Fermi surface be significant. This is usually the case for the high valence liquid metals in groups III, IV, and V, of the periodic table where the electron mean free path is only a few interatomic distances.

4.5 Temperature Dependence of the Electrical Resistivity

The temperature dependence of the electrical resistivity in liquid metals is entirely due to the temperature dependence of the liquid structure factor, $a(K)$. This is because the pseudo–potential used in the calculation of the electrical resistivity is dependent only on the density of the carriers in the liquid and independent of the arrangement of the atoms in the liquid[1,2].

The dependence of the liquid structure factor on temperature is complicated. However, for many liquid metals[1], the liquid structure factor at low K has a nearly linear dependence on temperature. This behavior is due to the expansion of the liquid with temperature making the liquid more gas like with

$a(K) \rightarrow 1$ for all K. Thus the increase in the structure factor at low K gives a larger contribution to the low K scattering in the resistivity. This means that the electrical resistivity of liquid metals would be expected to be proportional to the temperature.

For the monovalent liquid metals, Na and K, this is indeed what is observed[1]. However, for the other monvalent metals and all of the polyvalent metals the resistivity is seen to either decrease or remain nearly constant as a function of temperature[2]. The temperature dependence of the electrical resistivity for the monovalent liquid metals is attributed to changes in the pseudo–potential with temperature. The expansion of the liquid causes the Fermi level to fall, hence reducing the magnitude of the pseudo–potential near $2k_f$. The reduction in the pseudo–potential counters the increase in the structure factor so that the electrical resistivity of the other monovalent metals is only slightly temperature dependent.

The temperature dependence of the polyvalent metals (or the lack of a temperature dependence) can be explained since the primary peak in the structure factor lies in the range $K < 2k_f$. The increase of the structure factor at lower K is countered by a decrease in the structure factor at the primary peak which leaves little or no change in the integral over $2k_f$. If Fermi surface blurring is accounted for, one notes that the structure factor for $K > 2k_f$ is $a(K) \sim 1$ for the polyvalent metals already, so that there will be no additional contribution to the electrical resistivity from $K > 2k_f$.

The decrease in the electrical resistivity with temperature for the divalent metals is caused by a decrease in the structure factor as a result of thermal expansion. Since the mean free path for the divalent metals is usually more than a few interatomic distances[2], Fermi surface blurring is not important in the calculation of the electrical resistivity of the divalent liquid metals, so

that only the structure in the range $0 < K < 2k_f$ is important. As the liquid expands with temperature some of the intensity of the primary peak is moved toward smaller K and some is moved toward higher K. Since the primary peak in the structure factor lies close to $2k_f$, the decrease of the intensity of the primary peak is faster than the increase of the structure factor at small K causing an overall decrease in the electrical resistivity of the divalent liquid metals.

4.6 The Application of Liquid Metal Theory to Carbon

This section will apply the liquid metal theory discussed in the previous sections to liquid carbon. The goal is to construct a model for the transport properties of liquid carbon for comparison with the experimental results of the previous chapter and for more sophisticated numerical calculations of heat flow and diffusion. The section will start with a discussion of calculations done previously by Stevenson and Ashcroft[11] for high density ($> 25\text{g/cm}^3$) liquid carbon. The liquid structure factor and the model potential will then be calculated using the Percus–Yevick model and the Heine–Abarenkov model potential. Finally, the results of these calculations will be used to construct a model for liquid carbon in the low density ($\sim 2\text{g/cm}^3$) regime.

4.6.1 Previous Calculations

Stevenson and Ashcroft[11] have attempted to calculate the electrical resistivity of liquid carbon in the high density ($> 25\text{g/cm}^3$) regime, assuming that liquid carbon is metallic. In their work, the Ziman theory was applied using a structure factor for liquid carbon calculated from the Percus–Yevick theory, and using a potential similar to the Thomas–Fermi screening potential with ad-

ditional dielectric screening terms due to Hubbard[24]. The electrical resistivity was then calculated using the Born approximation. The results of the calculations by Stevenson and Ashcroft appear in Fig. 4.4. The electrical resistivity of liquid carbon is predicted to increase as the density of the liquid decreases. Note that the electrical resistivity has only a small temperature dependence at high temperature for the lower densities shown in Fig. 4.4. The lack of a temperature dependence in the electrical resistivity is due to the structure factor as discussed in section 4.5.

4.6.2 Properties of Low Density Liquid Carbon

The properties of low density liquid carbon ($\sim 2.0\text{g/cm}^3$) may be calculated using liquid metal theory and using the facts obtained from other experiments on liquid metals since experimental measurements show that liquid carbon is a liquid metal. Most of the information required to apply liquid metal theory to liquid carbon lies in the density of the liquid. This is mainly due to the simple relationship between the carrier density, n_e, and the atomic number density in the liquid given in Eq. 4.1.

Experimental work by Bundy[25] provides information about the density of liquid carbon through the use of the Clausius–Clapeyron relation[26]

$$\frac{dp}{dT} = \frac{L_f}{T_m \Delta V} \tag{4.56}$$

where dp/dT is determined from Bundy's phase diagram, L_f is the latent heat of fusion taken from Bundy's data, T_m is the melting temperature, and ΔV is the change in the molar volume upon melting. By multiplying the top and bottom of the right hand side of Eq. 4.56 by the atomic mass and rearranging terms, the liquid density is given by

$$\frac{1}{\mu_l} = \frac{L_{fm}}{T_m dp/dT} + \frac{1}{\mu_s} \tag{4.57}$$

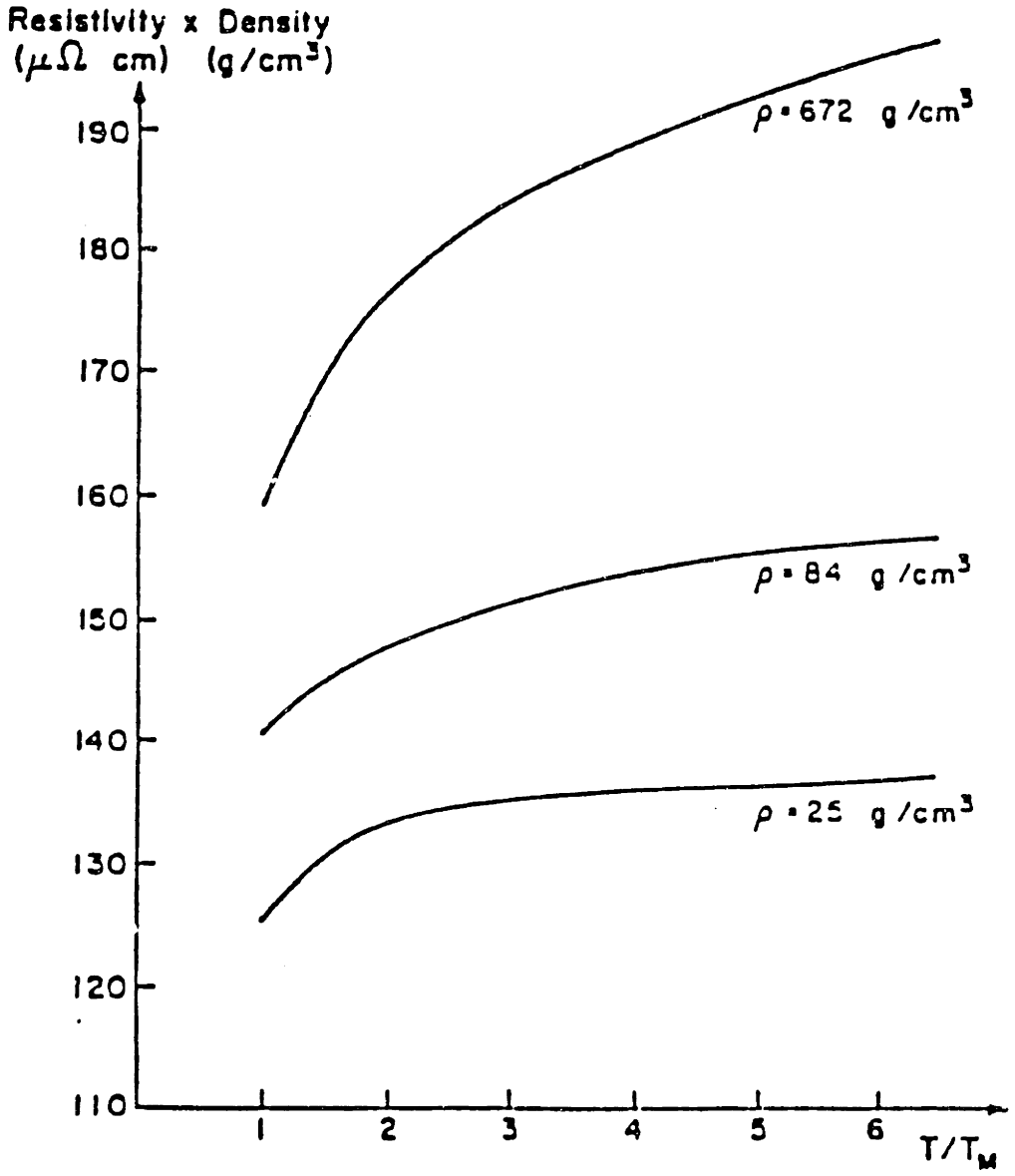

Figure 4.4: The results of calculations by Stevenson and Ashcroft[11] for liquid carbon in the high density regime. The product of the electrical resistivity and the liquid density is plotted versus temperature. Note that the electrical resistivity increases as the density of the liquid decreases.

Property	Formula	value
n_e	$n\frac{N}{V}$	$3.2 \times 10^{23}\text{cm}^{-3}$
k_f	$(3\pi^2 n_e)^{\frac{1}{3}}$	$2.1 \times 10^{8}\text{cm}^{-1}$
v_f	$\hbar k_f/m_e$	$2.45 \times 10^{8}\text{cm/sec}$
E_f	$(\hbar k_f)^2/2m_e$	16.9eV

Table 4.3: The parameters of liquid carbon calculated from a Fermi gas model.

where μ_l and μ_s are the densities of the liquid and solid, respectively, and L_{fm} is the heat of fusion per unit mass. From Bundy's data, we find that $dp/dT \sim 1.4 \times 10^8$dynes/cm^2–K and $L_f \sim 105kJ/mole$. By using Eq. 4.57 and the density of graphite at the melting point of $\mu_s = 1.96\text{g/cm}^3$ from chapter 2, the density of liquid carbon is determined to be $\mu_l \sim 1.6\text{g/cm}^3$.

Using this density, the carrier density for liquid carbon is calculated using Eq. 4.1. Since liquid metals have been shown to have nearly spherical Fermi surfaces, all of the parameters associated with a spherical Fermi surface may be calculated. These parameters are given in table 4.3. The parameters given in table 4.3 can now be used in the formulation of the liquid structure factor and the Heine–Abarenkov model potential for liquid carbon.

One point should be made concerning the electron mass. The parameters in table 4.3 assume that the free electron mass in liquid carbon is the rest mass of an electron. For other polyvalent liquid metals, the free electron mass has been taken as the rest mass of the electron also. The choice of the electron rest mass is made based only on a lack of good experimental data on the mass of the free electrons in polyvalent liquid metals.

4.6.3 The Liquid Structure Factor

By applying the Percus–Yevick theory to liquid carbon, the liquid structure factor for liquid carbon may be calculated as shown in Fig. 4.5. The plots in

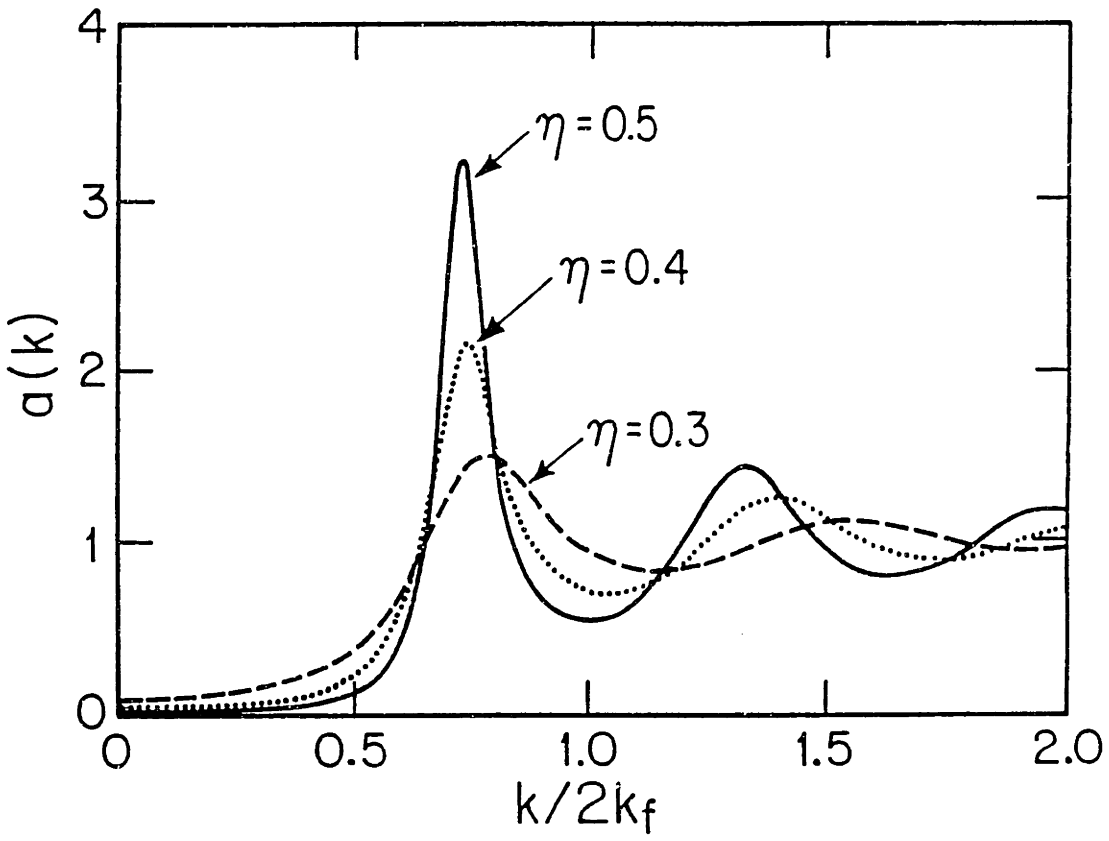

Figure 4.5: The structure factor for liquid carbon using the Percus–Yevick theory for packing fractions $\eta = 0.3, 0.4, 0.5$.

Fig. 4.5 show the structure factor for liquid carbon assuming the packing fraction, $\eta = 0.3, 0.4$, and 0.5. It has been pointed out by Ashcroft and Lekner[10], that the typical packing fraction for liquid metals lies in the range $0.4 < \eta < 0.5$. The trend in the structure factor is that the intensity of the primary peak increases with an increase in the packing fraction. This behavior merely reflects the fact that as more atoms are packed into a constant volume their positions become fixed due to the finite size of the atoms in the liquid.

The structure factor used for the calculation of the transport properties of liquid carbon appears in Fig. 4.6. The liquid structure factor in this case was calculated assuming a packing fraction $\eta = 0.41$. The packing fraction was calculated from the radius $R_m = 2a_0$ (a_0 is the Bohr radius) at which ion–ion repulsion should become important.

As mentioned in section 4.3.2, the compressibility of the liquid may be calculated from the structure factor, $a(K = 0)$, from the formula

$$\beta_C = \frac{a(0)V}{k_B T N}. \tag{4.58}$$

By using the N/V from section 4.6.2 and $a(0)$ from the calculation of the structure factor, the compressibility of liquid carbon at the melting temperature is $\beta_C = 6.4 \times 10^{-12}\text{Pa}^{-1}$.

4.6.4 The Model Potential

The model potential used to calculate the transport properties is the Heine–Abarenkov model potential described in section 4.3.4. Using the parameters for the electron gas from section 4.6.2, the model potential is calculated directly from Eqs. 4.43 and 4.44. The constants A_0, A_1, and A_2 were calculated using the energies of the carbon 3s, 3p, and 3d orbitals and tabulated values for the Coulomb wave functions[27] and the method described by Heine and Abarenkov[7]. The constants are given in table 4.4. The constants for other

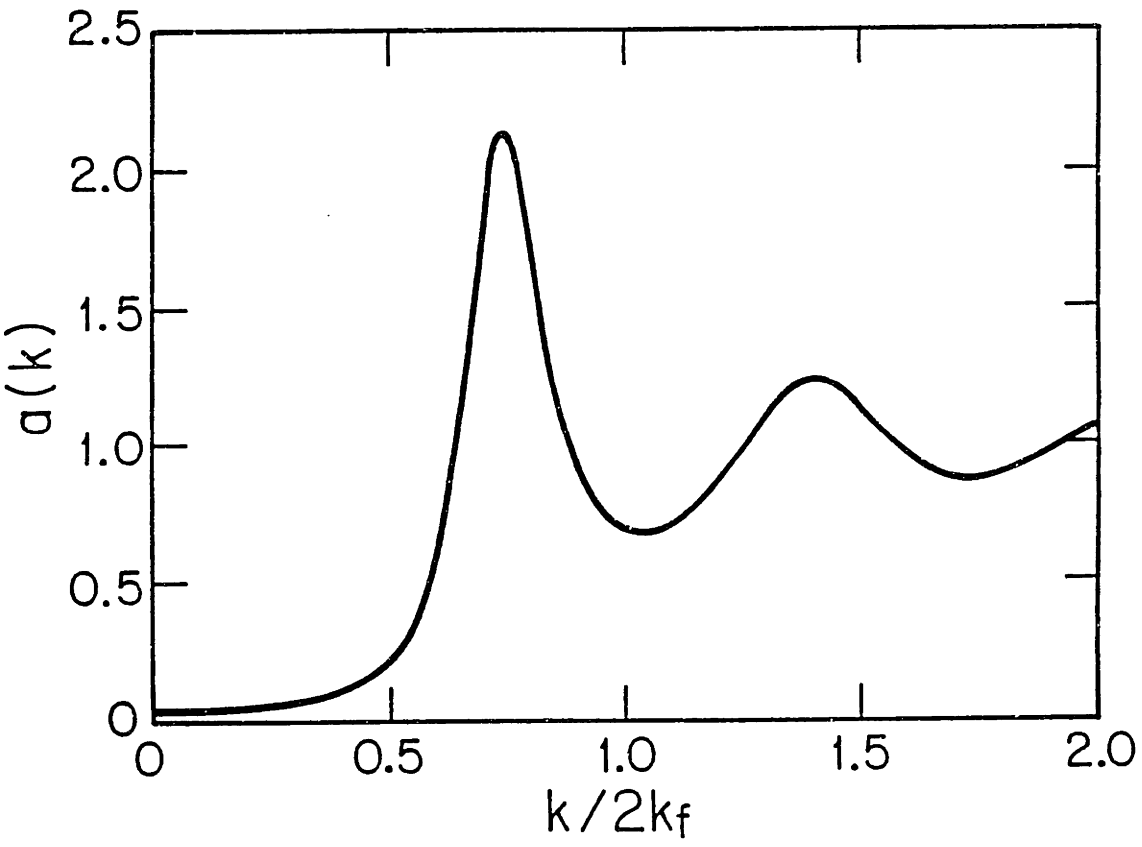

Figure 4.6: The structure factor for liquid carbon used in the calculation of the transport properties of the liquid. The packing fraction was assumed to be $\eta = 0.41$.

Element	A_0	A_1	A_2
C	2.05	2.44	2.65
Si	2.08	2.39	2.44
Ge	2.10	2.34	2.09
Sn	1.84	2.04	1.62
Pb	1.92	2.00	0.90

Table 4.4: The constants A_0, A_1, and A_2 used in the Heine–Abarenkov potential for group IV elements. The constants for carbon were calculated in this work while the constants for the other elements were determined by Heine and Abarenkov[8].

group IV elements calculated by Heine and Abarenkov[8] are given for comparison. From table 4.4 we see that the constant A_0 for carbon is the value obtained from $A_0 = Z/R_m$ while the other values follow in patterns similar to the rest of the group IV elements.

The calculated model potential appears in Figs. 4.7 and 4.8. In Fig. 4.7 the model potential for carbon is shown for $0 < k/2k_f < 2$ illustrating the rapid decrease in the potential as k becomes larger. In Fig. 4.8 the calculated potential for carbon is compared to the model potential calculated for Si by Heine and Abarenkov[8]. Note the similar behavior in the two potentials with the nodes at similar $k/2k_f$. Also note that the potential for carbon is much stronger than for silicon as $k \to 0$. This is due to the higher Fermi level in the liquid carbon due to higher carrier density.

A comparison of the potential to the structure factor is also useful to determine the effect of the node in the potential on the contribution of the primary structure peak to the transport properties of the liquid. The expanded model potential is overlapped with the structure factor in Fig. 4.9. The node in the calculated model potential is seen to occur at a k value which places it near the

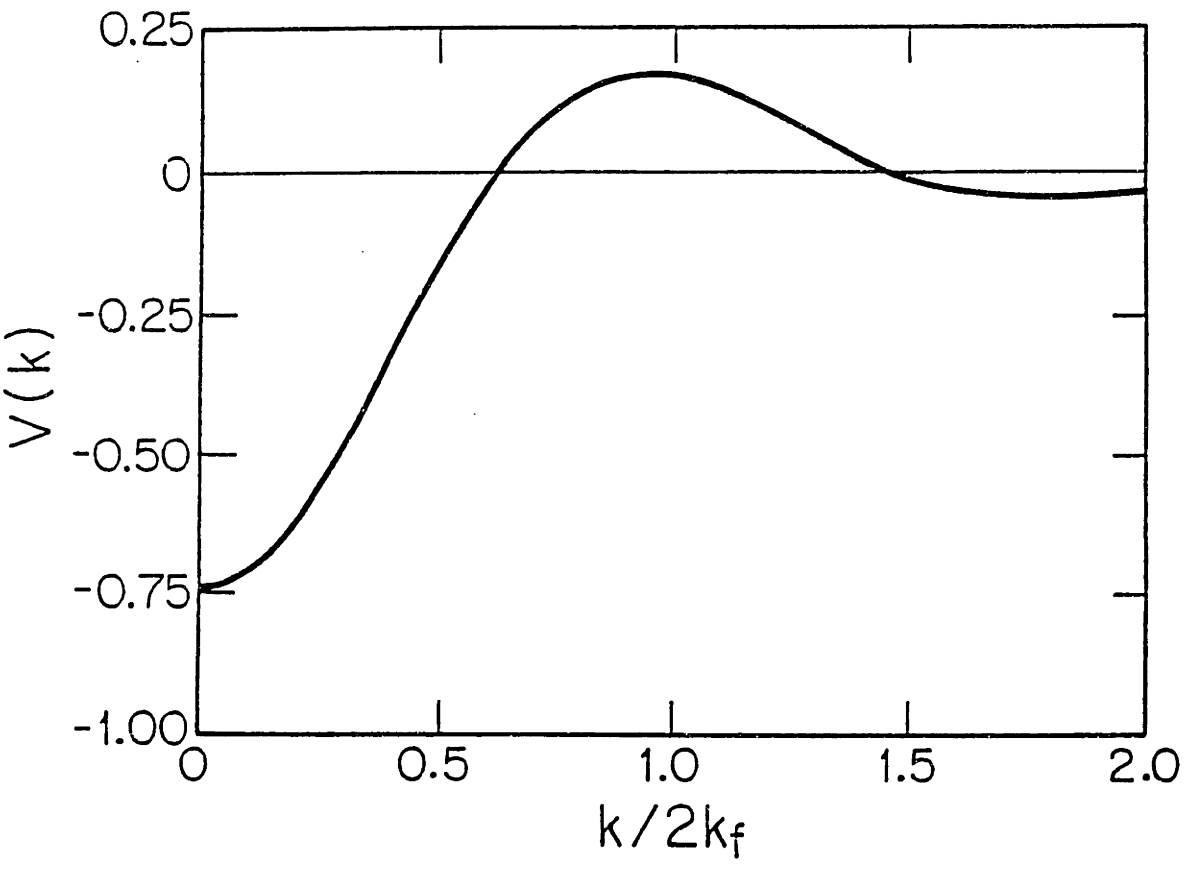

Figure 4.7: The calculated model potential used to calculate the transport properties of liquid carbon. The potential was calculated directly using the Heine–Abarenkov model potential with dielectric screening[5,6,7,8].

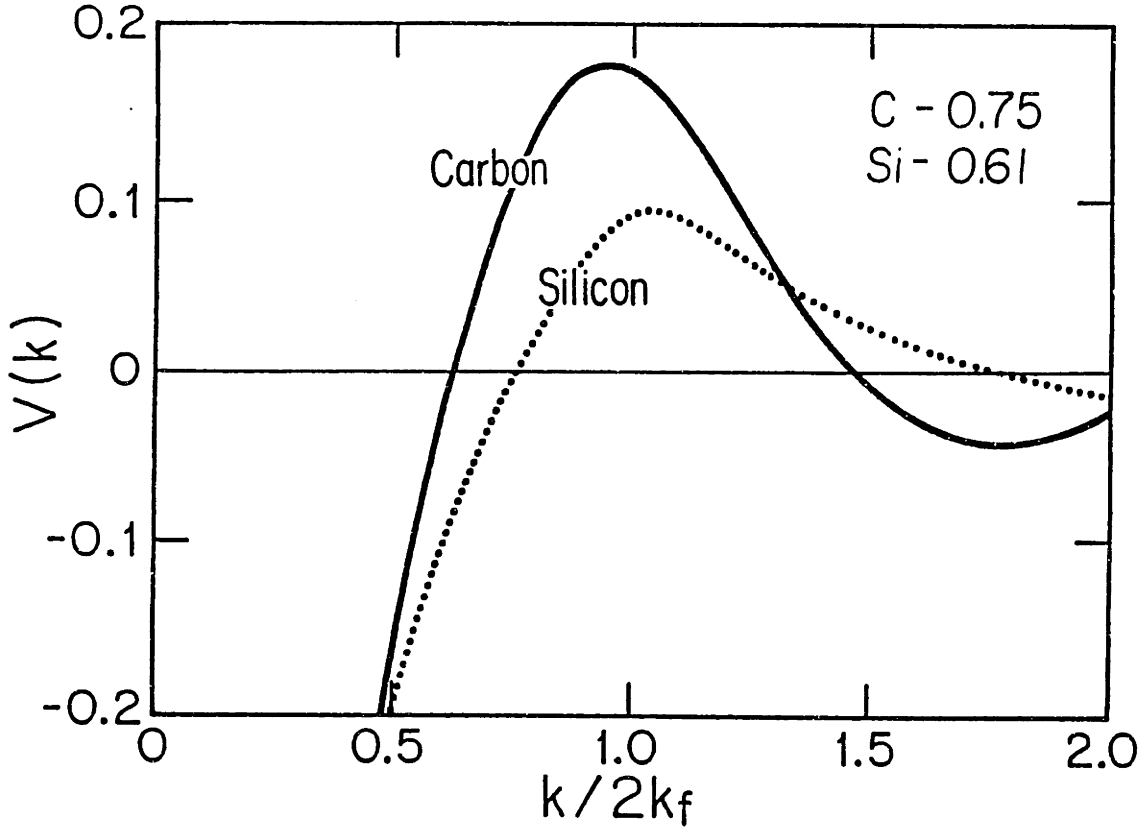

Figure 4.8: An expanded view of the model potential for carbon compared with the model potential for Si calculated by Heine and Abarenkov. The numbers in the inset are the values of the potential as $k \rightarrow 0$.

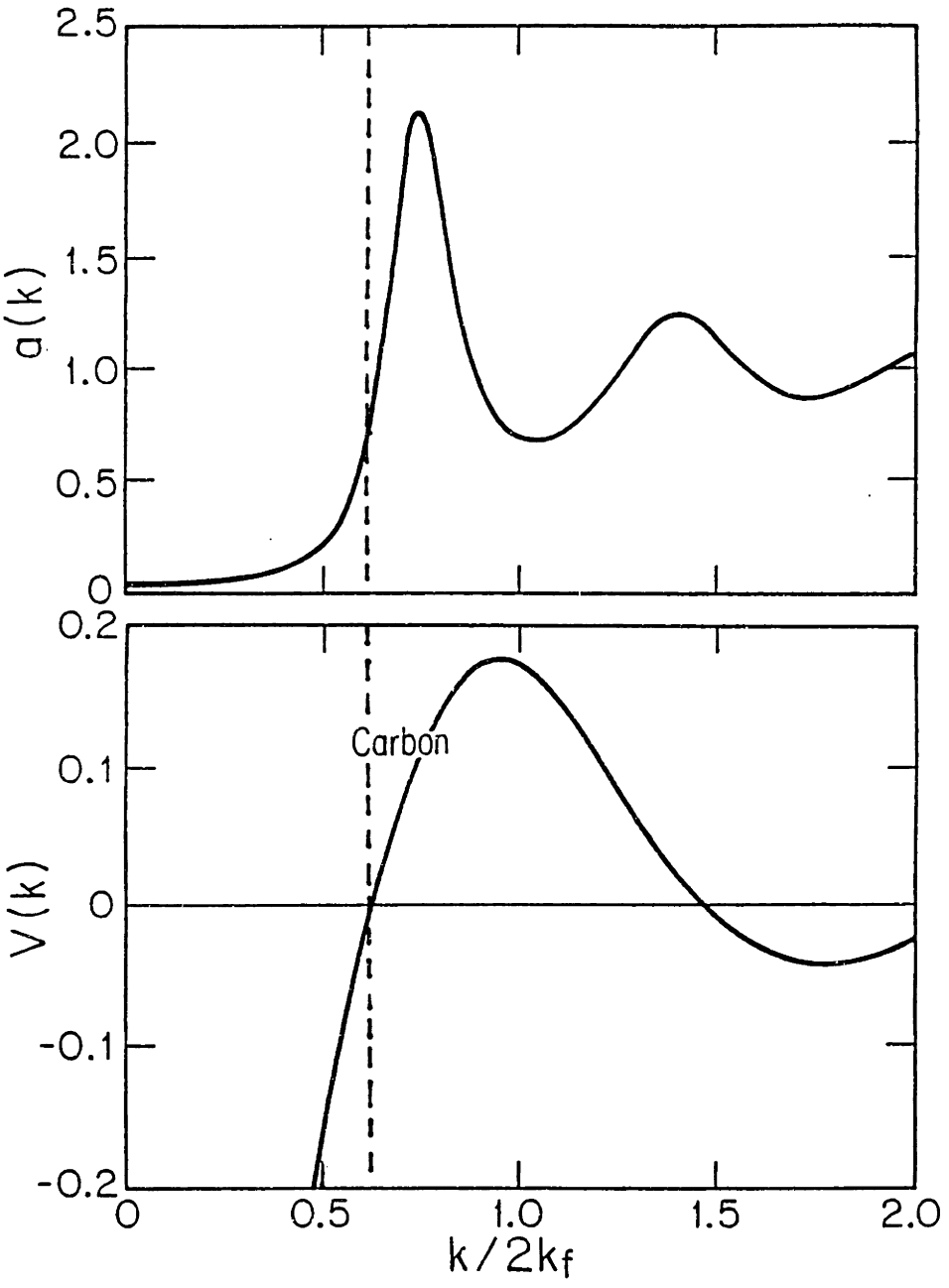

Figure 4.9: A comparison of the position of the node in the model potential with the primary peak in the liquid structure factor. Note that the node occurs at a k value which places it near the center of the primary peak in the structure factor.

center of the primary peak in the liquid structure factor. As stated previously in section 4.3.4, this means that there will not be a large contribution to the scattering from the k where the structure factor is greatest. This serves to increase the electron mean free path and hence decrease the electrical resistivity.

4.6.5 Fermi Surface Blurring

Calculations of the electrical resistivity of liquid carbon using the liquid structure factor and the model potential of the last sections show that the electron mean free path in liquid carbon is only on the order of one or two interatomic spacings. As discussed in section 4.4 this requires the calculations to account for the blurring of the Fermi surface. Figure 4.10 illustrates the effect of Fermi surface blurring on the calculation of the electrical resistivity of liquid carbon. From Fig. 4.10 the integral for the electron mean free path must be extended beyond $2k_f$ in order to account for the Fermi surface blurring caused by the finite electron mean free path.

4.7 The Properties of Liquid Carbon

4.7.1 The Electrical Resistivity of Liquid Carbon

From our calculated structure factor and model potential, the Ziman formalism may now be applied to calculate the electrical resistivity of liquid carbon in the low density regime ($\sim$ 2.0g/cm^3). Since we know that the electron mean free path will be only a few interatomic spacings, the effect of Fermi surface blurring must be included using the Ferraz and March formalism discussed in section 4.4. The electron mean free path is then calculated from

$$\frac{1}{\Lambda} = \left(\frac{1}{2k_f}\right) \int_0^\infty dK K^3 a(K) |v(K)|^2 \Gamma(K, l) \qquad (4.59)$$

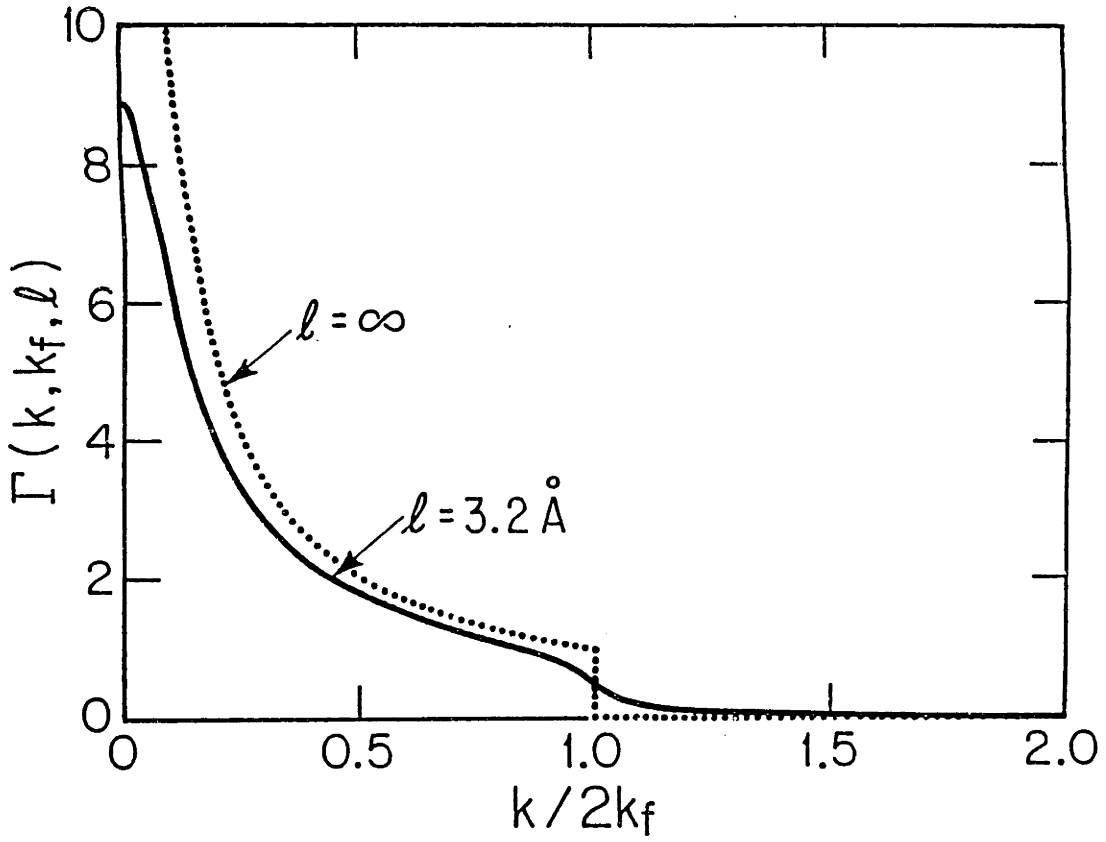

Figure 4.10: The functions Γ_0 and Γ plotted for liquid carbon illustrating the effect of a finite electron mean free path. Note that the integral for the mean free path must now be extended beyond $2k_f$.

where the integration variable K has been normalized to $2k_f$. Since the potential, $v(K)$ falls off more rapidly than K^4 the integral may be evaluated over a finite region. This prevents the integration of the structure factor at high K where it is known not to account for ion–ion interactions well. In fact it is only necessary to integrate over the first two diameters of the Fermi sphere, that is

$$\frac{1}{\Lambda} \sim \left(\frac{1}{2k_f}\right) \int_0^2 dK K^3 a(K) |v(K)|^2 \Gamma(K, l) \tag{4.60}$$

to obtain a good estimate of the electron mean free path. Evaluating the integral in Eq. 4.60 by numerical techniques, the electron mean free path for liquid carbon is $\Lambda = 3.4$Å. The small Λ verifies that the inclusion of Fermi surface blurring is important in the calculation.

From the calculated Λ, the electrical resistivity of liquid carbon immediately follows as

$$\rho_l = \frac{m v_f}{n_e e^2 \Lambda} = 39.5 \mu\Omega\text{–cm} \tag{4.61}$$

where we have again used the electron gas properties of section 4.6.2. This value for the electrical resistivity of liquid carbon is encouraging since the experimental value for the electrical resistivity of liquid carbon is $\sim 30 \mu\Omega$–cm[28]. It is also interesting to evaluate the electrical resistivity for the different structure factors to determine how sensitive the calculation is to the hard sphere radius for carbon. Table 4.5 shows that the variation of the structure factor over a broad range has little effect on the calculated electrical resistivity. The lack of a strong dependence of ρ_l on the packing fraction is due to the node in the potential which lies close to the primary peak in the structure factor. Since the position of the primary peak is not strongly dependent on the packing fraction, the calculated ρ_l will not be strongly correlated to the packing fraction. The second entry in table 4.5 for $\eta = 0.41$ shows the how accounting for Fermi surface blurring increases the electron mean free path.

η	$\rho_l(\mu\Omega$–cm)	Comment
0.41	39.5	
0.41	41.2	without Fermi surface blurring
0.3	42.6	
0.4	39.8	
0.5	37.3	

Table 4.5: The calculated electrical resistivity for liquid carbon. The packing fraction, η, was varied to determine the correlation between the packing fraction and the resistivity. The effect of Fermi surface blurring is also shown.

4.7.2 Thermal and Optical Properties of Liquid Carbon

Since liquid metals are known to be degenerate Fermi gases, we may use this fact to calculate most of the thermal properties of liquid carbon. The specific heat of the liquid at constant pressure is given by

$$C_p(T) = 3R + \frac{\pi^2 k_B T}{2E_f} R \tag{4.62}$$

where R is the gas constant. The first term on the right hand side of Eq. 4.62 is the atomic contribution to the specific heat while the second term on the right hand side is the electronic contribution. The thermal conductivity can be calculated using the Wiedemann–Franz relation so that

$$K = \frac{\pi^2 k_B^2}{3e^2} \frac{T}{\rho_l} \tag{4.63}$$

where ρ_l is the electrical resistivity calculated above.

Figures 4.11 and 4.12 show the temperature dependence of the specific heat and the thermal conductivity for graphite and liquid carbon over the temperature range $300 < T < 5000$K. Also plotted in Fig. 4.11 is the specific heat predicted by Leider *et. al.*[29] for graphite and liquid carbon. The agreement between the liquid metal theory prediction and the prediction by Leider *et. al.*[29] is good for liquid carbon, even though the specific heat predicted by the

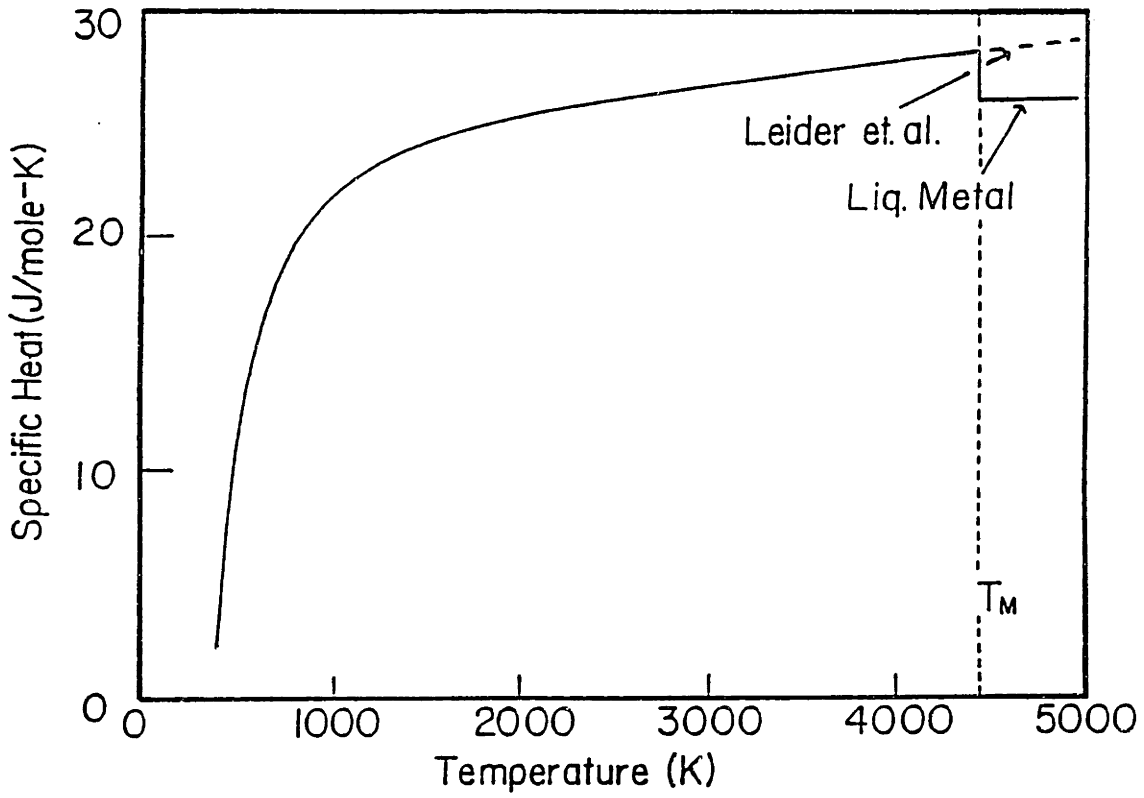

Figure 4.11: The specific heat for graphite and liquid carbon as predicted by liquid metal theory (solid curve) and by Leider *et. al.*[29]. Note the good agreement between the predictions for liquid carbon.

liquid metal model is somewhat smaller. The temperature dependence of the specific heat in both models is linear.

The thermal conductivity for both orientations in graphite and liquid carbon are plotted versus temperature in Fig. 4.12 for temperatures in the range $300 < T < 5000$K. The salient feature of the thermal conductivity is the large increase in the thermal conductivity when graphite melts. The increase in the thermal conductivity is more pronounced for the c–axis as expected. The thermal conductivity of liquid carbon is ~ 4 times larger than the inplane thermal conductivity of graphite at the melting temperature, while the liquid thermal conductivity is ~ 100 times the c–axis thermal conductivity of graphite at the melting temperature.

The optical properties of liquid carbon may also be calculated by noting that the Drude theory describes the properties of liquid metals. The real and imaginary parts of the dielectric function are given as

$$\epsilon_1(\omega) = \epsilon_{core} - \frac{4\pi\tau}{\rho_l(1+\omega^2\tau^2)} \tag{4.64}$$

$$\epsilon_2(\omega) = \frac{4\pi}{\omega}\frac{1}{\rho_l(1+\omega^2\tau^2)} \tag{4.65}$$

where ω is the frequency of the light.

Using these functions, the optical constants n and k may be calculated from

$$n(\omega) = \left[\frac{\epsilon_1(\omega) + \sqrt{\epsilon_1(\omega)^2 + \epsilon_2(\omega)^2}}{2}\right]^{\frac{1}{2}} \tag{4.66}$$

$$k(\omega) = \left[\frac{-\epsilon_1(\omega) + \sqrt{\epsilon_1(\omega)^2 + \epsilon_2(\omega)^2}}{2}\right]^{\frac{1}{2}} \tag{4.67}$$

and the reflectivity $R(\omega)$ is then given by

$$R(\omega) = \frac{(n(\omega)-1)^2 + k(\omega)^2}{(n(\omega)+1)^2 + k(\omega)^2}. \tag{4.68}$$

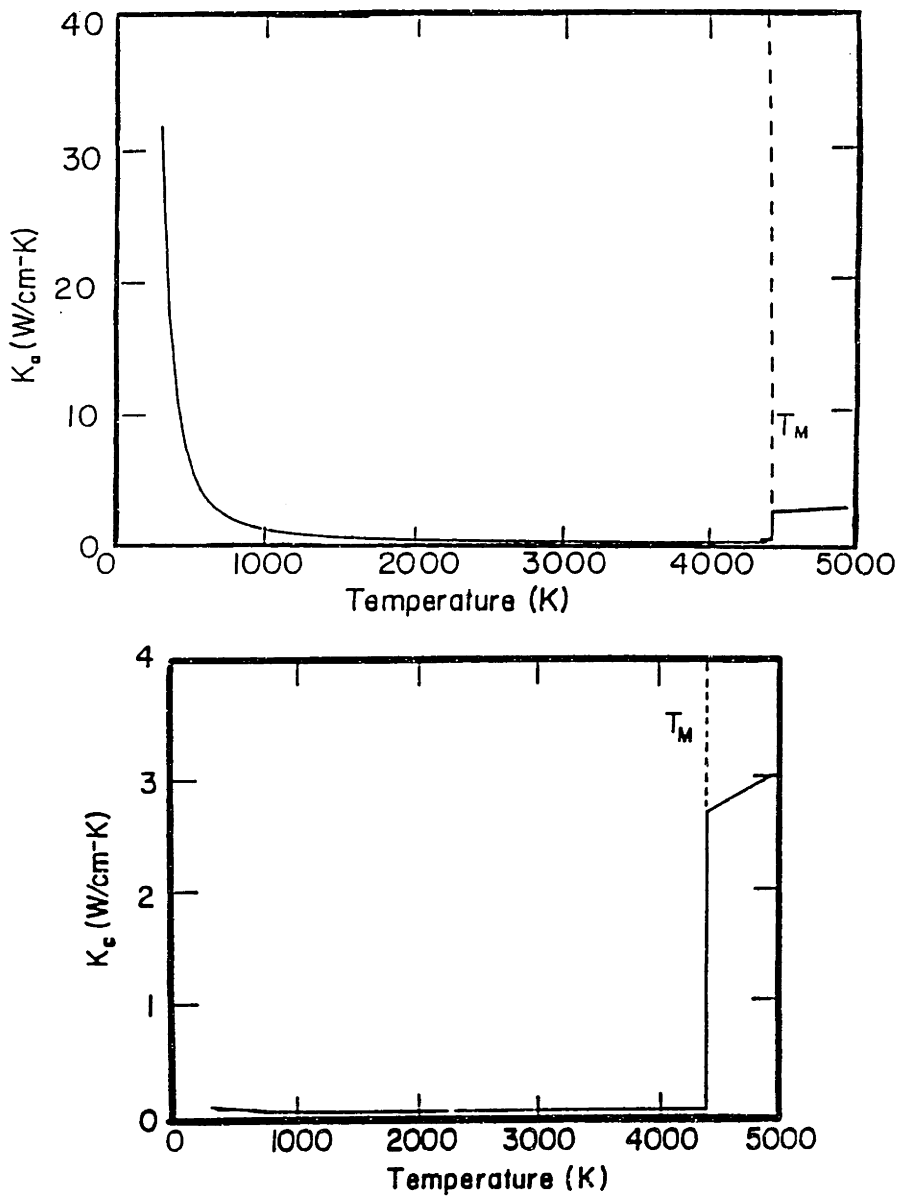

Figure 4.12: The thermal conductivity for graphite and liquid carbon predicted from liquid metal theory. The inplane thermal conductivity of graphite is plotted in (a) while the c–axis thermal conductivity is plotted in (b). Note the sharp increase in the thermal conductivity when graphite melts.

Property	Conditions	Value	Model
$C_p(T)$	$T = 4450$K	26J/mole–K	Fermi gas
$K(T)$	$T = 4450$K	2.9W/cm–K	Wiedemann–Franz
R	$\lambda = 6943$Å	0.82	Drude
R	$\lambda = 2480$Å	0.7	Drude
α	$\lambda = 6943$Å	$1.4 \times 10^6 \text{cm}^{-1}$	Drude
α	$\lambda = 2480$Å	$1.7 \times 10^6 \text{cm}^{-1}$	Drude

Table 4.6: A summary of the thermal and optical properties for liquid carbon.

The absorption coefficient $\alpha(\omega)$ can also be obtained from

$$\alpha(\omega) = \frac{2\omega k}{c} \tag{4.69}$$

where c is the speed of light. The calculated normal incidence reflectivity and the absorption coefficient, α, are plotted versus frequency in Figs. 4.13 and 4.14, respectively. The unscreened plasma frequency, calculated from the Fermi gas parameters, is $\omega_p = 21$eV.

Table 4.6 summarizes the thermal and optical properties of the liquid metal model for liquid carbon at the melting temperature. Included in table 4.6 are the optical properties for the pulsed lasers used to melt graphite.

4.7.3 Temperature Dependence of the Electrical Resistivity

Since liquid carbon is a polyvalent liquid metal, there will only be a small temperature dependence of the electrical resistivity. The reason is that changes in the structure factor at low K have little effect on changing the integral in Eq. 4.25 since the low K values will be depressed by the K^3 weighting of the integral, the fact that the primary peak in the structure factor falls close to the node in the pseudo–potential, and since $a(K) \sim 1$ for $K > 2k_f$ before considering thermal expansion. We may therefore assume that there will be not be a strong dependence of the electrical resistivity of liquid carbon

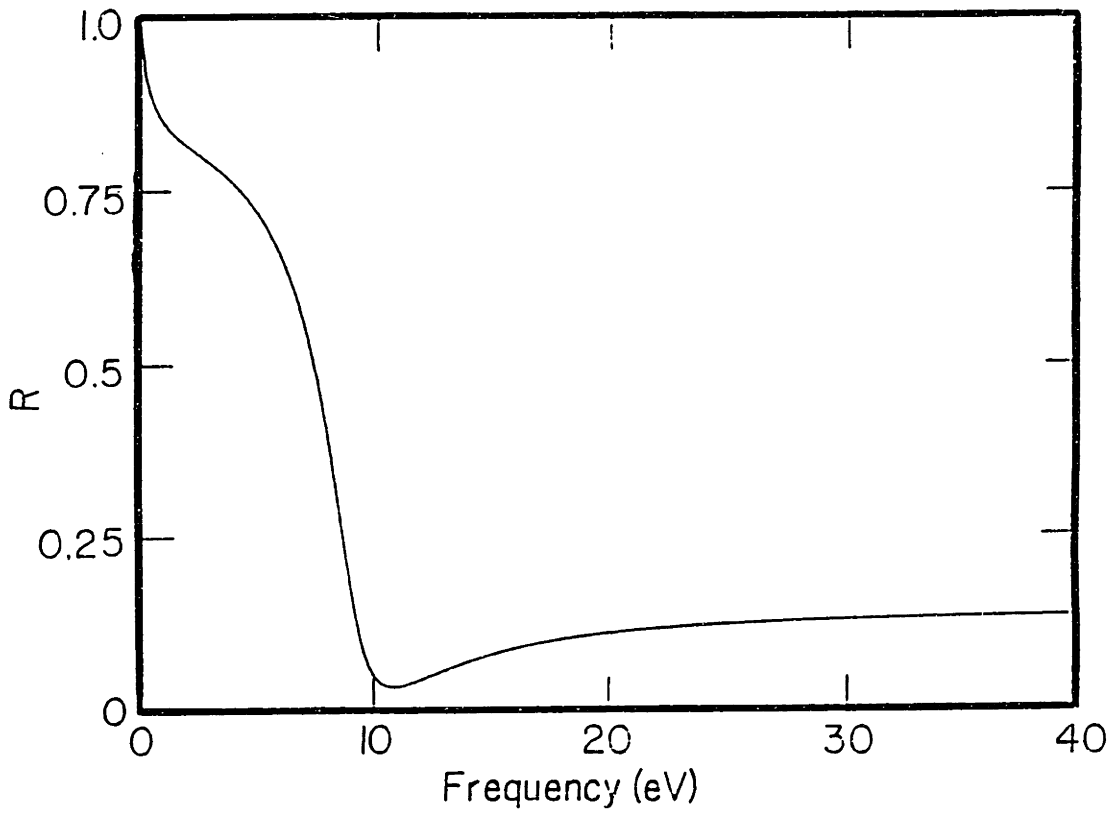

Figure 4.13: The reflectivity of liquid carbon versus frequency as calculated from the liquid metal model for liquid carbon.

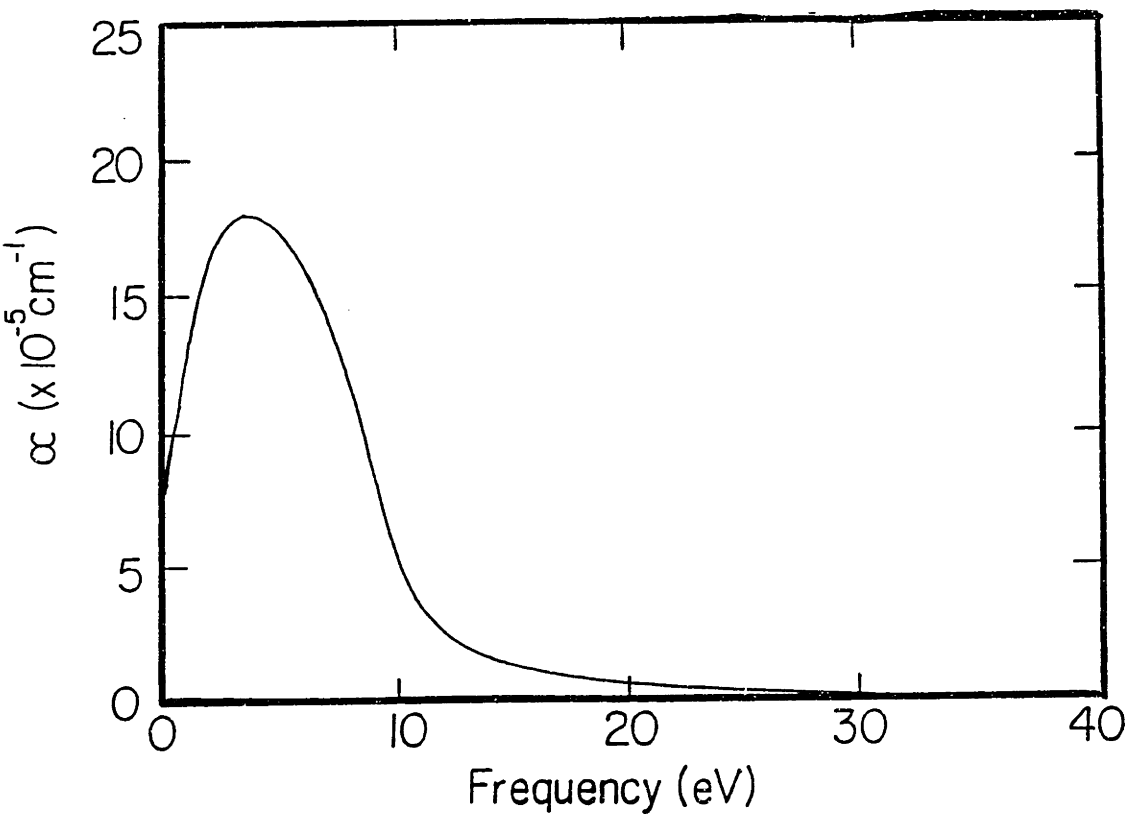

Figure 4.14: The absorption coefficient, α, versus frequency for liquid carbon.

with temperature. This again agrees with the experimental measurements by Heremans *et.al.*[28] where the temperature of the liquid carbon is known to have gone above 5000K, but no increase in the electrical resistivity is observed. The temperature dependence of the thermal properties of liquid carbon is therefore given by the equations describing each property in Eqs. 4.62 and 4.63.

References

[1] J.M. Ziman, *Phil. Mag.* 6, 1013 (1961).

[2] C.C. Bradley, T.E. Farber, E.G. Wilson, and J.M. Ziman, *Phil. Mag.* 7, 865 (1962).

[3] J.K. Percus and G.J. Yevick, *Phys. Rev.* 110, 1 (1958).

[4] J.K. Percus, *Phys. Rev. Lett.* 8, 462 (1962).

[5] V. Heine and I. Abarenkov, *Phil. Mag.* 9, 451 (1964).

[6] I.V. Abarenkov and V. Heine, *Phil. Mag.* 12, 529 (1966).

[7] A.O.E. Animalu, *Phil. Mag.* 11, 379 (1965).

[8] A.O.E. Animalu and V. Heine, *Phil. Mag.* 11, 1249 (1965).

[9] L.J. Sundstrom, *Phil. Mag.* 11, 657 (1965).

[10] N.W. Ashcroft and J. Lekner, *Phys. Rev.* 145, 83 (1966).

[11] D.J. Stevenson and N.W. Ashcroft, *Phys. Rev. A* 9, 782 (1974).

[12] M. Cutler, "Liquid Semiconductors", (Academic Press, New York, 1977).

[13] V.M. Glazov, S.N. Chizhevskaya, and N.N. Glagoleva, "Liquid Semiconductors", (Plenum Press, New York, 1969).

[14] J.N. Hodgson, *Phil. Mag.* 4, 183 (1959).

[15] L.G. Schulz, *Advanc. Phys.* 6, 102 (1957).

[16] L.I. Schiff, "Quantum Mechanics" 3ed., (McGraw–Hill, New York, 1968) p.324.

[17] G. Fournet, *Handb. Phys.* 32, 328 (1957).

[18] M.S. Wertheim, *Phys. Rev. Lett.* 10, 321 (1963).

[19] E. Thiele, *J. Chem. Phys.* 39, 474 (1963).

[20] N.S. Gingrich and L. Heaton, *J. Chem. Phys.* 34, 873 (1961).

[21] J.L. Ornstein and F. Zernike, *Amst. Proc.* 17, 793 (1914).

[22] J.M. Ziman in *Advances in Physics* 10, (Clarendon Press, Oxford, 1961) p.1.

[23] A. Ferraz and N.H. March, *Phys. Chem. Liq.* 8, 271 (1979).

[24] J. Hubbard, *Proc. Roy. Soc. A* 243, 336 (1957).

[25] F.P. Bundy, *J. Chem. Phys.* 38, 618 (1963).

[26] F. Reif, *Statistical and Thermal Physics*, (McGraw–Hill, New York, 1965), p.305.

[27] M. Blume, N. Briggs, and H. Brooks, *Tbales of Coulomb Wave Functions* Technical Report No. 260, (Harvard University, Cruft Laboratory, Cambridge MA) 1959.

[28] J. Heremans, C.H. Olk, G.L. Eesley, J. Steinbeck, and G. Dresselhaus, *Phys. Rev. Lett.* (to be published).

[29] H.L. Leider, O.H. Krikorian, and D.A. Young, *Carbon* 11, 555 (1973).

Chapter 5

Model Calculations

5.1 Introduction

A numerical method for solving the diffusion equation has been developed by Carslaw and Jaeger[1] and has been applied to the problem of laser heating of materials by many workers[2,3,4,5,6]. The next section will review the numerical technique of finite differences used to solve the diffusion equation by Carslaw and Jaeger. The following sections will describe the constraints that are placed on the way in which the numerical technique may be implemented. The constraints placed on the calculation include the boundary conditions needed to obtain a specific solution to the diffusion equation and the physical constraints imposed by the properties of the material forwhich the equation is being solved. The sections following these describe how the numerical technique has been applied to the specific cases of pulsed laser heating and pulsed current heating in carbon.

The third section of this chapter will focus on how the diffusion equation is used to determine the kinetics of the liquid–solid interface by simulating the segregation of impurities during pulsed laser heating. The calculation is based on a model by Aziz[7] which uses the diffusion equation. This work is of great interest since the calculations provide values for such quantities as a liquid

diffusion coefficient for liquid carbon and give estimates of the equilibrium concentrations of impurities in liquid carbon.

5.2 Heat Flow Calculations

5.2.1 The Finite Difference Technique

The equation which will be of primary interest in this work is the diffusion equation with an arbitrary source term. The diffusion of heat as a function of both space and time is given by

$$\rho C_p \frac{\partial T(\vec{x},t)}{\partial t} = \nabla \cdot K \nabla T(\vec{x},t) + S(\vec{x},t) \tag{5.1}$$

where $T(\vec{x},t)$ is the temperature as a function of space and time and S is a source term for heat flowing into and out of the system by means other than diffusion. The other quantities in Eq. 5.1 are: the mass density, ρ, the specific heat, C_p, and the thermal conductivity, K, which are all temperature dependent.

The solution of the generalized equation for practical problems is not possible due to the undetermined nature of the source terms which may be discontinuous and the variations which are known to occur in the thermal properties of materials as a function of temperature[1]. In addition, no algebraic solution of Eq. 5.1 can take account of changes in phase which will occur discontinuously at the melting and vaporization temperatures.

As in many other problems, the solution of Eq. 5.1 will be dependent on the boundary conditions which are imposed on the system. For the two cases which are solved in this work, laser heating and pulsed current heating, the geometry is such that Eq. 5.1 may be reduced to a one dimensional form. The justification for the reduction in the dimension will be discussed at length in the following sections where the calculations for the two heating techniques are

discussed in great detail. The one dimensional form of Eq. 5.1 is given by

$$\rho C_p \frac{\partial T(z,t)}{\partial t} = \frac{\partial}{\partial z} \cdot K \frac{\partial T(z,t)}{\partial z} + S(z,t) \tag{5.2}$$

where the only terms that have really changed in Eq. 5.2 are the spatial derivatives which are now taken only along a single direction.

In order to solve Eq. 5.2 for the temperature, $T(z,t)$, we would like to have all of the material parameters be functions only of the temperature. The fact that the thermal parameters of materials are usually measured as a function of temperature may be used to simplify Eq. 5.2 by an application of the chain rule

$$\frac{\partial}{\partial z} K(T) \frac{\partial T(z,t)}{\partial z} = K(T) \frac{\partial^2 T(z,t)}{\partial z^2} + \frac{dK}{dT} \left(\frac{\partial T}{\partial z} \right)^2 \tag{5.3}$$

where we have expressed the thermal conductivity in terms of the temperature, T, and have carried out the algebra.

To solve Eq. 5.2 numerically, the derivatives must be converted into algebraic equations which can be easily handled using a computer. This essentially means that the equation must be taken from its continuous form as in Eq. 5.2, and translating it into a discrete form. By using the definition of the derivative

$$\frac{dT}{dt} = \lim_{\tau \to 0} \frac{T(z,t+\tau) - T(z,t)}{\tau} \tag{5.4}$$

we can approximate the value of the first order derivative with

$$\frac{dT}{dt} = \frac{T(z,t+\tau) - T(z,t)}{\tau} \tag{5.5}$$

and substitute this algebraic representation of the time derivative in Eq. 5.2 directly. This effectively means that Eq. 5.3 will be solved over time intervals, τ.

The same transformation from a continous differential equation to a set of discrete algebraic equations must be done for the spacial variable. However, a

direct application of the method above would yield for the second derivative of T:

$$\frac{\partial^2 T}{\partial z^2} = \frac{\partial}{\partial z}\left(\frac{T(z+\epsilon,t)-T(z,t)}{\epsilon}\right) \tag{5.6}$$

$$= \frac{T(z+2\epsilon,t)-T(z+\epsilon,t)}{\epsilon^2} - \frac{T(z+\epsilon,t)-T(z,t)}{\epsilon^2} \tag{5.7}$$

where ϵ is the spatial element. A difficulty now arises in that the form of Eq. 5.7 assumes that the spatial behavior of thermal diffusion is a deterministic process. The equation does not take into account that the flow of heat is actually dependent on the boundaries on both sides of a given space element. Therefore, the spatial derivatives must be handled in a different way since the flow of heat is subject to boundary conditions and materials parameters.

The solution to this problem is to take elements which are half the size of the original ϵ and to take the first derivative as

$$\frac{\partial T}{\partial z} = \frac{T(z+\frac{1}{2}\epsilon,t) - T(z-\frac{1}{2}\epsilon,t)}{\epsilon} \tag{5.8}$$

so that the second derivative becomes:

$$\frac{\partial^2 T}{\partial z^2} = \frac{T(z+\epsilon,t)-T(z,t)}{\epsilon^2} - \frac{T(z,t)-T(z-\epsilon,t)}{\epsilon^2} \tag{5.9}$$

and it is now symmetric about the element for which we wish to calculate the temperature.

Since we want to use elements of size ϵ in the calculation, we must now express the first derivative of T in terms of ϵ. This can be done with little loss of generality by making the approximation

$$T(z \pm \frac{1}{2}\epsilon,t) \simeq \frac{1}{2}(T(z\pm\epsilon,t)+T(z,t)) \tag{5.10}$$

The first spatial derivative of T may now be approximated by a symmeteric relation,

$$\frac{\partial T}{\partial z} = \frac{T(z+\epsilon,t)-T(z-\epsilon,t)}{2\epsilon}. \tag{5.11}$$

Inspection of Eq. 5.11 shows that the derivative is taken as an average over an element of size ϵ just as was done in the computation of the time derivative in Eq. 5.5. The major difference in the two forms of the first derivative are that the Eq. 5.5 is deterministic while Eq. 5.11 is not.

Once the derivatives have been translated into algebraic form, it is straight forward to change the differential equation Eq. 5.2 in continuous space into a set of algebraic equations over a discrete set of n space elements. The space elements are of size ϵ and the equation is then solved for some number of time elements of size τ. Carrying out the algebra, the solution of Eq. 5.2 for the i^{th} spatial element at a time t is given by

$$\begin{aligned} T_i(t+\tau) &= T_i(t) + \frac{\tau}{\rho C_p}\left[\left(\frac{K_{i+1}(T_{i+1}(t)-T_i(t)) + K_i(T_{i-1}(t)-T_i(t))}{\epsilon^2}\right)\right. \\ &\quad \left. + \left(\frac{dK}{dT}\right)_i \left(\frac{T_{i+1}(t)-T_{i-1}(t)}{2\epsilon}\right)^2\right] \end{aligned} \tag{5.12}$$

where the heat source term has not yet been included. In Eq. 5.12 note that each term in the second derivative of the temperature with respect to z has a different thermal conductivity K_j. The K_j term is given by

$$K_j = \frac{1}{2}(K(T_j(t)) + K(T_{j+1}(t)) \tag{5.13}$$

and reflects the fact that we are interested in the flow of heat across the boundaries between space elements. The significance of the derivative of the thermal conductivity, $(dK/dT)_i$, can now be seen as a first order correction term to the flow of heat through the i^{th} element over the time τ. As heat flows through the i^{th} element, the thermal conductivity of that element will change as the temperature of the element changes and hence change the rate at which heat will flow through the element.

Adding the heat source term to Eq. 5.15 is simple once it has been converted from a continuous to a discrete form. To convert the heat source term $S(z,t)$

to discrete form, it must be integrated over one layer. That is

$$\hat{S}_i(t) = \int_{z_i}^{z_i+\epsilon} dz S(z,t) \tag{5.14}$$

where $\hat{S}_i(t)$ is the total energy input to the i^{th} layer at time t. By adding this term to Eq. 5.12, the complete solution for $T_i(t+\tau)$ becomes

$$\begin{aligned} T_i(t+\tau) &= T_i(t) + \frac{\tau}{\rho C_p}\left[\left(\frac{K_{i+1}(T_{i+1}(t)-T_i(t)) + K_i(T_{i-1}(t)-T_i(t))}{\epsilon^2}\right)\right. \\ &\left. + \left(\frac{dK}{dT}\right)_i \left(\frac{T_{i+1}(t)-T_{i-1}(t)}{2\epsilon}\right)^2 + \hat{S}_i(t)\right] \end{aligned} \tag{5.15}$$

where $\hat{S}_i(t)$ has simply been added to Eq. 5.12.

Solving the differential equation is now a simple matter of calculating the thermal properties of each element from known experimental data, or, from a theoretical model, and doing the algebra. For solid carbons, experimental data for the thermal properties are given in chapter 2 and properties for liquid carbon are derived from the nearly free electron model for liquid metals in chapter 4. The model calculation assumes that an individual element is in a single phase. After an element melts or solidifies, the calculation uses the thermal properties of the correct phase to calculate the new temperature. The transitions from one phase to another are discussed in great detail in the next section.

5.2.2 Incorporating Phase Changes

The second major obstacle to obtaining a closed form solution to Eq. 5.2 is the incorporation of phase changes in the calculation. A finite difference calculation does not suffer from this problem since a change in phase can be easily handled by simply changing the set of equations used to calculate the thermal properties of individual elements.

Melting and vaporization are the two phase changes of particular interest in laser heating studies and can be described by a single temperature at which the phase change takes place and by a latent heat necessary to change the entropy of the system accordingly. Another transition which may occur is one which is described by an activation energy, E_a, such that the probability, P, that the system has undergone the transition is given by

$$P = P_0 \exp(-E_a/k_B T) \tag{5.16}$$

where k_B is Boltzman's constant. The activated transition can be used to describe crystallization processes and vaporization.

First Order Phase Transitions

First order phase transitions are those which are characterized by a single transition temperature and a latent heat. The incorporation of this kind of phase transition in the calculation is simple and is described by the following procedure:

1. Hold the temperature of the element at the transition temperature.
2. Any increase in the temperature caused by the addition of energy to the element is used to overcome the latent heat of the transition.
3. Once the necessary latent heat has been supplied to the element, the element assumes the properties of the new phase and the temperature of the element is again allowed to vary.

This kind of treatment would be used to describe a first order phase transition such as melting. The algorithm for treating vaporization would be modified only in the last step which would become:

3. Once the latent heat has been supplied to the element, that element is removed from the system.

The other type of phase change which may occur is an activated process which may be described by Eq. 5.16. Vaporization may be described by an activated process since the rate at which a material will vaporize will depend on both the temperature of the material and the equilibrium vapor pressure on the material surface. The use of a free energy function to calculate the rate at which a material will vaporize is an illustration of an activated phase transition.

The free energy function is given as

$$\ln(p) = -\left(\frac{F(T) - H_0}{k_B T}\right)_g + \left(\frac{F(T) - H_0}{k_B T}\right)_{s,l} - \frac{\Delta H_v}{k_B T} \tag{5.17}$$

where p is the vapor pressure, $F(T)$ is the free energy at the temperature, T, H_0 is the enthalpy and ΔH_v is the latent heat of vaporization. The subscripts g, s, and l refer to the gaseous, solid, and liquid phases, respectively. The free energy may be calculated directly from a knowledge of the specific heats of the various phases from

$$-\left(\frac{F(T) - H_0}{T}\right) = \int_0^T \frac{dT'}{T'^2} \int_0^{T'} dT'' \frac{C_p(T'')}{T''} \tag{5.18}$$

where $C_p(T)$ is the temperature dependent specific heat at constant pressure.

In many cases, the temperature of the vapor is high enough so that it may be treated as an ideal gas so that the amount of material which must be removed from the surface, N, is given simply by

$$N = \frac{pV}{k_B T} \tag{5.19}$$

where V is a volume defined by the area of irradiation and the thermal velocity, v_{th}, of the gas,

$$v_{th} = \sqrt{\frac{k_B T}{M}} \tag{5.20}$$

where M is the mass of the molecule.

Since we have the temperature dependence of the properties of the solid and liquid from chapters 2 and 4, all that remains to be done in order to implement the calculation is to define the sizes of the time and space elements, τ and ϵ, and to define the source terms that put energy into the system.

Resolidification

First order phase transitions are simple to understand and handle numerically. However, resolidification processes are too difficult to do a discrete calculation due to their complexity which requires a full understanding of the liquid–solid interface[8]. Since we have very little knowledge of the properties of liquid carbon (and even less about the liquid–solid interface) resolidification of liquid carbon has been treated as a first order phase transition occurring at the graphite melting temperature. When the liquid solidifies, the same heat of fusion as for the graphite to liquid carbon transition is released back into the solid.

The results from Raman spectroscopy[9,10] and TEM[11] show that the resolidified material is disordered graphite. Using this information we can approximate the thermal properties of the resolidified material as a geometric average of the in–plane and out–of–plane thermal properties of graphite. This means that the thermal conductivity of the resolidified carbon will be taken as

$$K_{rs} = \left(K_a^2 K_c\right)^{\frac{1}{3}} \tag{5.21}$$

where K_{rs} is the thermal conductivity of the resolidified carbon.

The thermal conductivity given by Eq. 5.21 will only be a rough estimate for the thermal conductivity in the disordered carbon produced by laser heating. There are two reasons for this. First, the disordered layer is not composed

of crystals of pure graphite of random orientation. Actually, the disordered material is composed of crystallites of random *size* and of random orientation. The experimental measurements only provide an *average* crystallite size which is useful for qualitative comparisons between different laser heated samples. Second, small crystallites of graphite ($< 100\text{Å}$) may have thermal and electrical properties which are significantly different than large crystallites of graphite. The phonon contribution will dominate the thermal conductivity of disordered carbons. The weak bonding in dosordered carbons therefore makes the thermal properties of disordered carbon very different from graphite. For these reasons, Eq. 5.21 may be used only as an order of magnitude estimate for the thermal conductivity in the disordered layer of carbon formed by pulsed laser heating.

The effect of this approximation on the calculations will only be important for determining the length of time which liquid carbon exists and the velocity of the resolidification front. The penetration of the melt front into graphite and the vaporization of carbon vapor species from the surface, which are quantities we can match to experimental results, do not depend on the properties of the resolidified carbon. Other properties, such as solute trapping and impurity segregation, strongly depend on the velocity of the resolidification front as the liquid carbon solidifies. While these calculations may be affected directly by the properties of the resolidified carbon, many times it is sufficient to obtain an order of magnitude estimate of the resolidification front velocity in order to do useful calculations.

It should be noted that the solidification processes that occur for laser melted materials have some additional complications. The first is undercooling of the liquid. In many other laser heated systems, the liquid phase is known to be present at temperatures well below the melting temperature. Liquids may exist at temperatures below the equilibrium melting temperature if the

energy in the liquid can be extracted faster than the atoms can find a lattice site. With solid–liquid interface velocities in laser melted materials approaching 10m/sec, this condition can be readily achieved. The heat of formation from the liquid back to a solid phase also changes as a result of rapid solidification and undercooling. A more detailed discussuion of rapid solidification is given in section 6.2.

The changes in the melting temperature and the heat of formation between the solid and liquid phases during resolidification will again only affect the lifetime of the liquid and not the properties of the liquid directly. In order to account for these effects properly in the calculation it is necessary to know the properties of the liquid, and therefore, rapid solidification and undercooling have been omitted from these calculations.

5.3 Choosing the Time and Space Elements

The selection of proper time and space elements is crucial to obtaining useful results from a finite difference calculation. In addition, in order to simulate physical phenomena using computer calculations, it is important define the variable parameters so that the simulation is an accurate description of the physical process being modeled.

The physical constraint on ϵ will depend on the heating process used. For laser heating, ϵ must be chosen to be much less than one optical skin depth for the wavelength of the light in the irradiating pulse. This is necessary so that the energy output in the laser pulse will be similar to the actual deposition of energy in the system. For the case of pulsed current heating, there are no physical constraints from energy deposition so that the choice of of ϵ will be important only to obtain an accurate temperature profile.

The numerical constraint on the selection of the time element is that errors

should not grow as the calculation proceeds[1]. This can be accomplished by limiting the changes in $T_i(t+\tau)$ caused by small changes in the $T_j(t)$ used to calculate it. Mathematically this is expressed as

$$\begin{aligned} |dT_i(t+\tau)| &\leq M|dT_{i+1}(t)| + M|dT_{i-1}(t)| + |2M-1||dT_i(t)| \quad (5.22) \\ &\leq (2M + |2M-1|)\eta \quad (5.23) \end{aligned}$$

where η is the mean of the $dT_j(t)$. Since errors must not grow we must have

$$M = \frac{K\tau}{C_p \rho \epsilon^2} \leq \frac{1}{2} \quad (5.24)$$

so that the size of τ depends explicitly on the choice of ϵ for the problem being solved.

5.4 Laser Heating in Carbon

5.4.1 The Heat Source Term

The previous sections described the finite difference technique which will be used to solve the heat equation. This section will concentrate on the application of the technique when the heat source term, $S(z,t)$, is the result of optical absorption by a carbon surface. The heat source term may then be expressed as

$$S(z,t) = \alpha(z,t) I(\vec{x},t) \exp(-\alpha(z,t)z) \quad (5.25)$$

where $\alpha(z,t)$ is the absorption coefficient as a function of space and time and $I(\vec{x},t)$ represents the distribution of the laser energy on the surface.

The expression for both the absorption coefficient and the laser power distribution may be simplified by considering the laser heating problem as one dimensional. This approximation will be valid so long as the surface area irradiated by the laser is large compared to the thermal diffusion distance.

Numerically this is expressed as

$$4Dt << A \tag{5.26}$$

where A is the area of the laser irradiation, D is the thermal diffusivity and t is the time scale of the laser heating experiment. For the laser irradiation studies done in this work, the typical laser irradiated area is $\sim 0.2\text{cm}^2$ and the worst case thermal diffusion during the course of the experiment is

$$4Dt \sim 2.3^{-5}\text{cm}^2 \tag{5.27}$$

where $D \simeq 10\text{cm}^2/\text{sec}$ and $t \simeq 500\text{nsec}$, so that the approximation of a system with one dimension is valid for the laser irradiation case.

The one dimensional nature of the laser heating problem can be used to simplify the heat source term. The absorption coefficient will be determined by the properties of the individual layers in the sample. Since the properties will in turn be dependent on the temperature of the individual layers we can express the absorption coefficient solely as a function of temperature

$$\alpha(z,t) = \alpha(T(z,t)) = \alpha(T) \tag{5.28}$$

The functional form for the absorption coefficient has already been discussed in section 2.4. We can now simplify the expression for the laser power distribution to

$$I(\vec{x},t) \rightarrow I(t) \tag{5.29}$$

The time profile of the laser pulses used was essentially gaussian so that the heat source term from Eq. 5.2 becomes

$$S(z,t) = \alpha(T) I_0 \exp(-(t/w)^2) \exp(-\alpha(T)z) \tag{5.30}$$

where w is the width of the laser pulse.

5.4.2 Element Sizes

The selection of the time and space elements in the finite difference technique is critical in obtaining useful results from the calculations. For laser heating the critical parameter to be assessed is the optical absorption coefficient α. From section 2.4, $\alpha \simeq 300$Å for the lasers used in this work. In order to account for the diffusion of energy properly in laser heated graphite, it is necessary to choose the space element size ϵ to be less than α. From the condition Eq. 5.24 we can calculate an appropriate time element τ.

In the calculations carried out for laser heating in carbon, ϵ was chosen as 100Å which complies with the physical constraint imposed by the absorption coefficient. The time element was taken to be 1psec which when tested with Eq. 5.24 yields

$$\frac{K\tau}{C_p\rho\epsilon^2} \sim 0.06 < \frac{1}{2} \tag{5.31}$$

so that the errors inherent in our calculations will not grow with time. It should be noted that the calculation was tested using smaller values for ϵ and τ and no significant changes were observed in the results.

5.4.3 Boundary Conditions

In order to obtain a particular solution to Eq. 5.1 for specific heating conditions, it is necessary to specify a set of boundary conditions for the system. For the laser heating calculations, boundary conditions must be specified for the surface of the laser heated material and for the lowest lying layer used in the calculation.

The boundary condition at the surface is given by

$$\left.\frac{\partial T}{\partial z}\right|_{z=0} = 0 \tag{5.32}$$

meaning that the flow of heat across the surface is zero. Since we know that the surface layer will be much hotter than the atmosphere in which the sample

lies, the condition given by Eq. 5.32 can be justified by showing that the heat flowing out of the surface is negligible.

There are two contributions to the heat flowing out of the surface of the sample, blackbody radiation and thermal convection. The losses due to blackbody radiation may be calculated by using Stefan's law

$$B = \sigma_s T^4 \tag{5.33}$$

where B is the emitted power density and σ_s is Stefan's constant we find that even if the surface reached temperatures of 10^4K that the emitted power density would only be

$$B = 5.67 \times 10^4 \mathrm{W/cm}^2 \tag{5.34}$$

which is four orders of magnitude smaller than the incident laser power density; hence the emission of blackbody radiation is negligible.

The convection of heat away from the surface is also shown to be negligible by considering a simple diffusion model using the thermal conductivity, K, of air at 2800K and 20bar, which is

$$C = \frac{KTl}{A} \tag{5.35}$$

where A is the laser irradiated area. Allowing the surface again to reach 10^4K we find that the power density lost through convection is only

$$C = 20\mathrm{W/cm}^2 \tag{5.36}$$

and again this loss is negligible when compared to the input laser power density, typically $\sim 10^8 \mathrm{W/cm}^2$.

The boundary condition for the lowest lying layer is that the thermal gradient is zero so that

$$\left.\frac{\partial T}{\partial z}\right|_{z=n\epsilon} = 0 \tag{5.37}$$

where $n\epsilon$ is the depth of the lowest lying layer. This will be approximately true so long as the lowest lying layer is more than a thermal diffusion distance from the surface. Mathematically,

$$n\epsilon >> (4D_c t)^{\frac{1}{2}} \tag{5.38}$$

where D_c is the thermal diffusivity along the graphite c axis and t is a relavent time scale for laser heating. In all of our calculations $n\epsilon = 10^4$Å and the thermal diffusion distance is

$$(4D_c t)^{\frac{1}{2}} \sim 10^4 \text{Å} \tag{5.39}$$

so that for our calculations the boundary condition is valid.

5.4.4 Phase Transitions in Carbon

In order to calculate phase transitions in carbon it is necessary to know the temperatures and the heats of formation for first order phase transitions and the free energy functions for the activated transitions. The melting temperature for graphite used in the calculations was taken to be $T_M = 4450$K which is an intermediate value of those reported in chapter 1. The heat of fusion is $\Delta H_f = 105$kJ/mole taken from Bundy[12].

The free energy functions for carbon vapor species are not known directly, but they can be evaluated by fitting measured vapor pressure data of Leider *et. al.*[13]. The free energy function divided by the temperature may be expressed as

$$\frac{F(T)}{k_B T} = a + bT + cT^2 \tag{5.40}$$

where a, b and c are constants. The values of the constants used in the calculation appear in table 5.1. The values used in the calculation for the heats of formation for the vapor species were also taken from Leider *et. al.*[13] and are

Species	$a(\times 10^{-2})$	$b(\times 10^{2})$	$c(\times 10^{6})$
C_1	1.66	0.778	-0.328
C_2	2.15	1.42	-0.597
C_3	2.55	1.95	-0.725
C_4	2.74	3.02	-1.27
C_5	2.84	4.22	-1.77
C_6	3.43	4.70	-1.98
C_7	3.67	5.92	-2.50

Table 5.1: The constant coefficients a, b, and c needed to calculate the free energy functions for carbon vapor species C_1 to C_7 in Eq. 5.40. These values were determined by fitting the free energy function to vapor pressure data of Leider *et. al.*[13].

given in a table in chapter 1. The free energy function for the solid and liquid were calculated directly from the temperature dependence of the specific heat for the solid and the liquid using Eq. 5.18.

5.4.5 Results of Calculations

The results of our heat flow calculations are presented in this section for laser heated carbon with a 30nsec pulsed ruby laser and a 25nsec pulsed KrF laser. The thermal properties of solid graphite used in the model were taken from experimental data (section 2.3) and by extrapolating the experimental data up to the melting temperature. The model used for the liquid was the liquid metal model described in chapter 4.

Basic Calculation

For graphite laser heated with a 30nsec pulsed ruby laser (without considering the effects of vaporization) we obtain a set of profiles for temperature versus time, melt depth versus time and melt front velocity versus time as shown in Figs. 5.1, 5.2, and 5.3 respectively. The effects of vaporization have been

considered in an additional set of calulations. The temperature versus time profiles (Fig. 5.1) show the temperature at the surface of the laser heated carbon and the two layers on either side of the layer representing the maximum penetration of the melt. The center of the laser pulse occurs at 60nsec. During the laser pulse the temperature of all the layers rises sharply until the temperature reaches the melting temperature. After the heat of fusion has been absorbed by the surface layer, the layer becomes molten and the temperature again rises as the liquid is heated. The temperature maximum is reached $\sim$ 10nsec after the maximum in the laser pulse intensity. As the laser pulse intensity decreases, thermal diffusion carries energy away from the surface into deeper layers, melting the deeper layers and decreasing the temperature at the surface. The temperature then remains at the melting temperature while the layer resolidifies, releasing the heat of fusion back into the resolidified melt. After resolidification, the temperature of the surface layer again decreases due to thermal diffusion.

The temperature versus time profiles for the other two layers in Fig. 5.1 have similar features. The layer lying at 2400Å below the surface melts, but the temperature remains close to the melting temperature. This is due to a combination of two factors. First, the small c–axis thermal conductivity in graphite helps to generate large thermal gradients at the solid–liquid interface. Since the thermal conductivity in the liquid is large, according to the liquid metal model for liquid carbon, the thermal conductivity through the solid–liquid interface will be large and into the lower lying solid layers. Therefore, the temperature of the liquid layers lying close to the solid–liquid interface will remain close to the melting temperature since the flow of heat out of the liquid layer will be large near the interface.

The third temperature versus time profile shown in Fig. 5.1 is for the layer

lying just below the maximum penetration of the melt front at 2600Å. The salient feature of this profile is the cusp which appears at $\sim$ 110nsec. The cusp in the temperature versus time profile forms for two reasons. First, the layers which lie below the optical penetration depth of the laser are melted by the diffusion of heat from the layers closer to the surface. Because of the large thermal gradient at the solid–liquid interface, the temperature of the liquid near the interface never becomes much larger than the melting temperature as discussed before. The solid layer which lies below the solid–liquid interface is then heated by a layer of constant temperature so that as the temperature of the solid layer increases, the thermal gradient decreases and the flow of heat into the layer also decreases. This means that the rate of the temperature increase in the solid layer will decrease. This can be seen not only in the layer which lies below the maximum penetration of the melt front at 2600Å, but also in the layer lying at 2400Å just before it melts as well.

The second part of the cusp formed in the temperature versus time profile, labeled 2600Å in Fig. 5.1, is due to the solidification of the liquid layers lying above the layer at 2600Å. When the layers resolidify, the melt front is no longer being driven by a thermal gradient in the liquid, but rather is being driven by the thermal gradients in the solid. When a layer freezes at the solid–liquid interface, the properties of the layer revert back to the properties of solid carbon at the melting temperature. Since the heat of fusion has been extracted from the resolidified layer, all the energy which is removed from the layer results in a reduction in the layer temperature. The sharp reduction in the layer temperature results from the large thermal conduction due to the large thermal gradient.

When the other liquid layers resolidify, additional cusps appear in the temperature versus time profiles as can be seen by the small ripples in the profiles of

the layer at 2400Å and 2600Å in Fig. 5.1. The profiles then approach a "steady–state" when the solid–liquid interface is far from the layers. The "steady–state" is created by the liquid remaining at constant temperature.

At times near 250nsec, a similar cusp in the time versus temperature profile forms for the surface layer. Additionally, however, kinks in the profiles of the lower lying layers also appear. This is due to the same mechanism as decribed in the previous paragraph. When the surface layer resolidifies, no more energy may be extracted from a layer without a corresponding decrease in the layer temperature. The "steady–state" thermal gradient which is established by the liquid layers remaining at the melting temperature no longer exists and the temperature of all the layers is due entirely to the flow of heat in the solid.

The advance of the melt front with time is illustrated in Figs. 5.2 and 5.3. In Fig. 5.2 the molten layer thickness is zero until the surface layer melts. The time evolution of the melt depth in Fig. 5.2 is similar to the temperature versus time profile. The melt depth rises sharply until $\sim$ 10nsec after the intensity maximum in the laser pulse, and then decreases more gradually while the layers resolidify by having heat extracted by thermal diffusion. The maximum penetration of the melt front appears to be nearly linear with the incident laser pulse energy density. The duration of the melt is not linear with the incident laser pulse energy density.

The behavior of the melt duration is explained by the magnitude of the thermal gradients in the solid which control the flow of heat during resolidification. When only a small number of layers must resolidify, the thermal gradients between the solid and the liquid and the thermal gradients within the solid remain large. However, when a large number of layers must resolidify, the thermal gradients within the resolidified material decrease. This is due to the small thermal conductivity of the solid at high temperature which will keep

recently resolidified material at a high temperature. By keeping the resolified material at high temperature, the thermal gradients in the solid, and hence between the solid and the liquid, will decrease. This means that when a large liquid layer is created ($\sim$ 3000Å), the flow of heat, governed by the size of the thermal gradient, will decrease and extend the lifetime of the molten region.

The melt front velocity, calculated from the melt depth versus time, is shown as a function of time in Fig. 5.3. The melt front velocity is characterized by being large and positive during the laser pulse. Melt front velocities on the order of meters per second are common in laser heating experiments in other materials[4]. As the molten layer thickness saturates, the velocity of the front slows and eventually becomes negative as resolidification starts. The velocity of the resolidification front is characterized by an initially fast regrowth and then by regrowth which becomes more gradual. Note that for small laser pulse energy densities, the velocity of the resolidification remains large until nearly all of the liquid has resolidified. For large laser pulse energy densities, the velocity of the resolidification is slower overall, showing that the reduced magnitude of the thermal gradients extends the lifetime of the molten region.

A summary of the calculations and a comparison of our calculations to experimental results is shown in Fig. 5.4. Also included in Fig. 5.4 are the results of our calculations using an insulating liquid model which extrapolates the properties of the solid into the liquid regime. The salient feature of Fig. 5.4 is that for laser pulse energy densities below $\sim 1.8 J/cm^2$, the calculated melt penetration is comparable to the disorder layer thickness measured using ion beam channeling. However, for laser pulse energy densities greater than $1.8 J/cm^2$ there is a divergence between our calculated results and the experimental results. The solid extension model for the liquid consistently underestimates the maximum penetration of the melt front. From these results, we can conclude

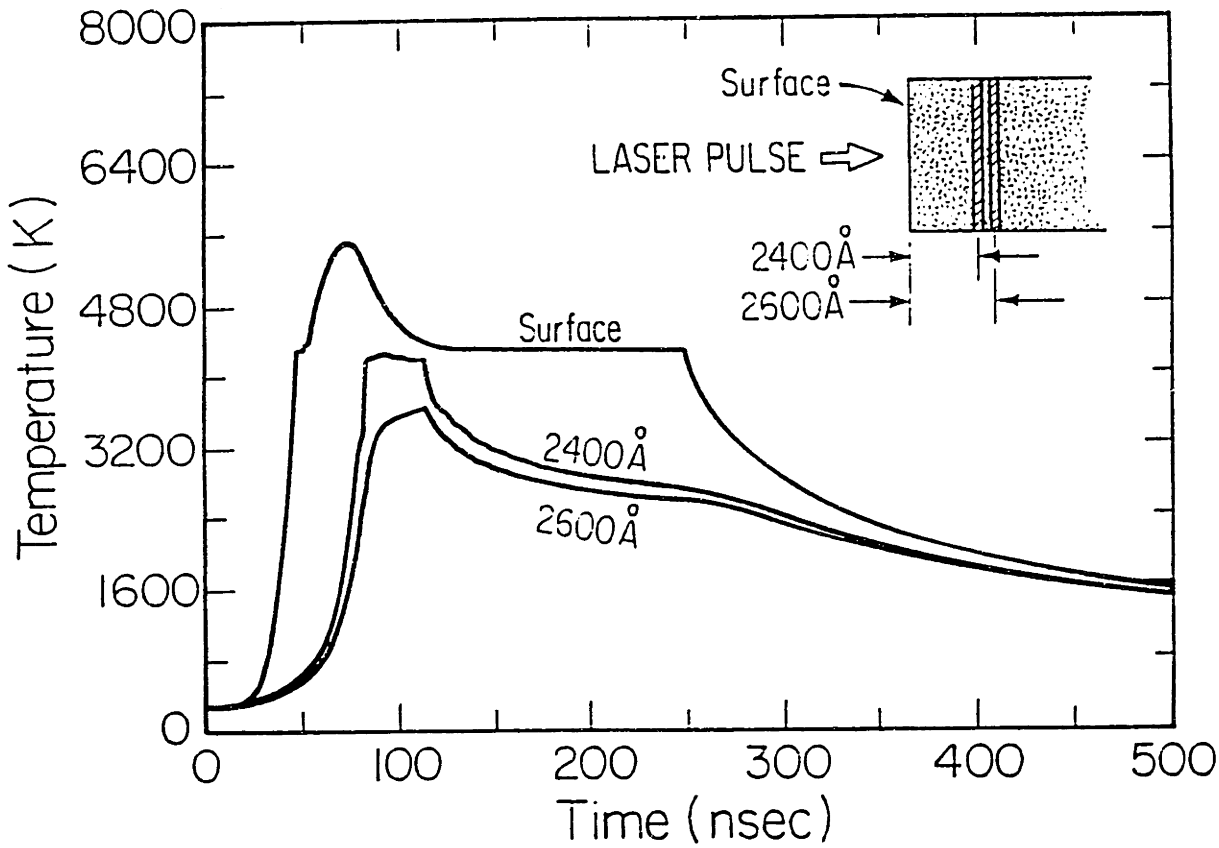

Figure 5.1: Calculated temperature versus time profiles for graphite laser heated with 2.0J/cm^2, 30nsec pulsed ruby laser. The laser pulse maximum occurs at 60nsec on the abscissa. Vaporization is not accounted for in the calculation[6].

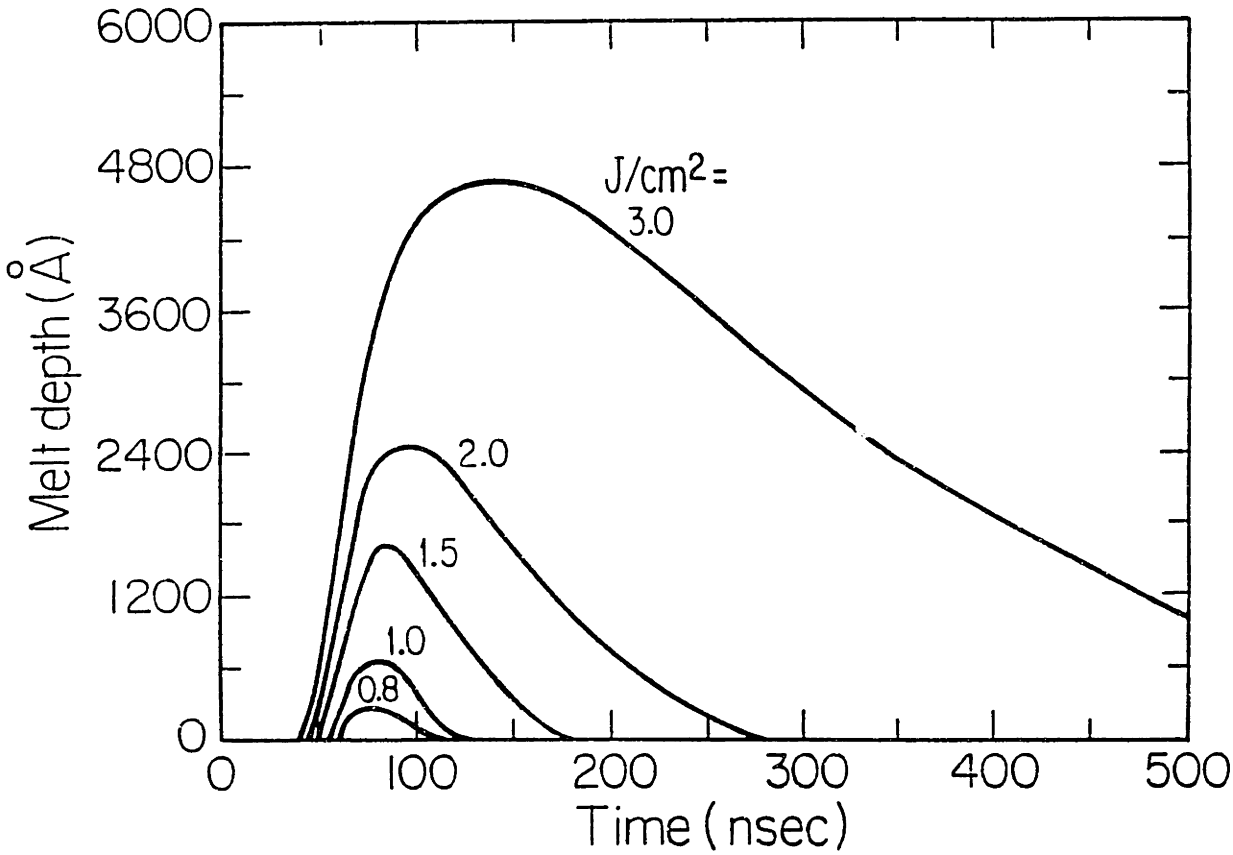

Figure 5.2: The calculated melt depth versus time for 30nsec pulsed ruby laser heated graphite. The laser pulse maximum occurs at 60nsec on the abscissa. The maximum melt penetration is used for comparison with ion beam channeling results[6].

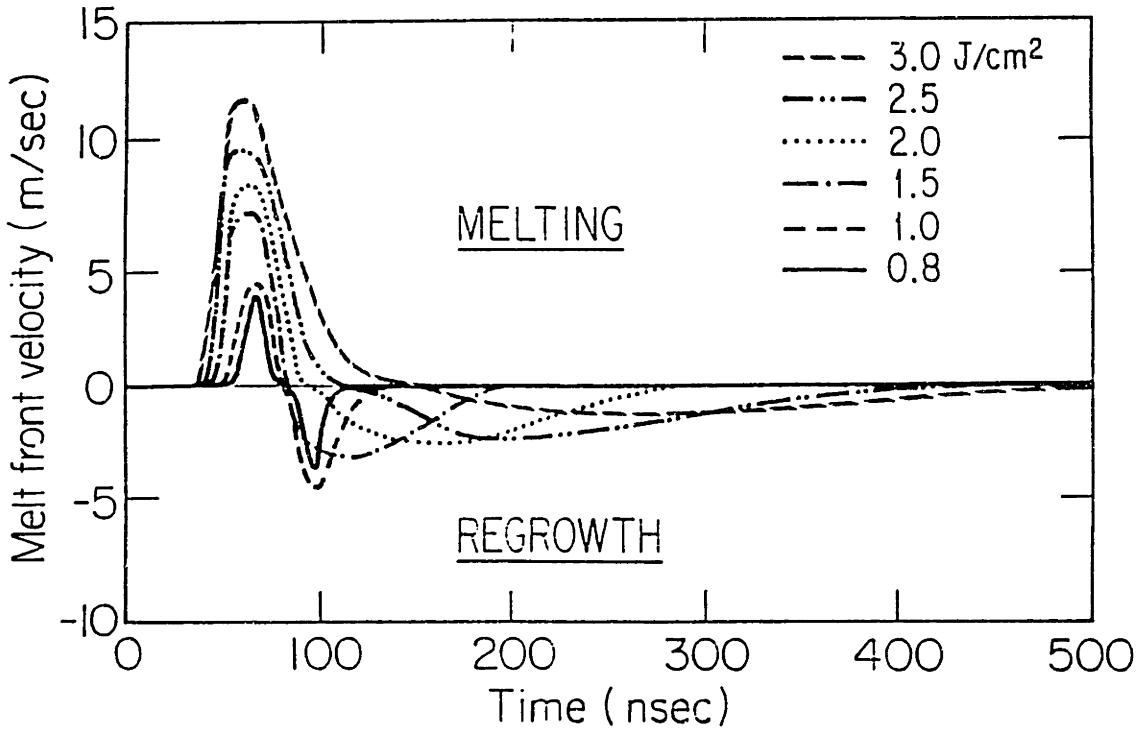

Figure 5.3: The melt front velocity is calculated from the melt depth. Positive velocities correspond to a penetrating melt front. These results are similar in magnitude and duration to results obtained for other materials[6].

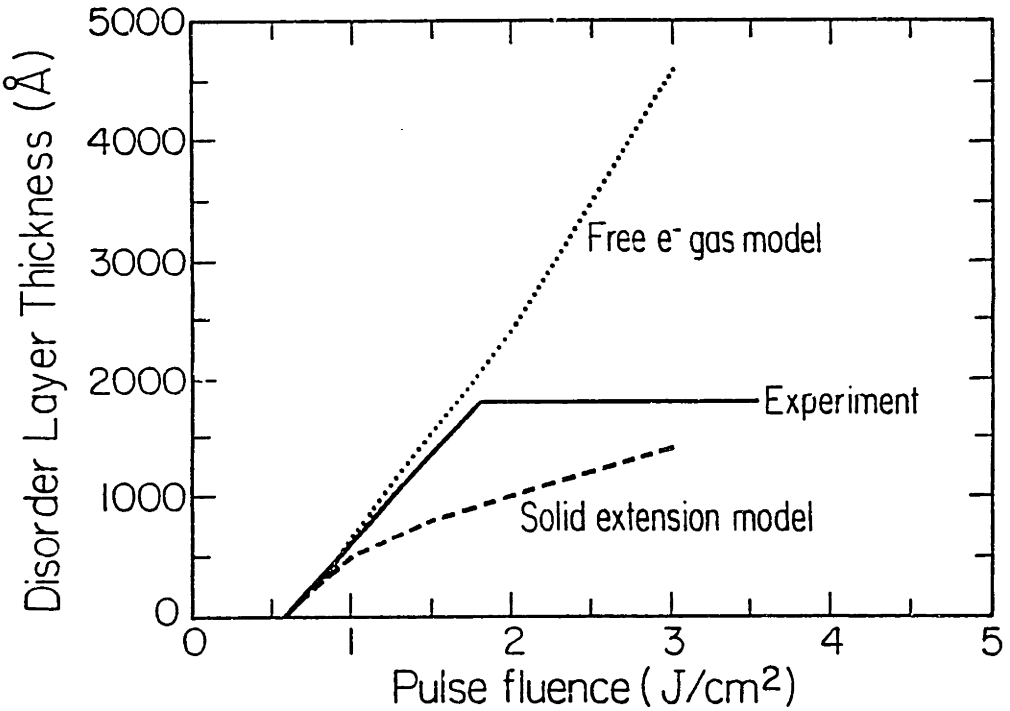

Figure 5.4: Comparison of the calculated melt penetration to the disorder layer thickness determined using ion beam channeling. The calculated results do not include the effects of vaporization[6].

that liquid carbon must have some metallic character. We further note that the effects of vaporization, which have not been included in this calculation, cannot improve the agreement between the solid extension model and our experimental results. This is because vaporization will remove material from the system and *decrease* the amount of material which will *resolidify*. Therefore, the actual disorder layer remaining after resolidification will be decreased, bringing the insulating model further from agreement with experiment. However, since the liquid metal model overestimates the melt penetration, especially at large laser pulse energy densities, the inclusion of vaporization in the calculation can only improve the agreement between the liquid metal model for liquid carbon and our experimental results.

Calculations Including Carbon Vaporization

Inclusion of carbon vaporization using the model described in section 5.2.2 improves the agreement between the liquid metal model for liquid carbon and the experimental results. The free energy functions for carbon vapor species from solid graphite are described in section 5.2.2. The free energy function for solid graphite was calculated from the temperature dependence of the specific heat given in section 2.3. The free energy function for the liquid was calculated directly from the specific heat in chapter 4. The vaporization model described in section 5.2.2 was used to calculate the carbon vapor species C_1 to C_7 being evolved from the surface of hot solid graphite and liquid carbon during and after pulsed laser heating.

The calculated profiles for the temperature versus time and the molten layer thickness versus time are changed due to the inclusion of vaporization, as can be seen in Figs. 5.5, 5.6, and 5.7 for 30nsec pulsed ruby laser irradiated graphite.

Figure 5.5 shows the temperature versus time profile for three layers in the calculation: the surface layer, the first layer which is not affected by vaporization, and the deepest layer which melts. The profile for the surface layer resembles the profile for the surface layer in the calculation without vaporization (Fig. 5.1) at the initial stages of laser heating. However, as the surface layer now becomes hot, material will be lost due to vaporization. Eventually, the surface layer completely vaporizes. This is shown by the abrupt end to the temperature versus time profile in Fig. 5.5. Each time a layer has completely vaporized, the next layer becomes the surface layer in the calculation.

The description of the other two curves is similar to the description given for the calculation which does not include vaporization. The rise and fall of the temperature and the formation of the cusps in the profiles of these layers originate from the same mechanisms described in the previous section. The main

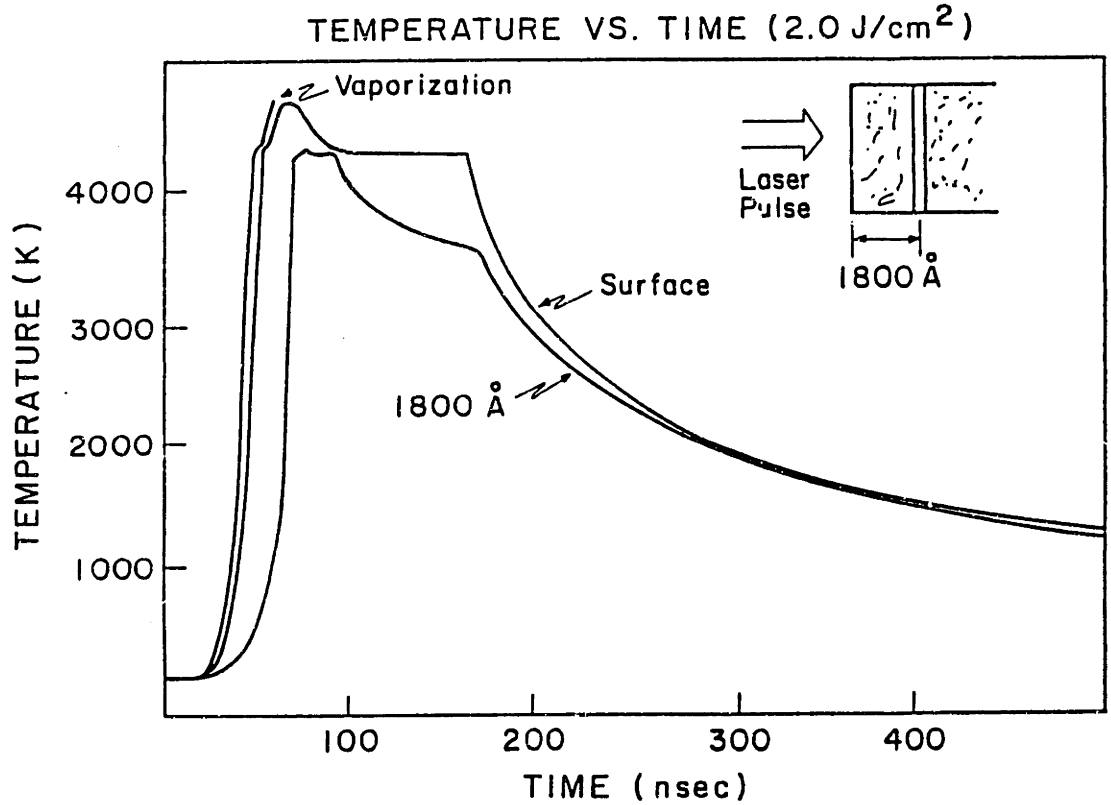

Figure 5.5: The calculated temperature versus time for various depths for a model which includes vaporization. The abrupt end to a trace in the figure indicates the time when the entire layer has been removed from the sample surface.

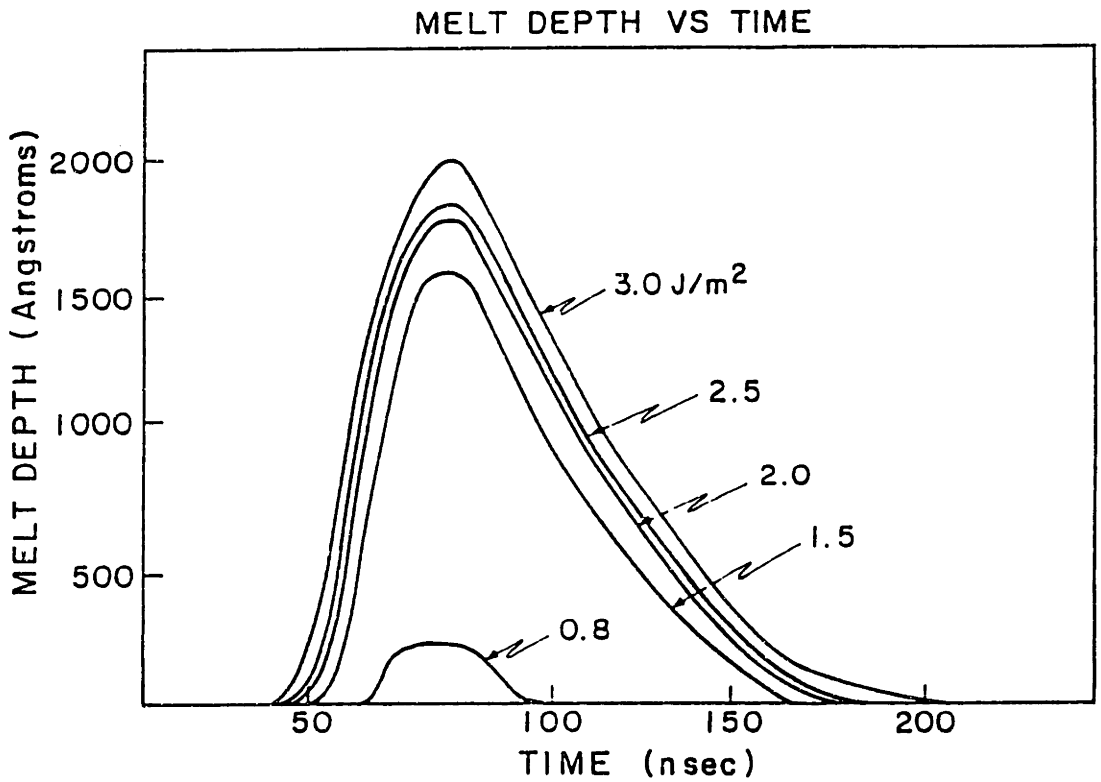

Figure 5.6: The calculated melt layer thickness versus time with vaporization included.

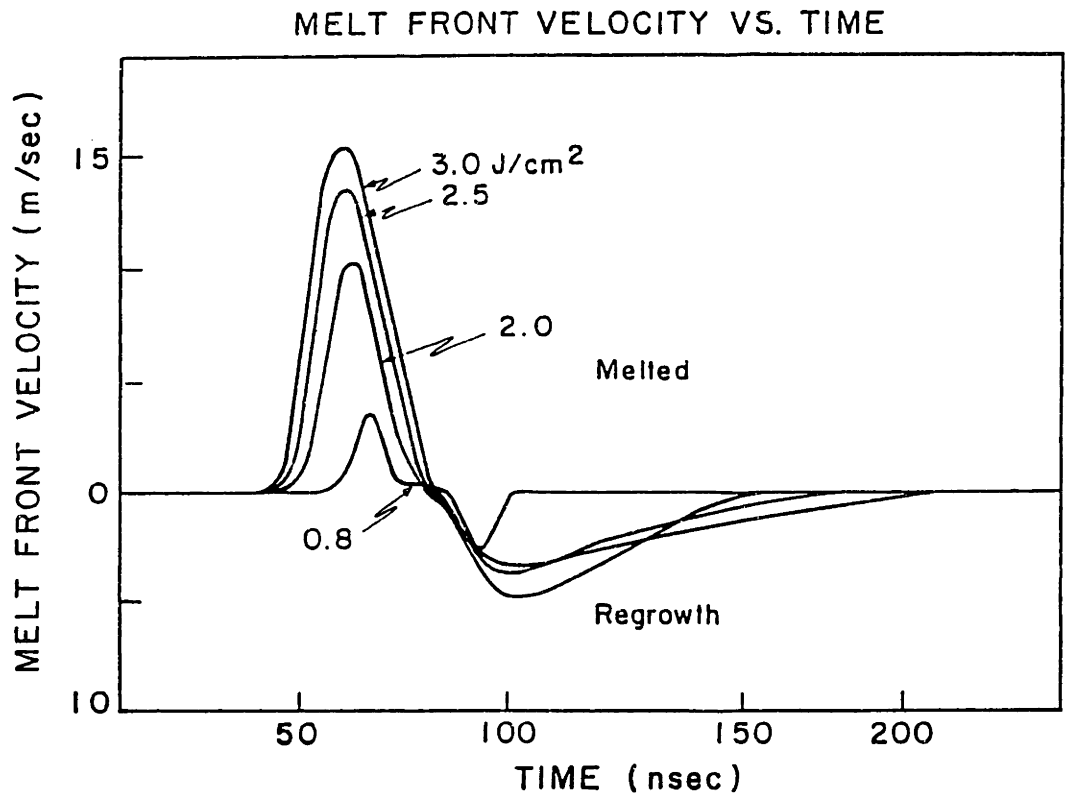

Figure 5.7: The calculated melt front velocity versus time for 30nsec pulsed ruby laser heated graphite. The laser pulse maximum occurs at 60nsec on the abscissa.

difference between the profiles for this calculation and the previous calculation is that the lifetime of the liquid layer is sharply reduced. This can be readily seen by comparing the position in time of the cusps in the profiles in Fig. 5.5 with those in Fig. 5.1.

The decrease in the lifetime of the liquid layer can be directly attributed to vaporization. When the solid or liquid carbon vaporizes, the vaporized species take both material and energy out of the system. Most of the material which is vaporized is in the molten state. Therefore, the total volume of liquid which must resolidify is reduced. The energy carried away by the vaporized species was used in the previous calculation to heat the liquid above the melting temperature and to melt layers which lie deeper from the surface. Since the vaporized species take this energy away, the energy does not have to be taken out of the liquid by thermal diffusion. Hence, it takes less time for the cold solid to extract the energy out of the liquid and cause the liquid to resolidify.

The liquid layer thickness versus time for the calculation including the effects of vaporization is shown in Fig. 5.6 for a range of laser pulse energy densities. These profiles are essentially the same as those for the calculation excluding vaporization except that the thickness of the liquid layer is smaller for all laser pulse energy densities than for the calculations where vaporization is excluded. The decrease in the thickness of the liquid layer and the lifetime of the molten phase are again attributed to the vaporization of the solid and liquid carbon for the reasons stated in the previous paragraph.

The melt front velocity for the calculation including vaporization is shown in Fig. 5.7. The evolution of the melt front velocity during the laser pulse is essentially unchanged from the calculation which does not include vaporization as can be seen by comparing Fig. 5.7 with Fig. 5.3 for times less than 80nsec. The major differences between the calculations appear during the resolidification of

the liquid.

For small laser pulse energy densities ($< 1.0 J/cm^2$), the regrowth velocities for both calculations have similar profiles. However, as the laser pulse energy density becomes greater than $1.0 J/cm^2$, the vaporization becomes significantly larger and we may speak of a vaporization front approaching the liquid–solid interface from the surface. The regrowth velocity and the velocity of the vaporization front are in opposite directions so that when they meet, the regrowth velocity terminates more abruptly than for the calculations which do not include vaporization.

To check the validity of the model for carbon vaporization, the calculated amount of vaporized material is compared in Fig. 5.8 to the amount of vaporized material measured using RBS and an ion implanted marker, as described in section 3.4. From Fig. 5.8, the calculated vaporization tracks the measured vaporization well for all laser pulse energy densities. Errors in the free energy functions for the carbon vapor species could cause significant errors in the calculated amount of vaporized material due to the exponential dependence of the number of vapor species emitted on the free energy function. Other errors may arise in the calculation since the vapor species have been treated as ideal gases. Finally, the amount of vaporization from ion implanted graphite resulting from laser heating may be somewhat larger than for the pristine graphite due to damage in the graphite caused by the implantation of the As marker, causing an increase in the number of carbon atoms which are weakly bound in the graphite lattice.

An additional point is that the calculated vaporization will occur predominatly at temperatures close to the melting temperature. This is simply because the liquid spends most of its time at temperatures near the melting temperature. This is due to the large thermal conductivity in the liquid metal model

which quickly reduces the liquid temperature and because most of the energy which must be extracted from the liquid is the heat of fusion as the liquid resolidifies. The rate of carbon vaporization at the melting temperature may then be estimated by simply dividing the amount of vaporized material by the lifetime of the liquid. By doing this we find that the rate of carbon vaporization is ~ 0.5m/sec for laser pulse energy densities greater than 1.5J/cm^2, an order of magnitude smaller than the velocity of the liquid–solid interface during melting and resolidification.

The temperature at which liquid carbon boils may also be extracted from these calculations. The abrupt end to the calculated temperature versus time profiles for the surface layer always occurs at $\sim$ 4700K. This would indicate that the boiling point of liquid carbon is near $\sim$ 4700K even though the vapor phase contains several different species of carbon molecules. The small relative temperature difference between the melting temperature for graphite and the boiling point for liquid carbon may also help to explain the difficulty in studying liquid carbon. From these calculations the relative temperature difference between the melting temperature, T_M, and the boiling point, T_V is only

$$t_{rel} = \frac{T_V - T_M}{T_M} \simeq 0.06 \tag{5.41}$$

while for silicon the relative temperature difference between the melting temperature and the boiling point is ~ 0.6 at low pressure. This means that very fine temperature control ($T \pm 5$ percent) is needed to study liquid carbon at low pressure, and this is difficult at temperatures exceeding 4000K.

The inclusion of vaporization in the calculation substantially alters the results in several ways: first, large amounts of energy are extracted from the system by the vaporized material. The loss of energy in the form of vaporized material does not allow this energy to diffuse into the sample and increase the melt penetration. The abrupt end to the surface layer trace in Fig. 5.5 indicates

the vaporization of an entire layer, thus bringing the next layer to the surface. Second, the duration of the molten phase is decreased markedly by the inclusion of vaporization, as can be seen by comparing the positions of the cusps on the time scale in Figs. 5.1 and 5.5. This is a direct result of the decrease in the total energy in the system, caused by vaporization, which means there is less energy to diffuse away from the hot liquid layer near the surface. Third, the maximum liquid layer thickness decreases, as can be seen by comparing the maxima in Figs. 5.2 and 5.6. The decrease in the molten layer thickness is directly attributable to the decrease in the energy available to the system for melting due to vaporization. Finally, Fig. 5.7 shows that the magnitude of the melt front velocity remains essentially unchanged from the calculations where vaporization is not included in the calculation.

The result of including vaporization in these calculations is a decrease in the disorder layer thickness remaining after laser melting and resolidification. This is illustrated in a summary of the results of the calculations including vaporization in Figs. 5.8 and 5.9. The calculations in Fig. 5.9, carried out for both a 30nsec pulsed ruby laser and a 25nsec pulsed KrF excimer laser, show that the measured and calculated disorder layer thicknesses are in agreement over a large range of pulse energy densities. The calculated amount of vaporized material is also in good agreement with the amount of vaporized material measured using an ion implanted marker and the RBS technique. The differences between the calculation and experiment may be due to uncertainty in the free energy functions for the carbon species. The exponential dependence of the C_n vapor pressure on its free energy function means that small errors in the free energy function could cause significant errors. Calculations including carbon species C_8 and higher do not alter the results significantly using the free energy function model. This is primarily due to the larger heat of vaporization needed

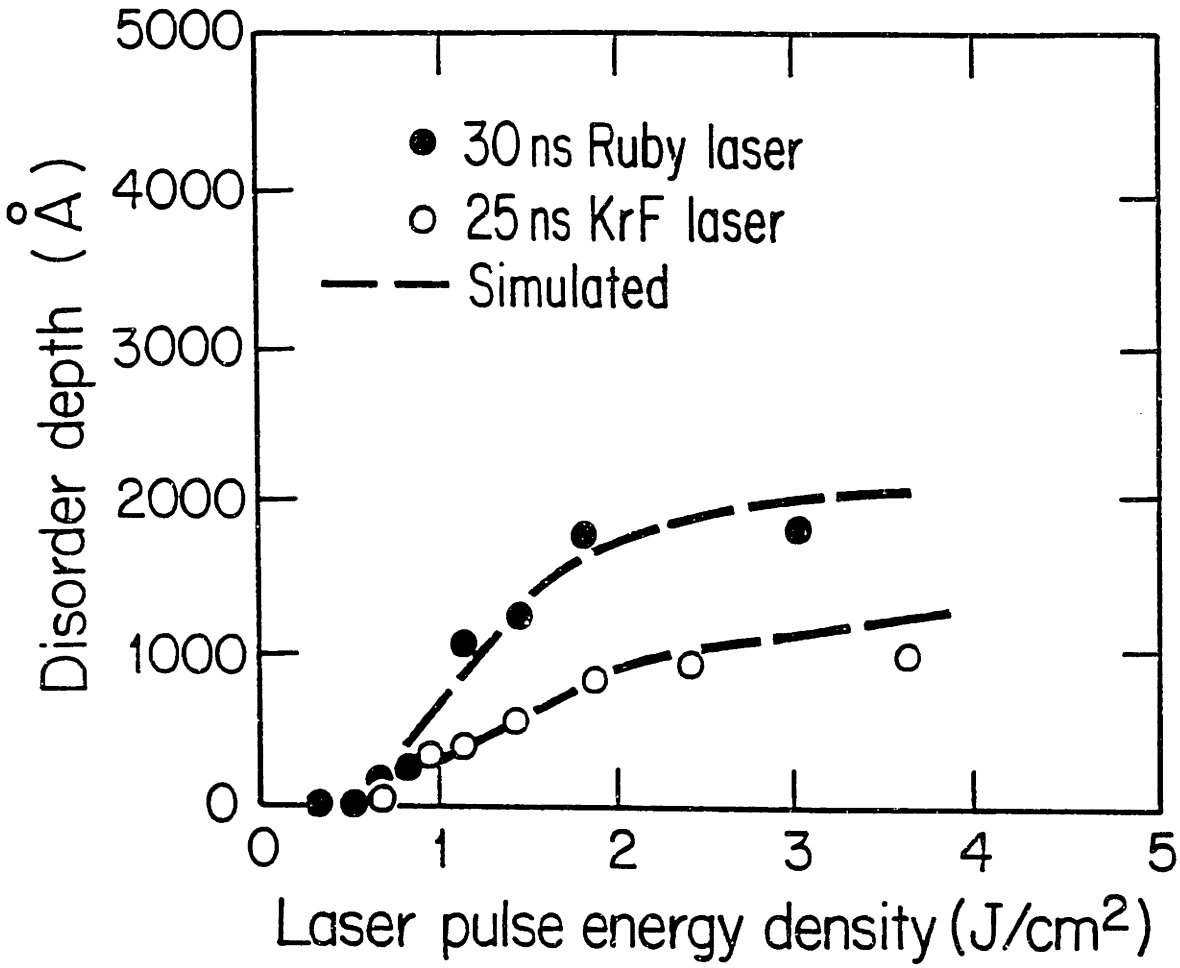

Figure 5.9: Comparison of the disorder layer thickness remaining after laser heating with calculated values using a model which includes vaporization. The comparison is made for both a 30nsec pulsed ruby laser and a 25nsec pulsed KrF laser.

to evolve larger species.

The results of the calculations for pulsed laser heating indicate that the liquid metal model for liquid carbon describes the properties of liquid carbon well. The free energy function model used to describe the vaporization of carbon also agrees with experimental results with an acceptable margin of error.

5.5 Picosecond Pulse Laser Heating

5.5.1 General Considerations

In attempting to overcome some of the difficulties encountered in doing transient optical measurements on liquid carbon during pulsed laser heating (see chapter 3), a Nd:YaG 20psec pulsed laser was employed to melt graphite. The picosecond time scale is also interesting because the energy in the laser pulse can be introduced into the solid surface faster than it can diffuse away from the surface. This means that less energy is needed to melt the surface of graphite for 20psec laser pulses compared to pulses of 30nsec duration. Using this fact, the melting temperature and the heat of fusion used in the calculations can be shown to be close to the values inferred from pulsed laser heating on the nanosecond time scale.

The heat flow calculations for picosecond pulse laser heating may be carried out in the same way as those for the nanosecond pulse case providing the electron–phonon scattering time, t_{ep}, is much shorter than the laser pulse duration. If t_{ep} is not shorter than the laser pulse duration, the diffusion of the excited carriers and the decay mechanisms for the carriers must be considered to obtain accurate results.

Fortunately, graphite is a semimetal and an estimate for t_{ep} may be obtained

from the electrical resistivity, ρ_e, from

$$t_{ep} \simeq \frac{m^*}{ne^2\rho_e} \tag{5.42}$$

where m^* is the effective mass of the carriers and n is the carrier density. Using appropriate values for holes and electrons in graphite[14], we find $t_{ep} \simeq 8 \times 10^{-13}$sec. Since this estimate for t_{ep} is much smaller than the laser pulse duration, the same formalism used to calculate the heat flow for 30nsec pulsed laser heating may be employed in calculating the heat flow for 20psec pulsed laser heating in graphite.

5.5.2 Time and Space Elements and Boundary Conditions

Since the laser pulse duration is now 20psec as opposed to 30nsec as in the previous sections, the time and space parameters must be adjusted accordingly. Since the calculation is still bound by the same constraints on the optical aborption, the space element is again taken as $\epsilon = 100$Å. The choice of ϵ to be smaller than 100Å will make the quantitative results of the calculation slightly different than the results obtained when $\epsilon = 100$Å. The ϵ we have chosen satisfies the physical constraint for energy absorption and the condition in Eq. 5.24 so that the errors in the calculation do not grow. The results obtained with $\epsilon = 100$Å will not be very different than the results which would be obtained with a smaller ϵ with an added bonus of reducing the time necessary to do the calculation.

Since ϵ is the same as in the nanosecond case, the restrictions on the time element τ will be the same as before. However, for our calculation to be meaningful for times during the laser pulse, the time element must be chosen to be small compared to the laser pulse duration. For the calculations carried out here, $\tau = 10^{-14}$sec was used.

The boundary conditions for the picosecond pulse calculations are the same as the boundary conditions for the nanosecond pulse calculation. The flow of heat out of the surface is considered to be zero as in Eq. 5.32 and the thermal gradient at the deepest layer is considered to be zero as in Eq. 5.37.

5.5.3 Results of Calculations

The calculations for picosecond pulse laser heating of graphite were carried out for a frequency doubled Nd:YaG laser (532nm) emitting pulses of 20psec duration. The thermal properties for the solid are again those given in chapter 2 and the thermal properties of liquid carbon were taken from the liquid metal model described in chapter 4. The calculations included the effects of carbon vaporization using the free energy function model in section 5.2.2.

The temperature versus time profiles for laser pulses of $0.2J/cm^2$ and $1.0J/cm^2$ appear in Figs. 5.10 and 5.11, respectively. In many respects, the temperature versus time profiles in Figs. 5.10 and 5.11 are similar to those for nanosecond pulse laser heating. During the laser pulse, there is a sharp rise in the temperature of the layers within an optical skin depth. The surface layers then become molten when they have absorbed enough energy. After becoming molten, the liquid is heated by the laser. The differences between the two sets of profiles in Figs. 5.10 and 5.11 has to do with the difference in the laser pulse energy density.

Figure 5.10 contains the temperature versus time profile for the surface layer, the last layer which becomes completely molten lying 100Å below the surface, and the first layer which remains completely solid lying 300Å below the surface for graphite irradiated with a $0.2J/cm^2$ laser pulse. The profiles in Fig. 5.10 show that the temperature of the surface layer becomes much larger than the melting temperature at 4450K and remains at such high temperatures

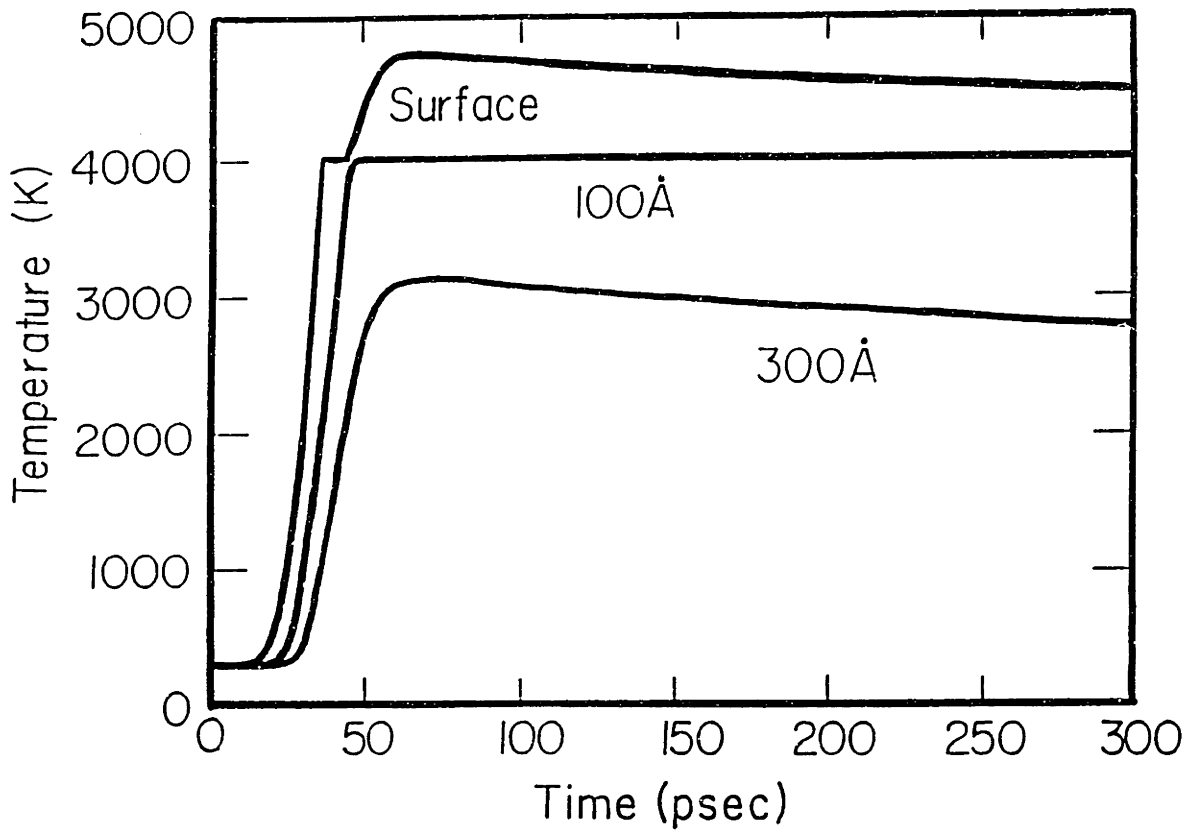

Figure 5.10: The temperature versus time profiles for graphite melted with a 20psec frequency doubled Nd:YaG laser pulse ($0.2J/cm^2$). Note that the temperature of the surface layer remains far above the melting temperature due to the short time scale.

long after the laser pulse. This demonstrates that the flow of heat in the liquid is dependent on the thermal parameters of the liquid and not simply on the shape of the laser pulse which is not completely clear from the calculations in the nanosecond regime. Also note that in Fig. 5.10 the profile representing the surface layer remains intact even though the temperature of the layer is near or above the boiling point determined in section 5.4. This means that the vaporization of carbon is not significant via equilibrium vaporization mechanisms for the $0.2J/cm^2$ laser pulse for times on the order of the laser pulse duration. This does not, however, eliminate the possibility of superheating the liquid or of nonequilibrium vaporization mechanisms, such as plasma formation above the surface of the graphite during and immediately after the irradiating laser pulse.

The maximum thickness of the liquid layer generated for a $0.2J/cm^2$, 20psec laser pulse may be determined from Fig. 5.10 since no additional energy enters the system after the laser pulse is over. From Fig. 5.10 the maximum liquid layer thickness is 200Å. According to the liquid metal model, a 200Å liquid layer thickness should be sufficient to determine the optical properties of liquid carbon using transient optical techniques since the absorption depth for optical wave lengths is $\sim$ 200Å.

The temperature versus time profiles for a $1.0J/cm^2$ 20psec laser pulse are shown in Fig. 5.11 and are similar to temperature versus time profiles for 30nsec pulse laser heating at high laser pulse energy density. The profile for the surface layer is shown to end abruptly indicating that the surface layer has vaporized. The next profile shown in the figure is the profile for a layer which originally lies 1100Å below the surface. This indicates that $\sim$ 1000Å of material have vaporized in a time period of 60psec. Since it is known that ionized vapor species are contained in the vapor created by pulsed laser heating (see chap-

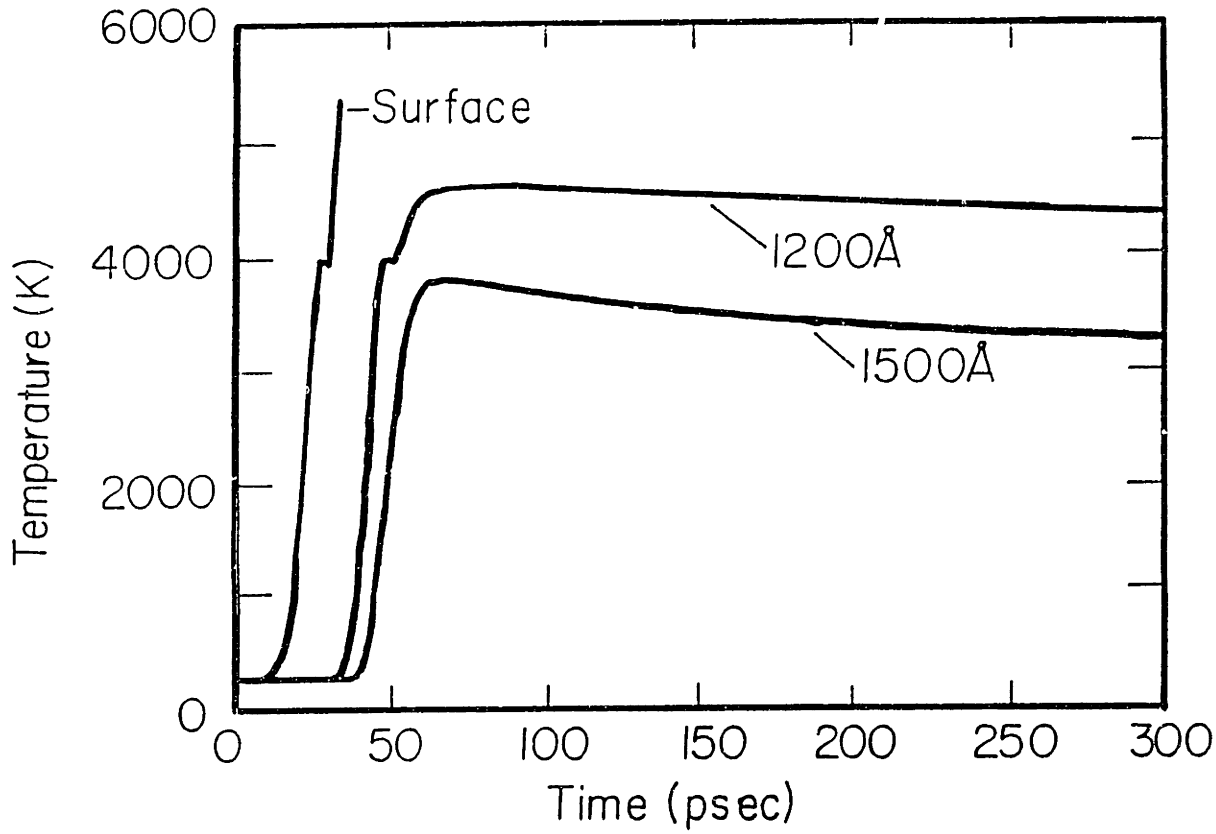

Figure 5.11: The temperature versus time profiles for graphite melted with a 20psec frequency doubled Nd:YaG laser pulse ($1.0 J/cm^2$).

ter 3), this result may cast doubt on the validity of transient optical measurements on a 100psec time scale since a large amount of ionized carbon vapor can change the optical properties of the space above the laser irradiated region. In addition, since the vaporization model used in the calculations consistently underestimates the amount of carbon lost to vaporization, the calculated vaporization results may also be in significant error for the calculation carried out for $0.2J/cm^2$.

The final profile shown in Fig. 5.11 is for the layer which originally lies 1300Å below the surface and is the first layer which does not melt at all. Since no more energy enters the system after the laser pulse is over, the maximium liquid layer thickness is the thickness of the liquid layer in Fig. 5.11 which is 200Å.

Because it is necessary to focus 20psec laser pulses down to an area of $\sim 10^{-4}cm^2$, no experimental measurements of the disorder layer thickness or the amount of vaporized material can be made using RBS and ion channeling as was done for nanosecond laser heating in section 3.4. The one thing that can compared between the calculations and experimentally measured quantities is the laser pulse energy density required to melt the surface. As discussed in section 3.8 the melting threshold for a frequency doubled Nd:YaG 20psec pulse laser is $\sim 0.14J/cm^2$. When the calculation is done for a 20psec frequency doubled Nd:YaG (532nm) laser pulse with an energy density of $0.14J/cm^2$ the surface layer is indeed found to melt. This means that the total energy per carbon atom needed to raise the temperature to the melting temperature (4450K) and to supply the heat of fusion (105kJ/mole), is close to the value inferred from pulsed laser heating on the nanosecond time scale. This strongly suggests that the melting temperature and heat of fusion during pulse laser heating on the nanosecond and picosecond time scales are the same.

Transient reflectivity measurements on both the nanosecond and picosecond time scale initially showed there is a drop in the reflectivity of graphite during pulsed laser heating (see section 3.4.3). By using transient optical transmission above the laser heated surface, the drop in the reflectivity for nanosecond pulse laser heating could be explained by the evolution of carbon vapor species. Similar measurements on the picosecond time scale are more difficult to make. We have shown in section 5.4 that the amount of vaporized material for nanosecond pulse laser heating can be calculated using the free energy function model in section 5.2.2. Since the results of the same calculations for picosecond pulse laser heating predict there will also be vaporization, the decrease in the reflectivity observed during transient reflectivity measurements on the picosecond time scale may also be explained by carbon vaporization and the ionized carbon associated with the carbon vapor.

5.6 Current Pulse Heating

5.6.1 General Considerations

The current pulse heating technique used to melt graphite fibers can be modeled using the finite difference method as well. The differences bewtween modeling pulsed current heating and pulsed laser heating mainly concern themselves with the geometry of the heating technique. For pulsed laser heating, the energy from the laser pulse is deposited at the surface of a sample. In contrast, pulsed current heating deposits energy into the solid through the entire volume being considered by the calculation.

Graphite fibers are ideal for use in a one dimensional calculation of heat flow. The large aspect ratio of their length to their width forms a natural one dimensional system. To calculate the heat flow in graphite fibers due to pulsed current heating, the fibers are divided into segments along the fiber axis to

form a network of series resistors. Each of the resistors is heated ohmically by the current which passes through the fiber segment. Heating may also occur as the result of diffusion from neighboring elements.

5.6.2 The Heat Source Term

For pulsed current heating, the heat source term becomes the ohmic heating term

$$S(\vec{x},t) = \beta(\vec{x},t)I(\vec{x},t)^2R(\vec{x},t) \tag{5.43}$$

where I is the current through the fiber, R is the resistance of the fiber, and β is a factor accounting for changes in the cross–sectional area of the fiber along the fiber length.

The heat source term can again be reduced to one dimensional form by noting that heat loss through the cylindrical surface of the graphite fiber will be negligible compared to the input power by the current pulse. An additional assumption is that the properties of graphite fibers are uniform across their diameters. Using the same arguments for the current pulse heating that have been made for pulsed laser heating, concerning blackbody radiation and thermal convection, Eq. 5.43 can be simplified to

$$S(z,t) = \beta(z,t)I^2R(z,t) \tag{5.44}$$

where z is the coordinate along the fiber axis and the heat source term is now expressed in terms of a single dimension.

The function β is used to simulate the variations in the diameter of a graphite fibers along the fiber axis. The modulation of the fiber diameter is necessary to simulate "hot" spots along the fiber length due to constrictions and heat sinks along the fiber due to sections of the fiber which have diameters larger than the mean fiber diameter. The β used in the calculations has the

form

$$\beta(z,t) = \frac{1.}{1 + 0.05\sin(2\pi nz)}\frac{1}{A} \tag{5.45}$$

where A is the mean cross–sectional area of the fiber and the factor $\sin(2\pi nz)$ puts n modulations of 5 percent in the fiber diameter which is common in graphite fibers[15]. In all of the calculations n was taken as $n = 10$.

5.6.3 Element Sizes

The choice of the space element size ϵ for pulsed current heating is determined by the modulation of the fiber diameter. In order to make sure the modulation of the fiber diameter is taken into account ϵ was chosen to be 1 percent of the fiber length. Since all of the fibers used in our experimental work were $\sim$ 2mm in length, the restriction on the choice of the time element τ is

$$\tau < \frac{\epsilon^2 C_p \rho}{2K_a} \sim 162\mu\text{sec} \tag{5.46}$$

In order to comply with the constraint in Eq. 5.46 and to simulate the experimental conditions described in section 3.7, τ was taken to be 10nsec.

5.6.4 Boundary Conditions

The electrical contacts to the graphite fibers are a large heat sink. The boundary conditions for the current pulse heating of graphite fibers must therefore account for the heat sinking of the ends of the fiber. The boundary conditions are therefore

$$T_0 = 293\text{K} \tag{5.47}$$

$$T_{n\epsilon} = 293\text{K} \tag{5.48}$$

where T_i is the temperature of the i^{th} space element. While these boundary conditions will not be strictly true for the actual experiment, they do serve to simulate the heat sink of the electrical contacts.

5.6.5 Results of Calculations

The calculations for pulsed current heating have been done for graphite fibers which have been previously heat treated at a temperature T_{HT} in the range $1700 < T_{HT} < 2850°C$. The thermal properties of the solid graphite fibers were again taken from experimental data and extrapolated up to the melting temperature as described in chapter 2. The thermal conductivity used in this calculation is the in–plane thermal conductivity of graphite since the graphite planes in the fibers are oriented along the fiber axis. The thermal properties for the liquid were taken from the liquid metal model calculations in chapter 4. The electrical resistivity for graphite fibers as a function of temperature and the fiber dimensions were derived from the experimental data as described in section 3.7.

The electrical circuit used to simulate the current pulse source is shown in Fig. 5.12. The pulsed current source was assumed to be a constant voltage source of 520V with an internal resistance of 48Ω. The current through the graphite fiber was then calculated by considering the graphite fiber in series with the internal resistance. The voltage was considered to be constant for a duration of 25μsec.

The calculation of the current through the fiber and the voltage across a graphite fiber ($T_{HT} = 2850°C$) as a function of time are shown in Fig. 5.13. From Fig. 5.13 the calculated voltage and current traces track the experimentally measured quantities well for the duration of the current pulse. The salient features of the voltage and current traces are the sharp increase in the current through the fiber and the sharp drop in the voltage across the graphite fiber at $\sim 6\mu$sec. This sharp change in the current and voltage is indicative of the melting transition to a liquid metal. The apparent noise seen in the calculated voltage and current is due to the melting of fiber segments which are close to

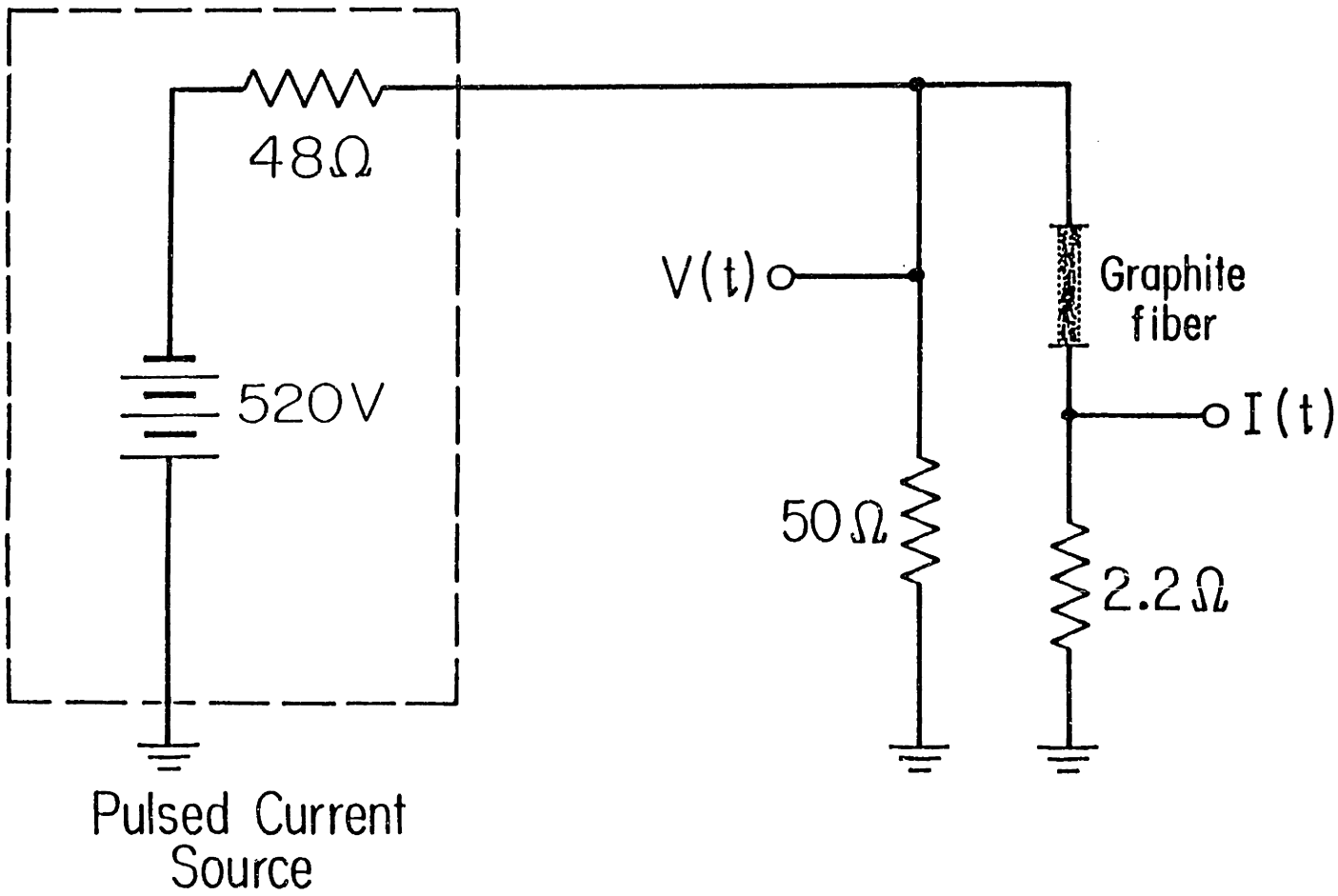

Figure 5.12: The electrical circuit used to simulate pulsed current heating. The circuit was assumed to put out a square voltage pulse of 520V and the current was determined by the fiber resistance and the internal resistance of the voltage supply of 48Ω.

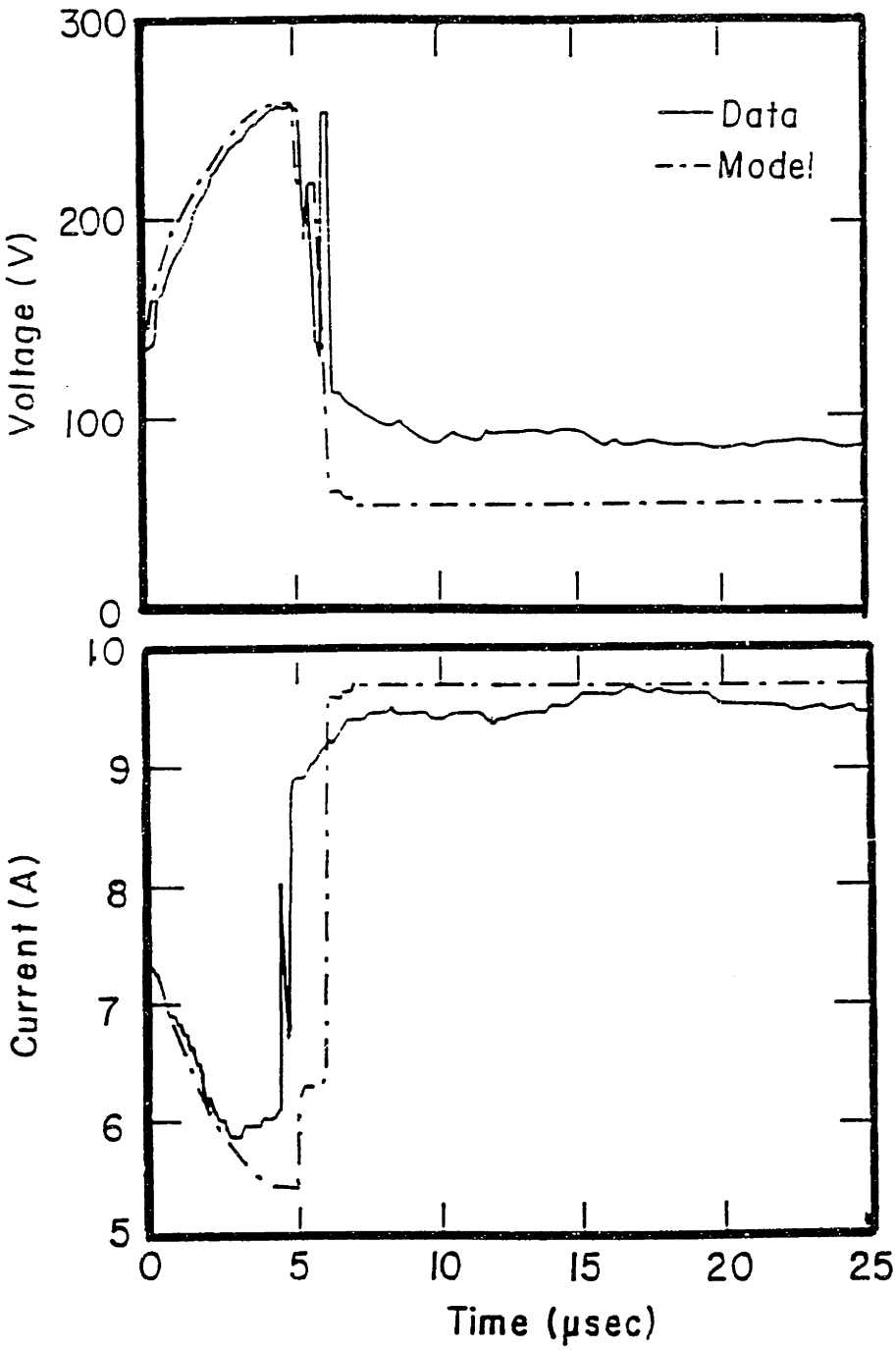

Figure 5.13: The calculated voltage across and the current through a graphite fiber (T_{HT} = 2850°C) as a function of time. The results are compared with experimental data for the same fiber.

the fiber ends.

The calculated resistance of the fiber as a function of time is compared to the resistance obtained from the measured current and voltage versus time in Fig. 5.14 for a fiber with $T_{HT} = 1700°C$ and a fiber with $T_{HT} = 2850°C$. The difference in the fiber resistances before melting is due to the different electrical conduction mechanisms in graphite fibers which have been heat treated at these two temperatures. As the fiber with $T_{HT} = 2850°C$ is heated, the resistance of the fiber increases because the electrical conductivity is due to carriers in the conduction band of the material and the carrier scattering is dominated by the electron–phonon interaction. For the fiber with $T_{HT} = 1700°C$, there is no band overlap and the electrical conduction is an activated process. Thus, as the fiber is heated, the carrier density increases, reducing the electrical resistance.

In both cases, the model calculation is able to reproduce the melting transitions in Fig. 5.14 and shows that the electrical resistivity predicted by the liquid metal model, $39.5\mu\Omega$–cm, is in good agreement with the experimental value. The noise which appears in the calculated traces after the melting transition is again due to the melting of segments which are close to the ends of the fiber.

The good fit of the calculated results with the experimental data for pulsed current heating also suggests that the model used for the high temperature properties of graphite is also valid. Recall that in chapter 2 the properties for high temperature graphite ($3000 < T < 4450K$) were calculated by extrapolating low temperature ($T < 3000K$) experimental data for the thermal properties of graphite up to the melting temperature. The good fit in the calculation using the extrapolated thermal properties would suggest that there are no intermediate phases between graphite and liquid carbon. Changes in the thermal properties of the graphite would be expected if there were an in-

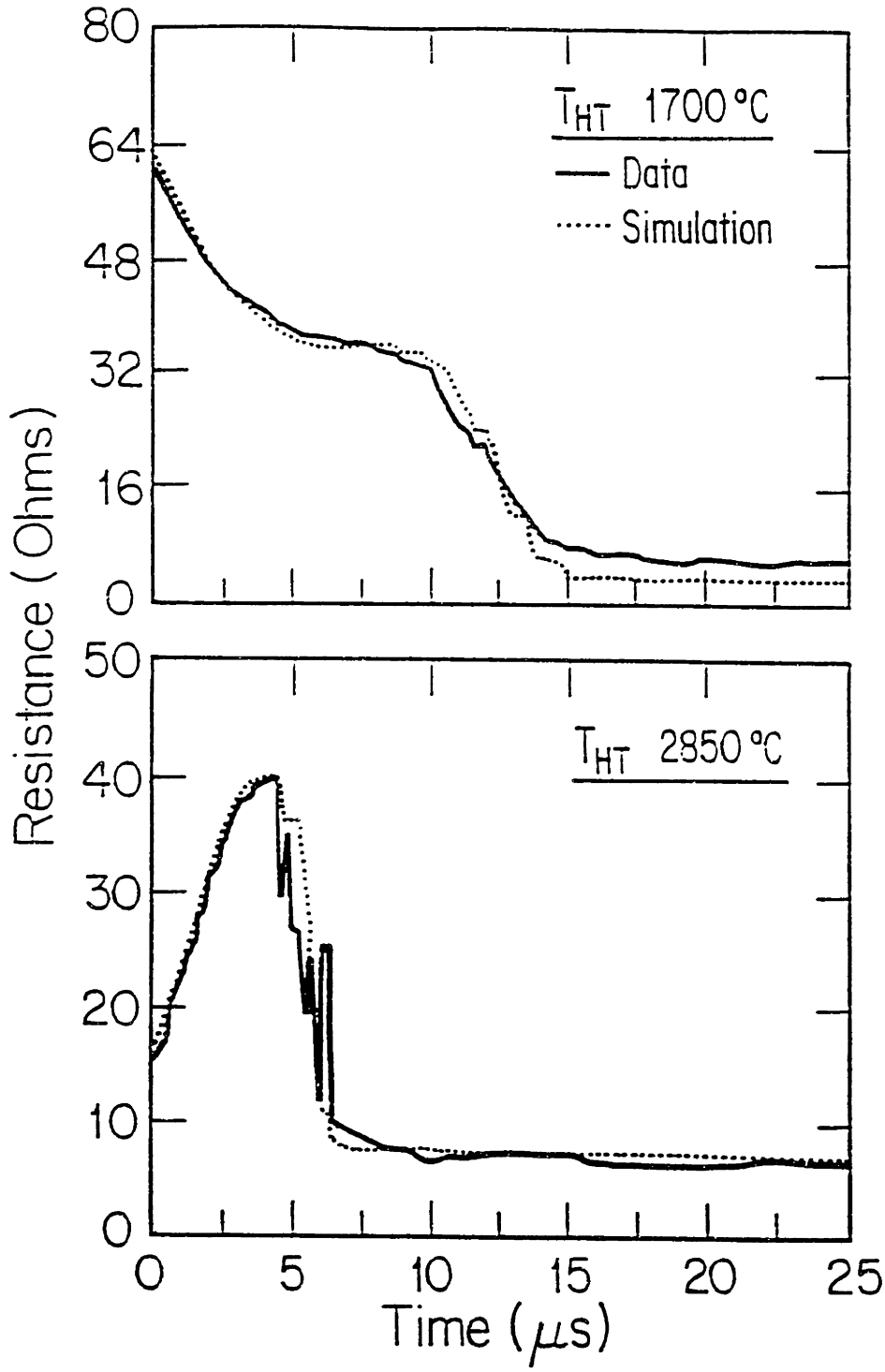

Figure 5.14: The observed and calculated resistance versus time for graphite fibers which have been pulse current heated. The measurements in (a) are for a graphite fiber with T_{HT} = 1700°C while in (b) the graphite fiber has T_{HT} = 2850°C. The shape of the resistance versus time curves for the solid fibers is indicative of the different electrical conduction processes associated with each heat treatment regime.

termediate molecular carbon phase[16] or an insulating liquid phase[17].

Experimental observations during pulsed current heating show that the temperature of the molten fiber becomes greater than 5000K (section 3.7). The calculated mean temperature ($\hat{T} = \frac{1}{n}\sum_{i=1}^{n} T_i$) of the fiber versus time appears in Fig. 5.15 for fibers with $T_{HT} = 2850°C$ and $T_{HT} = 1700°C$. The initial rise in the temperature shown in Fig. 5.15 is the solid fiber heating up. The temperature in both cases then reaches a plateau while the melting phase transition occurs. After the fiber has melted, the temperature is again allowed to rise as the liquid is heated. Note that the rate of the temperature rise is slower in the liquid than in the solid. This is due to the smaller electrical resistivity of the liquid relative to the hot solid which means that less power will be dissipated in the liquid column. The calculated mean temperature of fibers eventually does become greater than 5000K during the time of the current pulse.

It should be noted that the fiber temperatures shown in Fig. 5.15 appear to contradict the boiling point, T_V, established by pulsed laser heating. However, the calculation of the dissipated power in the liquid column is stongly influenced by the actual dimensions of the liquid column. Small variations in the diameter of the liquid column may reduce the calculated temperature of the fiber.

From these calculations, it is clear that the agreement with experimental results indicates that the electrical resistivity of liquid carbon is nearly temperature independent. This is also in agreement with theoretical predictions for polyvalent liquid metals described in chapter 4.

To show the importance of the modulation function β in the heat source term of Eq. 5.44, the calculation was performed with $\beta = 1$ (corresponding to a fiber with a uniform cross–section) for the fiber with $T_{HT} = 2850°C$ shown in Fig. 5.14b. The results of the calculation are shown in Fig. 5.16. The major differences between the two calculations are that the phase transition from the

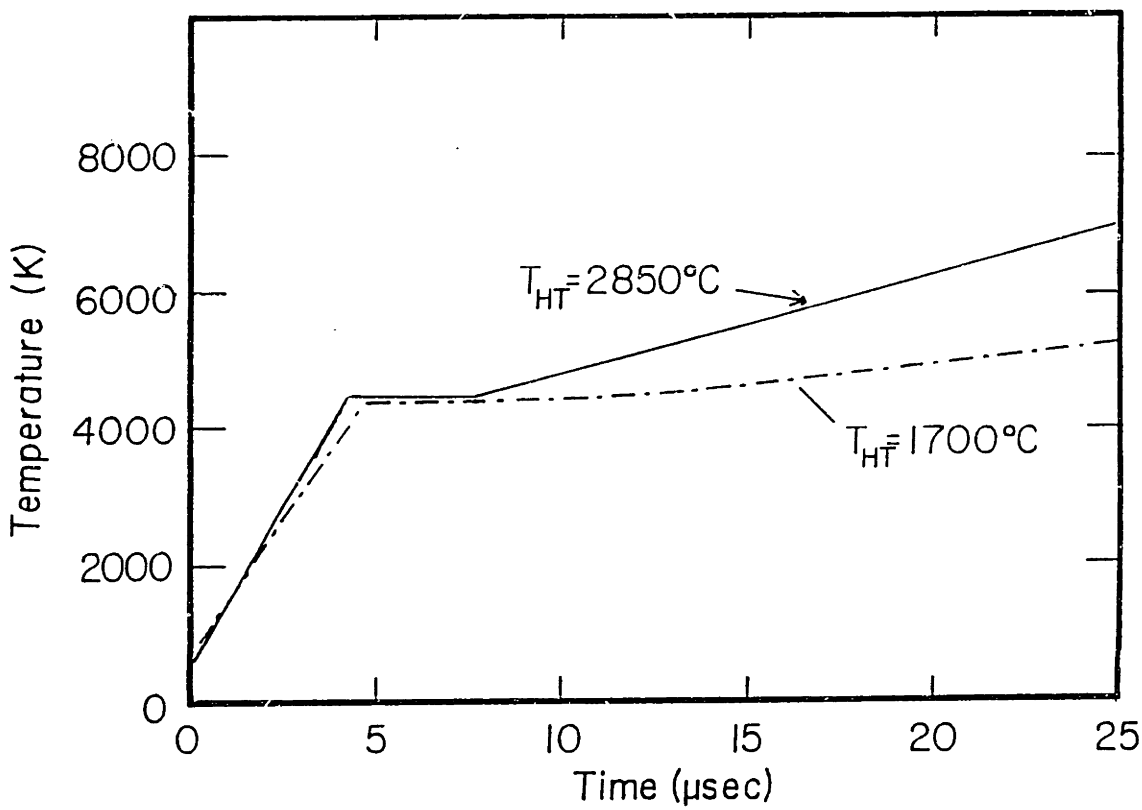

Figure 5.15: The mean calculated fiber temperature versus time for fibers with T_{HT} = 2850°C and T_{HT} = 1700°C. Note that the fiber temperature becomes larger than 5000K after the fiber has become molten in both cases.

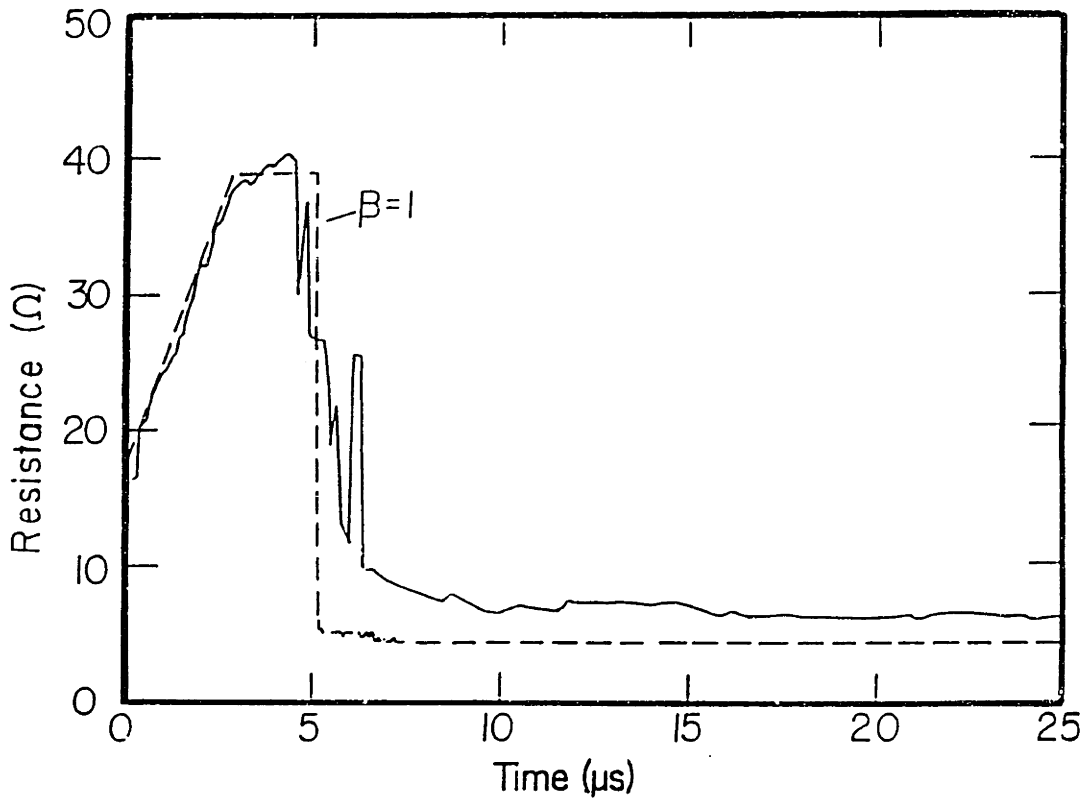

Figure 5.16: The resistance versus time for the calculation carried out for $\beta = 1$ on a fiber heat treated to 2850^{circ}K. Note that the transition from solid to liquid is much sharper indicating that the entire fiber melts simultaneously.

solid to liquid phase is much sharper in the case of $\beta = 1$ and that a plateau develops in the resistance while the fiber absorbs the heat of fusion. The sharp transition for the case of $\beta = 1$ indicates that a large portion of the fiber melts simultaneously. This is a direct result of the uniform temperature profile resulting from the perfect cylindrical geometry as shown in Fig. 5.17 for $\beta = 1$. Also shown in Fig. 5.17 is the temperature profile for β with the functional form given in Eq. 5.45. The plateau in the resistance for $\beta = 1$ forms since a large portion of the fiber reaches the melting temperature at the same time, so that most of the fiber will be absorbing the heat of fusion simultaneously. By modulating the fiber diameter with β in the form of Eq. 5.45, the segments of the fiber are not all at the same temperature and hence they will not all melt simultaneously. The result of modulating the fiber diameter is the broadening of the phase transition and the elimination of the plateau in the resistance.

Even though the temperature profile for the fiber with $\beta = 1$ is much more uniform than for the case when β is given by Eq. 5.45, the entire fiber is not at a uniform temperature. The ends of the fiber which are heat sunk to the electrical contacts are at a substantially lower temperature. The noise which occurs in the calculated resistance of the fiber for $\beta = 1$ after the large melting transition is due to the melting of segments close to the ends of the fiber.

5.7 Segregation and Solute Trapping

5.7.1 Introduction

Until now, the finite difference technique has been applied to solve the heat equation, Eq. 5.1, for laser heated and electric current pulse heated graphite. The finite difference method may in general be applied in solving any diffusion problem. In this section the finite difference method is applied in solving the diffusion equation for impurity diffusion in liquid carbon and incorporating

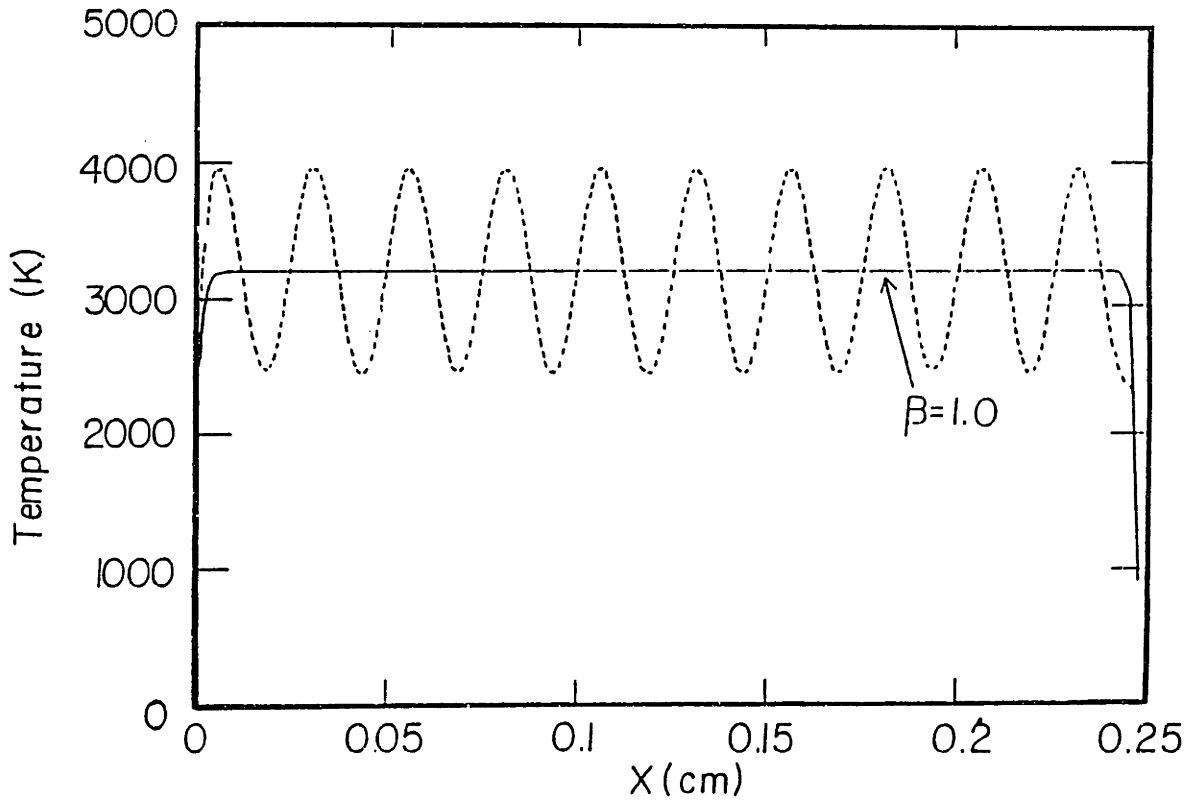

Figure 5.17: The fiber temperature profile for calculations done with $\beta = 1$ and β given by Eq. 5.45 for a graphite fiber with $T_{HT} = 2850°C$ two microseconds into the current pulse. Note that for $\beta = 1$ the temperature of the fiber is nearly uniform across the entire length of the fiber.

nonequilibrium segregation and solute trapping using the continuous growth model of Aziz[7] at the liquid–solid interface.

The calculations are carried out for a layer of liquid carbon generated by pulsed ruby laser heating. The melt front dynamics calculated in the heat flow calculations are used to determine the impurity segregation and solute trapping partition coefficient. The loss of carbon due to vaporization is also accounted for by using the heat flow calculations. The initial impurity profile in solid graphite is taken as the initial profile of ion implanted impurities in graphite measured using RBS.

5.7.2 The Diffusion Equation

The equation to be solved is

$$\frac{\partial N}{\partial t} = D_l \frac{\partial^2 N}{\partial z^2} \tag{5.49}$$

where N is the concentration of the impurity in a layer and D_l is the liquid diffusivity. There are two fundamental differences between Eq. 5.49 and the one dimensional heat equation, Eq. 5.2. First, there is no source term for impurities in Eq. 5.49 since no impurities are added during pulsed laser heating. The calculation utilizes an initial impurity distribution for ion implanted impurities measured using RBS. Second, the liquid diffusivity, D_l, is considered to be both temperature and concentration independent, unlike its thermal counterpart. The calculations of the previous sections show that the temperature of liquid carbon, formed by laser heating, remains close to the melting temperature for most of the time when the liquid state is present. Therefore, the temperature dependence of the liquid diffusivity will not be an important factor in the solution of Eq. 5.49. The independence of D_l on concentration is justified since the concentration of the ion implanted impurities in graphite is $\sim 10^{-3}$ per carbon atom.

The algebraic equations to be solved are the same as Eq. 5.15 without the last term on the right hand side. That is,

$$N_i(t+\tau) = N_i(t) + D_l\tau\left(\frac{N_{i+1}(t) + N_{i-1}(t) - 2N_i(t)}{\epsilon^2}\right) \tag{5.50}$$

where τ and ϵ are the time and space elements as before. Since the liquid diffusivity is assumed to be both temperature and concentration independent in these calculations, the interface diffusion coefficient in Eq. 5.13 reduces to D_l.

5.7.3 Segregation and Solute Trapping

The trapping of impurities by a liquid–solid interface is characterized by a partition coefficient k which is the ratio of the concentrations in the solidus and liquidus at the interface. Hence, k represents the fraction of impurities which will remain in the solid as the interface advances.

In the continuous growth model of Aziz[7], k is given by

$$k = \frac{v/v_D + k_e}{v/v_D + 1} \tag{5.51}$$

where v is the liquid–solid interface velocity, k_e is the equilibrium concentration of the impurity in the solid, and v_D is the diffusive speed of the liquid–solid interface given by the ratio of the interface diffusion coefficient and the width of the interface. For this calculation, the liquid–solid interface is assumed to be atomically sharp, so that the width of the interface is the mean atomic spacing between carbon atoms $w = 2.06$Å calculated from

$$w = \left(\frac{1}{n_i}\right)^{\frac{1}{3}} \tag{5.52}$$

where $n_i = 9\times10^{22}\text{cm}^{-3}$ is the atomic number density and the interface diffusion coefficient is taken as the diffusion coefficient of the liquid. When the liquid–solid interface advances the concentration of impurities remaining in the solid

is given by

$$N_s = kN_l \tag{5.53}$$

where the subscripts on N denote the liquid and solid phase.

5.7.4 Incorporation of Vaporization

The incorporation of vaporization in the impurity segregation problem in carbon is important for two reasons. First, as impurities diffuse toward the surface of the hot liquid, some impurities will be carried away as liquid carbon vaporizes. Second, and more important, the temperatures at which liquid carbon exists are far higher than the boiling point for the impurities introduced into the graphite. When the impurities segregate to the surface they may boil off of the surface due to the high temperatures. Consequently, the final concentration of impurities at the surface will be substantially smaller than might be expected.

The incorporation of the vaporization of liquid carbon can be accounted for by removing layers from the calculation based on the rate of vaporization of the liquid. The rate of liquid vaporization is determined from the heat flow calculations. To incorporate the loss of impurities at the surface due to the impurities boiling off, we consider the rate at which the surface cools and the solid state diffusion coefficients for graphite. The time required for the surface layer to cool below the boiling point, t_c, for the impurity in question is determined from the heat flow calculations. Using this time, we calculate the diffusion distance, d, for impurities in the surface layer as

$$d = (D_s t_c)^{\frac{1}{2}} \tag{5.54}$$

where D_s is the solid state diffusion coefficient for graphite. To account for the vaporization of the impurities, we say that all of the impurities within d of the

Impurity	E_p(J/cm^2)	t_c(nsec)	d(Å)
Ge	1.5	100	10
Ge	2.0	63	13
Ge	3.0	40	15
As	1.5	100	12

Table 5.2: The diffusion distances for impurities in disordered graphite used for calculating impurity losses due to vaporization. The solid state diffusion coefficient $D_s = 1.5 \times 10^{-7}$.

surface are able to diffuse to the surface and escape by vaporization. In our calculations, d is typically some fraction of the layer thickness ϵ so that the concentration of the impurities remaining after the sample has cooled, N_{0c}, is given by

$$N_{0c} = N_{0h}\left(1 - \frac{d}{\epsilon}\right) \tag{5.55}$$

where N_{0h} is the concentration before cooling. Table 5.2 lists the diffusion distances used for Ge and As. Note that the diffusion distance increases with increasing laser pulse energy density due to the longer times required for the heat to diffuse away from the hot surface. Also note that the diffusion distance for As is greater than the diffusion distance for Ge at the same laser pulse energy density due to the lower boiling point for As.

5.7.5 Calculation Procedure

The calculation is divided into three distinct parts. The first part is the calculation of the diffusion of impurities in the liquid layer which increases and decreases in size with the liquid–solid interface velocity. The loss of impurities due to the vaporization of liquid carbon is also contained in this part of the calculation. The second part of the calculation determines the amount of segregation and solute trapping that occurs as a result of the moving interface

using the continuous growth model of Aziz[18] as described above.

After the liquid–solid interface again reaches the surface of the graphite, the third part of the calculation accounts for the loss of impurities at the surface due to the boiling of the impurities and accounts for the resolution of experimental detectors. The loss of impurities due to boiling is accomplished using the diffusion model above. In order to account for the resolution of the detector used to measure the impurity distributions, the final result of the calculations are convoluted with the detector resolution of 25KeV.

5.8 Nonequilibrium Segregation and Solute Trapping in Laser Melted Graphite

5.8.1 Boundary Conditions

The boundary conditions used in this calculation are similar to those used for the heat flow calculation in the previous sections. Since the diffusion coefficient in the solid is many orders of magnitude smaller than in the liquid, no diffusion is assumed to occur in the solid. The condition for diffusion at the liquid–solid interface is that no diffusion occurs across the interface. Similarly, there is no diffusion out of the surface of the sample, so that the boundary conditions are the same as Eqs. 5.32 and 5.37

$$\left.\frac{\partial T}{\partial z}\right|_{z=0} = 0 \tag{5.56}$$

$$\left.\frac{\partial T}{\partial z}\right|_{z=n\epsilon} = 0 \tag{5.57}$$

where $n\epsilon$ is the last liquid layer.

5.8.2 Initial Conditions

Another difference between the heat flow calculations and the diffusion calculation is that the diffusion calculation has an initial impurity profile. The

initial impurity profiles used in the calculations were determined from RBS measurements of ion implanted graphite and are shown in Fig. 5.18. for initial distributions of ^{73}Ge implanted at 225KeV, ^{75}As implanted at 100KeV, and ^{75}As implanted at 230KeV.

5.8.3 Selection of the Time and Space Elements

The choice of τ and ϵ is again determined for the physical constraints and the condition in Eq. 5.24. The space element ϵ was chosen to be the resolution of our RBS measurements ($\sim$ 20Å). The determination of τ is now dependent on the condition in Eq. 5.24 which requires a knowledge of the liquid diffusion coefficient, D_l. In order to determine τ, we only need an order of magnitude estimate for D_l so a typical value for D_l will be appropriate for determining τ. From similar work in silicon, $D_l \sim 10^{-4}$cm^2/sec[7]. Using this value in the condition Eq. 5.24 we find

$$\tau < 4 \times 10^{-10}\text{sec} \tag{5.58}$$

For this calculation we have chosen $\tau = 10^{-10}$sec.

5.8.4 Results of Calculations

Calculations have been carried out for Ge implanted into graphite for a range of ruby laser pulse energy densities where the maximum penetration of the liquid–solid interface falls in the range of the implanted impurities and for large laser pulse energy densities, when the maximum penetration of the liquid–solid interface exceeds the range of the implanted impurities. The only free parameter in our calculations is the liquid diffusivity, D_l, which will be used to calculate the diffusive speed at the liquid–solid interface, v_D, used in the partition coefficient k.

The best value of the liquid diffusivity, D_l, for liquid carbon was deter-

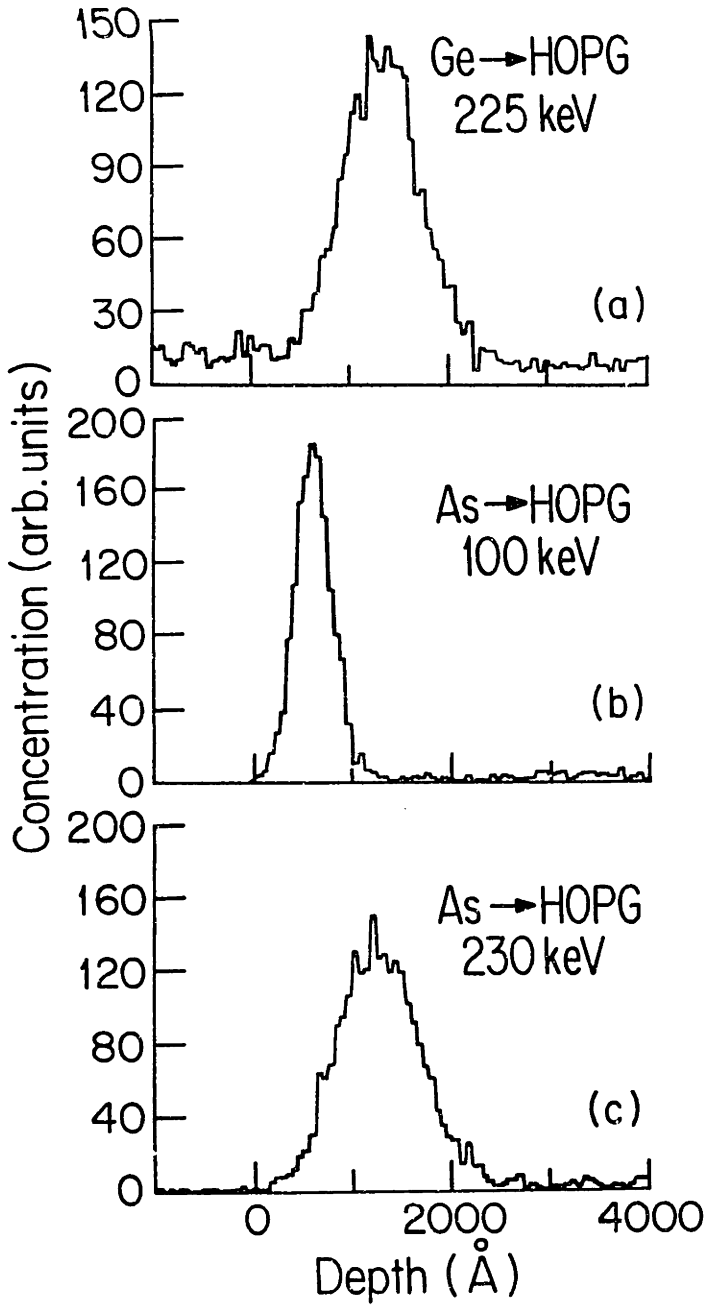

Figure 5.18: The initial distributions of impurities implanted in graphite. In (a) the distribution of ^{73}Ge implanted at 225KeV. In (b) and (c) the distributions of ^{75}As implanted in graphite at 100KeV and 230KeV respectively. Measurements of the distributions were made using RBS with 2MeV He^+

mined by obtaining the best fit to the distribution of Ge in graphite after being laser melted by a 30nsec pulsed ruby laser with a laser pulse energy density of 2.0J/cm^2. The redistribution caused by the 2.0J/cm^2 laser pulse was chosen for two reasons. First, the melt front penetrates into the impurity distribution, but does not surpass it. The importance of this is that we want to be assured that the error in D_l is minimized. Impurity vaporization at the surface, which will play a large role for the 3.0J/cm^2 laser pulse, and small amounts of impurity segregation (occurring for 1.5J/cm^2) could introduce substantial errors in determining D_l.

Figure 5.19 shows the results of the calculations compared to the experimentally measured Ge profile for three different values of D_l. In Fig. 5.19 the D_l which fits the data best is $D_l = 10^{-4}\text{cm}^2/\text{sec}$. The goodness of the fit was primarily determined by the fit of the profile in the region where no impurity segregation is expected and by the fit of the central region where impurity vaporization *will not* occur. One should note that the impurity vaporization model proposed in the previous section does fit the experimental data well for this case in both the magnitude and the integrated intensity of the surface impurity peak.

By using the results of the calculations shown in Fig. 5.19, other posible values for D_l can be excluded from consideration. If $D_l = 2.0 \times 10^{-4}\text{cm}^2/\text{sec}$, then too many Ge atoms diffuse to the surface and are removed from the graphite by vaporization. Similarly, if $D_l = 0.5 \times 10^{-4}\text{cm}^2/\text{sec}$, then too many Ge atoms are trapped by the rapidly moving liquid–solid interface. It should be noted that the peak which appears in the center of the profile for $D_l = 0.5 \times 10^{-4}\text{cm}^2/\text{sec}$ is due to the change in the partition coefficient k as the liquid–solid interface velocity changes. Values for D_l which are slightly smaller than $10^{-4}\text{cm}^2/\text{sec}$ may give better fits to the measured profile. However, the

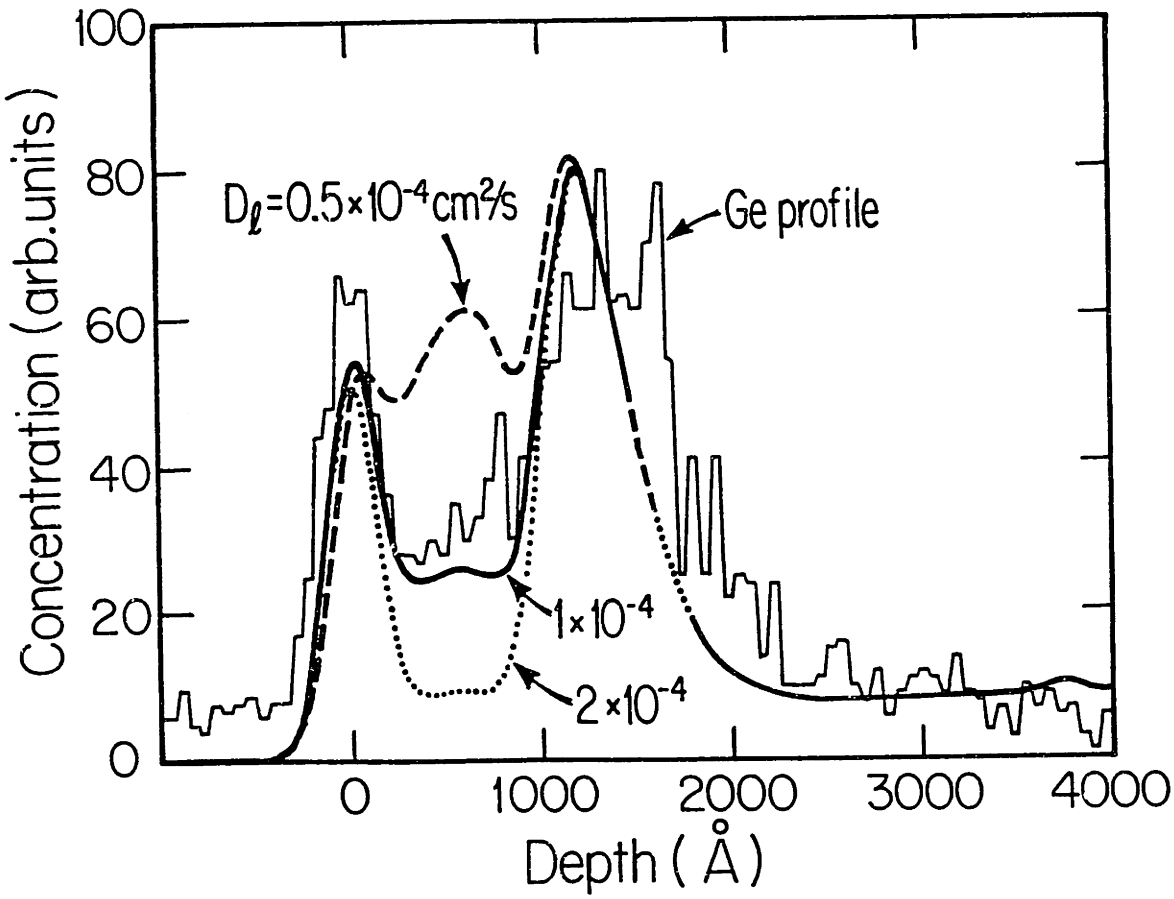

Figure 5.19: Comparison of the calculated Ge distribution to the measured impurity distribution (by RBS) of Ge in pulsed laser melted graphite for several values of the liquid diffusivity D_l. The laser pulse energy density was 2.0J/cm^2. The best value from these calculations is $D_l = 1.0 \times 10^{-4}$cm^2/sec while other values predict either too much diffusion or too much solute trapping.

accuracy with which we know the interface velocity is limited by the accuacy of our heat flow calculations, so that only an order of magnitude estimate can be made for the liquid diffusivity.

A comparison of our calculations to experimentally measured Ge profiles for several laser energy densities with $D_l = 10^{-4}\text{cm}^2/\text{sec}$ is shown in Fig. 5.20. In Fig. 5.20 the calculated profiles for all pulse ruby laser energy densities agree well with the measured Ge profiles after laser melting. The total integrated intensity of the Ge remaining in the graphite also agrees with the experimental values. In Fig. 5.20a the melt front generated by a $1.5\text{J}/\text{cm}^2$ ruby laser pulse just begins to penetrate the Ge distribution. Some of the impurities segregate to the surface while the rest of the Ge distribution remains intact. For the $2.0\text{J}/\text{cm}^2$ case, the melt front penetrates deeper into the Ge distribution and a large fraction of the Ge atoms diffuse to the surface. The velocity of the resolidification in the $2.0\text{J}/\text{cm}^2$ case is smaller than in the $1.5\text{J}/\text{cm}^2$ case so that a smaller number of impurities lie between the undisturbed portion of the distribution and the surface. Finally, in the $3.0\text{J}/\text{cm}^2$ case, the melt front overruns the Ge distribution and all of the Ge diffuses throughout the liquid. Because the resolidification velocity of the molten carbon is less than the $2.0\text{J}/\text{cm}^2$ case, even fewer impurities remain between the position of the original ditribution ($\sim 1500\text{Å}$) and the surface.

The importance of accounting for the loss of impurities at the surface due to the vaporization of the impurities is illustrated in Fig. 5.21. When the additional loss of Ge is not accounted for at the surface due to Ge vaporization, the calculated surface concentration of the Ge becomes much larger than the measured concentrations. However, the impurity profile beneath the surface remains unaffected showing that changes in the liquid diffusivity cannot account for the disagreement.

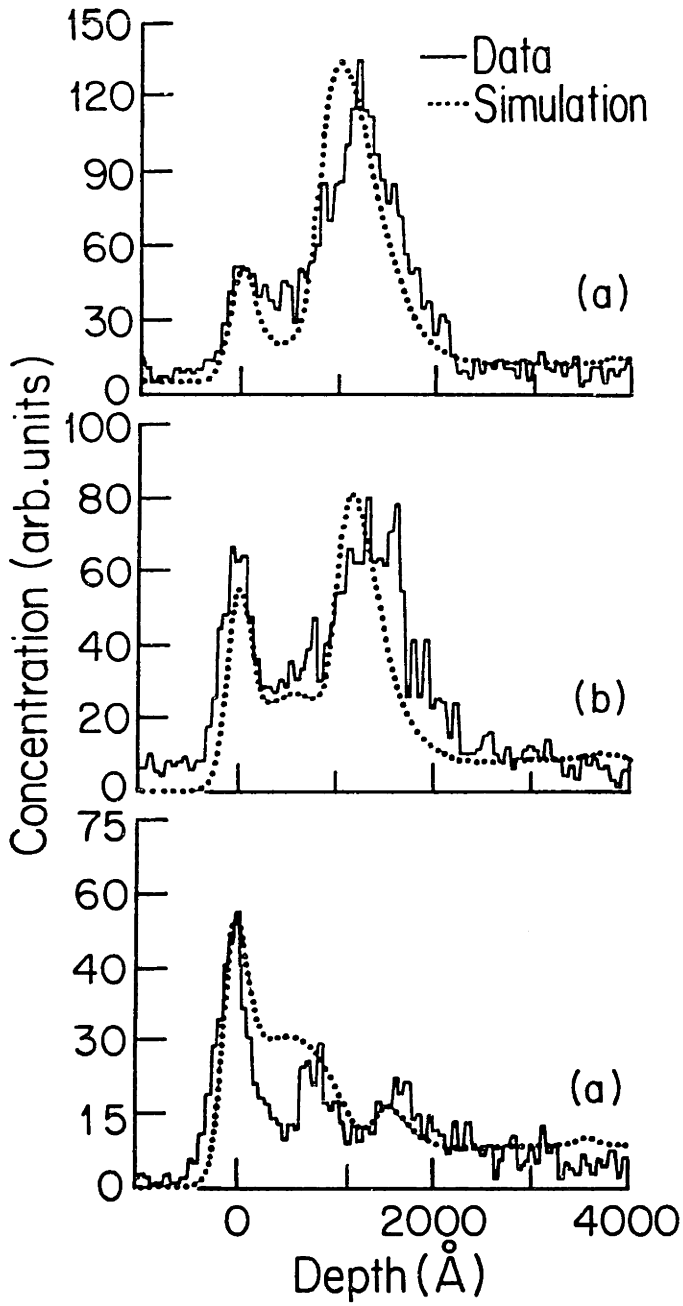

Figure 5.20: Comparison of the calculated redistribution of implanted Ge impurities to measured Ge profiles using RBS for laser melted graphite with laser pulse energy densities of 1.5, 2.0, and 3.0 J/cm^2.

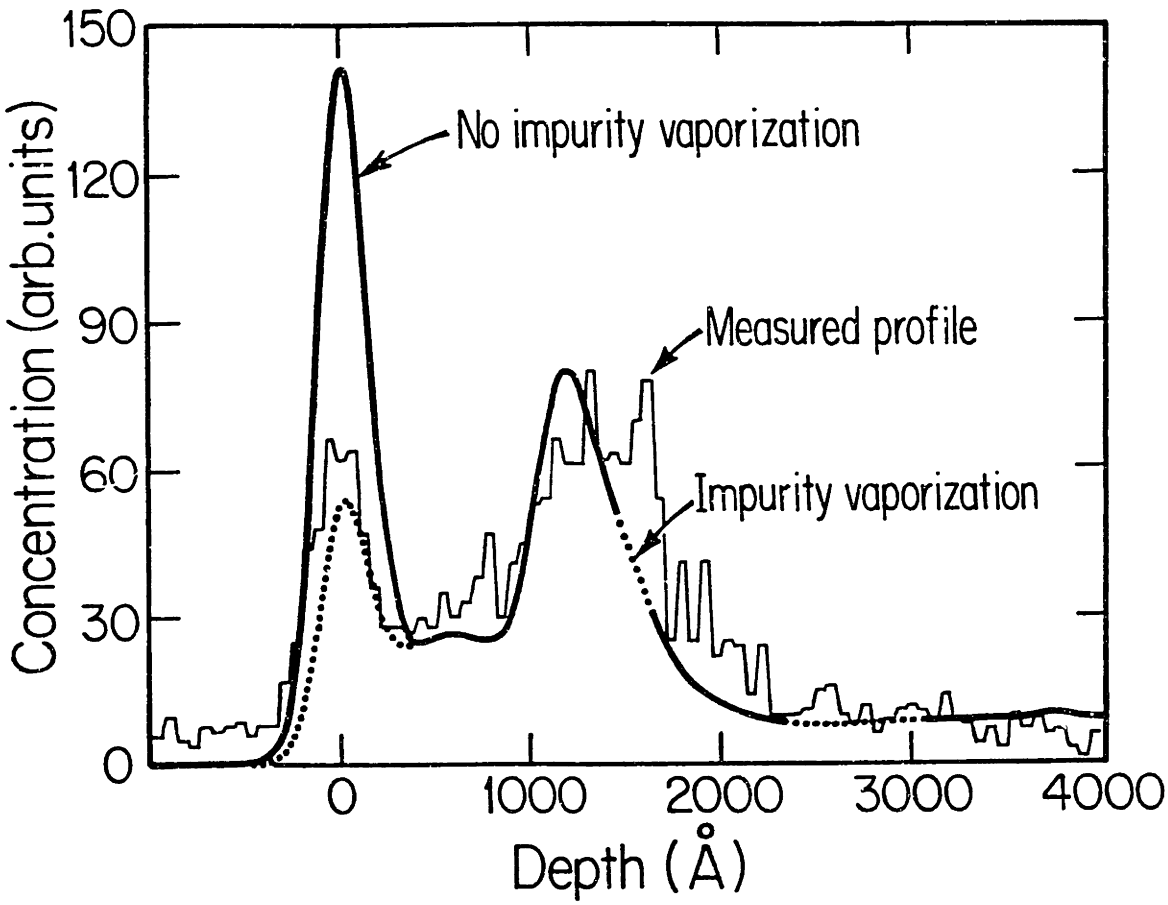

Figure 5.21: Comparison of the calculated Ge profile with and without impurity vaporization with the (RBS) measured Ge profile after pulsed laser melting. Note the much larger concentration of Ge at the surface in the calculated profiles for no impurity vaporization which does not agree with the measured Ge profiles using RBS.

The calculations were also carried out for ^{75}As implanted into graphite at 100KeV and 230KeV to show the insensitivity of the calculation to the initial impurity profile. The calculations included impurity vaporization of As on the hot resolidified carbon surface. The results of the calculations are shown in Fig. 5.22 where the calculated profiles are compared to experimentally measured profiles for graphite irradiated with 1.5J/cm^2. The liquid diffusivity is again taken as $D_l = 10^{-4}$cm^2/sec. From Fig. 5.22, the calculation is shown to be independent of the initial impurity position demonstrating that only the dynamics of the liquid–solid interface are important. Additionally, the effect of impurity vaporization again substantially decreases the concentration of impurities on the surface of the resolidified carbon.

The only free parameter in these calculations is the liquid diffusivity, D_l which is best fit by $D_l = 10^{-4}$cm^2/sec. This value of D_l is in qualitative agreement with the liquid diffusivity for other liquids including liquid silicon[7]. The diffusive speed of the liquid–solid interface is then

$$v_D = \frac{D_l}{w} = 25\text{m/sec} \tag{5.59}$$

where w is the interface width, $w = 2.06$Å. This velocity is also in good agreement with the diffusive speed determined for liquid silicon by Aziz *et. al.*[7] of $v_D \sim 32$m/sec. The partition coefficient k for the liquid–solid interface in carbon is plotted in Fig. 5.23 as a function of the liquid–solid interface velocity. For the velocities characteristic of pulsed laser melting with ruby laser pulse energy densities in the range $0 < E_p < 3.0$J/cm^2 the partition coefficient k has values in the range $0 < k < 0.17$.

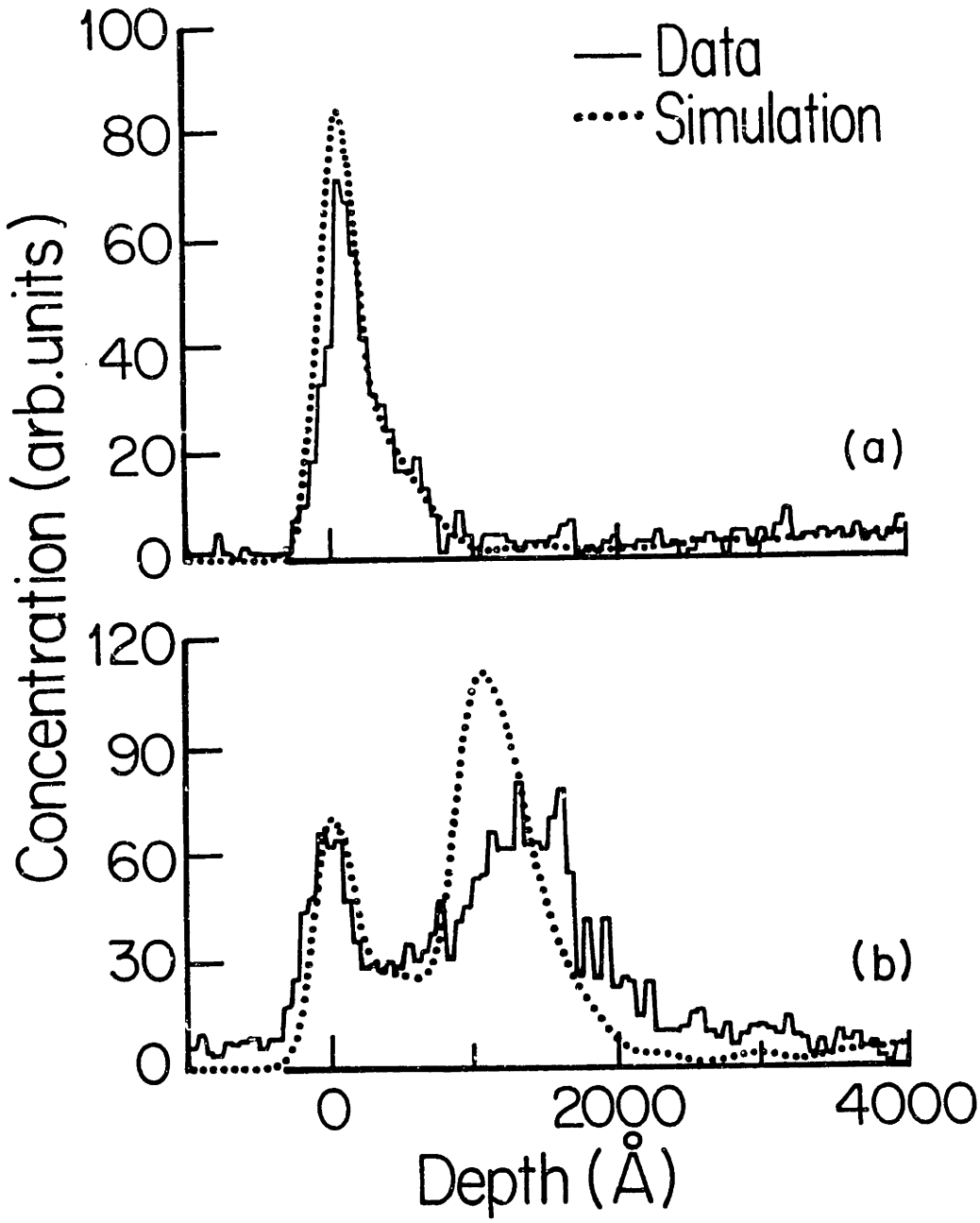

Figure 5.22: Comparison of calculated As profiles with experimentally measured As profiles. In (a) the As was originally implanted at 100KeV and in (b) at 230KeV. The ruby laser pulse energy density in both cases was $1.5 J/cm^2$. Impurity vaporization at the surface was included in the calculations.

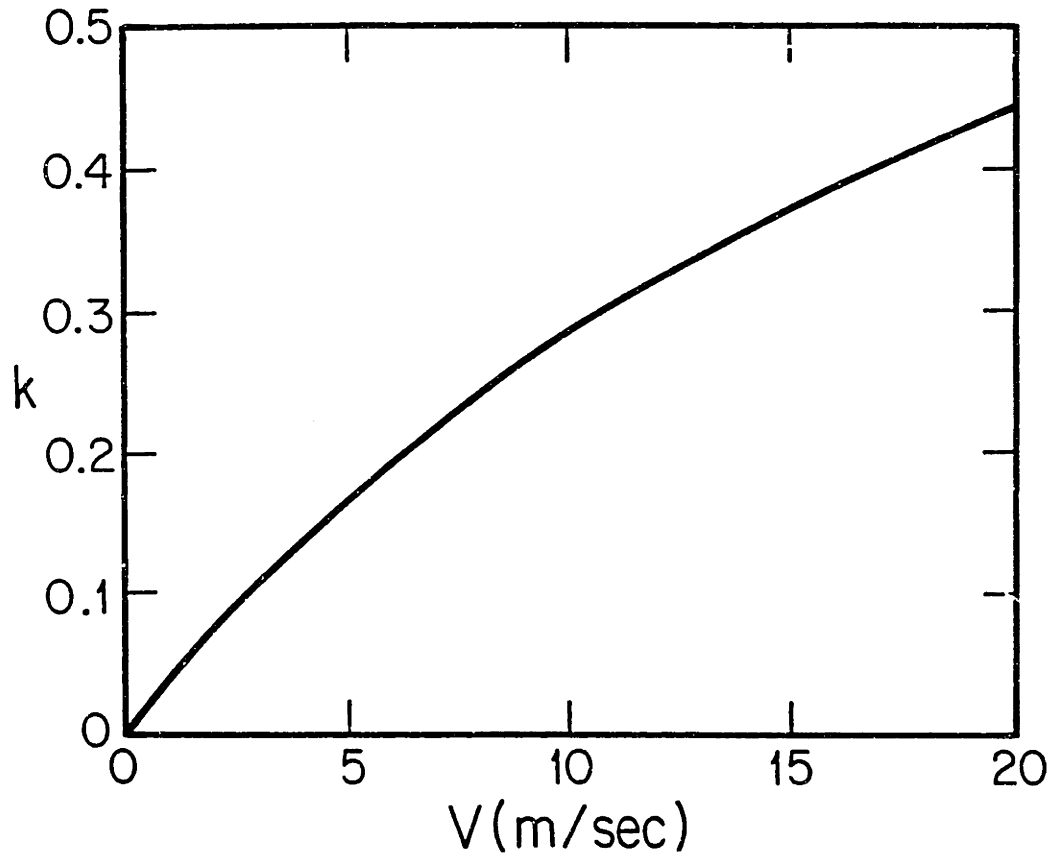

Figure 5.23: The partition coefficient k for the liquid–solid interface in carbon as a function of the interface velocity. Noted in the plot are the interface velocities characteristic of pulsed laser melted carbon with energy densities in the range $0 < E_p < 3.0\text{J/cm}^2$.

5.9 Summary

In this chapter, the diffusion equation is solved numerically for several geometries of pulsed laser and pulsed current heating in graphite using the finite difference technique. The model calculations utilize experimental data for the thermal properties of solid graphite, while the thermal properties of the liquid carbon have been calculated using a liquid metal model.

Using the diffusion equation to solve the heat flow problem in laser heated graphite, the basic calculation, neglecting vaporization, shows that the liquid metal model for the liquid is in satisfactory agreement with experimental data of the disorder layer thickness for laser pulse energy densities just above the melt threshold for 30nsec pulsed ruby laser heated graphite. Attributing the disagreement for large laser pulse energy densities to vaporization, the calculation was extended to include vaporization using the free energy functions for carbon vapor species. The results of these calculations show that vaporization accounts for the disagreement between earlier calculations and measurements of the remaining disorder layer thickness of carbon after pulsed laser melting with the ruby laser. The calculated amount of vaporized carbon is also in good agreement with experimental data. The calculations including vaporization also suggest a value for the boiling point, T_V, of liquid carbon. The values of other important properties suggested by these calculations are given in table 5.3.

The calculations were also carried out with an insulating model for liquid carbon. The results from the basic calculation show that the insulating model for the liquid does not give satisfactory agreement with experimental measurements of the disorder layer thickness at any laser pulse energy density. This suggests that the insulating models for liquid carbon are not correct.

Heat flow calculations were then done for 20psec pulse laser heating in an

attempt to show that transient optical measurements on a more rapid time scale could be informative. The calculations show that for small laser pulse energy densities (just above threshold energy density for melting) that there appears to be very little carbon vaporization for times on the order of the laser pulse duration. It is also found that the molten layer thickness should be large enough to be sensitive to optical probes. However, for laser pulse energy densities larger than the threshold value for melting with 20psec pulses, carbon vaporization (and the associated ionized carbon molecules) is significant; this might cast doubt on the validity of the present interpretation of optical data. Since the model we have used consistently underestimates the amount of vaporized carbon, optical data for small laser pulse energy densities may also be called into question.

The rapid vaporization of a thick layer of carbon during picosecond pulsed laser heating may induce a large pressure on the surface of the graphite causing an additional solid state phase transition to diamond, or, a melting transition in a part of the phase diagram where liquid carbon is less conducting than in the liquid metal model used in the present calculation. While an increase in the pressure may help to explain some experimental measurements of the transient electrical conductivity during picosecond pulsed laser heating[19], optical measurements will be more sensitive to the evolution of ionized carbon atoms and molecules. The present calculations cannot address these possibilities since the thermal properties of graphite and liquid carbon must be known as functions of both temperature and pressure.

The calculations for picosecond pulse laser heating near the melting threshold do give results for the melting temperature, T_M, and the heat of fusion, H_f, consistent with values inferred from pulsed laser heating on the nanosecond time scale. The melting temperature and the heat of fusion can be more

accurately determined with picoseond pulse laser heating since for times on the order of the laser pulse duration, thermal diffusion is not effective.

The diffusion equation was then solved for pulsed current heating of graphite fibers. This calculation is informative because the pulsed current heating experiments provide direct evidence for the liquid metal model. The results for the calculations show that the liquid metal model for liquid carbon, in particular the temperature dependence and the magnitude of the electrical resistivity in the liquid state, is in good agreement with experimental data. The calculations are able to reproduce the experimental data well as a function of time for fibers with varying degrees of crystallinity and hence, varying the temperature dependence of the electrical resistivity in the solid phase. The calculations also show that the electrical resistivity for liquid carbon is nearly temperature independent since the temperature of the liquid in the experiment is known to exceed 5000K from experimental measurements and from the results of heat flow calculations.

The diffusion equation was also solved to determine the segregation solute trapping resulting from the rapidly moving solid–liquid interface in laser–melted carbon. The liquid diffusivity,D_l, was determined to be comparable in magnitude to that in other liquids. The Aziz continuous growth model[7] was employed to determine the diffusive speed of the solid–liquid interface, v_D, and this was also shown to be comparable in magnitude to other liquids.

The key parameters which have been determined or confirmed using the calculations are given in table 5.3. The overall result of these calculations is to show the validity of a liquid metal model for the liquid state of carbon at low pressure ($<$ 1kbar). Insulating models for liquid carbon used in the calculations do not reproduce experimental results as is illustrated for both pulsed laser heating and pulsed current heating. The calculations also provide some information about diffusion in liquid carbon which may never be directly measurable in the laboratory.

Property	Description	Value
T_M	Melting teperature	4450K
T_V	Boiling point	4700K
H_f	Heat of fusion	105kJ/mole
D_l	Liquid diffusivity	10^{-4}cm^2/sec
v_D	Interface diffusive speed	25m/sec

Table 5.3: A summary of the values of important parameters suggested by the solution of the diffusion equation for pulsed laser heating, pulsed current heating, and impurity segregation and solute trapping. No value is specified for the heat of vaporization since teh carbon vapor is composed of several different species.

References

[1] H.S. Carslaw and J.C. Jaeger, *Conduction of Heat in Solids*, (Oxford University Press, New York 1959).

[2] P. Baeri, S.U. Campisano, G. Foti, and E. Rimini, *J. Appl. Phys.* 50, 788 (1979).

[3] R.F. Wood and G.E. Giles, *Phys. Rev. B* 23, 6 (1981).

[4] J.M. Poate, G. Foti, D.C. Jacobson (eds.), *Surface Modification and Alloying by Laser, Ion, and Electron Beams*, Plenum Press, New York, (1983).

[5] A.K. Jain, V.N. Kulkarni, and D.K. Sood, *Appl. Phys.* 25, 127 (1981).

[6] J. Steinbeck, G. Braunstein, M.S. Dresselhaus, T. Venkatesan, and D.C. Jacobson, *J. Appl. Phys.* 58, 4374 (1985).

[7] M.J. Aziz, J.Y. Tsao, M.O. Thompson, P.S. Peercy, and C.W. White, *Phys. Rev. Lett.* 56, 2489 (1986).

[8] J.Y. Tsao, *Proceedings of the American Physical Society Meeting* New York, New York, March 16–20 1987, p 455.

[9] J. Steinbeck, G. Braunstein, M.S. Dresselhaus, B.S. Elman, and T. Venkatesan, *Energy Beam–Solid Interactions and Transient Thermal Processing*, Proceedings of the Materials Research Society vol. 35, edited by D.K. Biegelson, G.A. Rozgonyi, and C.V. Shank, (Materials Research Society, Pittsburgh, 1985) p219.

[10] J. Steinbeck, G. Braunstein, M.S. Dresselhaus, T. Venkatesan, and D.C. Jacobson, *Proceedings of the 17th Biennial Conference on Carbon*, Lexington, Kentucky June 16–21 1985, p 429.

[11] J.S. Speck, J. Steinbeck, G. Braunstein, M.S. Dresselhaus, and T. Venkatesan, *Beam–Solid Interactions and Phase Transformations*, Proceedings of the Materials Research Society vol. 51, edited by H. Kurz, G.L. Olsen, and J.M. Poate, (Material Research Society, Pittsburgh, 1986) p263.

[12] F.P. Bundy, *J. Chem Phys.* 38, 618 (1963).

[13] H.R. Leider, O.H. Krikorian, and D.A. Young, *Carbon* 11, 555 (1973).

[14] M.S. Dresselhaus and G. Dresselhaus, *Adv. Phys.* 30, 139 (1981).

[15] J. Heremans, C.L. Olk. G. Eesley, J. Steinbeck, and G. Dresselhaus, *Phys. Rev. Lett.* , (1987).

[16] A.G. Whittaker, *Science* 200, 763 (1978).

[17] A. Ferraz and N.H. March, *Phys. Chem. Liq.* 8, 289 (1979).

[18] M.J. Aziz, *J. App. Phys.* 53, 1158 (1982).

[19] E.A. Chauchard, C.H. Lee, and C.Y. Huang, *Appl. Phys. Lett.* 50, 812 (1987).

Chapter 6

Other Considerations for Liquid Carbon

6.1 Introduction

This chapter will describe some other considerations which are important in determining the properties of liquid carbon from pulsed laser and pulsed current heating studies. Some of the effects which may have to be considered more carefully are rapid resolidification of molten carbon, nonequilibrium material ejection from the surface during pulsed heating, the exact form of the liquid carbon structure factor, and the possibility that liquid carbon may be a semiconducting liquid at low pressure as proposed by Ferraz and March[1].

The first section considers the effects of rapid solidification on the liquid diffusivity and segregation coefficients measured and calculated in chapters 3 and 5. The undercooling of liquid carbon is discussed from considerations of recent work in pulsed laser melted silicon. Also considered in this section is the effect of rapid solidification on the mean crystallite size in the resolidified material after laser heating.

The ejection of material by nonequilibrium mechanisms during pulsed laser heating is discussed in the second section. Recent work by Kelly *et. al.*[2,3,4]

has shown that there are several mechanisms by which material may leave the surface during pulsed laser heating. Each of the mechanisms proposed by Kelly *et. al.* is discussed in terms of pulsed laser heating of graphite.

The third section discusses the liquid structure factor and how the liquid structure factor for liquid carbon may be different if liquid carbon has a partial molecular character. The transport properties of a partially molecular liquid are discussed in terms of liquid metal theory. The results are then compared to liquid Si and Ge.

The final section considers semiconducting liquids and the possibility of semiconducting liquid carbon. The semiconducting liquid is considered to be comprised of molecular clusters which break up when heated or when pressure is applied. This is the model proposed by Ferraz and March[1] for liquid carbon at pressures below $\sim$ 1kbar.

6.2 Rapid Resolidification

Rapid solidification after pulsed laser heating is important for determining the structure of the resolidified material[5]. Rapid solidification also plays a role in the determination of the liquid diffusivity and the segregation coefficients of impurities in the liquid since the length of time the liquid exists and the velocity of the solidification front determine the fraction of impurities that will be trapped by the moving solid–liquid interface. This section considers the changes which may need to be made in our analysis of the liquid diffusivity and segregation coefficients for liquid carbon based on recent rapid solidification work done in pulsed laser melted silicon. Also included in this section is a discussion of the structure of the resolidified material versus the solidification front velocity for laser–melted graphite.

6.2.1 Liquid Diffusivity and Segregation

The liquid diffusivity and the segregation coefficient of liquid carbon depend on the rate at which the liquid resolidifies. Aziz *et. al.*[6] have pointed out that heat flow calculations are not the ideal way of determining the solid–liquid interface velocity during resolidification after pulsed laser melting in silicon. This is because of the undercooling of the molten silicon which occurs due to the rapid removal of energy from the liquid silicon. The large thermal transport comes as a result of the large thermal gradients created during pulsed laser heating. Other considerations are that the pulse laser energy density and the properties of resolidified material are always somewhat uncertain.

Heat flow calculations usually over estimate the regrowth velocity[6] for the reasons cited above. The result of this is an over estimation of the liquid diffusivity and the segregation coefficient since these quantities generally scale with the regrowth velocity (see section 3.5).

Pulsed laser melted graphite has many of the same problems encountered in pulsed laser melted silicon. The rapidly cooling liquid will most likely be undercooled to temperatures several hundred degrees below the equilibrium melting temperature[5], and, as stated previously, the properties of the resolidified carbon are not well known at high temperatures. This would make estimates of the liquid diffusivity and segregation coefficient using heat flow calculations questionable.

The best method for determining the velocity of the liquid–solid interface is to measure it using transient electrical conductivity measurements[6]. Unfortunately, this method of determining the liquid–solid interface velocity is not available for graphite due to the metallic properties of graphite and because thin, highly oriented films of graphite are difficult to make and support. Estimating the properties of the resolidified material by using calculations of the

resolidification process is difficult because the calculations require an intimate knowledge of the liquid–solid interface[7].

From this discussion, our estimates for the liquid diffusivity, D_l, and the segregation coefficient, k, for liquid carbon may be over estimated. Until a reliable transient electrical conductivity measurement can be made on pulsed laser melted graphite, the liquid diffusivity and the segregation coefficient may not be known to much higher accuracy. Our estimates therefore serve as an order of magnitude estimate of these parameters of liquid carbon.

6.2.2 Structure of the Resolidified Material

The structure of the resolidified material is also influenced by the rate at which resolidification takes place. Many studies have been carried out in metals and laser–melted silicon on the relationship between the liquid–solid interface velocity and the crystalline perfection of the resolidified material. The general trends of these studies indicate that the more rapidly the material resolidifies, the more disorder there is in the resolidified material. There is also a critical velocity, for some materials, such that for liquid–solid interface velocities below the critical value, epitaxical regrowth will occur.

The crystalline order of the resolidified material from pulsed laser melted graphite also exhibits a dependence on the velocity of the solidification rate of liquid carbon. Very large resolidification rates of liquid carbon produce highly disordered material while very slow rates of solidification produce polycrystalline material. The dependence of the solidification rate versus pulse energy density is shown in Fig. 6.1. The regrowth velocity was calculated using heat flow calculations (see chapter 5). As discussed in chapter 5, the regrowth rate will be determined by the thermal gradients in the material. As the laser pulse energy density is increased, the thermal gradients in the heated material are

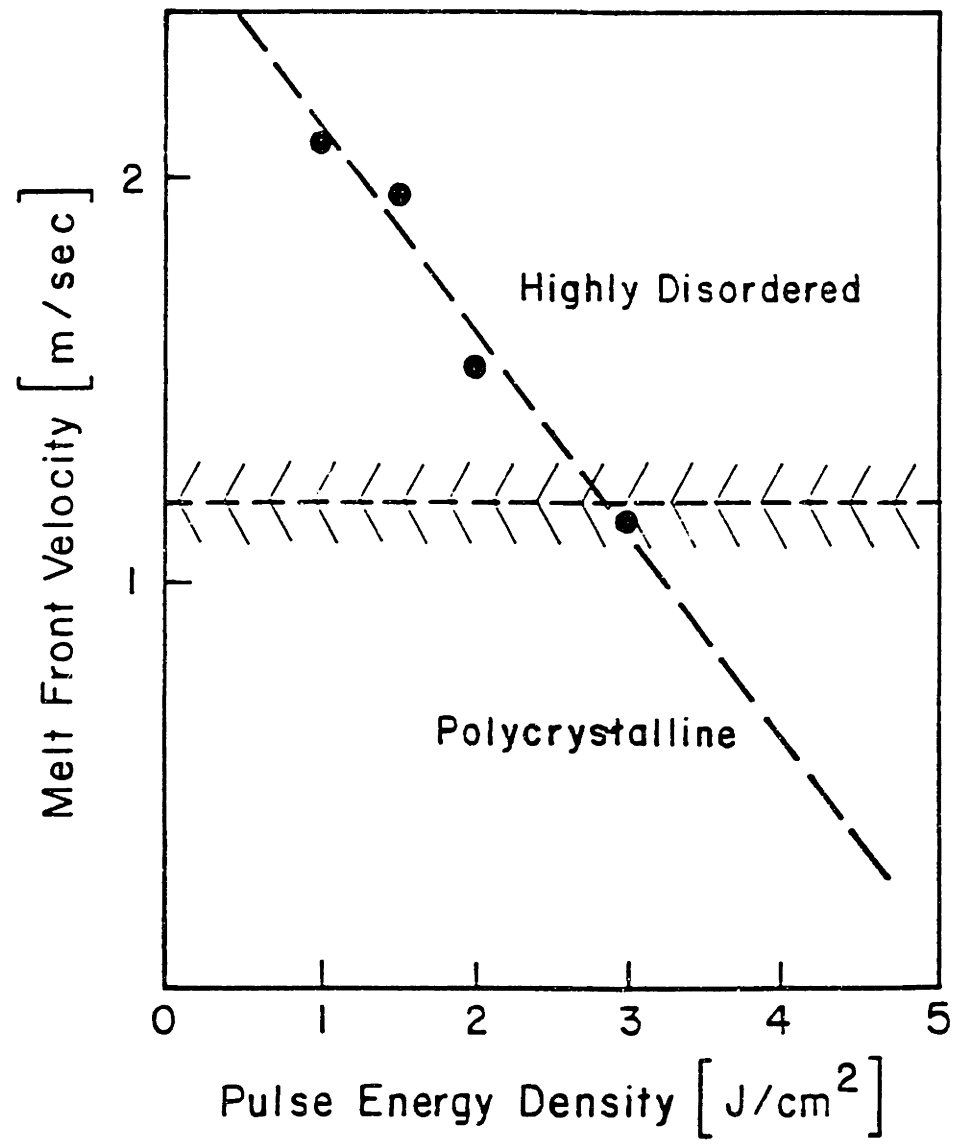

Figure 6.1: Solidification rate versus pulse laser energy density for a pulsed 30nsec ruby laser. The crystalline perfection of resolidified liquid carbon versus the regrowth rate and pulse laser energy density is also shown. The data were accumulated using Raman spectroscopy (see section 3.4).

able to relax via thermal diffusion. Hence, the rate at which the liquid solidifies is decreased.

Also shown Fig. 6.1 is a general characterization of the resolidified material remaining after laser heating. The crystallite size data in Fig. 6.1 were accumulated using Raman spectroscopy (see section 3.4). As can be seen in Fig. 6.1, the higher the regrowth rate, the more disordered the resolidified material will be.

The relationship between the crystalline perfection of the resolidified material and the regrowth velocity is similar to the relation between these quantities for pulsed laser–melted silicon, as the regrowth speed decreases, the crystalline perfection increases. The resolidified material is highly disordered at large velocities, but becomes polycrystalline as the velocity decreases. However, there is no expitaxical regrowth observed for laser melted graphite as there is in silicon. In fact, the maximum average crystallite size in the resolidified region of laser–melted graphite is $\sim 100\mathring{A}$[8,9]. This may be due to the vaporization of carbon during pulsed laser heating. The vaporization front will travel toward the liquid–solid interface. This may not allow the liquid–solid interface to become slow enough for epitaxical regrowth to occur.

6.3 Nonequilibrium Material Loss

Vaporization is known to occur in laser–heated carbon as demonstrated by RBS measurements in chapter 3. The analysis of the material loss using heat flow calculations in chapter 5 suggested that the material lost during pulsed laser heating is due to the sublimation and vaporization of carbon. However, recent experimental work by Kelly *et. al.*[2,3,4] has demonstrated that there are several other, nonequilibrium, processes which may remove material from the surface of a laser heated material. The nonequilibrium processes include plasma

formation, hydrodynamic effects, and material loss due to thermal shock.

6.3.1 Mechanisms of Nonequilibrium Material Loss

Material loss via nonequilibrium processes has been shown by Kelly *et. al.*[4] to occur primarily during laser heating of pure metals. The formation of electron–ion plasmas above the surface of a laser heated metal has been discussed in previous sections and is attributed to the large absorption coefficient in metals which vaporizes metals at relatively modest laser pulse power densities. The metal vapor is then partially ionized by the laser pulse and the plasma density increases from impact ionization until the critical density for electromagnetic propagation is reached. Electrons and ions are accelerated away from the surface by electrostatic attraction.

Hydrodynamic material loss is where the surface tension of the liquid causes the formation of liquid spheres which detach themselves from the substrate. The loss of material via hydrodynamic effects is initiated when the surface of the liquid becomes nonuniform, either by nonuniform heating, causing part of the liquid to expand more rapidly than the other parts, or by defects in the solid surface which allow liquid drops to form on the surface. The formation of the liquid spheres is shown in Fig. 6.2. Surface tension on the liquid drop then causes the drop to assume a spherical shape which pinches the drop off of the surface.

The loss of material via thermal shock is the result of rapid thermal expansion causing a stress to build in the solid which surpasses the yield stress of the material. The result is the expulsion of solid material from the surface. Material loss via the thermal shock mechanism is characteristic of materials with a large thermal expansion coefficient, a large Young's modulus and a high melting temperature.

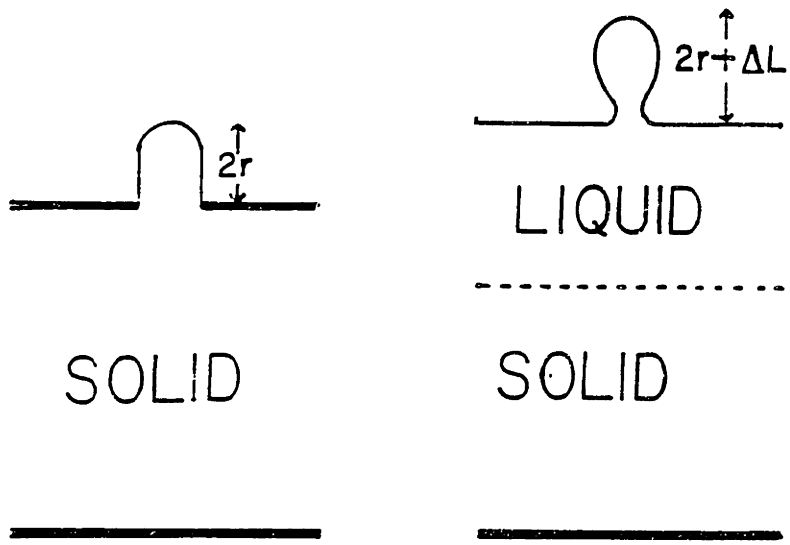

Figure 6.2: The formation of liquid spheres on the surface of a laser heated material. An initial defect in the surface is pinched off from the surface tension on the liquid. (Taken from Kelly and Rothenberg[4])

6.3.2 Nonequilibrium Material Loss in Graphite

Electron–ion plasma formation has been discussed in connection with transient optical measurements of graphite during pulsed laser heating. The effect of plasma formation on the vaporization of graphite during laser heating may be to increase the total amount of material removed from the surface.

The dominant features on the surfaces of metals after pulsed laser heating, observed using SEM, are cracks and spheres, similar in size to the spheres observed during pulsed laser heating of graphite (Fig. 3.15). This suggests that some of the material lost during pulsed laser heating of graphite may be in the form of liquid spheres which are pinched off of the surface by hydrodynamic forces.

The surface of the graphite used in this work is known not to be atomically smooth. Therefore, material loss via hydrodynamic mechanisms would not be surprising. As of this writing, there is no numerical method to account for material loss via this mechanism. This is due to the material loss being dependent on the quality of the surface being heated and the uniformity of the heating laser pulse.

The loss of material via a thermal shock mechanism is also suggested by Fig. 3.15 from the appearance of torn graphite on the surface. Graphite meets the criteria for material loss due to thermal shock: a high melting temperature ($\sim$ 4500K), a large thermal expansion (15 percent along the c–axis), and a large Young's modulus. From these considerations, the loss of material via the thermal shock mechanism seems likely.

The effect of nonequilibrium material loss on our numerical calculations (chapter 5) would be to increase the calculated material loss. The fraction of the material loss in laser heated graphite due to nonequilibrium mechanisms is probably small. Dreyfus *et. al.*[10] have shown that vaporization dominates the

material loss in graphite during pulsed laser heating. However, if nonequilibrium mechanisms increase the material loss by up to 20 percent, the calculated results for material loss would be in better agreement with experimental data.

The effect of nonequilibrium material loss on our estimates of the melting temperature and the heat of fusion in graphite is most likely small. This is because nonequilibrium material loss mechanisms have been shown not to be the dominant material loss mechanisms in laser heated graphite[10].

6.4 The Liquid Structure Factor

In order to apply liquid metal theory to liquid carbon, the structure factor for liquid carbon must be known. The calculations done in chapter 4 for liquid carbon assumed that the liquid structure factor may be calculated directly using the correlation function derived by Ashcroft and Lekner[11] from the special case of the Percus–Yevick[12] theory where hard spheres of radius σ, are packed together so that they fill a fraction of the total volume, η. The significance of the liquid structure factor in liquid metal theory is that the transport properties of liquid metals, calculated using the Ziman[13], are sensitive to the position and shape of the primary peak in the liquid structure factor[14].

6.4.1 Nonsimple Liquid Metals

The simple equation for the liquid structure factor derived by Ashcroft and Lekner does not approximate the liquid structure factor well for high valence liquid metals particularly near the melting temperature[15,16,17]. This is because the primary peak of the liquid structure factor in high valence liquid metals is asymmetric due to the molecular character of the liquid and/or vacancies in high valence liquid metals near the melting temperature[18]. This is particularly true for the group IV liquid metals Sn[19,20] and Ge[21] where

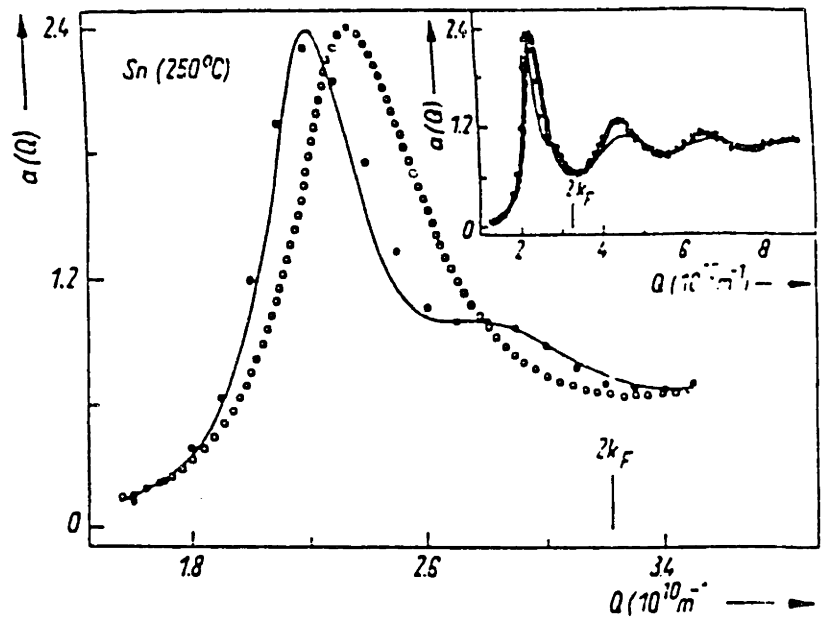

Figure 6.3: The liquid structure factor for Sn. The solid circles are experimental points[22] while the open circles represent the structure factor calculated from the Ashcroft and Lekner correlation function with $\eta = 0.43$. The solid line represents a more complex model proposed by Canessa *et. al.*[18].

the primary peak in the structure factor is asymmetric. The measured liquid structure factor for Sn at 250°C[22] is shown in Fig. 6.3 along with the liquid structure factor calculated using the Ashcroft and Lekner correlation function with $\eta = 0.43$. Also shown in Fig. 6.3 is the structure factor calculated using a more complex model by Canessa *et. al.*[18] which will be described below.

A more complex model for the liquid structure factor of liquid metals has been proposed by Canessa *et. al.*[18] which builds upon the Ashcroft and Lekner model. In their model, Canessa *et. al.* propose that the liquid is made up of two kinds of hard spheres requiring two different hard sphere radii, $\sigma_{i=1,2}$, and packing fractions, $\eta_{i=1,2}$. Canessa *et. al.*[18] also introduce correction

Component	η	σ (Å)	ϵ	δ
1	0.34	2.921	0.739	1.923
2	0.68	2.718	1.838	0.148

Table 6.1: The parameters used by Canessa *et. al.*[18] for calculating the liquid structure factor of Sn.

factors $\epsilon_{i=1,2}$ to the Ashcroft and Lekner packing fraction η_{AL} so that $\eta_i = \epsilon_i \eta_{AL}$. Also proposed by Canessa *et. al.*[18] are amplitudes of correction, $\delta_{i=1,2}$, to weight the equations to account for the fact that there are two liquids mixed together. The effect of adding these correction factors to the Ashcroft and Lekner model is that the liquid is now considered to be comprised of two kinds of hard spheres with two different substructures.

The structure factor for the liquid is calculated by taking the average of the structure factors of the two constituents of the liquid. That is

$$a(k) = \frac{1}{2}(a_1(k) + a_2(k)) \tag{6.1}$$

where a_i is given by

$$a_i(k) = \frac{1}{1 - \delta_i n c_i(k)} \tag{6.2}$$

which is the same as Eq. 4.20 except for the factor of δ in the denominator.

Canessa *et. al.*[18] have used their model to calculate the structure factors for several high valence liquid metals. Their results for Sn are in Fig. 6.3 using the parameters in Table 6.1. The calculated structure factor using the Canessa *et. al.* model provides a much better fit to the experimental data as seen in Fig. 6.3. The most noticeable improvement comes in fitting the shoulder which appears on the high Q side of the primary peak at $Q \simeq 2.2 \times 10^{-10}\mathrm{m}^{-1}$.

6.4.2 The Structure Factor of Liquid Carbon

The liquid structure factor of carbon is likely to be somewhat different from the structure factor calculated using the Ashcroft and Lekner correlation function. This is particularly true for temperatures near the melting temperature and at pressures below 10kbar as shown above due to the low liquid density. An application of the Cassena *et. al.* model to liquid carbon is meaningless without experimental data to make a comparison with the calculation. There is no reasonable way of selecting the ϵ_i and δ_i for liquid carbon required by the model.

Even though we cannot use the Cassena *et. al.* model to obtain a better estimate of the liquid structure factor, there are some trends in the experimentally determined structure factors for high valence liquid metals. The primary peak of the structure factor for high valence liquid metals appears to be consistently at smaller values of Q, relative to the calculated position of the primary peak using the Ashcroft and Lekner model. The implication of shifting the position of the primary peak downward means that the small Q contribution to the electrical resistivity will be greater than predicted by the Ashcroft and Lekner model.

When the Heine–Abarenkov model potential for the ions in liquid carbon is used, the down shifting of the primary peak in the liquid structure factor means that the large potential at small Q will play a greater role in determining the electrical resistivity of liquid carbon. The net effect would be to increase the electrical resistivity of liquid carbon; the exact amount of the increase will depend on the size of the shift of the primary peak.

6.5 Liquid Semiconductors

If the increase in the electrical resistivity of liquid carbon due to a shift of the structure factor is large, then liquid carbon might be considered a liquid semiconductor. A liquid semiconductor model for liquid carbon was proposed by Ferraz and March[1] in order to accommodate all of the experimental results on liquid carbon from Jones[23], suggesting an insulating liquid phase, and Bundy[24], suggesting a metallic liquid phase. The major difference between the liquid metal and semiconductor models is the appearance of a pseudogap in the density of states where the Fermi level lies in the liquid semiconductor model. The formation of the pseudogap may come from vacancies in the liquid or, from the atoms in the liquid being strongly correlated with their nearest neighbors and forming clusters.

Unfortunately, there is not a simple model (such as the free electron gas for liquid metals) which may be easily applied to liquid semiconductors. Reviews of liquid semiconductors have been given by Mott and Davis[25] and extensively treated by Glazov *et. al.*[26] and by Cutler[27]. In this section, the possibility of a semiconducting phase of liquid carbon is discussed in light of our experimental results.

6.5.1 Characteristics of Semiconducting Liquid Carbon

If a semiconducting phase of liquid carbon exists, then it is likely to be at temperatures close to the melting temperature, as demonstrated by experimental results for the liquid structure factor of other high valence materials shown in the previous section. It is also likely that the phase change from a semiconducting to metallic liquid would not be first order, as suggested by Ferraz and March[1], but second order, where there is a gradual change from a semiconducting to metallic liquid as vacancies in the liquid disappear or as clusters in

the liquid break up as the temperature is raised.

The properties of semiconducting liquid carbon which our experiments may be sensitive to are as follows: Semiconducting liquid carbon should have a relatively high electrical resistivity in the range of $300 < \rho_l < 5000\mu\Omega$–cm[27]. The thermal conductivity of semiconducting liquid carbon is still be dominated by the electronic component[27], but the magnitude of the thermal conductivity would be sharply reduced compared to metallic liquid carbon due to a much lower carrier density in the semiconducting liquid. The specific heat of the semiconducting liquid would be comparable to the specific heat of the metallic liquid since the specific heat will be dominated by the atomic contribution of $C_p \simeq 3R$ where R is the universal gas constant. The optical properties are difficult to estimate since the general theory for the optical properties of liquid semiconductors is not well developed.

A high resistivity for liquid carbon of $\rho_l \simeq 1\text{m}\Omega$–cm has been measured by Mitchell *et. al.*[28] for temperatures up to 6000K. These measurements were carried out during pulsed current heating of glassy carbon, a highly disordered carbon, and may be subject to errors based on the large thermal expansion observed after the measurements were made.

6.5.2 Experimental Measurements

From the properties outlined above, our pulsed current heating experiments would be the most sensitive to the properties of a semiconducting phase of liquid carbon. The transient electrical resistivity measured during pulse current heating should show a marked increase when the semiconducting liquid phase is formed. This is particularly true for graphite fibers with T_{HT}'s of 2300°C and higher, since these fibers possess 3-D ordering. However, the experimental results on graphite fibers with T_{HT}'s greater than 2300°C show that the electrical

resistivity of these fibers never deviates greatly from a linear increase with temperature and never becomes greater than 200$\mu\Omega$–cm (Fig. 3.37). The pressure exerted on the fiber and the liquid from differential thermal expansion and the dynamic vapor pressure is only a few hundred bar as discussed in section 3.7. These results suggest that a semiconducting liquid carbon phase would have to exist at pressures below a few hundred bar rather than at pressures up to 1.5kbar, as suggested by Ferraz and March[1].

Unfortunately, heat flow calculations will not be able to prove or disprove the existence of a semiconducting phase of liquid carbon. This is because the thermal properties of the semiconducting phase are somewhere between the properties of hot solid graphite and metallic liquid carbon. In similar fashion, post–heating studies of pulsed laser melted graphite cannot prove or disprove the existence of a semiconducting liquid carbon phase because of the unknown solidification properties of liquid carbon. As discussed in section 3.4.3, transient optical probing of carbon during laser heating is a complicated by carbon vaporization.

The heat flow calculations do indicate, however, that a metallic liquid is created by pulsed laser heating. Vapor pressure calculations in section 3.6 suggest that at times after the laser pulse, the pressure on the surface is only 200bar so that this would be an upper limit on the pressure of a semiconducting liquid carbon phase. If these results are taken together with the measurements of the triple point discussed in chapter 1, then a semiconducting phase of liquid carbon would only exist at pressures, P, in the range $100 < P < 200$bar and at temperatures in the range $4400 < T < 4800$K. A low pressure phase diagram which includes a semiconducting liquid phase and which incorporates our experimental results is shown in Fig. 6.4.

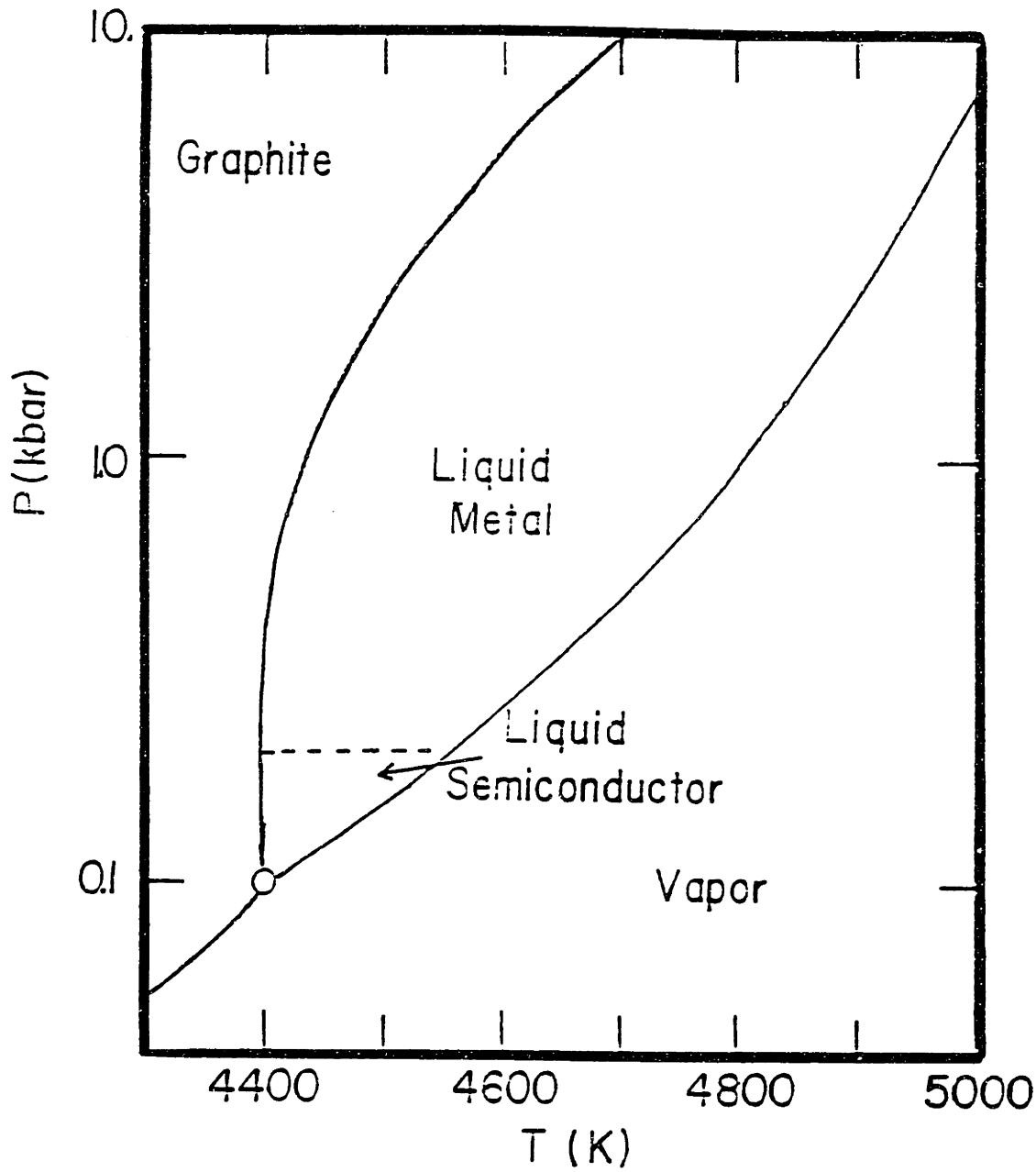

Figure 6.4: A low pressure phase diagram for carbon which includes a semiconducting liquid phase. The phase boundaries for the semiconducting liquid are suggested by our experimental data.

6.6 Summary

This chapter has presented some considerations which have not, until now, been included in our analysis. The effects of rapid solidification on the liquid diffusivity and segregation coefficients of impurities in liquid carbon have been discussed in terms of observed effects in liquid silicon. The liquid diffusivity and the segregation coefficients calculated in our analysis may be large since the effects of liquid undercooling have been neglected. The solidification front velocity of liquid carbon on graphite has also been shown to correlate with the structure of the resolidified material in a way similar to silicon.

Nonequilibrium material loss has been shown to occur during pulsed laser heating of graphite, but the amount of material lost by nonequilibrium processes is probably small. By taking account of material that is lost by nonequilibrium means, our calculated vaporization results may be brought into better agreement with the experimental measurements of material loss using RBS.

The liquid structure factor has been re–examined in lieu of structure factor measurements on Ge and Sn which demonstrate that the Ashcroft and Lekner[11] formula is not adequate when considering high valence liquid metals. The primary peak in the liquid structure factor of high valence liquid metals tends to be asymmetric and the position of the peak lies at lower values of Q than those predicted by the Ashcroft and Lekner formula. The effect of a shift of the primary peak in the liquid carbon structure factor would most likely increase the calculated electrical resistivity of liquid carbon.

The final section of the chapter considered the possible existence of a semiconducting liquid carbon phase. An outline of the properties of a semiconducting liquid carbon phase was presented. From our experimental results and calculations, a semiconducting phase of liquid carbon would only exist at pressures between 100 and 200bar and at temperatures between 4400 and 4800K.

References

[1] A. Ferraz and N.H. March, *Phys. Chem. Liq.* 8, 289 (1979).

[2] R. Kelly, J.J. Cuomo, P.A. Leary, J.E. Rothenberg, B.E. Braren, and C.F. Aliotta, *Nuc. Instr. and Meth. in Phys. Res.* B9, 329, (1985).

[3] J.E. Rothenberg and R. Kelly, *Nuc. Instr. and Meth. in Phys. Res.* B1, 291, (1984).

[4] R. Kelly and J.E. Rothenberg, *Nuc. Instr. and Meth. in Phys. Res.* B7/8, 755, (1985).

[5] A.G. Cullis, *Energy Beam–Solid Interactions and Transient Thermal Processing, Symposium Proceedings of the Materials Research Society* D.K. Biegelsen, G.A. Rozgonyi, and C.V. Shank eds., (MRS: Pitssburgh, 1984) p15.

[6] M.J. Aziz, J.Y. Tsao, M.O. Thompson, P.S. Peercy, and C.W. White, *Phys. Rev. Lett.* 56, 2489 (1986).

[7] J.Y. Tsao, *Proceedings of the American Physical Society Meeting* New York, New York, March 16–20 1987, p 455.

[8] J. Steinbeck, G. Braunstein, M.S. Dresselhaus, T. Venkatesan, and D.C. Jacobson, *Proceedings of the 17th Bienniel Conference on Carbon* Lexington, KY, 1985.

[9] J.S. Speck, J. Steinbeck, G. Braunstein, M.S. Dresselhaus, and T. Venkatesan, *Energy Beam–Solid Interactions and Phase Transformations, Symposium Proceedings of the Materials Research Society* H. Kurz, G.L. Olsen, and J.M. Poate eds., (MRS: Pitssburgh, 1985) p263.

[10] R.W. Dreyfus, R.E. Walkup, R. Kelly, and R. Srinivasan, (to be published) (1987).

[11] N.W. Ashcroft and J. Lekner, *Phys. Rev.* 145, 83 (1966).

[12] J.K. Percus and G.J. Yevick, *Phys. Rev.* 110, 1 (1958).

[13] J.M. Ziman, *Phil. Mag.* 6, 1013 (1961).

[14] E. Canessa and J. Vignolo, *Phys. Stat. Solidi B* 119, 429 (1983).

[15] P.D. Adams, *Phys. Rev. Lett.* 21, 1324 (1968).

[16] J.P. Badiali and C. Regnaut, *Phys. Stat. Solidi B* 49, 339 (1974).

[17] J.P. Badiali, A. Defrain, M. DuPont, and C. Regnaut, *Phys. Stat. Solidi B* 80, 533 (1977).

[18] E. Canessa, D.F. Mariani, and J. Vignolo, *Phys. Stat. Solidi B* 124, 465 (1984).

[19] D.M. North, J.E. Enderby, and P.A. Egelstaff, *J. Phys. C* 1, 1075 (1968).

[20] D. Jovic and I. Padureanu, *J. Phys. C* 9, 1135 (1976).

[21] M. Davidovic, M. Stojic, and D. Jovic, *J. Phys. C* 16, 2053 (1983).

[22] Y. Waseda and K. Suzuki, *Phys. Stat. Solidi B* 49, 339 (1972).

[23] M.T. Jones, Rep. PRC-3, Nat. Carbon Res. Lab., Parma, OH (1958).

[24] F.P. Bundy, *J. Chem. Phys.* 38, 618 (1963).

[25] N.F. Mott and E.A. Davis, *Conduction Processes in Non-Crystalline Materials*, (Clarendon, Oxford), 1979 p. 50.

[26] V.M. Glazov, S.N. Chizhevskaya, and N.N. Glagoleva, "Liquid Semiconductors", (Plenum Press, New York, 1969).

[27] M. Cutler, "Liquid Semiconductors", (Academic Press, New York, 1977).

[28] A.C. Mitchell, J.W. Shaner, and R.N. Keeler, *Physica* 140B, 386 (1986).

Chapter 7

Conclusions

7.1 General Summary

This work has been concerned with determining the high temperature properties of graphite and liquid carbon by using pulsed laser heating. Pulsed laser heating was used because the technique can be applied to highly oriented graphites and the graphite will form its own crucible. The pulsed current heating technique, traditionally used to study high temperature carbons, cannot work with highly oriented graphites because of the low electrical resistivity of graphite. The pulsed current heating technique also requires that the graphite be attached to other materials which have lower melting temperatures which may introduce impurities.

Previous work on the low pressure, high temperature portion of the carbon phase diagram has resulted in several very different proposals for this portion of the carbon phase diagram. The proposals include molecular phases of solid carbon[1], insulating and metallic liquids[2], and various triple points. The previous experimental work on liquid carbon suggests that there are two liquid carbon phases, one insulating[3] and one metallic[4]. No previous researcher has ever observed both of the proposed liquid phases with a single experiment.

The properties of solid graphite have been investigated up to temperatures

of 3000K. The properties of graphite beyond 3000K are little known, primarily due to experimental difficulties. Therefore, the model proposed for the properties of graphite above 3000K is an extrapolation of the properties at lower temperatures[5].

Post–heating analysis of the laser–irradiated region on a graphite surface demonstrated that graphite can be melted using pulsed laser heating. The disorder depth remaining after pulsed laser heating and the material lost during pulsed laser heating were measured using RBS and ion channeling. Studies of the microstructure in the laser–irradiated region by Raman spectroscopy and electron microscopy demonstrate that the average crystallite size in the disordered region increases as the laser pulse energy density increases, similar to the behavior observed in silicon[6].

Our experimental work using pulsed laser heating provides estimates for the melting temperature, $T_M \sim 4500$K, and heat of fusion, $\Delta H \simeq 125$kJ/mole of graphite which are comparable to those of other researchers[4,5]. Pulsed laser heating on the nanosecond time scale also demonstrates that there is a considerable loss of material during pulsed laser heating and that the released material drastically changes the optical properties of the space above the laser–irradiated region.

Segregation and solute trapping have been studied in liquid carbon. From the segregation of Ge and As, the liquid diffusivity of Ge and As in liquid carbon has been determined to be $D_l \sim 2.5 \times 10^{-4}$cm^2/sec which is comparable to the liquid diffusivity of liquid silicon. The segregation coefficients for Ge and As in liquid carbon have been estimated to be $k \sim 0.17$.

In order to try to overcome the difficulties encountered during transient measurements of nanosecond pulse laser heated graphite, picosecond pulse laser heating and electric current pulse heating of highly oriented graphite fibers

were done. By using picosecond pulse laser heating, it was thought that liquid carbon could be optically probed before the carbon vapor could significantly alter the optical properties above the surface. The pulsed current heating of graphite fibers has the potential of generating a large amount of liquid from an ordered form of graphite. At the same time, the pulsed current heating technique provides a direct measurement of the electrical resistivity of liquid carbon.

Transient optical measurements during picosecond pulse laser heating have been shown to be more difficult to analyze than originally thought by Malvezzi *et. al.*[7]. The results of picosecond pulse laser heating experiments suggest that vaporization is required for liquid carbon to be formed by pulsed laser heating. The results also give an estimate of the melting temperature and heat of fusion comparable to the values obtained during nanosecond pulsed laser heating.

The electrical resistivity of liquid carbon was determined by pulsed current heating of graphite fibers to be $\rho_l \simeq 30\mu\Omega$–cm. The temperature dependence of the electrical resistivity of graphite fibers was also determined from the pulsed current heating technique. The extrapolation model for the high temperature properties of graphite was shown to be consistent with the pulsed current heating results since the temperature dependence of electrical resistivity of graphite fibers at high temperature matched the temperature dependence of the electrical resistivity at lower temperatures.

The results of experimental work using pulsed laser heating and pulsed current heating suggest that liquid carbon is a liquid metal. Therefore, liquid metal theory was applied to model liquid carbon. The liquid structure factor was calculated using the Ashcroft and Lekner[8] formula, while the model Heine–Abarenkov model potential[9] was used to describe the carbon ions in

the liquid. The Ziman[10] integral for the electrical resistivity was then solved. In this framework, the electrical resistivity of liquid carbon is calculated to be $\rho_l \simeq 40\mu\Omega$–cm.

The Fermi gas model of liquid metals was then used to calculate the thermal and optical properties of liquid carbon. The specific heat is seen to be close to the specific heat for liquid carbon proposed by Leider *et. al.*[5]. The thermal conductivity is seen to increase sharply as graphite melts. The plasma frequency for liquid carbon is $\simeq$ 10eV.

The liquid metal model for liquid carbon was then tested using a numerical solution to the heat equation and the disorder depth and material loss information obtained from experiments on nanosecond pulsed laser heating of graphite. The results of these calculations strongly support the liquid metal model for liquid carbon. Similar calculations for picosecond pulse laser heating demonstrate that carbon vaporization may indeed cause difficulties with optical measurements. Calculations on pulsed current heating of graphite fibers are able to reproduce experimental results to within estimated limits of error.

The diffusion equation was also solved numerically to determine the liquid diffusivity and segregation coefficients of Ge and As in liquid carbon more accurately. The calculations utilized the melt front velocities calculated from the heat flow analysis above. The Aziz[11] continuous growth model was used to calculate the segregation coefficient from the velocity of the liquid–solid interface. The results of these calculations suggest that the liquid diffusivity is $D_l \simeq 1.0 \times 10^{-4}\text{cm}^2/\text{sec}$ and the diffusive speed of the liquid–solid interface is $v_D \simeq 25\text{m/sec}$.

Other considerations which may alter the properties of liquid carbon published in this work are rapid resolidification, nonequilibrium material loss, the precise shape of the liquid structure factor, and the possibility of the existence

of a semiconducting phase of liquid carbon. The effects of rapid solidification of liquid carbon will alter our results for the liquid diffusivity and segregation coefficient. The effects of nonequilibrium material loss have been shown to be negligible in terms of the total material lost during pulsed laser heating. The liquid structure factor is central to theoretically determining the properties of liquid carbon. Small deviations to the liquid structure factor obtained from the Ashcroft and Lekner[8] formula could predict a somewhat larger electrical resistivity for liquid carbon. The possibility of a semiconducting phase of liquid carbon was discussed. From our experimental data, the existence of a semiconducting liquid phase of carbon would be limited to pressures in the range $10 < P < 200$bar and temperatures in the range $4400 < T < 4800$K.

7.2 The Phase Diagram of Carbon

From our experimental work, the phase diagram for liquid carbon would appear to contain a single solid phase, graphite, a single metallic liquid phase, and a vapor phase comprised of many molecular forms of carbon. The proposed phase diagram is shown in Fig. 7.1. We have no evidence to support the existence of carbyne phases proposed by Whittaker[1] or to support the existence of a semiconducting and insulating phase of liquid carbon[3,12]. The triple point given in Fig. 7.1 has been taken at 120bar, to give the best agreement with existing data. The positive slope of the graphite melting lines and the vaporization lines has been retained from experimental data of Bundy[4].

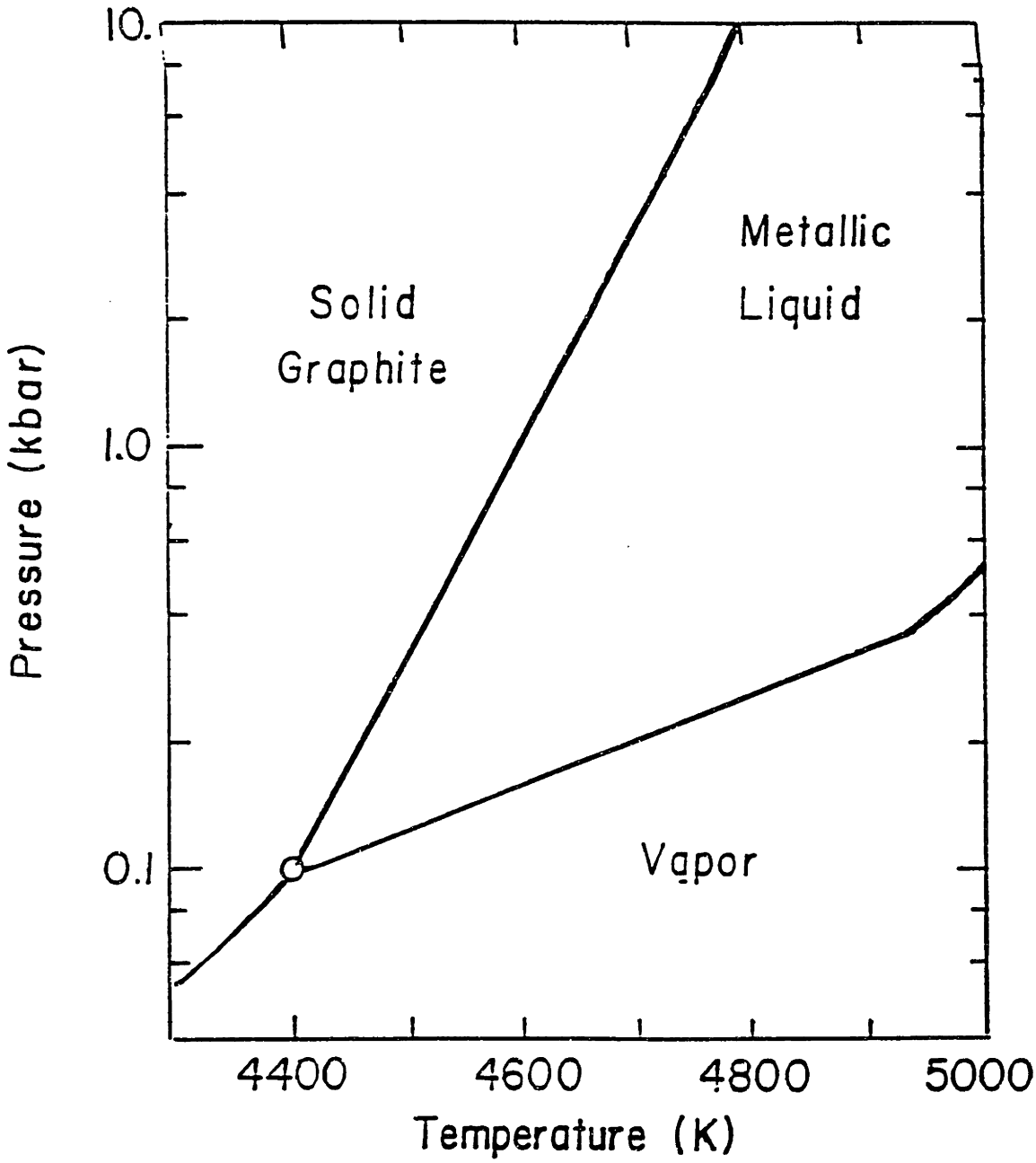

Figure 7.1: The low pressure phase diagram for carbon proposed by this work. Note that only a single metallic liquid phase has included.

7.3 The Properties of High Temperature Graphite and Liquid Carbon

The properties of high temperature graphite are extrapolations of the properties of graphite at lower temperatures. This is suggested by pulsed current heating of graphite fibers and by numerical calculations.

The properties of liquid carbon are those of a liquid metal. The specific heat for liquid carbon can be calculated directly from a Fermi gas model. The thermal conductivity is given by the Wiedermann–Franz relation while the optical properties may be calculated from the Drude model. The exact values for these properties will all depend on the electrical resistivity, calculated using the Ziman integral[10].

7.4 Suggestions for Future Work

The work presented in this thesis comes from a large number of experiments. While a consistent picture of the properties of high temperature graphite and liquid carbon has been obtained, it would be desirable to obtain a large amount of information from a single experiment or a very small number of experiments. To reach this goal, a more intense study of amorphous carbon may be appropriate. The high electrical resistivity of amorphous carbon eliminates some of the complications introduced by the metallic properties of graphite for transient measurements during pulsed laser heating. It would also be interesting to see the parallels between amorphous carbon and amorphous silicon during pulsed laser heating.

The use of diamonds in pulsed laser melting experiments may not provide the information sought. The high absorption edge in diamond make the use of pulsed laser–melting difficult. In addition, the diamond may undergo a

diamond–graphite transition which would add serious complications to analyzing the data obtained during transient measurements.

The key to the theoretical determination of the properties of liquid carbon lies in determining the liquid structure factor for liquid carbon experimentally. This may be done using synchrotron radiation during pulsed laser heating. If the liquid structure factor is very different from the the structure factor given by the Ashcroft and Lekner formula, then the transport properties for liquid carbon will be very different than those proposed in this work.

It would also be desirable to know the electron–phonon scattering time in graphite. This may be accomplished by using femtosecond excitations of graphite. This work would lay the ground work for understanding the results of picosecond pulse laser heating in graphite more thoroughly.

During the course of this work, several new discoveries were made about the properties of carbon. The photoconductance of disordered graphite, the large material losses during rapid heating of graphite, and the fast pregraphitization of amorphous carbon films certainly warrent further investigation. By understanding these properties of carbon, perhaps a better method for studying liquid carbon can be devised.

References

[1] A.G. Whittaker, *Proceedings of the 13th Bienniel Conference on Carbon*, (American Carbon Society), 413 1977.

[2] A. Ferraz and N.H. March, *Phys. Chem. Liq.* 8, 289 1979.

[3] M.T. Jones, Rep. PRC-3, Nat. Carbon Res. Lab., Parma, OH 1958.

[4] F.P. Bundy, *J. Chem. Phys.* 38, 618 1963.

[5] H.R. Leider, O.H. Krikorian, and D.A. Young, *Carbon* 11, 555 1973.

[6] A.G. Cullis, *Energy Beam–Solid Interactions and Transient Thermal Processing, Symposium Proceedings of the Materials Research Society* D.K. Biegelsen, G.A. Rozgonyi, and C.V. Shank eds., (MRS: Pitssburgh, 1984) p15.

[7] A.M. Malvezzi, N. Bloembergen, and C.Y. Huang, *Phys. Rev. Lett.* 57, 146 1986.

[8] N.W. Ashcroft and J. Lekner, *Phys. Rev.* 145, 83 1966.

[9] V. Heine and I. Abarenkov, *Phil. Mag.* 9, 451 1964.

[10] J.M. Ziman, *Phil. Mag.* 6, 1013 1961.

[11] M.J. Aziz, *J. Appl. Phys.* 53, 1158 1982.

[12] A.C. Mitchell, J.W. Shaner, and R.N. Keeler, *Physica* 140B, 386 1986.